Faculty of Science and Engineering

Department of Applied Physics

Metal Hydrides as Energy Storage for Concentrated Solar Thermal Applications

Seyd Payam Javadian-Deylami

This thesis is presented for the Degree of

Doctor of Philosophy

of

Curtin University

June 2017

Declaration

To the best of my knowledge and belief this thesis contains no material previously published by any other person except where due acknowledgement has been made. This thesis contains no material which has been accepted for the award of any other degree or diploma in any university.

Signature: Pangan Jandi

Date: June 2017

Abstract

The increase in world population is linked to a significant increase in worldwide energy consumption: mostly originating from fossil fuels, and has led to the search for a clean energy source that will fulfill the world's energy requirements. Hydrogen is considered a promising future carrier of renewable energy, compared to the conventional carbon polluting fossil fuels used in today's society. Utilization of hydrogen for mobile or stationary applications can eliminate harmful emissions of particles and exhaust gases. Since hydrogen is a gas at ambient conditions, the major challenge is to store hydrogen in a compact and dense way in the solid state. Solar energy is one of the most abundant renewable energy sources available on Earth; hence efficient solar energy conversion into electricity or power, is a highly focused research area. The issue with solar energy concentration is that the energy supply is limited to daylight hours. However by incorporation of a thermal energy storage system into a Concentrating Solar Thermal (CST) power plant, the energy supply will be available outside of daylight hours. In this proposal, metal hydrides and their thermochemical reactions are used as the medium for thermal energy storage in the CST systems-context. Concentrated solar energy is thermally stored in a coupled system of two different hydrides, with two different operating temperatures (high and low). By changing the applied pressure to the hydride bed, hydrogen will either absorb or desorb facilitating release and absorption of heat, respectively. The main research goal of this project is to synthesize different classes of high-temperature/low-temperature metallic hydrides/complex metal hydride (HTMH/LTMH) as thermal energy storage candidates and to characterize them with regards to: chemical composition, thermal stability, thermodynamic properties, sorption kinetics, and stability of hydrogen capacity during cycling.

$LiBH_4$ is of significant interest as a solid state hydrogen storage material, due to its relatively large hydrogen storage capacity. However it suffers from poor sorption kinetics and insufficient cyclic stability. To alter the hydrogen storage properties of $LiBH_4$, other complex hydrides such as $Ca(BH_4)_2$, $NaBH_4$ and $NaAlH_4$, may destabilise $LiBH_4$, and facilitate beneficial hydrogen storage properties due to an intimate interaction between the respective alkaline metals and boron, not to mention a relatively larger hydrogen storage capacity may be obtained. The cyclic stability of the following binary complex hydride systems $LiBH_4$-$Ca(BH_4)_2$, $LiBH_4$-$NaBH_4$ and $LiBH_4$-$NaAlH_4$ shows significant stability and due to their relative high gravimetric H_2 storage capacity and specific heat storage capacity, they may potentially act as both HTMH and LTMH.

The theoretical heat storage capacity of LiH is one of the highest for alkali metal hydrides (8397 kJ/kg). In fact it is the highest known for any metal hydride and it is also the highest known for any reversible solid-gas thermochemical reaction, which makes it a potential heat storage material. Unfortunately, the operating temperature for LiH at a 1 bar hydrogen equilibrium pressure is 956 °C, which is above the temperature regime required for the CPS system, not to mention the relative high

cost of Li. However, by adding Al to the system, facilitates destabilisation of LiH, thus decreasing the operating temperature to ~574 °C, while maintaining a reversible hydrogen content of 2.3 wt.%. The addition of Al not only favours improved kinetics, thermodynamics and high reversibility but up to 44 % cost reduction of the raw materials may be obtained. This highlights the potential of reducing the cost of HTMH by destabilisation.

Acknowledgements

I would like to thank many people who have been of great help for my accomplishments during my PhD studies.

First and foremost, I wish to acknowledge my supervisor, Professor **Craig E. Buckley** for his excellent guidance and supervision throughout the period of my work. He has been very helpful with every small or large problem that I have come across during my PhD.

Thanks to Dr. **Drew A. Sheppard** for is weekly guidance and for many hours of fruitful conversation about science. He has directed me in the right way, on everything from experimental setup to the writing process.

A large thanks to Professor **Torben R. Jensen**, for is fruitful collaboration during my PhD. I am grateful for being able to visit his lab at Aarhus University for various scientific experiments. His encouragement, guidance and support is highly appreciated.

I would like to acknowledge the organisations and facilities that supported my research. Curtin University and the Australian Research Council (ARC) for financial support.

I would also like to thank my colleagues Dr. **Veronica Sofianos**, Dr. **Terry Humphries**, Dr. **Matthew Rowles** and Dr. **Mark Paskevicius** from the "Hydrogen Storage Research Group" at Curtin for a nice working environment, both professionally and socially. Especially thanks to **Arnaud Camille "Maurice" Griffond**, **Mariana Soledad Tortoza**, **Enrico Ianni** and **Tam Nguyen**. My daily life would feel deep, dark and hollow without your presence. Thank you for the many laughs.

Finally, I would like to thank my family for love and support throughout my studies and all my endeavours in life.

List of Publications

A list of published papers related to the thesis. The published papers marked with asterix (*) form part of the thesis. The respective 2017 Impact Factors (IF) are also given.

- **Javadian, P.**; GharibDoust, S. P.: Li, H-W.; Sheppard, D. A.; Buckley, C. E.; Jensen, T. R., *J. Phys. Chem C*, **2017**, 121, 18439-18449 (*)

IF: 4.509

- Plerdsranoi, P.; **Javadian, P.**; Jensen, N. D.; Nielsen, U. G.; Jensen, T. R.; Utke, R., *Int. J. Hydrogen Energy*, **2016**, 42, 1036-1047.

IF: 3.205

- **Javadian, P.**; Sheppard, D. A.; Jensen, T. R.; Buckley, C. E., *RSC Adv*, **2016**, 6, 94927. (*)

IF: 3.289

- **Javadian, P.**; Sheppard, D. A.; Buckley, C. E.; Jensen, T. R., *Crystals*, **2016**, *6*, 70. (*)

IF: 2.075

- Utke, R.; Thiangviriya, S.; **Javadian, P.**; Jensen, T. R.; Milanese, C.; Klassen, T.; Dornheim, M., *Mater. Chem. Phys.*, **2016**, *169*, 136-141.

IF: 2.101

- **Javadian, P.**; Sheppard, D. A.; Buckley, C. E.; Jensen, T. R., *Int. J. Hydrogen Energy*, **2015**, *40*, 14916-14924. (*)

IF: 3.205

- **Javadian, P.**; Zlotea, C.; Ghimbeu, C. M.; Latroche, M.; Jensen, T. R., *J. Phys. Chem. C*, **2015**, *119*, 5819-5826.

IF: 4.509

- Thiangviriya, S.; Gosalawit-Utke, R.; Plerdsranoi, P.; Viset, N.; **Javadian, P**.; Jensen T. R., *J. Alloys Compd.*, **2015**, *633*, 484-493.

IF: 3.014

- **Javadian, P.**; Sheppard, D. A.; Buckley, C. E.; Jensen, T. R., *Nano Energy*, **2015**, *11*, 96-103. (*)

IF: 11.553

- Ampoumogli, A.; Charalambopoulou, G.; **Javadian, P.**; Richter, B.; Jensen, T. R., *J. Alloys Compd.*, **2015**, *645*, 480-484.

IF: 3.014

- **Javadian, P.**; Nielsen, T. K.; Ravnbæk, D. B.; Jepsen, L. H.; Polanski, M.; Plocinski, T.; Kunce, I.; Besenbacher, F.; Bystrzycki, J.; Jensen, T. R., *J. Solid State Chem.*, **2015**, *231*, 190-197.

IF: 2.265

- Gosalawit–Utke, R.; Thiangviriya, S.; **Javadian, P.**; Laipple, D.; Pistidda, C.; Bergemann, N.; Horstmann, C.; Jensen, T. R.; Klassen, T.; Dornheim, M., *Int. J. Hydrogen Energy*, **2014**, *39*, 15614-15626.

IF: 3.205

- Nielsen, T. K.; **Javadian, P.**; Polanski, M.; Besenbacher, F.; Bystrzycki, J.; Skibsted, J.; Jensen, T. R., *Nanoscale*, **2014**, *6*, 599.

IF: 7.76

- Gosalawit-Utke, R.; Milanese, C.; **Javadian, P.**; Laipple, D.; Karmi, F.; Puszkeil, J.; Wittayakhun, J.; Skibsted, J.; Jensen, T. R.; Marini, A.; Klassen, T.; Dornheim, M., *J. Alloys Compd.*,**2014**, *599*, 78-86.

IF: 3.014

- **Javadian, P.**; Jensen, T. R., *Int. J. Hydrogen Energy*, **2014**, *39*, 9871-9876.

IF: 3.205

- Gosalawit-Utke, R.; Milanese, C.; **Javadian, P.**; Jepsen, J.; Laipple, D.; Karmi, F.; Puszkeil, J.; Jensen, T. R.; Marini, A.; Klassen, T.; Dornheim, M., *Int. J. Hydrogen Energy*, **2013,** *38*, 3275-3282.

IF: 3.205

- Nielsen, T. K.; **Javadian, P.**; Polanski, M.; Besenbacher, F.; Bystrzycki, J.; Jensen, T. R., *J. Phys. Chem. C*, **2012**, *116*, 21046-21051.

IF: 4.509

- Nielsen, T. K.; Polanski, M.; Zasada, D.; **Javadian, P.**; Besenbacher, F.; Bystrzycki, J.; Skibsted, J.; Jensen, T. R. *ACS Nano*, **2011**, *5*, 4056-4064.

IF: 13.334

Statement of Contribution of Others

Payam Javadian's input into this study and the associated papers included the execution of all the experimental work as well as a dominant contribution to the intellectual input involved in the project. Other scientists made some contribution to the current work, as is almost always the case in the physical sciences. These contributions were significant enough to warrant co-authorship on the resulting journal articles. These are specified below.

Prof. Craig E. Buckley provided project supervision and manuscript editing.

Prof. Torben R. Jensen provided project supervision and manuscript editing.

Dr. Drew A. Sheppard provided project supervision and manuscript editing.

Payam Javadian

Prof. Craig E. Buckley

Table of Contents

List of Figures

List of Tables

Chapter 1: Introduction

Since the beginning of the Industrial Revolution in 1750 up to the present, the level of energy consumption has been increasing. Consequently, the demand for energy is also increasing. In the modern world, humans utilize energy for several everyday activities e.g. heating houses, preparing food, transportation, manufacturing of consumer goods etc. Especially, since the beginning of the 20th century there has been a large increase in the world's total energy consumption. In 1973, the world total energy consumption was 5.4×10^4 MWh. In 2014, this has increased by 51 %, consuming 1.1×10^5 MWh (International Energy Agency 2016). The energy consumption, originating mainly from burning of fossil fuels (natural gas, coal and oil) and cement production, has been propelled by the industrialization and technological advances of the 20th century, see Figure 1.1. Fossil fuels account for 81 % of the world total primary supply since 2014 (World Energy Outlook 2008). Even though, the energy provided by renewable sources (e.g. wind, solar, hydro) has doubled from 1.6 % (year 1973) this only account for 3.3 % (year 2014) of the current total energy consumption (World Energy Outlook 2008).

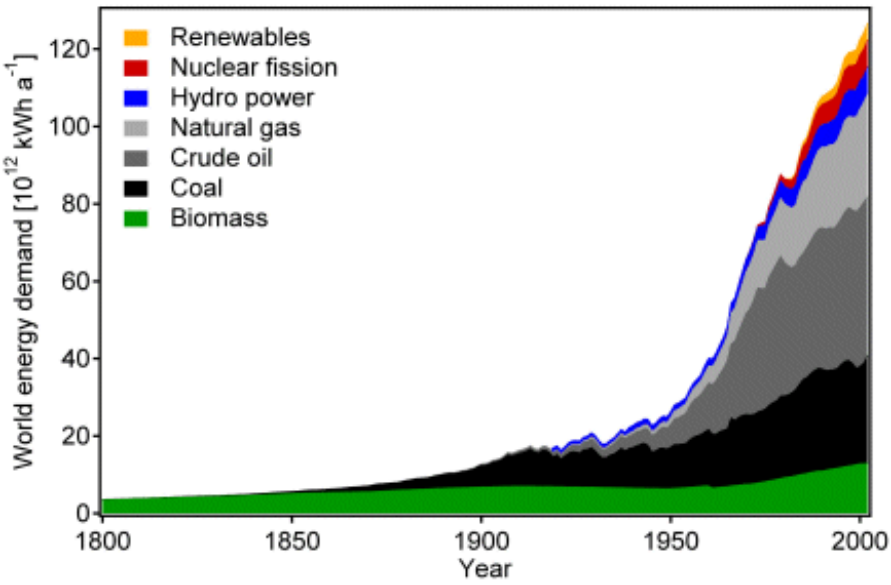

Figure 1.1 Illustration of the world energy demand since year 1800, in regards to respective energy types. Adapted from (World Energy Outlook 2008).

The energy consumption is expected to significantly increase over the next couple of decades, as a result of increased world population and rapid economic growth, especially from the developing countries such as China and India (IEA 2016).

The energy yield obtained from fossil fuels is derived from a combusting reaction, recovering the energy and an extensive amount of CO_2 is released into the atmosphere. Unfortunately there is a strong correlation between fossil fuel consumption and the amount of CO_2 in the atmosphere (Vitousek, 1994; World Energy Outlook, 2008). The current average level of atmospheric CO_2 (404

ppm) is at its highest and unless dramatic changes are carried out, it will keep rising proportional to time reaching 550 ppm in the year 2035(International Energy Agency 2016; IEA 2016). It is widely accepted by scientists that CO_2 emissions induce global climate changes and increase the average temperature on earth. The major consequence of global warming is abrupt climate changes *i.e.* summers are getting warmer due to change in the ecosystem. Consequently, drought, larger hurricanes, extinction of animal species etc, will be propagating. The increased temperature is melting glaciers worldwide at a rapid rate, causing rising sea levels (Vitousek 1994; Shaver et al. 1992). One scenario attracting significant attention, is the potential collapse, or shut down of the Gulf Stream (The Guardian 2003). As a consequence, the general circulation of the ocean driven winds will be diminished, thereby the delivery of substantial amount of heat to the Greenland-Norwegian-Iceland Seas and the land around will be diminished (Solomon et al. 2009).

Another essential issue derived from CO_2 emission, is acidification of the oceans *i.e* lowered pH level due to the reaction between water and CO_2. This has worrying effects on sea life and the ocean ecosystems.

The amount of fossil fuels left on earth is questionable, since new sources are continuously discovered. In combination with the different political and economic ulterior motives held by companies and superpowers involved in fossil fuel production, the quantity of fuel reserves may be up for debate. It is however believed that we will run out of fossil fuels in 250 - 300 years from now (Shafiee and Topal 2009), which is in parallel to subsequent increasing energy prices. For that reason, it is paramount to rapidly achieve fossil fuel independency for mankind and focus on fundamental changes in our approach to produce and consume energy.

1.1. **Renewable energy and the hydrogen storage society**

Fossil fuel depletion is inevitable. Constant depletion of the most crucial energy source on earth, especially scarce oil, has for the last few decades prompted new methods to harvest energy from independent energy sources. Renewable energy or green energy is a highly appreciated scientific field among researchers around the world. Wind power, solar energy, geothermal energy, hydrothermal energy and biomass are examples of renewable energy (Dorian, Franssen and Simbeck 2006). Most of these renewable energy sources are carbon free; however the drawback is that they are not evenly distributed in time and geography. For instance, wind power can only be utilized when the wind is blowing, solar energy when the sun is shining. In essence, the future energy system has to be reliable, available, clean and cost-efficient (Schlapbach and Züttel 2001; Ritter et al. 2003). Focus is mainly projected upon the transport sector which is responsible for 60 % of the consumed energy, harvested from fossil fuels. This corresponds to 25 % of the worlds energy consumption (IEA 2016). In political terms this is to ensure environmental viability and energy security in the future.

Hydrogen has been suggested as a future carrier of sustainable energy, due to its high gravimetric energy content (120 MJ/kg H_2), which is approximately three times higher than that of hydrocarbon based fuels *e.g.* petrol (43.9 MJ/kg) (Schlapbach and Züttel 2001). However the volumetric energy density of liquid hydrogen (8 MJ/L), is four times lower than for that of liquid gasoline (32 MJ/L). Furthermore, the low hydrogen density in both gas and liquid state is 0.089 and 71 g/L, at 25 and -252 °C, respectively (Schlapbach and Züttel 2001; Züttel, Borgschulte and Schlapbach 2008). Hydrogen is a clean, carbon free energy carrier and no CO_2 or other green-house gas emission is constituted at the end-user level, which makes it suitable for energy storage applications. Furthermore, it is the most abundant element on earth, albeit it is not naturally present as hydrogen gas, H_2, but it can be produced electrochemically by electrolysis of water. The most efficient way of using hydrogen is by generating electricity using a fuel cell. Fuel cells offer small scale electricity production as hydrogen gas H_2 is converted to usable electricity, which can be converted to other forms of energy such as mechanical energy. Currently in the transport sector, proton-exchange membrane fuel cells (PEM) fuel cells are the most promising candidate to be used for mobile electricity production, and it is already used by several companies (Sarkar and Banerjee 2005; Conte, Prosini and Passerini 2004; Satyapal et al. 2007).

Using hydrogen as an energy carrier for on board mobile systems is still highly energy intensive *e.g.* to store and liberate hydrogen in terms of heating, pressurizing and cooling etc. It requires further research and significant investment to obtain more efficient and cheaper storage method, not to mention the massive investment in infrastructure for hydrogen fuel stations.

1.2. **Concentrated Solar Thermal energy**

Hydrogen is considered a promising future carrier of renewable energy, compared to the conventional carbon polluting fossil fuels used in today's society. Utilization of hydrogen for mobile or stationary applications can eliminate harmful emissions of particles and exhaust gases. Solar energy is the largest energy source on Earth, and it is inexhaustible, non-toxic and safe to handle. Every year Australia receives 58 million petajoules of solar radiation, however the majority of this energy is wasted as this is 10,000 times more than Australia's total energy consumption. Solar energy only accounts for 0.1 % of Australia's total primary energy consumption (Geoscience Australia 2013). Solar photovoltaic (PV) converts solar energy into electricity using photovoltaic cells. This technology is available and is highly competitive among solar energy companies. However, the International Energy Agency (IEA) has established some goals for the future regarding utilization of PV worldwide. The IEA, estimates that by 2050, the cumulative capacity of installed PV could account for 11% of global electricity production, and avoid 2.3 gigatonnes of CO_2 per year (International Energy Agency 2016).

The emission of harmfull carbon gases from solar thermal power is negligible, and in terms of the global environment, there are no emissions of CO_2 involved in the operation of a solar thermal power plant. There are three main methods for storing thermal energy; sensible, latent and chemical heat storage. Sensible heat is the energy released (absorbed) by a material as its temperature is reduced (increased). Sensible heat storage media can either be a solid (mainly high temperature concrete or castable ceramics) or a liquid (molten salts, mineral oils and synthetic oils). The simplest liquid is comprised of binary nitrate liquid molten salt mixtures (60% $NaNO_3$; 40% KNO_3) with potential corrosion problems. Furthermore, a large volume is required to store sufficient heat to operate the plant for several hours during insufficient solar radiation hours (Harries et al. 2012; Liu et al. 2016) (these nitrate salt mixtures have a maximum useable temperature of ~590 to 600 ^{o}C as they begin to decompose above this temperature (Freeman 1956)). The second form of thermal storage uses "latent" heat, which is associated with the phase change of materials (PCM) at isothermal conditions e.g. heat of phase change such as heat of vaporization (liquid-vapour transition) or heat of fusion (solid-liquid transition). The issue with PCM is sluggish heat transfer and low charge and discharging rates (Khudhair and Farid 2004). The third storage mechanism is assigned to chemical reactions *i.e.* chemical heat storage (thermochemical energy storage). This type of heat storage relies on a completely reversible chemical reaction. Principally, heat from solar radiation received, is used to drive an endothermic chemical reaction and the necessary heat is available whenever desired by allowing the reverse reaction to occur. The advantages of this storage type are, for instance, the high energy storage densities and long storage durations at near ambient temperatures (Liu et al. 2016).

Metal hydrides are considered a class of thermochemical candidates for efficient thermal energy storage systems. They react reversibly with hydrogen over a wide range of constant pressures or temperatures. By changing the applied hydrogen pressure (or temperature) a metal hydride is made to either absorb hydrogen (release heat) or desorb hydrogen (absorb heat). Furthermore, the theoretical heat storage capacities of metal hydrides are significantly higher than for molten salts (See Table 1.1), thus solar thermal storage systems using metal hydrides require a smaller storage tank and less storage material compared to molten salt.

Table 1.1 Examples of Energy Storage Densities of Sensible heat, Latent Heat, Thermochemical Energy Storage Materials and Metal Hydrides (Harries et al. 2012).

Type of thermal energy storage (TES)	Example of TES material	Total heat storage capacity (kJ/kg)
Sensible heat	Molten salt mixtures	153*
Latent heat / phase change materials	$NaNO_3$	282
Thermochemical	Oxidation of Co_3O_4	1055
Metal Hydride	$MgH_2 \rightarrow Mg + H_2$	2814

***The value is for a 100 °C temperature change. NB: if the temperature change is larger than this, the heat storage capacity of molten salts is higher.**

The principle of using metal hydrides for thermal storage in a concentrated solar power plant is shown in Figure 1.2. During the day time solar radiation is concentrated and received. This heat will be provided to a heat engine and converted to electricity. Any excess energy in the form of heat is used to desorb hydrogen from the metal hydride (by an endothermic reaction) from the high temperature (HT) hydride bed to be absorbed and stored by the low temperature hydride bed (LT). At night, the reverse exothermic reaction takes place. As the HT hydride bed is allowed to cool, the hydrogen released from the LT hydride bed is absorbed by the HT hydride bed in an exothermic reaction that releases heat that is utilized to run the heat engine. Evidently, this system is capable of providing energy/electricity 24/7 (Harries et al. 2012; Fellet et al. 2013).

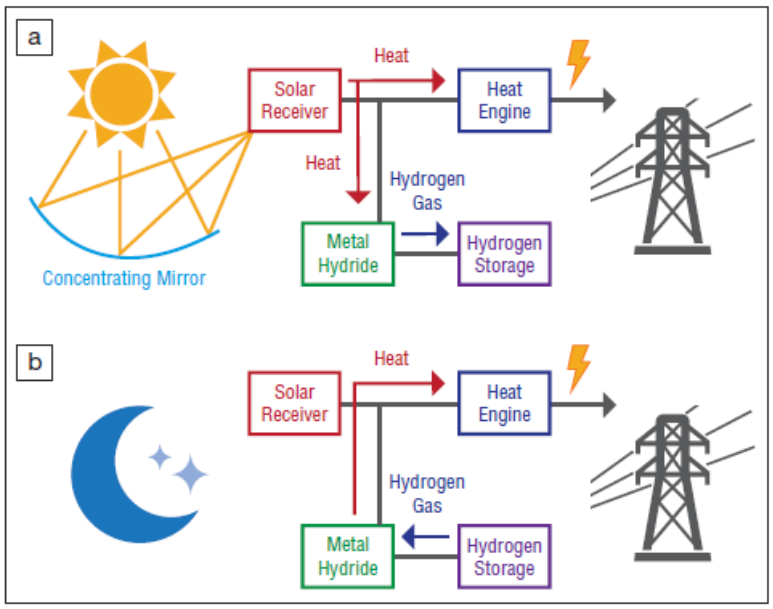

Figure 1.2 (a) Day time operation of metal hydrides as a thermal storage medium (b) Night time operation of metal hydrides as a thermal storage medium. “Metal Hydride” and ”Hydrogen Storage” are assigned to the high and low temperature hydride bed, respectively (Fellet et al. 2013).

The U.S. department of Energy launched the Sunshot Initiative in 2011, with the goal of making solar electricity cost-competitive with conventional generated electricity by 2020 without any subsidies. This meant reducing Photovoltaic (PV) and Concentrated Solar Thermal power (CST) prices by ~75 %. The target for 2030 is to reduce the solar electricity price down to 3 US cents/kWh. (Sunshot 2030) (Sunshot 2012).

The technical targets set by DoE on thermal energy storage are; i) The operating temperature for CST is in the range of 600 – 800 °C in order to obtain high efficiency of the power plant; ii) The exegetic efficiency of the thermal heat storage should be > 95 %; iii) The specific cost of thermal energy storage should be < 15 $/kWh$_{th}$; iv) The volumetric energy density should be > 25 kWh$_{th}$/m^3 and v) operational lifetime of 20+ years or 10,000+ cycles (Corgnale et al. 2014; Sunshot 2012).

The best HTMH candidates for CST are those with; (1) high reaction enthalpy; (2) high operating temperatures, which affects the overall efficiency of the power plant; (3) high hydrogen storage capacity, which determines the amount of material is requires (also relates to the price of the material) and; (4) low cost of the raw material which will reduce the cost of the HTMH system cost. The best LTMH candidates are those with; (1) low reaction enthalpy, (2) low operating temperature, which allows heat to be transferred with a low temperature source; (3) high hydrogen storage capacity, which determines the mass of material required and also affects the price and; (4) low raw material cost in order to reduce the cost of the LTMH system (Corgnale et al. 2014; Sunshot 2012).

1.3. **Hydrogen storage categories**

Overall there are three ways to store hydrogen *i.e.* gas, liquid and in solid state form. This section describes the conditions of the three methods

1.3.1 Pressurized gas tanks

The most commercially developed method of storing hydrogen is currently in pressurized tanks. In order to improve the energy density of hydrogen gas, it must be stored at high pressures. The most common way of storing hydrogen is at 200 - 300 bar. However, the latest type of tanks for high pressure storage are Carbon fiber-reinforced material capable of withstanding H_2 pressures up to ~700 - 800 bar, reaching a gravimetric and volumetric hydrogen content of 13 wt.% and 40 g H_2/L, respectively (Züttel, Borgschulte and Schlapbach 2008; Züttel 2004; Felderhoff et al. 2007). These are already used in commercially produced hydrogen powered vehicles. The materials used for construction of these tanks are expensive and rather heavy. For an ideal gas, the volumetric density and pressure is linearly proportional to each other. This however is not the case for hydrogen at high pressure. Hydrogen behaves like an ideal gas with a linear relation between energy density and pressure up to 10 bars and subsequently the volumetric energy density increases in a non-linear matter (see Figure 1.3). Furthermore, storage at higher pressure needs reinforced and more expensive storage tanks, thus there is an upper limit for the utilization of this method.

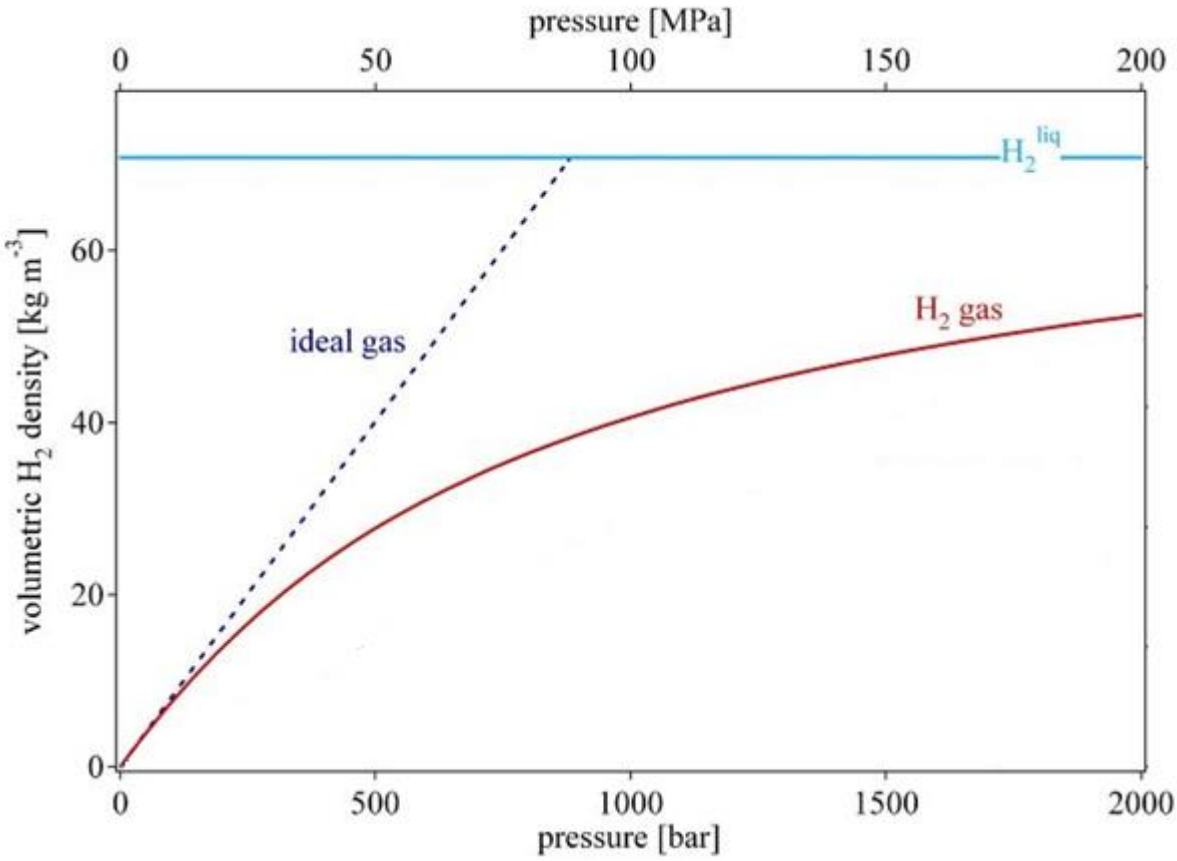

Figure 1.3 Illustrating the non-ideal behaviour of hydrogen gas. Adapted from (Hydropole).

1.3.2 Liquefied Hydrogen Storage

The volumetric capacity of liquid hydrogen (71 g/L) is almost twice that of hydrogen stored as gas (39 g/L) in tanks at room temperature and 700 bar of pressure (Züttel 2004). Liquid hydrogen is stored in cryogenic tanks at very low temperatures (T < -250 °C) at ambient pressure. Furthermore, approximately 30 % of the hydrogen energy content is required for its liquefaction, owing to the phase-change enthalpy of about 0.45 MJ per kg of H_2 between the liquid and gaseous state (Eberle, Felderhoff and Schueth 2009). Another challenge is that it has to be stored in open systems in order to avoid overpressure, due to the low critical temperature of hydrogen (-241°C), causing a continuous boil-off of hydrogen from the tank. This has to be minimized, due to cost and safety reasons, thus making liquefied hydrogen inconvenient for mobile applications. The major automotive company BMW has developed the concept car “BMW Hydrogen 7”, which focuses consistently on liquid hydrogen as source of drive energy. This hybrid vehicle has a dual-mode combustion engine that is powered by a hydrogen combustion engine combined with a fuel combustion engine, offering an overall cruising range of approximately 700 kilometers. The on-board hydrogen tank stores liquid hydrogen at 20 K at 5.1 bar of pressure (Wallner et al. 2008).

1.3.3 Solid-state hydrogen storage

Finally the last way of storing hydrogen is in the solid state. This is done by physical storage (physisorption), and chemical storage (chemisorption)

1.3.3.1 Physically bound hydrogen

Physisorption, also known as physical sorption or adsorption, is the phenomena of a gas, or in this case H_2, being molecularly adsorbed onto the surface of a porous solid (see Figure 1.4). This interaction between gas and adsorbents is generated by weak Van der Waals forces *i.e.* with the adsorption enthalpy in the order of ΔH_{ads} = -1 to -10 kJ/mol (Schlapbach and Züttel 2001; Ritter et al. 2003; Eberle, Felderhoff and Schueth 2009; Panella and Hirscher 2005). The adsorption process does not cause H_2 bond breaking, and occur with fast kinetics. Due to the weak forces, it is possible to improve the hydrogen adsorption/desorption properties by designing new scaffold materials that have stronger interactions with molecular hydrogen. Pore size, shape and surface area are some of the factors that affect the hydrogen adsorption/desorption properties. As the hydrogen molecules never react chemically with the solid material, there is no change in the crystal structure, meaning that it is possible for multiple cycling of the material.

Typical examples of materials exhibiting physisorption are materials such as carbon nanotubes, zeolites and metal organic frameworks (MOF). MOFs are highly porous with open structures, possessing a large surface area, and large cavities making it suitable for hydrogen adsorption. The disadvantage of physisorption, is that it is only feasible at the low temperatures of liquid N_2 with low weight capacity of hydrogen at high pressures. For example, MOF-177 with a specific BET surface area of 4750 m^2/g stores 7.5 wt% H_2 and 32 g H_2/L at $p(H_2)$ = 66 bar and T = -196 °C (Furukawa, Miller and Yaghi 2007).

Table 1.2 Hydrogen sorption properties for conventional and metal hydrides storage (Panella and Hirscher 2005; Løvvik and Opalka 2005; Løvvik, Swang and Opalka 2005).

	ρ_m(wt %)	ρ_V(g H_2/L)	T_{des}(°C)*	p(H_2) (bar)
Physical Storage				
High-pressure tanks	6	58	RT	700
Liquid Hydrogen	100	71	-252	1
MOF-5	4.5	27	-196	20
Light & Complex metal hydrides				**Bond type**
$LiBH_4$	18.5	121	380	Covalent
$NaAlH_4$	7.5	94	210	Covalent
MgH_2	7.7	110	~280	Ionic
$LaNi_5H_6$	1.4	121	~50	Metallic

***At 1 bar.**

1.3.3.2 Chemically bound hydrogen

In **Chemisorption**, the materials used for chemical storage are usually light/complex metal hydrides containing high gravimetric and volumetric densities of hydrogen. The H_2 molecules react with the material forming chemical bonds of covalent, metallic or ionic character (See Table 1.2). Hence, the enthalpy difference created in this process is up to 20 times greater for that of physisorption, *i.e.* typically between -50 to -200 kJ/mol (Collins and Zhou 2007). The hydrogen storage materials include metals or alloys that react with hydrogen gas forming metal hydrides *i.e.* such as MgH_2, or as complex metal hydrides *i.e.* such as $NaAlH_4$ and $LiBH_4$. Light metals such as lithium and magnesium are desired for high storage capacity,

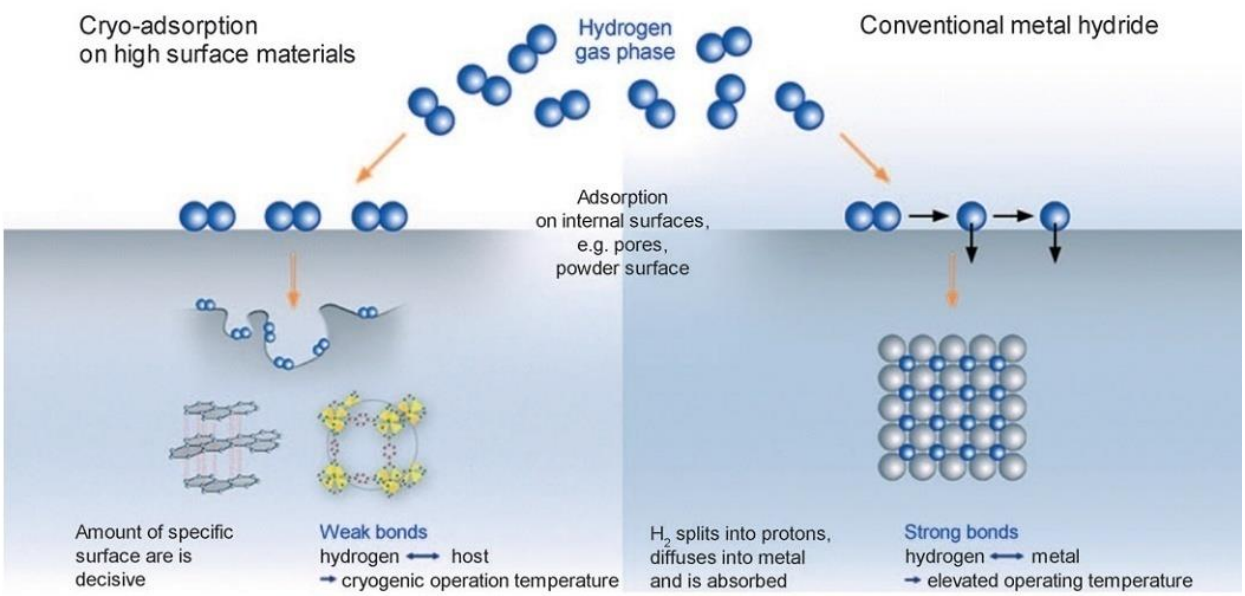

Figure 1.4 Illustration of cryo-adsorption (left) and chemisorptions (right). Adapted from (Eberle, Felderhoff and Schueth 2009).

An essential parameter for metal hydrides is the enthalpy of hydrogenation (e.g. enthalpy of formation), ΔH_f. $LaNi_5H_6$ has a formation enthalpy of ΔH_f = -30 kJ/mol H_2 and shows fast hydrogen absorption and desorption at room temperature. In addition its volumetric hydrogen content (121 g H_2/L) is significantly higher than for liquid hydrogen (71 g H_2/L). Unfortunately the gravimetric hydrogen content of $LaNi_5H_6$ is very poor (1.4 wt%) (see Table 1.2). The drawbacks of metal hydrides with a high gravimetric hydrogen capacity such as $LiBH_4$, $NaAlH_4$ and MgH_2 is their high temperature of hydrogen release at ambient pressures (T_{des}). The challenge is to destabilize the metal hydride and reduce T_{max}. This can be done by various approaches for destabilization of the hydride, for instance by reducing the particle size.

1.4. **Metal Hydrides**

Metal hydrides consist of a metal lattice with hydrogen guest atoms bonded interstitially between the metal atoms. It is formed from hydrogen reacting as metallic bonding with metals or alloys leading to solid-state hydrogen storage under moderate temperatures and pressures. This makes solid state hydrogen storage relative safe compared to other storage methods such as in the liquid or gaseous state. Metal hydrides can usually contain two phases; α-phase where hydrogen is absorbed as a solid solution and β-phase where the hydride is fully formed. The β-phase is described by the structural characteristics of the material (Züttel 2003). The coexistence of the solid solution and the hydride is represented by a pressure, composition, temperature, PCT, plateau curve *i.e.* a function between hydrogen equilibrium pressure, p_{eq}, as a function of hydrogen concentration in the metal composite, at a fixed temperature (Züttel 2003) (see Figure 1.5). The length of the plateau corresponds to the amount of hydrogen reversibly absorbed/desorbed into the metal lattice at a set temperature with

minimal pressure changes. Increasing temperature results in increasing equilibrium pressure, p_{eq}, up to a certain critical temperature, T_C, at which the flat plateau ends and the α → β transition is direct (Principi et al. 2009). From sufficient PCT data, thermodynamic parameters such as enthalpy and entropy of formation can be obtained via a van't Hoff plot. A van't Hoff plot can be constructed from the linear correlation between the natural logarithm of p_{eq} and $1/T$ (see Figure 1.5). The slope of the line is equal to the enthalpy of formation ΔH divided by the ideal gas constant R (R = 8.314472 J/mol/K), and the intercept of the line is equal to the entropy of formation ΔS divided by the ideal gas constant R. Thermodynamic parameters are useful information for determining whether a particular metal hydride is a potential hydrogen storage material.

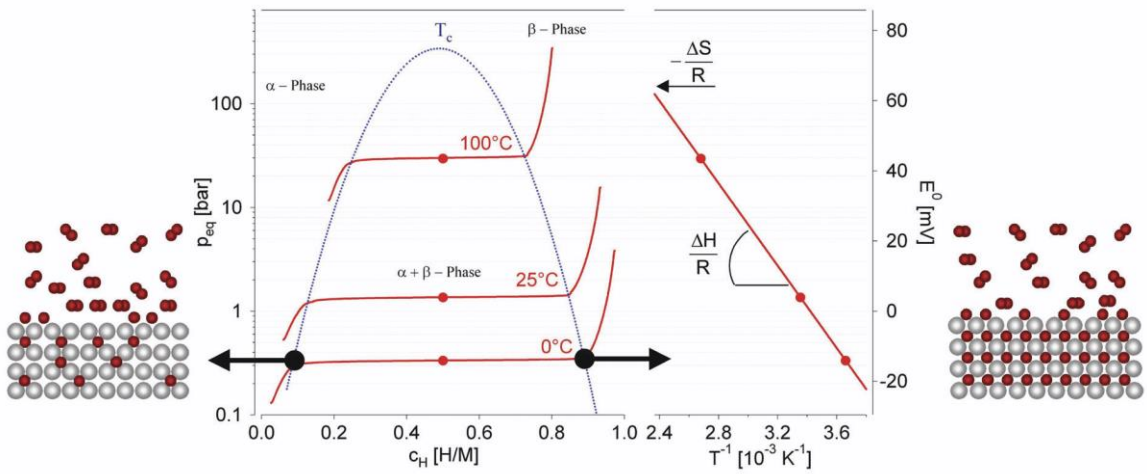

Figure 1.5 Illustration of Pressure-Composition-Isotherm plot of a typical hydrogen absorption/desorption into a metal lattice (left) and the corresponding van't Hoff plot (right) (Züttel 2003)

The relation between absorption enthalpy, entropy and equilibrium pressure is described by the van't Hoff equation (1)

$$\ln\left(\frac{f_{eq}}{f_0}\right) = \frac{\Delta H}{RT} - \frac{\Delta S}{R} \qquad (1)$$

where, f_{eq} is the equilibrium fugacity of hydrogen (in bar), f_0 is the reference fugacity. The fugacities are related to the changes ΔH and ΔS in enthalpy and entropy, respectively. R is the ideal gas constant and finally T is temperature (K)(Züttel 2003; Klose and Stuke 1995). It should be noted that the van't Hoff plot is often provided with a pressure (p) term instead of fugacity when described in the litterature. The pressure term is only valid at very low pressures close to ideal conditions, however at non-ambient pressure conditions, the fugacity, which is the activity of the real gas, provides a better representation of the chemical potential of the system (Klose and Stuke 1995). Hydrogen storage properties of metal hydrides are influenced by the characteristics and impurity or additive content

(Schlapbach and Züttel 2001; Sakintuna, Lamari-Darkrim and Hirscher 2007; David 2005; Eberle, Arnold and Von Helmolt 2006).

1.4.1. Interstitial hydrides

Intermetallic compounds are a well-studied research area regarding materials for hydrogen absorption. Examples of studied intermetallic alloys are $LaNi_5$ (Tanaka, Clewley and Flanagan 1977; Leisure et al. 2003; Seta and Uchida 1995), $TiCr_2$ (Beeri et al. 2003; Dos Santos, Bououdina and Fruchart 2002) or Mg_2Ni (Sun et al. 1999; Aizawa, Kuji and Nakano 1999; Bliznakov et al. 2005). However TiFe is one of the most promising alloy candidates as a hydrogen storage material due to its high hydrogen storage capacity of 1.8 wt.% at room temperature, not to mention the abundance and relative low cost of the respective alloy metals (Reilly and Wiswall Jr 1974; Nambu et al. 1999; Shang et al. 2004) though it suffers from poor hydrogen discharge kinetics and unfavorable thermodynamics (Lee and Perng 2000, 1999; Miyamura et al. 2003).

For the past decades the majority of hydrogen storage research was conducted with the focus on mobile applications. However, thermochemical heat storage is also a potential technological research field for stationary applications. The majority of work done on Ti-based alloys is for instance considered for mobile applications, with the aim of lowering the operation temperatures to achieve favorable thermodynamic and kinetic conditions. However studies show that high temperature reactions of Ti-based alloys are also suitable for thermal energy storage (Rönnebro et al. 2015).

The other important factor that can be used as a selection criterion is the total system cost (Sheppard et al. 2014). In a CST power plant, the price of the raw materials for the HT and LT metal hydrides is important for the system to be feasible. Generally, the price of the low temperature metal hydride (e.g. $TiMn_{1.5}$) is the most expensive component of the system. In order to reduce the total cost, it would be necessary to optimize the HT metal hydride by improving its electrical efficiency conversion; and increasing the enthalpy of formation, thus enhancing the thermal heat storage capacity. The intermetallic alloying of Ti is one way to improve this. Depending on the material composition, the overall theoretical heat storage capacity of the reaction can be calculated.

Looking at the Ti-H system at 707 ˚C operating between TiH_1 to $TiH_{1.7}$ (1.30 wt.% H_2) in the pressure range of ~4.7 to ~12 bar, an overall theoretical heat storage capacity of 943 kJ/kg is obtained. In contrast to Ti-Cu-H (overall reactions 2-4, corresponding to 1.49 wt.% H_2), operating between 4.7 to ~17.4 bar, the calculated heat storage capacity is 1013.6 kJ/kg.

1.4.2. Complex Metal hydrides

The complex metal hydride sodium alanate, $NaAlH_4$, has a relative high gravimetric and volumetric hydrogen content of 7.5 wt% and 94 g H_2/L, respectively, (see Table 1.2). The thermodynamic

properties of $NaAlH_4$ are also promising. $NaAlH_4$ decomposes in three steps releasing hydrogen (reaction I, II and III) in each step, with Na_3AlH_6 as an intermediate (Mueller and Ceder 2010; Gao et al. 2010; Bogdanović and Schwickardi 2001).

$3NaAlH_4(s) \leftrightarrow Na_3AlH_6(s) + 2\ Al(s) + 3\ H_2(g)$ (3.7 wt% H_2) $T > 180$ °C (I)

$Na_3AlH_6(s) \leftrightarrow 3\ NaH(s) + Al(s) + 11/2\ H_2(g)$ (1.85 wt% H_2) $T > 240$ °C (II)

$NaH(s) \leftrightarrow Na(l) + ½\ H_2(g)$ (1.85 wt% H_2) $T > 425$ °C (III)

The reaction yields 3.7, 1.85 and 1.85 wt% H_2 in the first, second and third reaction step, respectively. The enthalpy of hydrogen release are ΔH_D = 37, 47 and 56 kJ/mol H_2 in step (I), (II) and (III), respectively, corresponding to a hydrogen release temperature taking place at T_{eq} = 30 and 100 °C at $p(H_2)$ = 1 bar for reaction step (I) and (II), respectively. However due to kinetic limitations, $NaAlH_4$ releases hydrogen at $T > 180$ °C and $T > 240$ °C for step (I) and (II), respectively. Hydrogen release via step (III) occurs at too high temperature for most applications and so is usually not considered. Studies show that addition of Ti, Sc and Ce based additives, improves the hydrogen desorption properties of $NaAlH_4$ (Gross, Thomas and Jensen 2002; Wang et al. 2005; Bogdanović and Schwickardi 2001; Rongeat et al. 2009).

Complex borohydrides such as $LiBH_4$, $NaBH_4$, $Ca(BH_4)_2$ and $Mg(BH_4)_2$ are considered potential candidates for hydrogen storage due to their relative high capacity of hydrogen, typically > ρ_m = 10 wt.%. Unfortunately, these complex metal borohydrides are known to suffer from sluggish kinetics and unfavorable thermodynamics, not to mention the limited cyclic stability during hydrogen release and uptake cycling. The difficult reversibility of complex borohydrides is either due to kinetic or thermodynamic limitations, or both. The kinetics can be improved in a number of ways. For instance by reducing the particle size of the bulk hydride either by mechano-chemical treatment or by nanoconfinement (as described in the next paragraph) which creates a larger surface area and facilitate closer contact between the grain boundaries that makes diffusion of the reactive species faster. Another approach is to increase the temperature of the hydride, which is untypical in hydrogen storage for vehicle applications hence scant reference is made of this in the literature. However, increasing the temperature to > 500 °C is ideal operating conditions for thermal heat storage

provided that the H_2 equilibrium pressure remains moderate. For example bulk $Ca(BH_4)_2$ is not suitable for high temperature heat storage because of its equilibrium pressure for decomposition becomes too high for practical applications. $Ca(BH_4)_2$ forms at ~350 °C and 90 bar H_2 pressure (Kim et al. 2008), although 500 °C and 140 bar H_2 does not form it (see chapter 3.5 of this dissertation). This indicates that at 500 °C, the H_2 equilibrium pressure for bulk $Ca(BH_4)_2$ is > 140 bar, which is too high for thermal energy storage. Studies have shown reversibility of complex borohydrides conducted under higher temperatures and pressure, but the targets are usually at low temperatures for mobile applications. Orimo reported reversibility of $LiBH_4$ at 600 °C and 35 MPa (Orimo et al. 2005). Moeller reported formation of $LiBH_4$, $NaBH_4$ and $Ca(BH_4)_2$ under conditions of $p(H_2)$ = 600 bar at T = 350-400 bar for 12 hours (Møller et al. 2016).

1.5. **Nanoconfinement**

Nanoparticles have large surface areas compared to bulk materials (hydrides). If the surface energy of the hydride phase is lower than the surface energy of the nonhydride phase, nanoparticle formation reduces the enthalpy of formation (Berube, Chen and Dresselhaus 2008; Bérubé, Dresselhaus and Chen 2009). The kinetic properties of nanoparticles are significantly improved due to (*i*) increased surface area of the hydride, (*ii*) intimate contact between hydride phases (*iii*) increased number of atoms in the grain boundaries and, (*iv*) nano-scale diffusion distances that give rise to faster hydride reaction rates (Berube, Chen and Dresselhaus 2008; Bérubé, Dresselhaus and Chen 2009; Zaluska, Zaluski and Ström–Olsen 1999; Yao et al. 2008). The most widely utilized method for preparing hydride nanoparticles is by ball milling (see Figure 1.6). During ball milling, fresh surfaces are created and defects on the surface and interior of the material are formed. This top-down synthesis technique reduces the particle size of the bulk hydride mechanically down to nano sizes below 100 nm. However, a consequence of nanoparticles is phase segregation upon hydrogen exchange and heating, e.g. nanoparticles tends to grow into larger agglomerates (Bérubé et al. 2007; Dornheim et al. 2007; Gertsman and Birringer 1994). Furthermore, the ball milled compound product often contains possible metal traces/impurities originating from vial and balls.

Nanoparticle decomposition is different from bulk decomposition since in both cases, the size of the reaction products must be considered. A particle may decompose into smaller particles, or its decomposition products may be added to existing particles. Decomposition into smaller particles requires more energy since a larger total surface area is created. Reaction I only occurs for $NaAlH_4$ nanoparticles above 52 nm in size, and reaction III is predicted to occur at temperatures of 65 °C for nanoparticles of 52 nm in size. Because of the high energy of the decomposition products of 2 - 10 nm particles, it is expected that these particles start releasing hydrogen at 94 °C (Mueller and Ceder 2010).

An alternative method for preparation of nanoparticles is by nanoconfinement. This concept is based on hydride nanoparticles, being synthesized or melt infiltrated into a nanoporous inert scaffold material, see Figure 1.6. In this bottom-up approach, the hydride nano composite are size restricted by the pore size of the scaffold which is highly suitable for hydrogen absorption and desorption, thus phase segregation upon hydrogen cycling will be prevented.

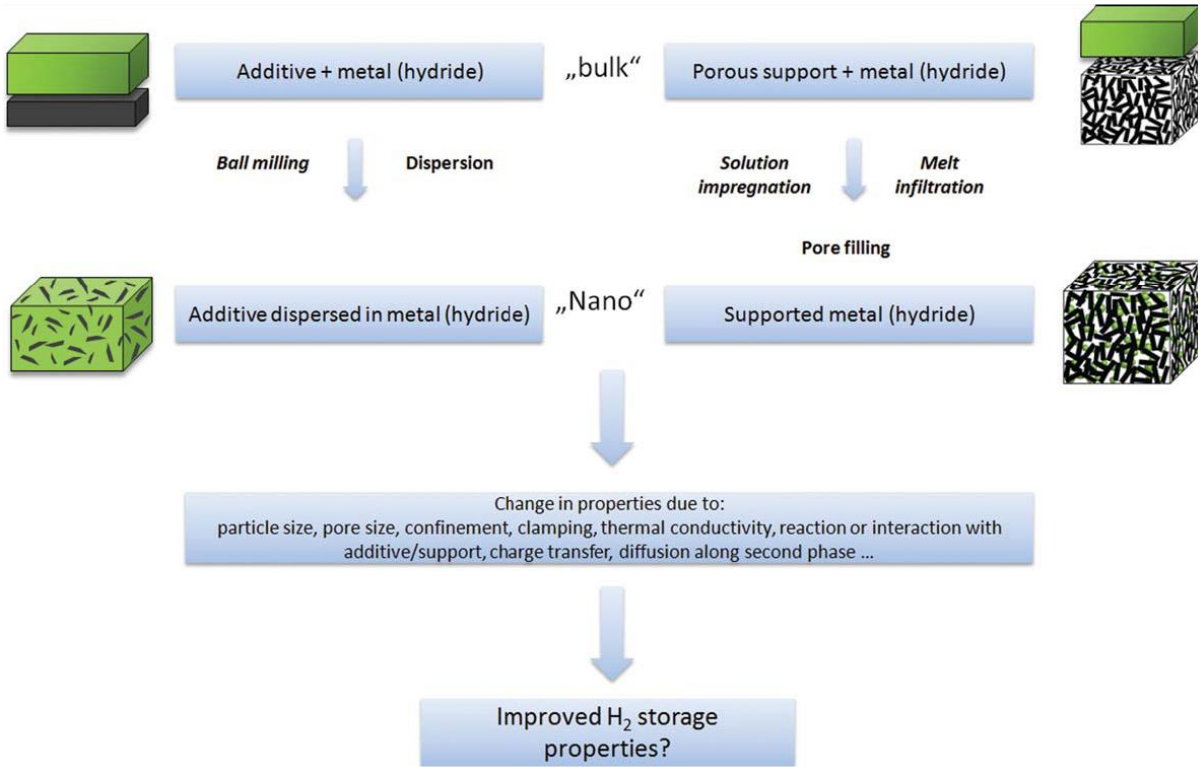

Figure 1.6 The result of hydrogen storage properties using two approaches of metal hydride formation either by ball milling or by supporting on a porous scaffold material using solvent infiltration or melt infiltration. The resulting nano composite materials possess different properties compared to the bulk. Adapted from (Adelhelm and De Jongh 2011).

Nanoconfinement of metal hydrides is a popular scientific field of interest for hydrogen storage, and this principal is applied for numerous metal hydrides such as $NaAlH_4$, $LiBH_4$, and MgH_2. As an example, nanoconfined $NaAlH_4$ has been studied intensively using carbon as porous material. Faster hydrogen desorption rates and improved re-hydrogenation of $NaAlH_4$ loaded into nanoporous scaffold materials, compared to bulk $NaAlH_4$ has been reported (Zheng et al. 2008; Stephens et al. 2009; Adelhelm and De Jongh 2011). Furthermore, the effect of the reaction mechanism for hydrogen desorption can be enhanced depending on the average pore size of the scaffold, in which $NaAlH_4$ is embedded. $NaAlH_4$, confined into porous carbon with a pore size distribution centered around 13 nm is reported to release hydrogen in three steps in accordance to reaction (I) and (II) (Stephens et al. 2009). Nanoconfinement of $NaAlH_4$ into porous carbon, with smaller pores of 2 - 3 nm, results in a change in thermodynamic stability of $NaAlH_4$, which suppress the formation of Na_3AlH_6 and NaH, thus releasing hydrogen in one step rather than two (Gao et al. 2010). Furthermmore, significant

improvement in reversibility of $NaAlH_4$ nanoconfined in porous carbon, compared to bulk $NaAlH_4$ is reported (Li et al. 2011; Adelhelm et al. 2010). The nanosized $NaAlH_4$ reversibility of H_2 release and uptake is partially attributed to the synergetic effect of nanoconfinement, and the catalytic effect of the carbon support.

Similar results show that nanoconfinement of $LiBH_4$ into 25 nm nanoporous carbon scaffolds enhances the kinetics for hydrogen exchange in $LiBH_4$, and gives rise to faster dehydrogenation rates up to 50 times compared to bulk $LiBH_4$ (Gross et al. 2008). Furthermore, a reduction in activation energy for hydrogen desorption, and a reduction in desorption temperature has been observed *e.g.* hence faster kinetics of the system. This clearly demonstrates an improvement in release and uptake of hydrogen during cycling of $LiBH_4$ when nanoconfined into a porous scaffold (Gross et al. 2008).

It is reported that infiltration of $Mg(BH_4)_2$ into active carbon with pore size diameter < 2 nm achieves a lower shifted decomposition temperature and lower activation barrier for dehydrogenation compared to bulk $Mg(BH_4)_2$ (Fichtner et al. 2009). Furthermore, magnesium nanoparticles supported by carbon has been confined by melt infiltration, proving that the size of the crystallites, varied from 2 – 5 nm to below 2 nm by choosing carbons with different pore size distributions (de Jongh et al. 2007).

1.6. **Nanoconfined Complex Borohydrides**

This section reviews the up to date progress of work publish on hydrogen storage properties of various complex metal borohydrides nanoconfinement in various carbon templates for hydrogen storage. Table 1.3 shows a list of nanoconfined system, with various scaffold used. There has been extensive studies on nanoconfined $LiBH_4$ in various types of carbon templates with different pore sizes on the nanoscale. Bulk $LiBH_4$ releases hydrogen at 350 ˚C in 1 bar, however Liu et al (Liu et al. 2011) reveals that nanoconfinement of $LiBH_4$ into 4 - 15 nm highly ordered hexagonally packed cylindrical nanoporous carbon (NPC) starts releasing H_2 at 300 ˚C. Furthermore they show that the quantity of the detected decomposition gas B_2H_6, is reduced with decreasing pore size, due to interruption in decomposition reaction pathways. Solid state NMR studies of $LiBH_4$ reveals that nanoconfined $LiBH_4$ facilitate peak broadening in the ^{7}Li and ^{11}B NMR spectra compared to bulk, due to anisotropic susceptibility effects from the presence of the carbon host, leading to significant diffusional mobility of borohydride anions and lithium in the nano-composite (Verkuijlen et al. 2012). Other carbon templates such as carbon nano fibers (CNF), C_{60}, carbon nano tubes (CNT), mesoporous silica (SBA-15), activated carbon (AC) and Poly(methyl methacrylate) PMMA have also been used to reduce to the temperature for hydrogen release and cyclic stability upon hydrogen release and uptake of $LiBH_4$ (Thiangviriya and Utke 2015; Ward et al. 2013; Wang et al.; Ngene et al. 2010; Gosalawit-Utke, Meethom, et al. 2014). Ngene et al and Shao et al has also been working on functionalizing high

surface area carbon with Ni and NbF_5 nanoparticles, respectively, which acts as a catalyst for hydrogen desorption of $LiBH_4$ (Ngene, Verkuijlen, et al. 2011; Ngene, van Zwienen and de Jongh 2010; Shao et al. 2014). Nanoconfinement of other complex borohydrides such as $Mg(BH_4)_2$ and $Ca(BH_4)_2$ have also been reported. Bulk $Ca(BH_4)_2$ starts releasing hydrogen at 350 ˚C. However, Comanescu et al, incorporated $Ca(BH_4)_2$ into activated mesoporous carbon by the incipient solvent infiltration, and their results revealed that by nanoconfinement, the temperature for hydrogen desorption was reduced to 100 ˚C (Comanescu, Capurso and Maddalena 2012). Ordered mesoporous carbon (CMK-3) functionalized with $TiCl_3$ nanoparticles has also been used to nanoconfine $Ca(BH_4)_2$, and the onset temperature for hydrogen desorption is reduced by 100 ˚C compared to nanoconfinement in pristine CMK-3 (Ampoumogli et al. 2012). These results are similar to what is obtained by Comanescu using larger pore sizes. Similar to $Ca(BH_4)_2$, investigation of $Mg(BH_4)_2$ has also been done. Experiential results compare desorption properties of bulk $Mg(BH_4)_2$ with $Mg(BH_4)_2$ infiltrated into AC. Bulk and nanoconfined $Mg(BH_4)_2$ releases hydrogen in two steps starting at 150 ˚C. However, the first desorption step of bulk and nanoconfined $Mg(BH_4)_2$ peaks at 269 ˚C and 257 ˚C, respectively. The temperature difference between the second desorption peak is larger *i.e.* ΔT = -59 ˚C. Furthermore, the activation energy, E_A, is reduced by 134 kJ/mol in the first decomposition step, and by 28 kJ/mol in the second decomposition for the composite sample (Fichtner et al. 2009). Sartori et al has investigated nanoconfined $Mg(BH_4)_2$ into AC by SANS and SAXS measurements and finds that upon heating to 400 ˚C, nanoconfined particles maintain their size distribution, and the decomposition affects only the morphology of the particle surface (Sartori et al. 2010; Sartori et al. 2009). Nanoconfinement of $NaBH_4$ has also been of interest for Ngene et al and Peru et al. Ngene has infiltrated $NaBH_4$ into high surface area graphite (HSAG-500, pore volume 0.66 cm^3 g^{-1}, BET surface area 500 m^2 g^{-1}, broad pore size distribution dominated by 2–3 nm pores). Ngene et al were the first group to demonstrate the reversibility of $NaBH_4$ (Ngene, van den Berg, et al. 2011). They found that nanosizing and confinement of $NaBH_4$ into HSAG reduced the onset temperature of hydrogen release from 470 ˚C for the bulk to below 250 ˚C for the nanocomposites. $NaBH_4$ decomposes to Na and the *closo* borane $Na_2B_{12}H_{12}$, during heating to 600 ˚C. They managed to rehydride the nanocomposite after being decomposed, to reversibly form $NaBH_4$ at 60 bar H_2 and 325 ˚C, maintaining 43 % of the initial hydrogen storage capacity. As previously mentioned, bulk $LiBH_4$ is considered a candidate for hydrogen storage due to its high gravimetric hydrogen content of 13.9 wt.% H_2 (excluding the decomposition of LiH) (Züttel et al. 2003; Mauron et al. 2008). However, $LiBH_4$ suffers from poor hydrogen release kinetics, not to mention the insufficient cyclic stability during hydrogen release and uptake. $LiBH_4$ is reversible under relative harsh conditions *i.e.* at 600 ˚C and at a pressure of 155 bar H_2 (Mauron et al. 2008). One way to improve the kinetic and thermodynamic properties of potential hydrogen storage materials is by combining exothermic and endothermic chemical reactions to facilitate a destabilised state. For instance, bulk $LiBH_4$ is

destabilised by a mix of additional metal hydride such as MgH_2. Numerous publications on the binary system $2LiBH_4$-MgH_2 nanoconfined in carbon aerogel scaffold (CAS) is done by Nielsen and Gosalawit-Utke et al. (Gosalawit-Utke et al. 2011; Gosalawit−Utke et al. 2012; Gosalawit-Utke, Milanese, Nielsen, et al. 2013; Nielsen et al. 2010). During heating to 470 ˚C, bulk $2LiBH_4$-MgH_2 releases 9.2 wt.% H_2, corresponding to 80 % of the theoretical available hydrogen content, thus hydrogen desorption is not completed at 470 ˚C. On the contrary nanoconfined $2LiBH_4$-MgH_2 (MgH_2 infiltrated via solvent infiltration of $MgBu_2$ in heptane solution) into CAS with an average pore size of 21 nm release most of the available hydrogen in the sample (Nielsen et al. 2010). More complex systems explore the properties of binary complex hydrides for nanoconfinement, such as $LiBH_4$-$Ca(BH_4)_2$ (Lee et al. 2011; Lee et al. 2012; Ampoumogli et al.; Javadian, Sheppard, et al. 2015a), $LiBH_4$-Mg_2NiH_4 (Javadian, Zlotea, et al. 2015), $LiBH_4$-$Mg(BH_4)_2$ (Sabrina et al. 2012; Liu et al. 2014; Zhao-Karger et al. 2013; Javadian and Jensen 2014), $LiBH_4$–$LiAlH_4$ (Xia, Meng, et al. 2013) and $LiBH_4$-$NaAlH_4$ (Thiangviriya et al. 2015). These systems all form eutectic melts when physically mixed together, which makes them suitable for melt infiltration into porous scaffolds. As reported for the respective systems, nanoconfinement either in CAS, CMK-3, IRH-33, and NPC does facilitate hydrogen desorption and does improve the rehydrogenation of the hydride.

Table 1.3 Various published complex metal borohydride nanoconfined in scaffold with or without catalytic funcktionalization of the scaffold.

System	Functionalization	Scaffold	Reference
$LiBH_4$		CAS, NPC, effect of pore size	Liu(Liu et al. 2011)
$Mg(BH_4)_2$		AC	Sartori(Sartori et al. 2009; Sartori et al. 2010)
$Mg(BH_4)_2$		CAS	Yan (Yan, Au, et al. 2013)
$LiBH_4$-$Ca(BH_4)_2$		In situ NMR, CMK-3	Lee(Lee et al. 2012)
$2LiBH_4$-MgH_2		CAS	Gosalawit-Utke(Gosalawit-Utke, Milanese, Nielsen, et al. 2013; Gosalawit-Utke et al. 2011; Gosalawit−Utke et al. 2012; Gosalawit–Utke et al. 2014)
NH_3BH_3		CMK-3	Wahab(Wahab, Zhao and Yao 2012)
$LiBH_4$ & $NaBH_4$		CuS hollow nanospheres	Lai(Lai, Christian and Aguey-Zinsou 2014)
$Ca(BH_4)_2$	$TiCl_3$	CMK-3	Ampoumogli(Ampoumogli et al. 2012)
$Li^{11}BD_4$–$Mg(^{11}BD_4)_2$		IRH33	Sartori(Sabrina et al. 2012)
$LiBH_4$		HSAG-500	Remhof(Remhof et al. 2013)
$LiBH_4$		HSAG-500	Verkuijlen(Verkuijlen et al. 2012)
$2NaBH_4$+MgH_2		SBA-15	Mulas(Mulas et al. 2012)

$LiBH_4$		CNF	Thiangviriya(Thiangviriya and Utke 2015)
$LiBH_4$	NbF_5	Mesoporous carbon	Shao(Shao et al. 2014)
$LiBH_4$-Mg_2NiH_4		CAS + CMK-3	Javadian(Javadian, Zlotea, et al. 2015)
$LiBH_4$-$Ca(BH_4)_2$		CMK-3/AEROSIL300/non-porous Carbon discs	Ampoumogli(Ampoumogli et al.)
$LiBH_4$-$Ca(BH_4)_2$		CMK-3	Lee(Lee et al. 2011)
$Mg(BH_4)_2$	Ni	CAS	Au(Au et al. 2014)
$LiBH_4$		C_{60}	Ward(Ward et al. 2013)
$Ca(BH_4)_2$		Mesoporous carbon	Comănescu(Comanescu, Capurso and Maddalena 2012)
$LiBH_4$		CNT	Wang(Wang et al.)
$LiBH_4$-$Mg(BH_4)_2$		nanoporous carbon NPC	Liu(Liu et al. 2014)
$LiBH_4$		nanoporous carbon NPC	House(House et al. 2014)
$2LiBH_4$-MgH_2		CMK-3	Wang(Wang et al. 2014)
$LiBH_4$		CMK-3	Liu(Liu et al. 2010)
$LiBH_4$-$Ca(BH_4)_2$		CAS	Javadian(Javadian, Sheppard, et al. 2015a)
$LiBH_4$		SBA-15	Ngene(Ngene et al. 2010)
$LiBH_4$-$Mg(BH_4)_2$		IRH33	Zhao-Karger(Zhao-Karger et al. 2010; Zhao-Karger et al. 2013)
$NaZn(BH_4)_3$		SBA-15	Xia(Xia, Li, et al. 2013)
$LiBH_4$		PMMA	Gosalawit-Utke(Gosalawit-Utke, Meethom, et al. 2014; Plerdsranoy et al. 2015)
$2LiBH_4$–$LiAlH_4$		Mesoporous carbon	Xia(Xia, Meng, et al. 2013)
$LiBH_4$-$Mg(BH_4)_2$		CAS	Javadian(Javadian and Jensen 2014)
$LiBH_4$		AC	Fang(Fang et al. 2008)
$2LiBH_4$-MgH_2	$TiCl_3$	CAS	Gosalawit-Utke(Gosalawit-Utke, Milanese, Javadian, et al. 2013)
$2LiBH_4$-MgH_2	$TiCl_4$	CAS	Gosalawit-Utke(Gosalawit-Utke, Milanese, et al. 2014)
$Mg(BH_4)_2$	Ni	CMK-3	Wahab(Wahab et al. 2013)
$NaBH_4$		HSAG-500	Ngene(Ngene, van den Berg, et al. 2011)
$LiBH_4$	Ni	HSAG-500	Ngene(Ngene, van Zwienen and de Jongh 2010; Ngene, Verkuijlen, et al. 2011)
$NaBH_4$		CMK-3	Peru(Peru et al. 2013)
$2LiBH_4$-MgH_2		CAS	Nielsen(Nielsen et al. 2010)
$2LiBH_4$-$NaAlH_4$		CAS	Thiangviriya (Thiangviriya et al. 2015)

$Mg(BH_4)_2$	AC	Fichtner(Fichtner et al. 2009)

In this thesis, the nanoconfined systems of $LiBH_4$-$Ca(BH_4)_2$, $LiBH_4$-$NaBH_4$ and $LiBH_4$-$NaAlH_4$ are investigated as candidates as the low temperature metal hydride (LTMH) medium for the concentrated solar thermal power plant. However, complex metal borohydrides may also be considered as potential high temperature metal hydrides (HTMH), as illustrates in Table 1.4. Considering the heat storage capacity and gravimetric H_2 content of for instance $LiBH_4$ and $NaBH_4$, at their respective operating temperatures, do resemble the heat storage capacity of known HTMH such as CaH_2, MgH_2 and $TiH_{1.72}$.

The operating temperature of borohydrides can be decreased by destabilisation or reactive hydride composites. If the temperature can be decreased enough to satisfy the operating temperatures for the LTMH, they could be alternatives to other low temperature metal hydrides proposed for CST. Borohydrides have the potential to be used as either: (1) the low temperature H_2 storage (if they can be destabilised and their kinetics improved); (2) The high temperature hydride (if their kinetics are improved enough at high temperatures) (3) their reversibility of hydrogen release and uptake can be stabilised. Both of these are generally a result of the high hydrogen storage capacity of borohydrides. An example of a destabilised borohydride system is $LiBH_4$-Al that can be used as a low temperature H_2 storage material, due to decomposition taking place at $T < 500$ °C with a high hydrogen storage capacity of 11.4 wt.% H_2 (the $2LiBH_4$-Al system) (Ravnsbæk and Jensen 2012). However complex borohydrides can also be used for high temperature systems, such as pure $LiBH_4$, which shows significant cyclic stability of 3.4 wt% H_2 during cycling, see Table 1.3. Furthermore, decomposition of $LiBH_4$ from the molten state at 627 ºC reduces the enthalpy of H_2 release to 56.9 kJ/mol.H_2 from a value of 66.8 kJ/mol.H_2 at room temperature. Despite this, pure molten $LiBH_4$ at 627 ºC (900 K) has a theoretical heat storage capacity of 3915 kJ/kg (El Kharbachi et al. 2012). If the operating temperature is instead 727 ºC (1000 K) then the heat storage capacity of pure molten $LiBH_4$ increases to 4936 kJ/kg, as this temperature is above the melting point of LiH, 689 ± 5 ºC (J. Sangster 2000). These thermochemical heat storage capacities are some of the highest known.

Table 1.4 Hydrogen and thermal heat storage properties of complex borohydrides, LTMH and HTMH

Compound groups	T/p(opr.) (C/bar)	H_2 capacity (wt.%)	Heat storage capacity (kJ/kg)	Reference
Complex Borohydrides				
$LiBH_4$	727/1	18.5	3915	(El Kharbachi et al. 2012; J. Sangster 2000)
$NaBH_4$	500/1	10.7	4388	(Martelli et al. 2010)
$Ca(BH_4)_2$	727/1	11.5	3584	This work
LTMH				
$TiFeH_2$	0-120/2-70	1.9	-	(Harries et al. 2012; Corgnale et al. 2014)
$TiCr_{1.8}H_{3.5}$	0-70/85-600	2.4	-	(Harries et al. 2012; Corgnale et al. 2014)
$TiMn_{1.5}H_{2.5}$	0-120/3-140	1.9	-	(Harries et al. 2012; Corgnale et al. 2014)
$NaAlH_4$	80-120/10-60	5.6	-	(Harries et al. 2012; Corgnale et al. 2012; Hardy and Anton 2009; Bonnetot et al. 1980)
HTMH				
CaH_2	900-1100/0.1-1.5	5	4934	(Corgnale et al. 2014)
LiH	950-1150/0.1-1.5	12.6	8397	(Corgnale et al. 2014; Chemistry 2007)
MgH_2	300-500/10-200	7.6	2811	(Chaise et al. 2010)
$TiH_{1.72}$	650-950/0.5-10	3.5	2842	(Corgnale et al. 2014)

1.7. **Resorcinol Formaldehyde Carbon Aerogels**

The backbone of this thesis is the synthesis of resorcinol formaldehyde carbon aerogels, utilized as porous scaffold throughout the work. The scaffold material constitutes of resorcinol (R) and formaldehyde (F) carbon aerogels (RF-gels). The RF-aerogels are synthesised by a mixture of resorcinol, formaldehyde, catalyst Na_2CO_3 (C) and water (W). The mechanism consist of two important reactions (Al-Muhtaseb and Ritter 2003; Tian et al. 2008); an initial addition reaction, followed by a condensation reaction which determines the final nanostructure of the aerogel, see Figure 1.7.

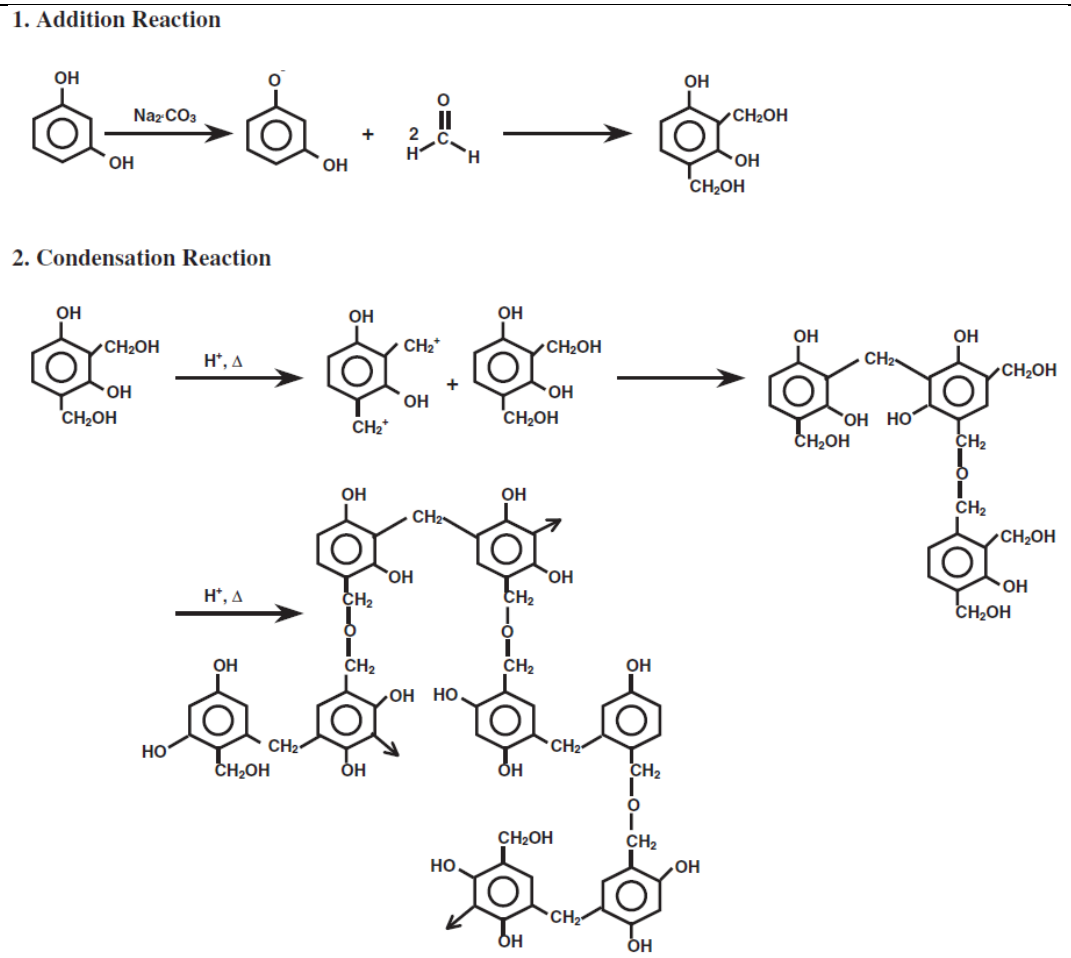

Figure 1.7 Molecular illustration of the addition and condensation reaction mechanism, for the sol gel polymerization of resorcinol and formaldehyde. Adapted from (Lin and Ritter 1997).

The two reactions consist of: (*i*) the formation of resorcinol anions by deprotonation of the hydroxy group HO- due to Na_2CO_3. An addition reaction between formaldehyde and the reactive resorcinol anions takes place in which hydroxymethyl derivate are formed; (*ii*) condensation reaction between hydroxymethyl derivate and cluster growth, which upon heating gives rise to the solid shape of the gel. The catalyst concentration *i.e.* amount of Na_2CO_3 added in the initial state of the synthesis controls the particle size and the degree of dilution (added water) determines the density of the sol-gel solution. Both the mentioned reactants are important contribution factors to the final structure of the aerogel material. In this study, all possible factors are kept constant, and only the amount of Na_2CO_3 is varied *i.e.* the initial pH of the RF solution.

In further details, the role of Na_2CO_3 plays an important role as it works as a basic catalyst by deprotonating the hydroxyl group from R creating very reactive R anions (see Figure 1.7). These are reactive with formaldehyde, forming hydroxyl methyl derivate (-CH_2OH). The resorcinol anion is quite active compared to the stable resorcinol, so the quantity of Na_2CO_3 is essential for the condensation reaction. Upon heating or curing, the condensation reaction initiates the methyl derivate

into forming compounds of methylene ether (-CH_2OCH_2-) bridges. This creates cluster growth monomers, and polymerizes into a three-dimensional cross linked structure, see Figure 1.8.

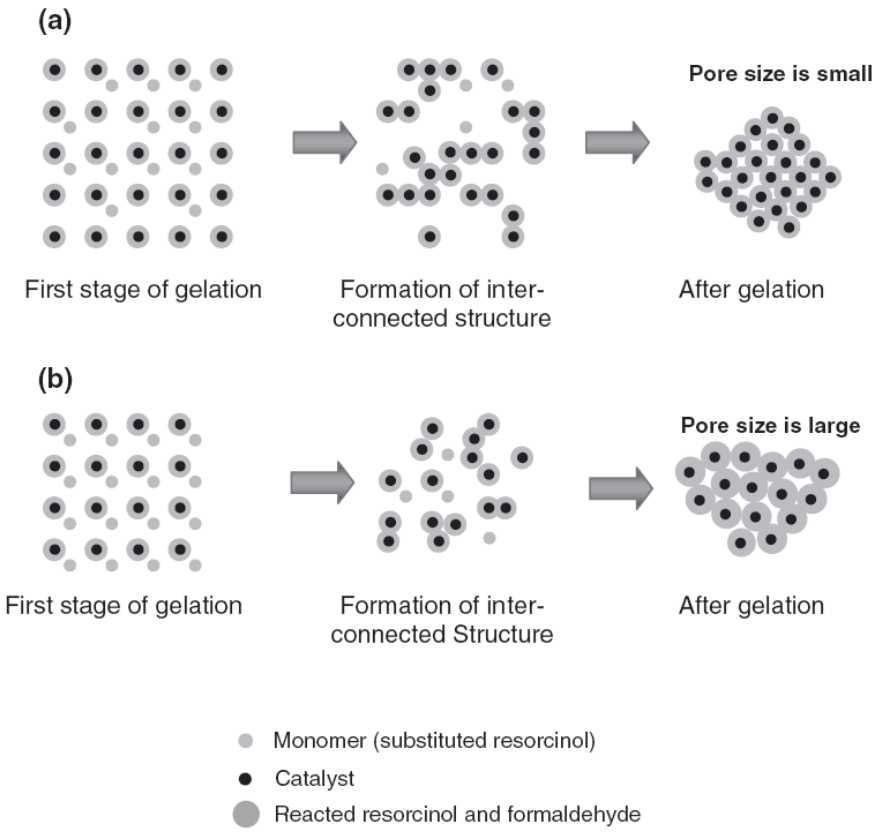

Figure 1.8 Model of gelation progress with a) high and b) low catalyst to water ratio, C/W. Adapted from (Al-Muhtaseb and Ritter 2003).

The final structure is dependent on how close the cluster bridges are assembled towards each other, determining the pore size. The drying condition also have an impact on the final structure (Saliger et al. 1997). The ratio of resorcinol R and catalyst C denoted R/C, is important for the final structure. A high R/C –ratio results in a small pore size and vice versa.

Several other parameter adjustments can be made in the gelation, in order to tune the structure. This include variations in reactant concentration (R/F, R/W, or R/C) or variations of the drying conditions (Al-Muhtaseb and Ritter 2003). It is established in the literature that the initial synthesis pH determines the surface area, the total pore volume and the average pore diameter of the gels, in the sense that increasing pH is accompanied by a decrease of the before mentioned parameters. However there is a minimum and maximum limitation of the pH range for obtaining a porous RF-gel (Al-Muhtaseb and Ritter 2003; Lin and Ritter 1997; Job et al. 2004; Zanto, Al-Muhtaseb and Ritter 2002). It is reiterated that several parameters can be adjusted during the gelation process, which affects the final structural on the nanoscale *i.e.* such as average pore size distribution, specific pore surface area

and internal pore volume (Al-Muhtaseb and Ritter 2003; Lin and Ritter 1997; Saliger et al. 1997; Lin and Ritter 2000; Pekala 1989; Pekala and Schaefer 1993).

As a homogenous sol-gel solution is obtained the solution needs to age for a prolonged time under a constant temperature of 90 °C for 72 h. This treatment affects the hardness of the solution, also known as curing. The curing creates a stiff porous structure forming a material known as aquagels. This is necessary because it allows the formed polymer particle to assemble into a crosslinked matrix, which forms the final solid shape of the gel. In fact, to make sure that the crosslinking reaction takes place completely a prolonged curing time is necessary, in order to prevent swelling during the subsequent solvent shift (Al-Muhtaseb and Ritter 2003; Tian et al. 2008). The color, transparency and hardness of the RF aquagels depends on the R/C, R/W or R/F ratio used in the polycondensation.

Figure 1.9 Illustration of resorcinol formaldehyde aerogel after curing (left) placed in a Al_2O_3 crucible and the pyrolized aerogel chopped into monolithic pieces of ~0.4 cm^3 (right) which results in a graphite like structure. Photo credit: Payam Javadian.

The pores of the aquagels are filled with water after the curing process, since a condensation reaction has taken place. Water has a high surface tension and needs to be removed. So in order to avoid "shrinking" *i.e.* collapsing of pores, the aquagels need to be washed multiple times with an organic solvent, typically acetone due to a lower surface tension compared to that of water (Al-Muhtaseb and Ritter 2003), although shrinking is not completely avoided. When all the acetone is evaporated the aquagels are cut into monolithic chunks ~(0.4 cm^3). The aquagels are pyrolized in N_2(g) at > 800 ^oC, which forms the carbon material known as carbon aerogels (see Figure 1.9.

1.8. **Carbon Dioxide Activation of Carbon Aerogels**

Carbon dioxide activation of carbon aerogels increases the specific surface area, S_{BET}, and total pore volume, V of the scaffold, while maintaining the pore size distribution (Hanzawa et al. 1996; Baumann et al. 2008). The exact mechanism is unknown but, it is reported that CO_2 – activation

changes the skeletal density by burning out oxygen atoms from the aerogel resulting in an inert graphitized curvature. This allows for larger quantities of material to be confined while maintaining the nanoscale particle, and decreases the potential occurrence of chemical reaction or oxide formation between the metal hydrides and the scaffold.

1.9. **Cycling of complex borohydrides.**

Complex borohydrides are known for their poor reversibility or cyclic stability during hydrogen release and uptake. This is usually do to the formation of the stable *closo*- boranes $B_{12}H_{12}$ compounds eg. $Li_2B_{12}H_{12}$ as known from $LiBH_4$ decomposition (Mark Paskevicius 2017). Numerous work on hydrogen storage properties of complex borohydrides has been reported, however not much work focuses on the reversibility of these compound. The attempts on rehydrogenation of complex borohydrides usually requires severe rehydrogenation conditions that are outside the regime for practical applications either for mobile application or as heat storage. Table 1.5 displays several attempts on reforming pure borohydrides such as $LiBH_4$, $Ca(BH_4)_2$ and $Mg(BH_4)_2$. It is worth of note that Table 1.5 is only displaying the best results obtained on reversibility that the author was able to find in the literature. Many published unsuccessful attempts has been made but these are not taken into account. The highest reversibility obtained from bulk $Mg(BH_4)_2$ is 11.4 wt.% H_2 but require extreme rehydrogenation conditions (T = 400 °C, $p(H_2)$ = 960 bar, t = 108 h), and only one rehydrogenation was attempted in this case (Severa, Rönnebro and Jensen 2010).

The cycling in reactive hydride composites (RHC) systems of complex borohydrides has also been reported as shown in Table 1.5. In RHC such as $LiBH_4$-MgH_2, the combination of decomposition reaction between the two hydrides facilitate in improved cyclic stability of a large hydrogen capacity due to multiple reversible reactions. The significant rehydrogenation of $LiBH_4$-MgH_2 retains 9.2 wt.% H_2 after 20 cycles, when rehydrogenated 350 °C and 50 bar (Jepsen et al. 2013).

Table 1.5 Cycling properties reported of selected bulk complex borohydrides and reactive hydride composite (RHC). The rehydrogenation conditions and notes on reversibility are displayed.

Compound	Rehydrogenation Conditions (*T/p/t*)	Cycling Stability	Reference
Pure Borohydride Systems			
$LiBH_4$@ZTC-750	260/120/12	54 % after 5 cycles	(Shao et al. 2015)
$LiBH_4$	265/90/5	D1: 3.5 wt.%, D2: 1.85 wt.%	(Wan and Shaw 2011)
$LiBH_4$-C_{60}	330/100/5	9 cycles. D1: 13.2 wt.%, D9: 3 wt.%	(Ward et al. 2013)
10wt.% Pt/C - $LiBH_4$	600/30/24	30 cycles 6.1 wt.% stable	(Xu et al. 2008)

10wt.% Pt/C - $LiBH_4$	600/30/24	D1: 9.3 wt.%, 4.3 wt% stable, 30 cycles	(Xu et al. 2009)
CA-$LiBH_4$	400/100/2	70 % retained after 3 desorption	(Gross et al. 2008)
Bulk $LiBH_4$	600/155/3.5	D1 to 600 °C = 10.9 wt.% H_2. D2 to 600 °C = 8.3 wt.%.	(Mauron et al. 2008)
US patent - bulk $LiBH_4$	650/150/48	4 cycles. 77 % reversible after 4 cycles	(Muller et al.)
$Ca(BH_4)_2$	350/90/24	1 rehyd. 50 % rehydrogenation. 3.8 wt.%	(Kim et al. 2008)
$Mg(BH_4)_2$	400/960/108	11.4 wt.% rehydrided	(Severa, Rönnebro and Jensen 2010)
Borohydrides in RHC Systems			
$2LiBH_4$-MgF_2	450/100/24	3 cycles. 6.2 wt.% stable	(Yuan, Liu and Li 2011)
$6LiBH_4$-CaF_2	450/92/-	3cycles D1: 9.3 wt.% D3:8 wt.%	(Yuan et al. 2011)
CA-$2LiBH_4$-MgH_2	425/145/12	4 cycles stable 3.5 wt%	(Gosalawit-Utke et al. 2011)
$LiBH_4$-$NaAlH_4$	400/140/10	4 desorptions, not stable, 3.38 wt.% after 4th desorption	(Javadian et al. 2016)
CA-$LiBH_4$-$NaAlH_4$	400/140/10	4 desorptions, not stable, 3.4 wt.% after 4th desorption	(Javadian et al. 2016)
$LiBH_4$-MgH_2	350/50/-	20 cycles. 9.2 wt.% H_2 after 20 desorption. Slowly decreasing pr. cycle	(Jepsen et al. 2013)
$LiBH_4$ – Al	400/100/2	10 cycles. Not stable. 1.8 wt% H_2 after 10th cycle	(Hansen et al. 2013)
$LiBH_4$ - MgH_2 - Al	400/100/2.5	3 cycles. Not stable, 6.2 wt.% H_2	(Hansen et al. 2014)
CA-$LiBH_4$-Mg_2NiH_4	450/176/10	5 cycles. Not Stable. 1.7 wt.% after 5th cycle	(Javadian, Zlotea, et al. 2015)
$4LiBH_4$ + YH_3	350/90/-	1 rehyd. 5.2 wt.% H_2	(Shim et al. 2009)
$LiBH_4$-CaH_2 - $TiCl_3$	450/80/16	10 cycles not fully stable. 7.1 wt.% after 10 desorption	(Li, Li and Qu 2017)
$LiBH_4$-$NaBH_4$	400/140/10	4 cycles. Not Stable after 4 cycle. 1.6 wt.% H_2 stable	(Javadian, Sheppard, et al. 2015b)
CA-$LiBH_4$-$NaBH_4$	400/140/10	4 cycles. Stable after 1 cycle. 6.4 wt% stable	(Javadian, Sheppard, et al. 2015b)
$LiBH_4$-$Mg(BH_4)_2$	400/140/10	4 cycles. Stable after 3 cycle. 3.1 wt% stable	(Javadian and Jensen 2014)
CA-$LiBH_4$-$Mg(BH_4)_2$	400/140/10	4 cycles. Stable after 2 cycle. 4.4 wt% stable	(Javadian and Jensen 2014)
$LiBH_4$-$0.2MgCl_2$-$0.1TiCl_3$	600/70/-	D1:4.9 wt.%, D2:4.9 wt.%, D3: 4.24 wt.%	(Au and Jurgensen 2006)
$LiBH_4$-$Ca(BH_4)_2$	330/40/-	1 Cycle 7 wt.%	(Yan, Remhof, et al. 2013)
$LiBH_4$-$Ca(BH_4)_2$	400/140/10	3 cycles, 73 % after 3rd desorption	(Javadian, Sheppard, et al. 2015a)

Complex hydrides show capacity loss when nanoconfined due to irreversible reaction with oxygen in the scaffold (Ngene, van den Berg, et al. 2011). This capacity loss can be recovered by adding extra alkali metal to compensate for the alkali metal that was initially oxidised. In our system we have full reversibility of the nanoconfined $LiBH_4$ because the calcium is preferentially oxidised *i.e.* the calcium acts an oxygen scavenger and since the calcium decomposition products are not participating in the rehydrogenation process, no capacity loss due to its oxidation is occurring.

The TPD results in Section 3.5 of the thesis show that three cycles are needed before the temperature of desorption for the nanoconfined sample stabilises. This seems to be a general trend for nanoconfined hydrides, as similar trend is observed for the $LiBH_4$-$NaBH_4$, $LiBH_4$-$Mg(BH_4)_2$ system (Javadian and Jensen 2014; Javadian, Sheppard, et al. 2015).

1.10. Significance

The scarcity of fossil fuels combined with the detrimental ecological and environmental impact of fossil fuel consumption, has facilitated an increased focus on alternative energy sources. High temperature thermal energy storage technologies are suitable for concentrating solar power production. Reversible gas-solid thermal energy storage has the potential to achieve high energy storage densities while being adjustable to various plant configurations (Liu et al. 2016).

The full reversibility of $LiBH_4$ combined with its low mass means that it may have application as a high performance heat storage material. At 727 °C. Pure $LiBH_4$ has one of the highest known heat storage capacities, 4936 kJ/kg, with a mild hydrogen equilibrium pressure of 13.2 bar. Even taking into account the additional mass starting from $Ca(BH_4)_2$, the practical heat storage capacity is 2964 kJ/kg. Pure molten $LiBH_4$ at 627 ºC (900 K) has a theoretical heat storage capacity of 3915 kJ/kg (El Kharbachi et al. 2012). If the operating temperature is instead 727 ºC (1000 K) then the heat storage capacity of pure molten $LiBH_4$ increases to 4936 kJ/kg, as this temperature is above the melting point of LiH, 689 ± 5 ºC (J. Sangster 2000). These thermochemical heat storage capacities are some of the highest known and are only exceeded by two oxidation reactions of methane (Pardo et al. 2014) and three metal hydride systems (Chemistry 2007; Sheppard et al. 2016). The methane oxidation reactions have the disadvantages of requiring high temperatures (950 ºC) for the heat charging reactions and a large temperature decrease (>400 ºC) for the heat release reactions (Pardo et al. 2014).

The thermochemical heat storage capacity of $LiH_{(l)}$ and $CaH_{2(s)}$ are 8376 kJ/kg and 4388 kJ/kg respectively but require operating temperatures above >950 ºC to generate H_2 pressures greater than 1 bar (Chemistry 2007). The theoretical heat storage capacity of $NaBH_{4(s)}$ at 500 ºC is ~5445 ± 264 kJ/kg (Chemistry 2007; Martelli et al. 2010) and its $T_{(P = 1\ bar\ H2)}$ is more practical, ~515 ºC. However, its viability for heat storage is hindered by limited reversibility due to the volatile nature of the molten sodium metal decomposition product. Even taking into account the weight penalty associated with

the $LiBH_4$-$Ca(BH_4)_2$ eutectic composition, the heat storage capacity is still 2351 kJ/kg and 2964 kJ/kg at 627 ºC and 727 ºC, respectively. Optimisation of minimum amount of $Ca(BH_4)_2$ required to allow $LiBH_4$ reversibility would increase these values.

The 1 bar H_2 decomposition temperature of molten $LiBH_4$ is approximately 460 ºC (El Kharbachi, 2012) and since the H_2 equilibrium pressure increases exponentially with increasing temperature, a natural concern would be that at a temperature of 727 ºC, (267 ºC above the $T_{(P = 1\ bar\ H2)}$), the H_2 equilibrium pressure over molten $LiBH_4$ would be too high for practical applications. For instance, operating MgH_2 or Mg_2FeH_6 at 267 ºC above their $T_{(P = 1\ bar\ H2)}$ would result in H_2 equilibrium pressures of ~183 bar and ~165 bar, respectively (Paskevicius, Sheppard and Buckley 2010; Bogdanović et al. 2002). Unlike MgH_2 and Mg_2FeH_6, $LiBH_4$ decomposes from the molten state. Consequently the entropy change during H_2 release is substantially lower (ΔS($LiBH_4$ at 460 ºC) ~ 78.5 J/mol.H_2.K (El Kharbachi 2012) compared to ΔS(MgH_2 at 330 ºC) ~ 133.4 J/mol.H_2.K (Paskevicius, Sheppard and Buckley 2010) and the H_2 equilibrium pressure does not increase as rapidly with temperature and even at 727 ºC is only ~13.2 bar (El Kharbachi et al. 2012).

One obvious problem associated with the large scale use of $LiBH_4$ for either H_2 or heat storage is the high cost of lithium. This would limit its use to high performance and niche applications. A possible way to optimize the system is to determine the minimum amount of $Ca(BH_4)_2$ required to allow reversibility of $LiBH_4$.

Chapter 2: Characterization Techniques

This chapter, gives a basic introduction to the experimental techniques in this thesis.

2.1. Gas Sorption Analysis

The phenomenon of all solid surfaces attracting surrounding gas molecules, is called gas sorption. Monitoring the gas adsorption of porous materials provides useful information about characteristics of the mesoporous materials such as the BET surface area (S_{BET}), maximum average pore size (D_{max}), microporous pore volume (V_{micro}), mesoporous pore volume (V_{meso}) and total pore volume (V_{tot}).

The apparatus of gas sorption analysis is connected to nitrogen and helium gas bottles. Furthermore a bath of liquid nitrogen (T ~ -196 °C) is used, in order to keep the sample cool at constant temperature, (isotherm) during data collection. A known amount of sample is loaded in a sample tube and attached to a chamber with a well-established volume, and sealed tightly. The empty space in the sample tube is calibrated, utilizing helium gas. A known amount of nitrogen gas is loaded into the sample cell. The sample is pressurized with nitrogen gas, and the sample adsorbs the gas, due to Van der Waals interactions. The apparatus measures the amount of adsorbed nitrogen gas as a function of pressure in the range 0 - 1 p/p_0, where p_0 refers to the atmospheric pressure. Subsequently, desorption is measured in the pressure range 1 - 0 p/p_0. The amount of absorbed/desorbed gas is determined by the gas law from precise measurements of the pressure after introducing/removing a known quantity of N_2. The volume of nitrogen gas adsorbed is expressed per unit mass of sample, thus it is important to establish the correct mass of sample prior to the analysis. As a result, the collected data is displayed as a graph with accumulated N_2 volume (V/m) as a function of relative pressure (p/p_0), see Figure 2.1. The resulting graph is called an adsorption isotherm. The temperature of the liquid nitrogen (T ~ -196 °C) used to cool the sample depends on the atmospheric pressure p_0. This means that if the pressure of the sample cell exceeds the atmospheric pressure (*i.e.* $p/p_0 > 1$) nitrogen condenses inside the sample tube, resulting in invalid data (Roque-Malherbe 2007). If the porous material has an average pore size ranging in the mesoporous domain (2 - 50 nm), capillary condensation of nitrogen takes place, which is associated with a gas to liquid phase transition (Brunauer, Emmett and Teller 1938). Thus a surface tension is created in the pores by Van der Waals forces, which is attributed to pressure differences between the equilibrium pressure, p, and the atmospheric pressure, p_0. As a result of pressure difference and surface tension in the pores, condensation of nitrogen is initiated on the walls of the pores, also known as capillary condensation. Capillary condensation occurs when fluid is confined in the meso pores and is attributed to a shift in the vapor-liquid coexistence. That is, a fluid is confined in the pores at pressures lower than the saturation pressure, p_0.

To characterize the porous materials it is useful to determine the parameters; BET surface area, pore volume and average pore size. These parameters are determined from the data by mathematical

models applied on the sorption isotherm. A chronological stepwise process of capillary condensation taking place in the pores is illustrated on the basis of the nitrogen sorption isotherm (see Figure 2.1).

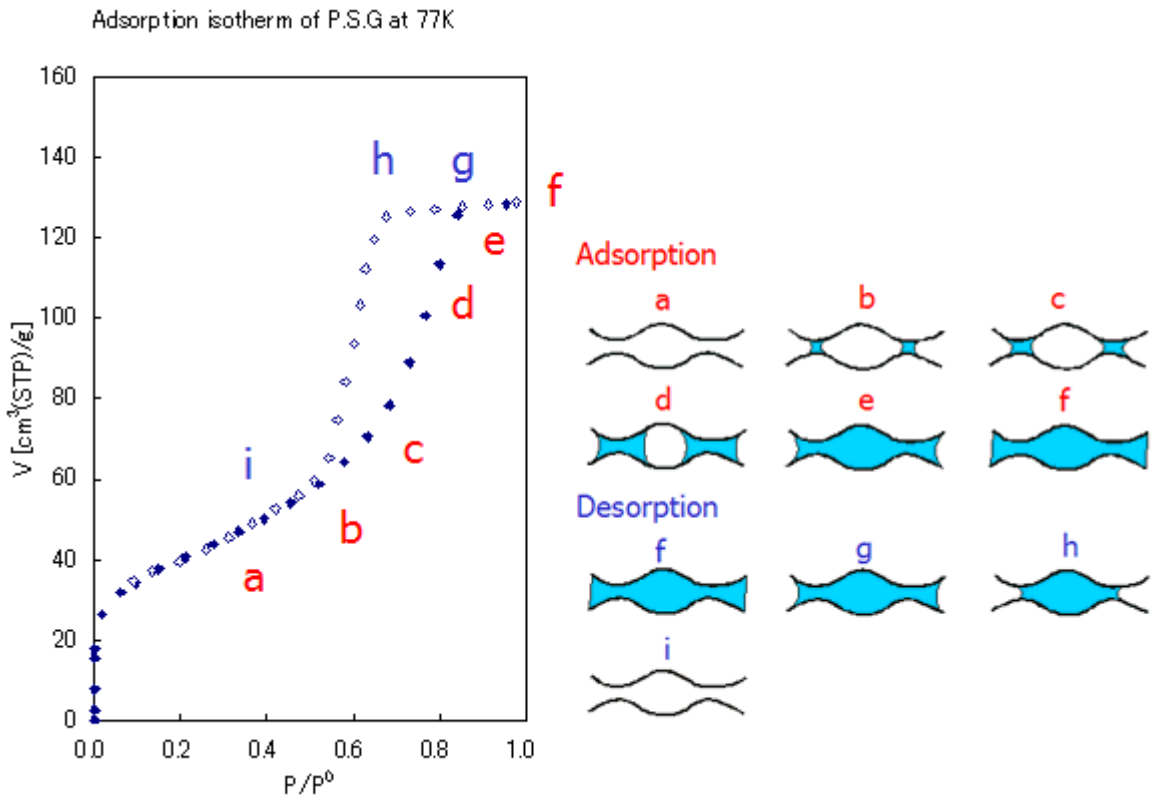

Figure 2.1 Graphical representation of an adsorption isotherm and pore condensation in a mesoporous material.

Usually the gas is not absorbed and desorbed at the same pressure, which is illustrated by a hysteresis effect of the adsorption isotherm. The hysteresis appearance depends on the pore size, of when the sorption layer is created and where micro pore filling takes place. If the sample has micro pores (< 2 nm) the analysis region is lowered to 0.01 - 0.1 p/p_0 where micro pore filling takes place (Roque-Malherbe 2007; Brunauer, Emmett and Teller 1938).

As mentioned, the adsorbate gas used is nitrogen N_2, which has a known dimension and therefore a known monolayer thickness can be calculated. In the pressure range of ca. (0.05 - 0.3 p/p_0), the monolayer of gas covers the surface of the sample. This makes calculation of the surface area (S_{BET}) possible by using the Brunner Emmet Teller (BET) method. The equation used is:

$$S = AN\left(1 - \frac{P}{P_0}\right)\frac{V_a}{M} \qquad (2)$$

where A is Avogadro´s number, N (16.2 Å^2) is a constant factor expressing the area of each N_2 molecule absorbed, the V_a is the molar volume of the gas absorbed at a partial pressure p, p_0 is the saturation pressure of N_2 and M is the molar volume of N_2 (22,414 cm^3/mol) at standard pressure and temperature, STP (Zanto, Al-Muhtaseb and Ritter 2002).

In the pressure range 0.35 - 1 p/p_0, capillary condensation takes place for mesoporous materials. In this area it is possible to determine the average pore size distribution D_{max} by the Brunauer Joyner Halenda (BJH) method. The total pore volume, V_{tot} is calculated by tagging the single highest sorption point $0.9 < p/p_0 < 0.95$ with the assumption that all pores are being filled with condensate. The equation used is:

$$V_{tot} = \left(\frac{M_l}{M}\right) V_a \qquad (3)$$

where M_l is the molar volume of N_2(l), and M and V_a are as mentioned above (Zanto, Al-Muhtaseb and Ritter 2002).

2.2 Powder X-ray Diffraction

It is known that if a crystal is irradiated with X-rays then the beam scatters due to the long range order of the atoms in the crystal structure. If the wavelength of the radiation is similar to the crystals lattice spacing, the electrons of the atoms interact with the incoming beam resulting in diffraction. This phenomenon is known as X-ray diffraction. As irradiation of the ordered crystal structure takes place, X-rays are scattered upon variation of the scattering angle, 2θ. This causes electrons interfering with each other in either constructive or destructive interference. Destructive interference occurs when the incoming X-rays cancel each other out *i.e.* no diffraction pattern is detected. However constructive interference occurs when the diffracted X-rays are in phase *i.e.* diffraction occurs, and the condition is described by Bragg's law, with the assumption of crystals being built as layers of semi-transparent mirrors

$$2d\sin\theta = n\lambda \qquad \text{where } n = 1, 2, 3, ..$$

d is the distance between the lattice planes and θ is the Bragg angle or half the scattering angle depending on the integer number n of the wavelength λ, see Figure 2.2.

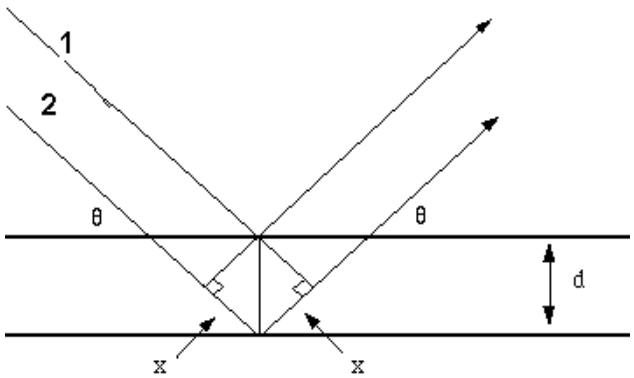

Figure 2.2 Illustration of Bragg's law showing two incoming beams, (1&2), being reflected constructively at two parallel planes with distance d, making an angle θ (Langford and Louer 1996).

In powder X-ray diffraction (PXD) a large number of randomly oriented crystalline domains are irradiated. The data obtained from PXD are presented in a diagram with the diffracted intensity, plotted against the scattering angle, 2θ. The position of the peaks depends on the symmetry of the unit cell while the intensity depends on the atomic coordination and the type and number of atoms. That is why powder diffraction serves as a unique fingerprint for a given crystalline compound. Crystal structure information and powder X-ray diffractions are in databases for a vast number of crystalline compounds. Therefore powder X-ray diffraction is a powerful tool for identification of crystalline materials.

2.1.1. In house powder X-ray diffraction

The majority of samples and starting materials were initially investigated using in house PXD in order to identify known reaction products, estimate the crystallinity of the samples and test purity of chemicals. These measurements were performed using a Stoe diffractometer equipped with a curved Ge(111) monochromator (Cu Kα1 radiation) and curved position sensitive detector. Measurements were performed in Debye-Scherrer transmission geometry with the samples mounted in glass capillaries (o.d. 0.4 to 0.7 mm) sealed with glue or vacuum grease inside the glove box. Data were collected at room temperature (*RT*) between 4 and 127° 2θ. Counting times were varied from 0.25 to 4 hours depending on the data quality for the specific sample.

2.1.2. *In situ* synchrotron radiation powder X-ray diffraction

In order to solve crystal structures of novel compounds, data of high quality is required. Furthermore, to conduct *in situ* studies of fast reactions involving metastable compounds and intermediate decomposition products, relatively short acquisition times are essential. Therefore high intensity X-ray radiation is needed. Synchrotrons can produce X-ray radiation with intensity many orders of magnitude higher than that of conventional X-ray tubes of in house instruments. Furthermore, synchrotron radiation has a high brilliance. This reduces the required exposure times significantly. In addition, the synchrotron beam has a low divergence and can be considered nearly parallel at the distances typically used in PXD. This further increases the instrumental resolution.

In this project synchrotron measurements have been made at the MAX- lab in Lund, Sweden. In a synchrotron, electrons are accelerated as a beam at the speed close to that of light. As the electrons reaches an energy level of approximately 400 MeV, the beam is injected into a synchrotron storage ring. The X-ray beam from a synchrotron is very intense, making it possible to obtain high resolution diffraction measurements on the timescale of seconds, compared to minutes for a conventional laboratory diffractometer (MAXLAB 2016).

2.3 The Sieverts´ Method

The Sieverts´ method, also known as the volumetric technique, is used to determine the amount of gas (hydrogen) being absorbed or desorbed during a chemical reaction. The setup resembles somewhat that of the gas sorption apparatus. The Sieverts´ apparatus consist of one or more reservoirs with known volume, being calibrated by helium gas. These are connected to supplies of hydrogen and helium gas *i.e.* being the investigated and calibration gas, respectively and with controlled gas outlet by an isolation valve. A pump is connected to the system for gas evacuation. The reservoirs are connected to temperature and pressure gauges, monitoring the equilibrium pressure p_{eq}, whenever new equilibrium is established by opening of the isolation valve. The sample holder, containing the sample, with a known volume determined by inert helium gas calibration, is connected to a reservoir with a known volume and pressure. A thermocouple is situated close to the sample holder and the temperature is regulated by a proportional-integral-derivative controller (PID controller).

Upon heating of the sample holder, pressure changes occur as the isolation valve is opened due to hydrogen release or uptake from the sample in question, mediating increase or decrease of pressure. Gas sorption is determined by the difference in actual measured pressure versus calculated pressure assuming no gas absorption/desorption. Using the Sieverts´ method, quantitative hydrogen desorption is evaluated *e.g.* hydrogen release or uptake as a function of time or temperature. Thus, the hydrogen storage material (hydride) can de characterized, with regards to hydrogen storage capacity, reaction kinetics and stability towards charge/discharge in regards to gas uptake and release. To prevent any oxidation the system must be purged several times with argon gas and evacuated. This substantial procedure is conducted prior to every desorption measurements. It is worth noting that the pressure difference calculated by the Sieverts´ method is calculated on the basis of any gas, released from the sample. Gasses other than hydrogen are not considered, for that reason the measurements are carried out under the assumption, that the released gas is hydrogen (Blach and Gray 2007; Blackman, Patrick and Snape 2006).

2.4 Thermal Programmed Desorption Mass Spectrometry

Thermal desorption mass spectrometry, also known as Thermal Programmed Desorption (TPD) is used to detect any gaseous species released from a material as a function of time and temperature. The sample is placed in a vacuum chamber for the duration of the measurement. As heat is applied, the material releases gas which is detected using a quadruple mass spectrometer. The recorded mass spectrometer signal (the ion count) depends on the desorption rate. The instrument detects the species of gas that is desorbed in a given temperature range at high sensitivity. The mass spectrometer settings are predefined to detect selected gasses with different mass *e.g.* such as methane and hydrogen.

The characteristic data parameters obtained from the TPD measurements, are the onset temperature T_{onset} which is the temperature at which hydrogen desorption is first detected, and the hydrogen desorption temperature at which the desorption rate reaches its maximum, T_{max}. From these parameters it is possible to quantitatively compare the sample hydrogen desorption kinetics between samples. A TPD spectrum can consist of several maxima, depending on the material. Several hydrides possess multiple decomposition steps, which are detected using this method (Von Zeppelin, Haluška and Hirscher 2003). The desorption profile reveals indirect information about the number of various desorption phases and the population of the individual phases. Furthermore the peak shape can be used to determine the order of the desorption reaction, and distinguish nanoconfined and bulk properties of the samples.

Chapter 3: PUBLICATIONS FORMING PART OF THESIS

This chapter is sectioned into four different hydrogen storage systems for thermal heat storage that have been studied and published during this thesis.

The thermodynamics of lithium, Li, and its interaction with hydrogen has been investigated as a potential high temperature metal hydride. Lithium is an alkali metal that can form alloys with other metals e.g. aluminum, to produce intermetallic compounds that are used for numerous purposes, both in industry and on a daily basis. In order to reduce the cost of lithium, aluminum is added to destabilize lithium and improve the hydrogen absorption and desorption properties. The thermodynamic properties of the Li-Al-H is investigated.

Complex hydrides generally have problems with hydrogen release and uptake kinetics and reversibility. Nanoconfinement of hydrides can improve the kinetics and could also results in destabilisation (Paskevicius 2013). There is also some evidence that the formation of a eutectic in complex hydride systems can result in destabilisation relative to the individual components (Paskevicius 2013).

Hence the motivation for testing nanoconfined complex hydrides is the potential for:

- Improvement in kinetics and destabilisation which means that they may potentially act as LTMH
- If there is no destabilization but the kinetics/reversibility are improved then they instead have potential as the HTMH

The other three systems are investigated as potential low temperature hydrides such as nanoconfined binary complex borohydride that can operate near ambient temperatures *i.e.* at room temperature; the hydrides can either absorb or desorb large quantities of hydrogen. The following potential low temperature hydride systems have been investigated; $LiBH_4$-$Ca(BH_4)_2$, $LiBH_4$-$Na(BH_4)_2$ and $LiBH_4$-$NaAlH_4$. The initial results from the $LiBH_4$-$Ca(BH_4)_2$ showed interesting results, therefore further investigations on this system were conducted in order to further optimize hydrogen absorption and desorption conditions, resulting in two published papers on the system.

3.1. Destabilization of lithium hydride and the thermodynamic assessment of the Li-Al-H system for solar thermal energy storage

The Li-Al-H system shows significant potential as a HTMH for heat storage, due to its cyclic stability during hydrogen absorption and desorption above 500 °C at and equilibrium of below 2 bar.

RSC Advances

PAPER

View Article Online
View Journal | View Issue

Cite this: *RSC Adv.*, 2016, **6**, 94927

Destabilization of lithium hydride and the thermodynamic assessment of the Li–Al–H system for solar thermal energy storage†

Payam Javadian,[a] Drew A. Sheppard,*[a] Torben R. Jensen[b] and Craig E. Buckley[a]

Received 1st July 2016
Accepted 27th September 2016

DOI: 10.1039/c6ra16983j

www.rsc.org/advances

Lithium hydride destabilised with aluminium, LiH–Al (1 : 1 mole ratio) was systematically studied and its suitability as a thermal energy storage system in Concentrating Solar Power (CSP) applications was assessed. Pressure composition isotherms (PCI) measured between 506 °C and 652 °C were conducted to investigate the thermodynamics of H_2 release. Above the peritectic temperature (596 °C) of LiAl, PCI measurements were not consistently reproducible, possibly due to the presence of a molten phase. However, below 596 °C, the hydrogen desorption enthalpy and entropy of LiH–Al was $\Delta H_{des} = 96.8$ kJ (mol H_2)$^{-1}$ and $\Delta S_{des} = 114.3$ J (K mol H_2)$^{-1}$, respectively $LiH_{(s)}$ at 956 °C, $\Delta H_{des} = 133.0$ kJ (mol H_2)$^{-1}$ and $\Delta S_{des} = 110.0$ J (K mol H_2)$^{-1}$. Compared to pure LiH, the Li–Al–H system has a reduced operating temperature (1 bar H_2 pressure at $T \sim 574$ °C) that, combined with favourable attributes such as high reversibility, good kinetics and negligible hysteresis, makes the Li–Al–H system a potential candidate for solar thermal energy storage applications. Compared to pure LiH, the addition of Al can reduce the cost of the raw materials by up to 44%. This cost reduction is insufficient for next generation CSP but highlights the potential to improve the properties and cost of high temperature hydrides *via* destabilisation.

Introduction

The essential properties of hydrogen powered devices are the requirement of high capacity hydrogen storage materials and reversible hydrogen sorption reactions. Particularly, complex hydrides of alkali metal (Li, Na, K) combined with Al have attracted significant attention due to the high hydrogen storage capacity of 5.5–7.4 wt%,[1–3] and the possibility of a reversible reaction by the addition of a catalyst such as Ti.[4,5] This paper describes the reaction between Li–Al with H_2 at elevated temperatures. The high thermal stability of the Li–Al–H system (*i.e.*, LiH + Al) makes it a potential thermal energy storage material for next-generation concentrating solar power (CSP) applications that are expected to operate in the 600 to 800 °C temperature range.[6,7] To the best of the authors knowledge, the thermodynamic investigation of the Li–Al–H system has previously only been studied experimentally by Veleckis in 1980.[8]

There are three main methods for storing thermal energy; sensible, latent and chemical heat storage. Sensible heat is the energy released (absorbed) by a material as its temperature is reduced (increased). Sensible heat storage media can either be a solid (mainly high temperature concrete or castable ceramics) or a liquid (molten salts, mineral oils and synthetic oils). The simplest is comprised of binary nitrate liquid molten salt mixtures (60% $NaNO_3$; 40% KNO_3) which have potential corrosion problems, not to mention the larger volume required to store sufficient heat to operate the plant for several hours during insufficient solar radiation hours (these nitrate salt mixtures have a maximum useable temperature of ~590 to 600 °C as they begin to decompose above this temperature).[6,9] The second form of thermal storage uses "latent" heat, which is associated with the phase change of materials (PCM) at isothermal conditions *e.g.* heat of phase change such as heat of vaporization (liquid–vapour transition) or heat of fusion (solid–liquid transition). The issue with PCM is sluggish heat transfer and low charge and discharging rates.[10] The third storage mechanism is assigned to chemical reactions *i.e.* chemical heat storage (thermochemical energy storage). This type of heat storage relies on a completely reversible chemical reaction. Principally, heat from solar radiation received, is used to excite an endothermic chemical reaction and the necessary heat is available whenever desired. The advantages of this storage type are, for instance, the high energy storage densities and long storage durations at near ambient temperatures *i.e.* the heat storage capacity is 150 kJ kg^{-1} (290 < T < 600 °C) for molten salt mixtures, 200–500 kJ kg^{-1} (300 < T < 800 °C) for latent heat

[a]*Department of Physics and Astronomy, Curtin University of Technology, Fuels and Energy Technology Institute, GPO Box U 1987, Perth, Western Australia 6845, Australia. E-mail: drew.sheppard@gmail.com; Fax: +61 8 9266 2377; Tel: +61 8 9266 1381; +61 406 966 146*

[b]*Center for Energy Materials, Interdisciplinary Nanoscience Center (iNANO), Department of Chemistry, Aarhus University, DK-8000 Aarhus, Denmark*

† Electronic supplementary information (ESI) available. See DOI: 10.1039/c6ra16983j

compounds and 1160–8400 kJ kg^{-1} ($250 < T < 1000$ °C) for metal hydrides depending on hydride composite system.[9,11]

The cheap and abundant metal hydrides MgH_2 and Mg_2FeH_6 (ref. 12 and 13) have been previously considered for thermal energy storage at temperatures above ~350 °C. The drawback with MgH_2 is the narrow operating temperatures ranging between 400 to 480 °C due to its high equilibrium pressure, which means that the energy efficiency involved between conversions of heat to electricity is too low.[14,15]

More recent work suggests substitution of fluorine in $NaMgH_3$ forming $NaMgH_2F$ which enhances the stability relative to pure $NaMgH_3$. Furthermore, cost assessment based on $NaMgH_2F$ suggests the metal hydride system to be suitable for concentrated solar thermal storage.[16–18]

The advantages of LiH for concentrated solar thermal storage applications is the high hydrogen content of $\rho_m = 12.7$ wt% and high theoretical heat storage capacity of 8397 kJ kg^{-1}. However LiH suffers from a high operating temperature of above 850 °C, a high temperature to reach a hydrogen equilibrium pressure of 1 bar, denoted T(1 bar) ~ 956 °C,[19] and a relatively high cost of the raw material.

The advantages of adding another element, such as Al, are destabilization of the system, potentially reducing the cost and decreasing the 1 bar H_2 equilibrium temperature in comparison to pure LiH. Moreover, it is important to understand the thermodynamics and to evaluate beneficial reactions involved in the Li–Al–H system. In addition LiH + Al are often end products of complex metal hydrides that contain Li and Al (*e.g.* $LiAlH_4$ and $LiBH_4$ + Al[20–22]). Of note, the destabilization of LiH has previously been attempted with the addition of various elements such as Ge, Si and Sn.[23–26] A similar alternative system such as Li–Mg–H system has been investigated for energy storage.[27] However, the drawback of this system, according to the Mg–Li phase diagram,[28] is that no line compounds form between Li–Mg and this limits the ability of the system to produce a hydrogen desorption/absorption plateau at near constant pressure.

This study investigates the thermodynamic and kinetic properties for hydrogen desorption of the Li–Al–H system using pressure composition isotherm (PCI) data and kinetic measurements. The potential application of this system for thermochemical heat storage in CSP is also assessed.

Experimental details

The samples were prepared from commercially available LiH (Aldrich, 95%) and commercially available Al flakes (Aldrich, 99.5%) in the molar ratio 0.51LiH–0.49Al (resulting in an approximate Li : Al ratio of 1 : 1 once purity levels of the reagents were taken into account). We note here that we use the terms LiAl and $Li_{0.5}Al_{0.5}$ interchangeably throughout as the former is usually used in relation to the phase and phase diagram while the latter is more convenient in manipulating chemical formulae. The hydride mixture was ball milled using a stainless steel bowl (80 mL) and balls (Ø: 10 mm), with a planetary mill and a powder to ball ratio of 1 : 24. The milling was performed at 380 rpm with a total milling time of 2 h uninterrupted.

The pressure-composition isotherms and kinetic data were collected using a Sieverts type apparatus (PCTpro 2000 E&E). The samples were sealed in a specially treated (see further details below) 316L stainless steel autoclave under argon and attached to the Sieverts' apparatus. Hydrogen desorption and absorption PCI's were collected at the temperatures 506, 540, 560, 573, 585, 608, 619, 634 and 652 °C, using the same sample. Desorption and absorption measurements were conducted between 0 to 15 bar and the time to reach equilibrium varied but were typically around 2 or 3 hours for each PCI equilibrium data point.

Hydrogen permeability through stainless steel increases exponentially with increasing temperature. The stainless steel autoclave was specially treated *via* an aluminium dip coating process that was followed by oxidation to produce a coating of Al_2O_3.[29] The purpose of the Al_2O_3 coating is to reduce the diffusion of H_2 but, due to technical limitations, the coating only covered the inner and outer surface of the 1/2″ diameter stainless steel tube and not the 1/2″ end cap that seals the tube. Since H_2 permeated through the endcap of the autoclave, all of the collected data was corrected for the hydrogen loss by calculating the amount of hydrogen leaked per desorption step using the permeability of steel at the measured temperatures and pressures.[30]

Results and discussion

According to literature and the phase diagram of Li–Al, the system is known to have four homogenous solid solution (ss) phases; α: which is a dilute solution of Li in Al, β: "LiAl", γ: "Li_3Al_2" and δ: "Li_9Al_4".[31] As the focus of our study is to investigate the thermodynamic properties of the α and β coexisting phases *i.e.* plateau pressure region, the γ and δ line compounds are irrelevant to this study as they are unlikely to ever be present based on the selected starting ratios of Li and Al.[32] The phase diagram of Li and Al suggests that LiH should react with Al to form a solid solution of Li in Al up to a temperature-dependent composition limit according to reaction (1) below the peritectic line at 596 °C.

$$x\mathrm{LiH} + (1 - x)\mathrm{Al} \rightarrow \mathrm{Al}_{1-x}\mathrm{Li}_x + x/2\mathrm{H}_2, \text{ where } 0 < x < \text{limit of Li solubility in Al} \quad (1)$$

Provided that the system is maintained below the peritectic temperature (596 °C), this solid solution of Li in Al can then further react with LiH at constant hydrogen pressure to yield an equilibrium plateau described by reaction (2).

$$2\mathrm{LiH} + 3.273\mathrm{Al}_{0.87}\mathrm{Li}_{0.13} \rightarrow 5.273\mathrm{Al}_{0.54}\mathrm{Li}_{0.46} + \mathrm{H}_2,\ 2.11 \text{ wt\% } \mathrm{H}_2 \quad (2)$$

A generic equation reaction describing the reaction process after the plateau that depends on the composition, is described as the following:

$$y\mathrm{LiH} + (1 - y)\mathrm{Al}_{y\_\mathrm{min}}\mathrm{Li}_{y\_\mathrm{min}} \rightarrow \mathrm{Al}_{(1-y)y\_\mathrm{min}}\mathrm{Li}_{y(1-y\_\mathrm{min}+y\_\mathrm{min}\ \mathrm{y}^{-1})} + y/2\mathrm{H}_2, \text{ where } y\_\mathrm{min} < y < y\_\mathrm{max} \quad (3)$$

View Article Online

Paper RSC Advances

Above 596 °C, a peritectic reaction between the Al–Li solid solution $(Al, Li)_{ss}$ and LiH takes place. According to the phase diagram of Li–Al, two co-existing phases are prevailing; one with Al and a liquid phase, and the other with a solid solution of LiAl and the liquid phase. Two reactions are taking place across these regions, which can be described by reaction (4) and (5) at 627 °C.

$$2LiH + 20.25Al_{0.89}Li_{0.11} \rightarrow 22.25Al_{0.81}Li_{0.19} + H_2,\ 0.4\ wt\%\ H_2 \quad (4)$$

$$2LiH + 6.75Al_{0.70}Li_{0.30} \rightarrow 8.75Al_{0.54}Li_{0.46} + H_2,\ 1.28\ wt\%\ H_2 \quad (5)$$

A complete set of H_2 sorption pressure-composition isotherms (PCIs) have been conducted at the following temperatures; 506.3, 540.0, 559.9, 573.3, 584.8, 608.6, 618.9, 634.2 and 652.4 °C. A sufficient amount of dwell time is crucial during data collection in order to reach true equilibrium, as prematurely halting time can lead to erroneous equilibrium pressure, artificial hysteresis and the incorrect calculation of thermodynamic quantities.[33] Often the effect of severe kinetic limitation is preventing true equilibrium to be reached and if true equilibrium is not met, PCI curves often display large amounts of hysteresis between absorption and desorption isotherms. Furthermore, measured absorption pressures will be higher than actual true equilibrium and measured desorption pressures will be lower than actual true equilibrium, resulting in apparent hysteresis. Insufficient measurement time will also lead to false plateau and equilibrium pressure, and hence incorrect thermodynamic calculations. Furthermore, the equilibrium plateau can also by shortened due to short measurement times at low temperatures, indicating equilibrium has not been reached. These features can be due to kinetic limitations, especially in regions before and after the plateau region. Increasing the temperature of measurement leads to improved kinetics but it must be emphasised that kinetic data should be collected during PCI measurements to ensure sufficient time for equilibrium to occur. The kinetics of decomposition in the Li–Al–H system are relatively fast, thus equilibrium can be reached within 2 hours.

The PCI desorption data below 596 °C, *i.e.* reaction (2) are displayed in Fig. 1(a). The plateau curves are very flat, with less than a 0.2 bar pressure variation between the start and the end of the plateau, and a total of ~2.3 wt% H_2 is desorbed along the plateau at all temperatures below 596 °C. In accordance with the phase diagram,[34] the amount of H_2 desorbed along the plateau gradually decreases as the temperature increases due to the increased solubility of Li in the $(Al, Li)_{ss}$ phase.[33] The total hydrogen desorption capacity ranges between 2.5–2.6 wt%. Since the composition of the starting material in the dehydrogenated state is known to have the composition $Al_{0.54}Li_{0.46}$ at the end of the plateau,[28] the theoretical hydrogen storage capacity of a 1 : 1 molar mixture of LiH and Al is calculated to be 2.89 wt%. Thus at 506 °C the amount of desorbed hydrogen corresponds to 90% of the available theoretical content, whereas at 584.8 °C the amount of desorbed hydrogen corresponds to 87%. It is worth noting that there is a very slight slope evident in the plateaux and may be due to an impurity in the starting reagents *i.e.* LiOH was observed by XRD to be present in the as-received LiH.

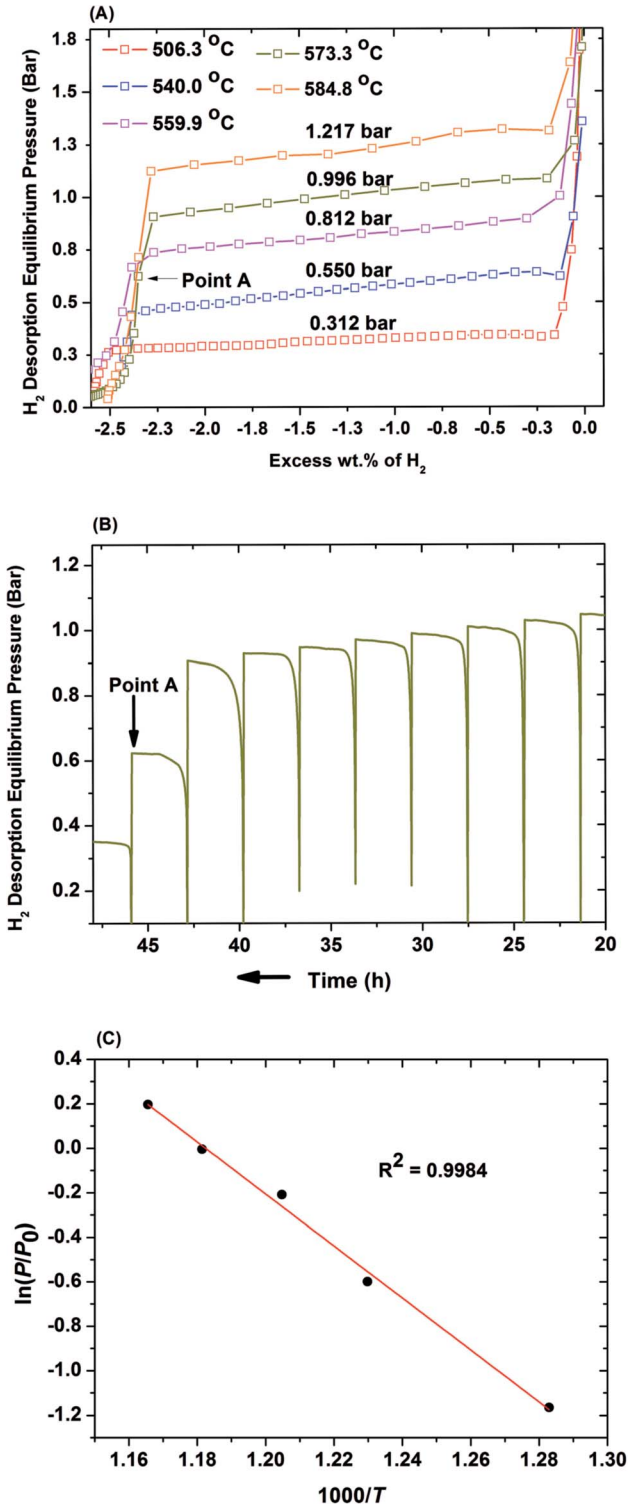

Fig. 1 (a) Hydrogen desorption pressure – composition isotherms for reaction (1) performed at various temperatures below 596 °C. (b) Kinetic H_2 desorption data of reaction (1) performed at 573.3 °C. (c) van't Hoff plot of H_2 desorption equilibrium pressures and the linear fit to the data.

View Article Online

RSC Advances Paper

Fig. 1(b) displays the kinetics of H_2 during each desorption step measured at 573 °C and corresponds to the isotherm presented in Fig. 1(a). Each end point of the kinetic measurement is associated with a pressure point on the isotherm *i.e.* point *A* in Fig. 1(a) and (b) corresponding to the same value point.

Dehydrogenation isotherms collected at 506.3, 540.0, 559.9, 573.3 and 584.8 °C, were used to construct a van't Hoff plot, Fig. 1(c), using the equilibrium pressure values taken from the approximate midpoint of each plateau at the same hydrogen composition (−1.354 wt% H_2). The desorption enthalpy (ΔH_{des}) and entropy (ΔS_{des}) were determined to be 96.8 kJ mol^{-1} H_2 and 114.3 J K^{-1} mol^{-1} H_2, respectively. These values are comparable to those obtained by Veleckis,[8] $\Delta H_{abs} = -98.2$ kJ mol^{-1} H_2 and $\Delta S_{abs} = -117.2$ J K^{-1} mol^{-1} H_2, derived from constructing a van't Hoff plot from their reported hydrogen equilibrium pressures.

It is worth noting that in the PCI desorption data below 596 °C a dip occurs at the beginning of the plateau (at H_2 wt% of between −0.2 and −0.3). This phenomenon appears to be similar to what was previously observed for the Ti–Fe–H[35] and U–H system.[36–38] However the desorption PCI's of the LiH–Al system measured above 596 °C do not display the above-mentioned dip, indicating that at higher temperatures, the dip becomes less pronounced and at a certain temperature regime (possibly around ∼600 °C) it disappears completely. This observation is also in good agreement with previous work,[35] where it disappeared above a critical temperature and was suggested to be due to the supersaturation of hydrogen vacancies in the hydride phase.[35,37] Whether this is the case for the LiH–Al system requires further verification.

PCI desorption isotherms at selected temperatures (608.6, 618.9, 634.2 and 652.4 °C) above the peritectic temperature are shown in ESI Fig. S2(a).† The PCI isotherms measured at 608.6, 618.9 and 634.2 °C indicate clear equilibrium plateaux with a minor slope but we note here that is was difficult to obtain reproducible results on different samples above 596 °C. Measurements (652.4 °C) closer to the melting point of Al (660 °C) resulted in significant changes to the PCI curves with a drastic shortening of the equilibrium plateau. We note that two plateaux would be expected for the PCI measurements conducted at temperatures above the 596 °C but that due to the factors discussed, thermodynamic calculations were not possible and the exact decomposition process could not be determined (see Fig. S2(b)†).

One of the crucial properties of a metal hydride for thermal energy storage is its kinetics, hysteresis and reversibility of hydrogen release and uptake. Fig. 2(A) shows both the absorption and desorption PCT measurements performed below the peritectic temperature at 584.8 °C while Fig. 2(B) and (C) show the kinetic curves for the desorption and absorption, respectively. Fig. 2(A) shows that there is negligible hysteresis in the plateau region but that there is some minor hysteresis before and after the plateau where only the solid-solution α and β phases exist. Examination of the kinetic curves, Fig. 2(B) and (C), reveals that this hysteresis is actually an artefact of slower kinetics and thus a longer measurement time is required in these regions. In contrast, PCT absorption and desorption

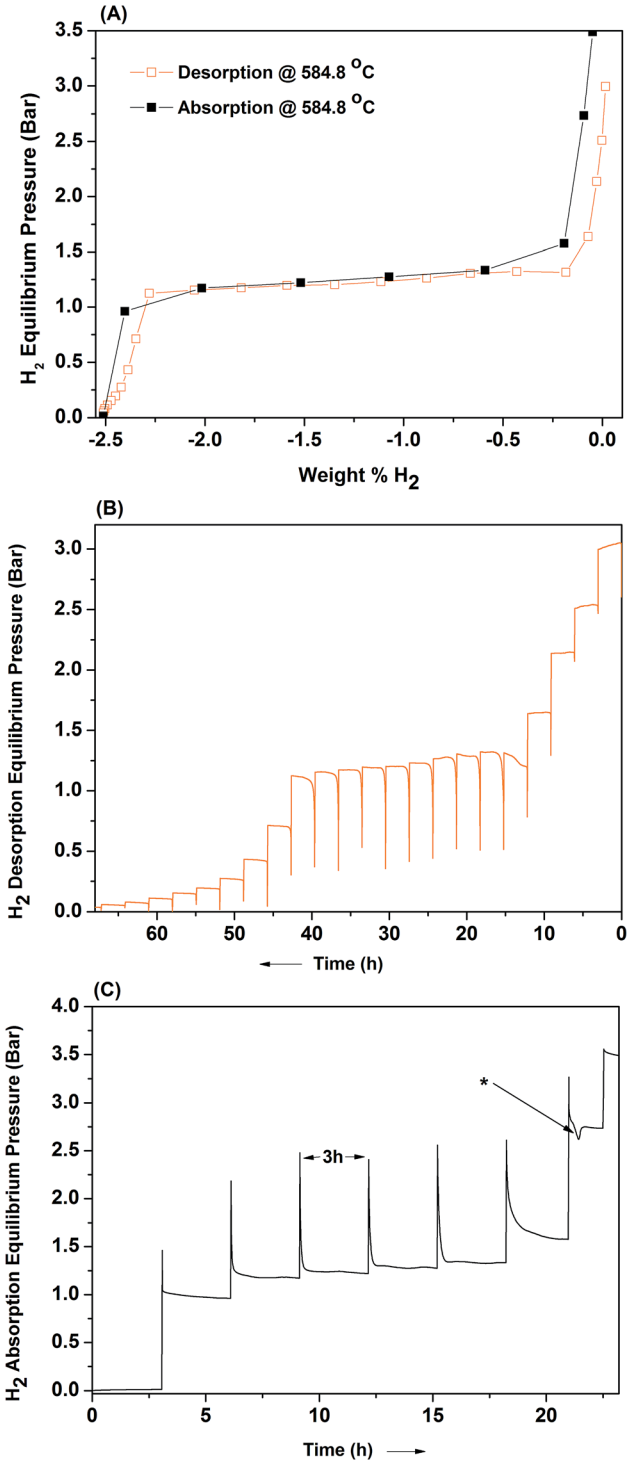

Fig. 2 (A) Desorption–absorption PCT at 585 °C. The respective desorption kinetics (B) and absorption kinetics (C) are also displayed. * is due to a sudden temperature fluctuation in the furnace set-point.

measurements in the plateau region reach equilibrium within 1 hour. An equivalent result was obtained for PCT measurements measured at 618 °C, above the peritectic point (see Fig. S1(A)–(C)†). In PCT measurements, the hydrogen absorption/desorption kinetics are a complex interplay between the PCT step size (large aliquot effect), the thermodynamic driving force,

the hydride enthalpy of formation/decomposition, the sample size and the thermal conductivity of the sample.[33] Of these, the dominant limitation is the low thermal conductivity of the hydride powder, typically less than 1–2 W m^{-1} K^{-1}. This means that heat accumulation and heat flow become the rate-limiting steps[39] and this is only exacerbated in high-temperature hydrides with large negative heats of formation. As a result, the direct quantitative comparison of sorption kinetics between different hydrides is challenging. However, a single-step hydrogen absorption measurement performed at 618 °C (not shown) using an applied hydrogen pressure of 20 bar (*versus* $P(H_2)_{eq}$ at 618 °C of ~2 bar) facilitates a hydrogen overpressure equivalent to an excess thermodynamic driving force of ΔG_{exc}, of −17.1 kJ mol^{-1} H_2 ($\Delta G_{abs} = \Delta G_{eq} + \Delta G_{exc} = \Delta G_{eq} + RT \ln(P_{eq}/P_{abs})$, ΔG = Gibbs free energy) and resulted in complete absorption within 4 hours. This easily meets the U.S. Department of Energy (U.S. D.O.E.) SunShot charge/discharge target of 6 hours (ref. 40) for a CSP thermal energy storage system and suitable engineering to improve the thermal conductivity of the hydride bed would only further enhance the kinetics. Though highly suggestive, such a result would need to be confirmed using single-step absorption measurements using a lower hydrogen overpressure. The negligible hysteresis between the absorption–desorption isotherms in conjunction with kinetics that easily meet U.S. D.O.E. targets makes Li–Al–H a potential high temperature solar thermal heat storage medium.

In order to confirm the hydrogen sorption reactions, X-ray diffraction was performed after both desorption and absorption at 618 °C. XRD performed after desorption (Fig. S2(A) in ESI†) reveals that the main product is LiAl, as expected, with a trace amount of residual LiH. Likewise, after hydrogen absorption at 618 °C, XRD (Fig. S2(B) in ESI†) reveals the main products to be LiH and Al, along with a small amount of $LiAlO_2$ that results from slight oxidation of the sample. It should be noted that trace amounts of an unknown phase were identified in the sample after both desorption and re-absorption.

Metal hydrides have the potential to be the next generation of heat storage materials to replace molten salts in CSP.[6,11] As such, the cost of the metal hydride is of crucial importance. The cost comparison of pure LiH compared to LiH–Al, based on both theoretical and practical capacities, is given in Table 1. The addition of Al improves the operating temperature by decreasing the 1 bar H_2 equilibrium temperature by ~300 °C and decreases the enthalpy of formation. While the consequence of the additive

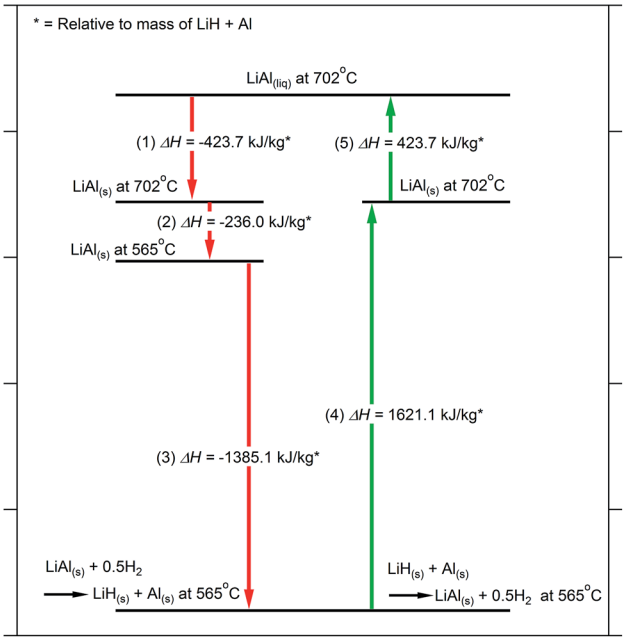

Fig. 3 An alternative thermodynamic cycle that utilises both the heat of fusion of LiAl and its enthalpy of hydrogen absorption. Green arrows indicate "day-time", heat absorbing reactions while red arrows indicate "night-time" heat releasing reactions.[41]

is a decrease in the practical heat storage capacity by approximately 83%, the cost per kW h of thermal energy stored is reduced by ~44%. For thermal energy storage, it has been proposed that the high-temperature metal hydride would operate at a near constant temperature. However, additional heat could be stored in the Li–Al–H system if its temperature is allowed to fluctuate to take advantage of the heat of fusion of LiAl at 702 °C. The thermodynamic cycle would include (Fig. 3):

(1) Night-time: at night-time the heat of fusion of molten $LiAl_{(liq)}$ ($\Delta H = -14.8$ kJ mol^{-1} of LiAl)[41] is exploited at 702 °C to release ~423.7 kJ kg^{-1}* (* relative to mass of LiH + Al).

(2) Night-time: cooling the, now solid, $LiAl_{(s)}$ down to 565 °C (*i.e.* below the peritectic point) exploits the heat capacity of LiAl to release a further 236 kJ kg^{-1}* of heat.

(3) Night-time: by reacting $LiAl_{(s)}$ at 565 °C with hydrogen to form LiH and Al, releasing 1385.1 kJ kg^{-1} of heat, according to the reaction $LiAl_{(s)} + 1/2H_2 = LiH_{(s)} + Al_{(s)}$.

Table 1 A comparison of the properties of pure LiH compared to the LiH + Al system

		H_2 capacity (wt%)	ΔH_{des} (kJ mol^{-1} H_2)	T(1 bar) in °C	Heat storage capacity (kJ kg^{-1})	Cost[a,b] US$ per kg of metal	US$ per kW h_{th}
LiH	Theor.	12.68	133.5	956	8397.3	61.12	26.23
	Pract.	7.61	133.5	956	4198.6	61.12	52.46
LiH + Al	Theor.	2.89	96.8	573	1412.5	13.51	35.12
	Pract.	2.06[c]	96.8	573	1150.3	13.51	49.20
	Pract.[c,d]	2.06[c]	96.8	573	1888.1	13.5	29.51

[a] Li raw material cost of US$70.00 per kg taken from ref. 17. The cost of hydrogen was not taken into account. [b] Al raw material cost of US$1.48 per kg taken from ref. 41. The cost of hydrogen was not taken into account. [c] Assuming the reaction is $2LiH + 3.40Li_{0.142}Al_{0.858} \rightarrow 5.40Li_{0.46}Al_{0.54} + H_2$. [d] Using the reaction scheme from Fig. 3.

(4) Day-time: the reverse of steps (2) and (3) can be combined to absorb 1621.1 kJ kg^{-1} of thermal energy during heating from temperature 565 to 702 °C while desorbing H_2.

(5) Finally, at 702 °C the latent heat of melting of LiAl is utilised to absorb 423.7 kJ kg^{-1}.

According to our calculations, this cycle would decrease the practical cost of the Li–Al–H system by ∼44%. While the calculated cost for the raw materials using this cycle is high (∼US$29.5 per kilowatt hour of thermal energy (kW h_{th}) not including low temperature hydrogen storage, engineering and installation) compared to current state-of-the art molten salt systems (∼US$25–40 per kW h_{th} (ref. 42)), it does highlight a general method for reducing the cost of thermal energy storage based on metal hydrides.

Conclusion

Ball milling of LiH with Al has created a homogenously dispersed aluminium within the LiH phase, leading to reaction of LiH with Al. The thermodynamic assessment of the solid solution phase between LiAl and Al determined a desorption enthalpy and entropy of 96.8 kJ mol^{-1} H_2 and 114.3 J K^{-1} mol^{-1} H_2. It was shown that at temperatures above 596 °C, the determination of thermodynamics parameters were difficult to establish, due to the co-existence of the solid solution of LiAl and a liquid phase. Below 596 °C, the Li–Al–H system has a low hydrogen equilibrium pressure (<2 bar), rapid kinetics, a flat desorption/absorption plateau with minimal hysteresis between absorption and desorption. This means that the Li–Al–H system shows many of the characteristics required by a metal hydride for use as a heat storage material (such as in concentrated solar thermal power plants). However, the relatively high cost of the raw material, even with the cost-reducing addition of aluminium, means that its use would probably be limited to niche applications.

Acknowledgements

CEB, DAS and PJ acknowledge the financial support of the Australian Research Council (ARC) for ARC Linkage Grants LP120100435 and LP150100730. CEB also acknowledges ARC LIEF grants LE0989180 and LE0775551, which enabled the XRD and gas sorption studies to be done. TRJ acknowledge the Danish National Research Foundation, Center for Materials Crystallography (DNRF93), The Innovation Fund Denmark (project HyFill-Fast), the Danish Research Council for Nature and Universe (Danscatt) and the Carlsberg Foundation.

References

1 Q. Lai, M. Paskevicius, D. A. Sheppard, C. E. Buckley, A. W. Thornton, M. R. Hill, Q. Gu, J. Mao, Z. Huang, H. K. Liu, Z. Guo, A. Banerjee, S. Chakraborty, R. Ahuja and K.-F. Aguey-Zinsou, *ChemSusChem*, 2015, **8**, 2789–2825.
2 M. B. Ley, L. H. Jepsen, Y. Lee, Y. W. Cho, J. Bellosta von Colbe, M. Dornheim, M. Rokni, J. O. Jensen, M. Sloth, Y. Filinchuk, J. E. Jørgensen, F. Besenbacher and T. R. Jensen, *Mater. Today*, 2014, **17**, 122–128.
3 E. Callini, Z. Ö, K. Atakli, B. C. Hauback, S. I. Orimo, C. Jensen, M. Dornheim, D. Grant, Y. W. Cho, P. Chen, B. Hjörvarsson, P. de Jongh, C. Weidenthaler, M. Baricco, M. Paskevicius, T. R. Jensen, M. E. Bowden, T. S. Autrey, A. Züttel and M. Hirscher, *Appl. Phys. A*, 2016, **122**(353), 1–22.
4 B. Bogdanovic and M. Schwickardi, *Appl. Phys. A*, 2001, **72**, 221–223.
5 B. Bogdanovic and M. Schwickardi, *J. Alloys Compd.*, 1997, **253–254**, 1–9.
6 D. N. Harries, M. Paskevicius, D. A. Sheppard, T. E. C. Price and C. E. Buckley, *Proceedings of the IEEE*, 2012, **100**, 539–549.
7 U.D.O. Energy, *Sunshot Vision Study, Chapter 5: Concentrating Solar Power Technologies, Cost and Performance*, 2012.
8 E. Veleckis, *J. Less-Common Met.*, 1980, **73**, 49–60.
9 F. Schaube, A. Worner and R. Tamme, *J. Sol. Energy Eng.*, 2011, **133**, 3.
10 A. M. Khudhair and M. M. Farid, *Energy Convers. Manage.*, 2004, **45**, 263–275.
11 M. Fellet, C. E. Buckley, M. Paskevicius and D. A. Sheppard, *MRS Bull.*, 2013, **38**, 1012–1013.
12 J. C. Crivello, R. V. Denys, M. Dornheim, M. Felderhoff, D. M. Grant, J. Huot, T. R. Jensen, P. de Jongh, M. Latroche, G. S. Walker, C. J. Webb and V. A. Yartys, *Appl. Phys. A*, 2016, **122**(85), 1–17.
13 J. C. Crivello, B. Dam, R. V. Denys, M. Dornheim, D. M. Grant, J. Huot, T. R. Jensen, P. de Jongh, M. Latroche, C. Milanese, D. Milčius, G. S. Walker, C. J. Webb, C. Zlotea and V. A. Yartys, *Appl. Phys. A*, 2016, **122**(97), 1–20.
14 M. Groll, A. Isselhorst and M. Wierse, *Int. J. Hydrogen Energy*, 1994, **19**, 507–515.
15 B. Bogdanović, A. Reiser, K. Schlichte, B. Spliethoff and B. Tesche, *J. Alloys Compd.*, 2002, **345**, 77–89.
16 D. A. Sheppard, C. Corgnale, B. Hardy, T. Motyka, R. Zidan, M. Paskevicius and C. E. Buckley, *RSC Adv.*, 2014, **4**, 26552–26562.
17 C. Corgnale, B. Hardy, T. Motyka, R. Zidan, J. Teprovich and B. Peters, *Renewable Sustainable Energy Rev.*, 2014, **38**, 821–833.
18 D. A. Sheppard, T. D. Humphries and C. E. Buckley, *Mater. Today*, 2015, **18**, 414–415.
19 J. Sangster and A. D. Pelton, *"H–Li (Hydrogen–Lithium)" in Phase Diagrams of Binary Hydrogen Alloys*, ed. F. D. Manchester, ASM International, Materials Park, OH, USA, 2000, pp. 74–81.
20 A. Andreasen, T. Vegge and A. S. Pedersen, *J. Solid State Chem.*, 2005, **178**, 3672–3678.
21 X. F. Liu, G. S. McGrady, H. W. Langmi and C. M. Jensen, *J. Am. Chem. Soc.*, 2009, **131**, 5032.
22 B. R. S. Hansen, D. B. Ravnsbaek, D. Reed, D. Book, C. Gundlach, J. Skibsted and T. R. Jensen, *J. Phys. Chem. C*, 2013, **117**, 7423–7432.
23 M. A. Abbas, D. M. Grant, M. Brunelli, T. C. Hansen and G. S. Walker, *Phys. Chem. Chem. Phys.*, 2013, **15**, 12139–12146.

24 A. Jain, H. Miyaoka, T. Ichikawa and Y. Kojima, *J. Alloys Compd.*, 2013, **580**, S211–S215.
25 A. Jain, E. Kawasako, H. Miyaoka, T. Ma, S. Isobe, T. Ichikawa and Y. Kojima, *J. Phys. Chem. C*, 2013, **117**, 5650–5657.
26 K. Doi, S. Hino, H. Miyaoka, T. Ichikawa and Y. Kojima, *Mater. Sci. Forum*, 2010, 2815–2818.
27 X. B. Yu, D. M. Grant and G. S. Walker, *Chem. Commun.*, 2006, 3906–3908.
28 M. Seiersten, *Eur. Comm.*, 1994, 24–28.
29 S. L. Han, H. L. Li, S. M. Wang, L. J. Jiang and X. P. Liu, *Int. J. Hydrogen Energy*, 2015, **35**, 2689–2693.
30 C. S. Marchi, B. P. Somerday and S. L. Robinson, *Int. J. Hydrogen Energy*, 2007, **32**, 100–116.
31 K. Puhakainen, Exploring metal hydrides using autoclave and multi-anvil hydrogenations, *Doctoral Thesis*, Arizona State University, 2013.
32 A. J. McAlister, *Bull. Alloy Phase Diagrams*, 1982, **3**, 177–183.
33 D. A. Sheppard, M. Paskevicius and C. E. Buckley, *Chem. Mater.*, 2011, **23**, 4298–4300.
34 C. Sigli and J. M. Sanchez, *Acta Metall. Mater.*, 1986, **34**, 1021–1028.
35 J. J. Reilly and R. H. Wiswall, *Inorg. Chem.*, 1973, **13**, 218–222.
36 G. G. Libowitz, *J. Nucl. Mater.*, 1960, **2**, 1–22.
37 E. Wicke and K. Otto, *Zeitschrift für Physikalische Chemie*, 1962, **31**, 222–248.
38 F. H. Spedding, A. S. Newton, J. C. Warf, O. Johnson, R. W. Nottorf, I. B. Johns and A. H. Daane, *Nucleonics*, 1949, 4–15.
39 N. Gérard and S. Ono, 'Hydride Formation and Decomposition Kinetics', Chapter 4, p. 174 and G. Sandrock, S. Suda and L. Schlapbach, 'Applications', Chapter 5, p. 204 in Topics in Applied Physics: Hydrogen in Intermetallic Compounds II – Surface and Dynamic Properties, Applications, Springer-Verlag, volume 67, Editor: L. Schlapbach.
40 D.O.E. ARPA-E High Energy Advanced Thermal Storage, DOE-FOA-0000471, 2011, https://arpa-e-foa.energy.gov/FileContent.aspx?FileID=79a5de09-8bfd-4590-9cb4-e42578248d90, accessed September 2016.
41 B. Hallstedt and O. Kim, *Int. J. Mater. Res.*, 2007, **98**, 961–969.
42 G. Kolb, C. Ho, T. Mancini and J. Gary, Power tower technology road map and cost reduction plan, *Sandia Report SAND2011-2419*, April 2011.

3.2. **Hydrogen storage properties of nanoconfined $LiBH_4$-$NaBH_4$**

$LiBH_4$ and $NaBH_4$ are both individually considered as high temperature. However, due to the significant improvement in reversibility and kinetics obtained from the nanoconfined $LiBH_4$-$NaBH_4$ eutectic mixture, this system may potentially serve as both HTMH and LTMH.

INTERNATIONAL JOURNAL OF HYDROGEN ENERGY 40 (2015) 14916–14924

Available online at www.sciencedirect.com

ScienceDirect

journal homepage: www.elsevier.com/locate/he

Hydrogen storage properties of nanoconfined $LiBH_4$–$NaBH_4$

Payam Javadian [a,b], *Drew A. Sheppard* [b], *Craig E. Buckley* [b], *Torben R. Jensen* [a,*]

[a] *Center for Energy Materials, Interdisciplinary Nanoscience Center (iNANO), and Department of Chemistry, Aarhus University, DK-8000 Aarhus, Denmark*

[b] *Department of Imaging and Applied Physics, Curtin University, GPO Box U 1987, Perth, Western Australia 6845, Australia*

ARTICLE INFO

Article history:
Received 29 June 2015
Received in revised form
20 August 2015
Accepted 23 August 2015
Available online 26 September 2015

Keywords:
Nanoconfinement
Eutectic melting composite
Carbon dioxide activation
Cyclic stability

ABSTRACT

In this study a eutectic melting composite of $0.62LiBH_4$–$0.38NaBH_4$ has been infiltrated in two nanoporous resorcinol formaldehyde carbon aerogel scaffolds with similar pore sizes (37 and 38 nm) but different BET surface areas (690 and 2358 m^2/g) and pore volumes (1.03 and 2.64 mL/g). This investigation clearly shows decreased temperature of hydrogen desorption, and improved cycling stability during hydrogen release and uptake of bulk $0.62LiBH_4$–$0.38NaBH_4$ when nanoconfined into carbon nanopores. The hydrogen desorption temperature of bulk $0.62LiBH_4$–$0.38NaBH_4$ is reduced by ~107 °C with the presence of carbon, although a minor kinetic variation is observed between the two carbon scaffolds. This corresponds to apparent activation energies, E_A, of 139 kJ mol^{-1} (bulk) and 116 −118 kJ mol^{-1} (with carbon aerogel). Bulk $0.62LiBH_4$–$0.38NaBH_4$ has poor reversibility during continuous hydrogen release and uptake cycling, maintaining 22% H_2 capacity after four hydrogen desorptions (1.6 wt.% H_2). In contrast, nanoconfinement into the high surface area carbon aerogel scaffold significantly stabilizes the hydrogen storage capacity, maintaining ~70% of the initial capacity after four cycles (4.3 wt.% H_2).

Introduction

Our anthropogenic effect on the environment originated from utilization of fossil fuels consumption has facilitated research in alternative energy storage materials. Particularly, hydrogen is considered a suitable substitute for gasoline, due to its high energy content and non-toxic, carbon-free composition [1].

$LiBH_4$ is considered a potential candidate for solid state hydrogen storage due to its hydrogen storage capacity of 13.9 wt.% H_2 (excluding the decomposition of LiH) [2,3]. However, the hydrogen desorption and absorption of $LiBH_4$ suffers from poor sorption kinetics and insufficient reversibility during hydrogen release and uptake cycling, not to mention its high melting point of T_{melt} = 275 °C [4]. In the 1970s, Semenenko and Adams reported that $LiBH_4$ could be destabilized by

* *Corresponding author*. iNANO and Department of Chemistry, Langelandsgade 140, DK-8000 Aarhus C, Aarhus University, Denmark. Tel.: +45 8715 5939, +45 2272 1486 (mobile); fax: +45 8619 6199.
E-mail address: trj@chem.au.dk (T.R. Jensen).

http://dx.doi.org/10.1016/j.ijhydene.2015.08.075

INTERNATIONAL JOURNAL OF HYDROGEN ENERGY 40 (2015) 14916–14924

the addition of $NaBH_4$ in the stoichiometric ratio of $0.62LiBH_4$–$0.38NaBH_4$ by forming a eutectic melting composite with a melting point of ~220 °C [5,6]. However, no data was presented on the hydrogen storage properties. Recently, Paskevicius et al. revealed data showing the thermal decomposition of the system, confirming a eutectic melting in the temperature range of 210–220 °C [7]. Furthermore, similar results for binary borohydride composites systems have already been published for eutectic composites comprised of $LiBH_4$ mixed with $Mg(BH_4)_2$, $Ca(BH_4)_2$, KBH_4 or $Mn(BH_4)_2$, respectively [7–13]. In the present study, the eutectic melting point of $LiBH_4$–$NaBH_4$ was exploited for nanoconfinement by melt infiltration into a high surface area nanoporous resorcinol formaldehyde carbon aerogel scaffold [14–17]. Nanoporous carbon based scaffolds may enhance hydrogen release/uptake kinetics and improve reversibility of the nanocomposite, in addition more favourable thermodynamic properties may be achieved [18–20]. A few studies have been conducted on attempting to enhance the kinetics and reduce the temperature for hydrogen desorption of similar complex binary eutectic borohydride systems, by introducing carbon scaffolds. Several systems explore the properties of binary complex hydrides for nanoconfinement such as $LiBH_4$–$Ca(BH_4)2$ [8,21–23], $LiBH_4$–Mg_2NiH_4 [24], $LiBH_4$–$Mg(BH_4)_2$ [11–13,25], $LiBH_4$–$LiAlH_4$ [26] and $LiBH_4$–$NaAlH_4$ [27]. These systems all form eutectic melts when mixed together which makes them suitable for infiltration into porous scaffolds. Reactive hydride composites have also been nanoconfined, e.g. the system $LiBH_4$–MgH_2 [20,28–31]. As reported for the respective systems, nanoconfinement either in CAS, CMK-3, IRH-33 and NPC facilitate hydrogen desorption and also improve the rehydrogenation of the hydride.

The hydrogen storage properties of the nanoconfined and bulk binary metal borohydride system are investigated experimentally with powder X-ray diffraction (PXD), temperature programmed desorption – mass spectroscopy (TPD-MS), the Sieverts' method and Fourier transformed infrared spectroscopy (FTIR). We find that $LiBH_4$–$NaBH_4$ can be confined inside the mesoporous carbon scaffold via melt infiltration, the presence of the scaffold reduces the temperature for hydrogen emission and improves the reversibility of hydrogen release and uptake.

Experimental details

Sample preparation

Synthesis of resorcinol formaldehyde carbon aerogel (CA) was done by mixing 82.87 g resorcinol (Aldrich, 99%), 113.84 mL formaldehyde, (37 wt.% stabilized by ~10–15% methanol, Merck), 113.28 mL deionized water and 0.0674 g Na_2CO_3 (Aldrich, 99.999%) during continuous stirring until complete dissolution was obtained. The pH of the final sol gel solution was 5.91. The following synthesis procedure and characterization of the aerogel was conducted as previously described [32–35]. Portions of the prepared CA were CO_2-activated according to previous methods [32,34,36]. Before hydride infiltration, the CA monoliths were degassed at 400 °C under dynamic vacuum for five hours to remove adsorbed air and water from within the porous structure. All subsequent handling was performed in a glovebox with purified argon atmosphere.

Commercially available $LiBH_4$ (Aldrich, ≥ 95%) and $NaBH_4$ (Aldrich, 99.99%) were mixed in the molar ratio $0.62LiBH_4$–$0.38NaBH_4$ which is reported to show eutectic melting (~220 °C) [5–7]. The mixture of bulk hydrides was ball milled according to previously published methods [13] and this sample is denoted LiNa. Briefly, a Fritsch P4 planetary mill with a tungsten carbide bowl and balls was used at a ball-to-powder (BTP) ratio of 24:1 with 2 min milling cycles followed by 2 min cooling cycles. The sample was milled for a total of 60 min at 250 rpm. The theoretical hydrogen content of bulk LiNa, based on the stoichiometric composition $0.62LiBH_4$–$0.38NaBH_4$, was calculated to be ρ_m(LiNa) = 12.2 wt.% H_2.

The added amount of hydride was selected in order to obtain a degree of pore filling corresponding to ~60 vol%, calculated based on the total pore volume, V_{tot}, of the scaffold and the average bulk densities ρ(LiNa) = 0.787 g/mL. Melt infiltration was performed using gas handling components and a stainless steel pressure cell that heated the sample to T = 240 °C ($\triangle T/\triangle t$ = 2 °C/min) under a H_2 pressure of 140–168 bar at 240 °C for 30 min. The furnace was then turned off and the sample allowed cooling to room temperature.

Sample characterization

Synchrotron radiation powder X-ray diffraction (SR-PXD) data were collected at beamline I711 at MAX-lab in Lund, and at PETRA III beamline P07 of DESY in Hamburg. While in the glovebox, the samples were mounted in a sapphire capillary tube (0.79 mm. I.D.), in an airtight sample holder inside an argon filled glovebox [37]. The sample holder was removed from the glovebox and attached to a gas control system at the synchrotron diffractometer. The data was collected using a CCD detector with a selected wavelength of λ = 0.99185 Å (MAX-lab) and λ = 0.23088 Å (PETRA III).

A Perkin Elmer STA 6000 coupled with a Hiden Analytical quadrupole mass spectrometer was used to perform thermogravimetric analysis (TGA), differential scanning calorimetry (DSC) mass spectroscopy (MS) measurements. Thus, temperature-programmed desorption mass spectroscopy (TPD-MS) data is provided. The measurements were performed in constant flow (64 mL/min) of argon (99.99%). A powdered sample (<5 mg), was placed in an Al_2O_3 crucible with lid and were heated in the temperature range of 40–500 °C ($\triangle T/\triangle t$ = 2 °C/min). The MS signals at m/e = 2, 18 and 34 were monitored so as to detect the presence of H_2, H_2O and B_2H_6. Kissinger plots were obtained from the DSC data by heating selected samples at 2, 5 10 and 15 °C/min from which the temperature for maximum DSC signal of hydrogen desorption is utilized.

Sieverts' measurements were conducted on nanoconfined and bulk $0.62LiBH_4$–$0.38NaBH_4$ during four hydrogen release and uptake cycles. Hydrogen desorption data was collected on a PCTPro 2000 Sieverts' apparatus in the temperature range of RT to 500 °C ($\triangle T/\triangle t$ = 2 °C/min), with the temperature maintained at 500 °C for 10 h, at $p(H_2)$ = 1 bar. Hydrogen absorption was performed in the pressure range of 140–150 bar,

at a temperature of 400 °C ($\triangle T/\triangle t = 5$ °C/min) during 10 h, and then the sample was cooled naturally to RT.

The Fourier transform infrared spectrometry (FTIR) analyses were carried out on a NICOLET 380 FT-IR from Thermo-Electronic Corporation with a permanently aligned optics and proprietary diamond-turned pinned-in-place mirror optics. A small amount of sample was placed on the base plate and subsequently the diamond pin was pressed on to the sample, forming a thin film. The samples were examined within the wave number range of 4000–400 cm^{-1}.

Results and discussion

The structural parameters of pristine carbon aerogel (CA) are determined from nitrogen adsorption analysis using the BET, BJH and t-plot method [38,39] and are given in Table 1. CA has a specific BET surface area of $S_{BET} = 690$ m^2/g, a total pore volume of $V_{tot} = 1.03$ mL/g and a pore size distribution centred around $D_{max} = 37$ nm. CO_2-activation of CA for 4 h (CA-4) results in significant increase of structure parameters; $S_{BET} = 2358$ m^2/g, $V_{tot} = 2.64$ mL/g and $D_{max} = 38$ nm. The amount of LiNa added to the scaffold is also provided in gravimetric and volumetric quantities, corresponding to a pore filling of ~60 vol% which ensures complete infiltration of the hydride. After infiltration of LiNa, the structure parameters of the carbon composite are significantly reduced (see Supporting Information) suggesting infiltration into the pores of the scaffold.

In-situ SR-PXD study of nanoconfined $LiBH_4$–$NaBH_4$

The eutectic melting composite prepared by mechanical ball milling of $LiBH_4$–$NaBH_4$ forms a physical mixture of the two hydrides. *In-situ* synchrotron radiation powder X-ray diffraction (SR-PXD) is used to follow the melt infiltration process of LiNa into scaffold CA under hydrogen pressure, as shown in Fig. 1. Initially, the diffraction patterns of the low temperature polymorph *o*-$LiBH_4$ and $NaBH_4$ are present, which during heating to 110 °C gives rise to a phase transition to *h*-$LiBH_4$. The melting of the eutectic composite occurs at ~225 °C. As expected, at 240 °C, the Bragg peaks of $NaBH_4$ and *h*-$LiBH_4$ almost completely disappears, which is associated with the eutectic melting regime. After 15 min at 240 °C the sample is cooled to RT allowing the eutectic hydride composite to recrystallize inside the pores of the carbon aerogel. During cooling, *h*-$LiBH_4$ transforms to *o*-$LiBH_4$ and the diffraction pattern at RT also exhibit $NaBH_4$ peaks, as shown in Fig. 1. This indicates that no reaction occurs between $LiBH_4$ and $NaBH_4$ but miscibility results in formation of a molten phase. The Bragg peaks are significantly reduced and broadened, indicating nano crystallite formation of LiNa inside the pores of CA. Unfortunately, ball milling of $0.62LiBH_4$–$0.38NaBH_4$ resulted in contamination by the ball-milling media, tungsten carbide WC, as indicated by three distinct diffraction peaks at 2θ values 21°, 23° and 31°.

Hydrogen desorption

Thermogravimetric analysis (TGA), differential scanning calorimetry (DSC) and temperature programmed desorption mass spectroscopy (TPD-MS), has been used to investigate the first hydrogen desorption of bulk $0.62LiBH_4$–$0.38NaBH_4$ (LiNa) and LiNa physically mixed with CA (CA mix) and melt infiltrated in CA (CA melt), see Fig. 2. The TPD-MS of bulk LiNa exhibits two minor hydrogen release peaks with onset at 200 and 270 °C *i.e.* peak **a** and **b**, respectively. The first desorption peak may be assigned to the eutectic melting of LiNa, which is expected to occur around 224 °C [5,6]. The major hydrogen desorption event begins at 350 °C and the release of hydrogen continues until 500 °C with two local maxima observed at 380 and 440 °C (denoted **c** and **d**, respectively). The total amount of released hydrogen from the bulk LiNa hydride is only 7.56 wt.% in the temperature range of 50–500 °C and corresponds to 62% of the available hydrogen in the sample content, possibly due to partial decomposition of LiNa. More hydrogen may be released from the sample at higher temperatures or prolonged heating at 500 °C but may also be limited due to formation of stable *closo*-boranes like $Li_2B_{12}H_{12}$ or $Na_2B_{12}H_{12}$. Formation of *closo*-boranes is facilitated by low partial pressures of hydrogen (TGA measurements is conducted in argon flow, i.e. $p(H_2) \sim 0$ bar) [40].

The addition of carbon aerogel (CA), whether as physically mixed with LiNa or melt infiltrated into the scaffold, significantly improves the hydrogen release kinetics compared to that of bulk LiNa *i.e.* the major hydrogen desorption rate of sample CA occurs at 333 °C (**d′** is 107 °C lower than for that of bulk, **d**). The reduced temperature is elucidated in Fig. 2C, as peaks **a′**, **c′** and **d′**, in which these peaks are equivalent to those presented in the bulk desorption profile. Furthermore, the onset temperature for hydrogen release is as low as 150 °C, possibly assigned to the effect induced by nanoconfinement or the presence of the carbon surface, acting as a catalyst for hydrogen desorption [18]. Comparing the mixed and nanoconfined samples, it is worth noting that the hydrogen desorption profile of the physical mixed sample displays an

Table 1 – Structural parameters; BET surface area, (S_{BET}), micro, meso and total pore volume, (V_{micro}, V_{meso}, V_{tot}), and pore size (D_{max}) of as prepared carbon aerogel scaffold (CA) and CO_2-activated scaffold (CA-4). The added amount of $0.62LiBH_4$–$0.38NaBH_4$, in the samples is also provided gravimetrically and volumetrically.

Scaffold	S_{BET} (m^2/g)	V_{micro} (mL/g)	V_{meso} (mL/g)	V_{tot} (mL/g)	D_{max} (nm)	LiNa[a] wt.%	LiNa[a] vol%	ρ_m (H_2) wt.% H_2/sample
CA	690 ± 12	0.22 ± 0.02	0.96 ± 0.09	1.03 ± 0.14	37 ± 0.4	32.8	60.0	4.0
CA-4	2358 ± 82	0.77 ± 0.02	2.10 ± 0.38	2.64 ± 0.33	38 ± 0.4	55.5	60.0	6.8

[a] Added amount of $0.62LiBH_4$–$0.38NaBH_4$ in the sample relative to weight and volume of the scaffold.

INTERNATIONAL JOURNAL OF HYDROGEN ENERGY 40 (2015) 14916–14924

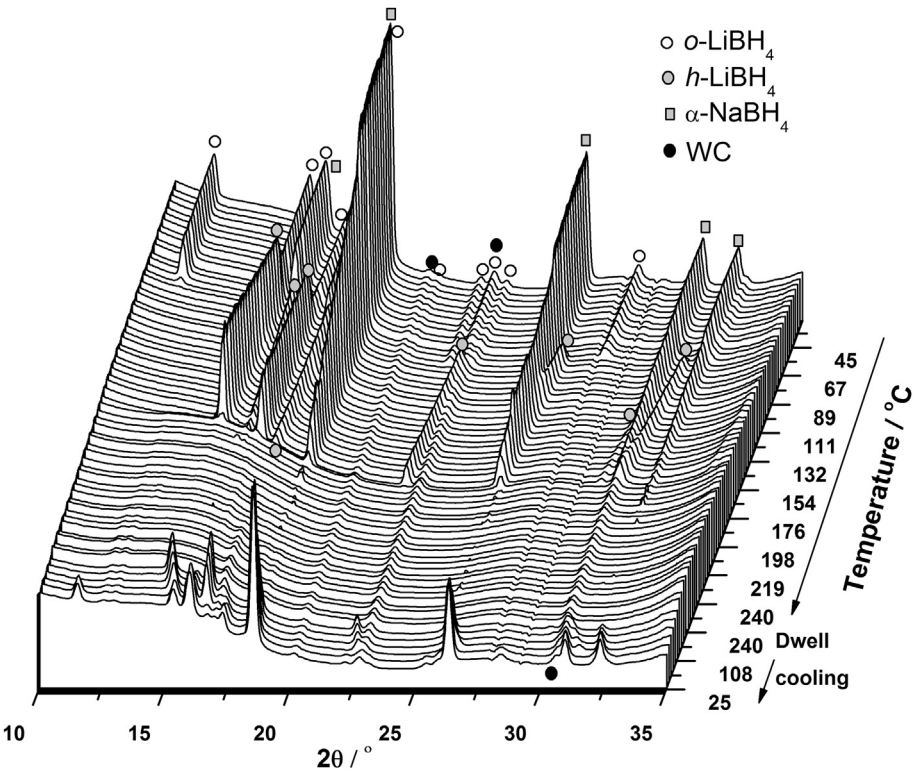

Fig. 1 – *In-situ* synchrotron radiation powder X-ray diffraction (SR-PXD) of CA mixed with $0.62LiBH_4$–$0.38NaBH_4$ measured between RT and 240 °C (△T/△t = 2 °C/min) with the temperature held constant at 240 °C for 15 min at $p(H_2)$ = 120 bar (λ = 0.99185 Å). Afterwards the sample was naturally cooled to RT.

intense peak at 232 °C (a′), which is not present in the nanoconfined sample. This is due to the pretreated process during melt infiltration and states that a fraction of hydrogen is desorbed during the melting of $LiBH_4$–$NaBH_4$. The weight loss fraction of hydrogen release for the melt infiltrated sample (CA melt) is 3.95 wt.%, upon heating from 50 to 500 °C, corresponding to 98% of the samples theoretical available hydrogen content (4.0 wt.% H_2). However, the physical mixed sample only releases 2.73 wt.% H_2, in the same temperature range, corresponding to 66% of the available hydrogen content. This demonstrates that the nanoconfined sample facilitate destabilization of LiNa and larger hydrogen loss, in contrast to the physically mixed sample. From the DSC curve (Fig. 2B) of bulk LiNa, the polymorphic transformation from *o*-to *h*-$LiBH_4$ (T = 98 °C) and the endothermic signal of the eutectic melting (T = 224 °C) is observed. The metal borohydrides $LiBH_4$ and $NaBH_4$ decompose 'individually', therefore, the DSC heat flow signal from this event occurs over a broader temperature range and appear weaker. In the case of the physically mixed sample the signal for the melting occur at significantly lower temperature and in addition, a subsequent exothermic peak (T = 226 °C) is observed which could possibly be assigned to the wetting of CA by molten LiNa [8]. The DSC signals of the melt infiltrated sample, CA-LiNa, are also shifted towards lower temperatures compared to bulk LiNa. Three endothermic signals are displayed at 96, 214 and 316 °C, see Fig. 2B. The first signal corresponds to the polymorphic transformation of $LiBH_4$ and is shifted 2 °C lower than for bulk LiNa. The second corresponds to the melting of the eutectic mixture and occurs 10 °C lower than the bulk. Finally, the third broad peak is assigned to the major hydrogen desorption of LiNa.

The TPD peaks **c** and **d** seems to relate to the decomposition of $LiBH_4$ and $NaBH_4$, respectively. However, it is not clear from the data collected which peak corresponds to which borohydride. The temperature difference between **c**′ and **d**′ compared to **c** and **d** may be due to the difference in the interaction between the carbon scaffold and the respective borohydrides, *i.e.* a possible catalytic effect [18].

Employing the high surface area scaffold (CA-4), for nanoconfinement of LiNa, does not facilitate major alterations in hydrogen desorption kinetics compared to the as prepared scaffold (CA), *i.e.* the temperature for maximum hydrogen release rate is 336 °C, see Figure S3 in Supporting Information. Interestingly, sample CA-4 rehydrogenated for 10 h at 140 bar H_2 pressure (after 4 desorption cycles) shows reduced hydrogen release temperatures compared to the nanoconfined sample CA-4, with the maximum temperature for hydrogen released reduced to 315 °C. However, in the first hydrogen desorption, the binary hydride composite possibly reacts to the scaffold facilitating an earlier release of hydrogen.

The kinetics for hydrogen release of LiNa, CA and CA-4 is further analyzed the Kissinger approach, see Fig. 3. A significant decrease in apparent activation energy, E_A, for hydrogen release of nanoconfined LiNa compared to bulk LiNa is observed. The apparent activation energies (E_A) of hydrogen desorption of bulk and nanoconfined LiNa, in CA and CA-4 and

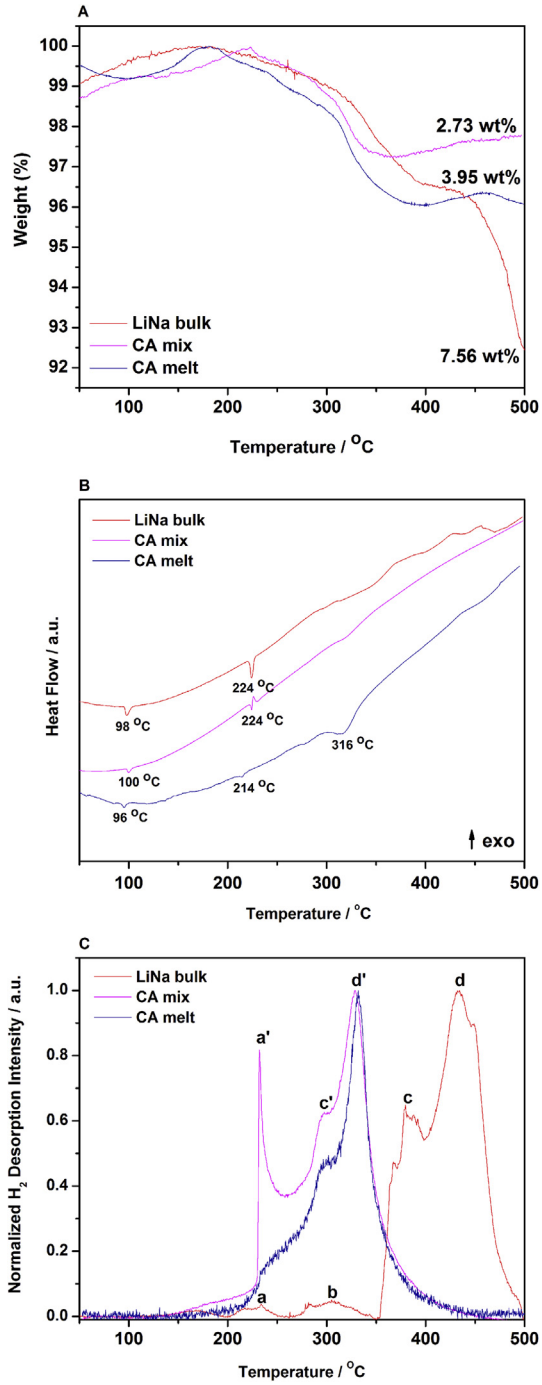

Fig. 2 – Thermal analysis of bulk 0.62LiBH$_4$–0.38NaBH$_4$, LiNa (red), a physical mixture of LiNa with CA (pink) and LiNa melt infiltrated into CA (blue). A) shows TGA data, B) DSC data and C) TPD-MS profiles of H$_2$ signals (*m/e* = 2). Samples are heated from 50 to 500 °C (△*T*/△*t* = 2 °C/min). (For interpretation of the references to colour in this figure legend, the reader is referred to the web version of this article.)

are estimated to be 139, 116 and 118 kJ·mol^{-1}, respectively (see Fig. 3). Thus, CO$_2$-activation has no significant effect on the activation energy. Nanoconfinement and different carbon materials have previously been shown to have a significant

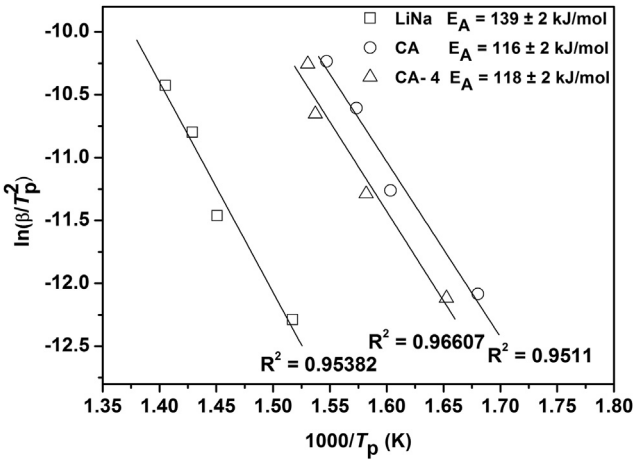

Fig. 3 – Kissinger plot obtained from DSC data at heating rates of 2, 5, 10 and 15 °C/min for bulk 0.62LiBH$_4$–0.38NaBH$_4$ (LiNa) and LiNa nanoconfined in CA and CA-4.

improvement of kinetics and a reduction of the apparent activation energy for hydrogen release reactions [18].

Cyclic stability and reversibility

Sieverts' measurements have been conducted to investigate the stability of the hydrogen capacity over four desorption/absorption cycles. The four desorption profiles of bulk 0.62LiBH$_4$–0.38NaBH$_4$ (LiNa) and LiNa nanoconfined in 'as-prepared' (CA) and CO$_2$-activated (CA-4) carbon aerogels are displayed in Fig. 4. The amount of hydrogen released is presented relative to the gravimetric amount of 0.62LiBH$_4$–0.38NaBH$_4$ in the samples (wt.% H$_2$/LiNa), as a function of time and temperature.

Bulk LiNa releases 7.2 wt.% H$_2$/LiNa during the first desorption that corresponds to 59% of the available hydrogen content in the sample, ρ_m(LiNa) = 12.2 wt.% H$_2$. This compares well with the result obtained from the TGA measurement. A significant decrease of more than 70% is observed during the second, third and fourth desorption *i.e.* 2.1, 1.6 and 1.6 wt.% H$_2$, corresponding to 29.2, 22.2 and 22.2% of the calculated hydrogen content of the LiNa, respectively, see Table 2.

Hydrogen release of LiNa nanoconfined into CA is significantly enhancing the cyclic stability compared to bulk LiNa. During the first desorption 10.5 wt.% H$_2$/LiNa (corresponding to 86% of the theoretical available hydrogen content). In the second, third and fourth desorption 6.3, 5.8 and 5.4 wt.% H$_2$/LiNa is released which is equivalent to 60, 55 and 51% of the initial hydrogen content, respectively. The amount of hydrogen released relative to the total mass of LiNa-CA nanoconfined is 3.4 wt.% H$_2$ during the first desorption and is in good agreement with the TGA data (Fig. 2). The increased amount of released hydrogen during the second to fourth cycle may be due to facilitated hydrogen absorption for the nanoconfined sample.

The gravimetric hydrogen storage capacity and the cyclic stability of LiNa nanoconfined into CO$_2$ activated carbon

INTERNATIONAL JOURNAL OF HYDROGEN ENERGY 40 (2015) 14916–14924

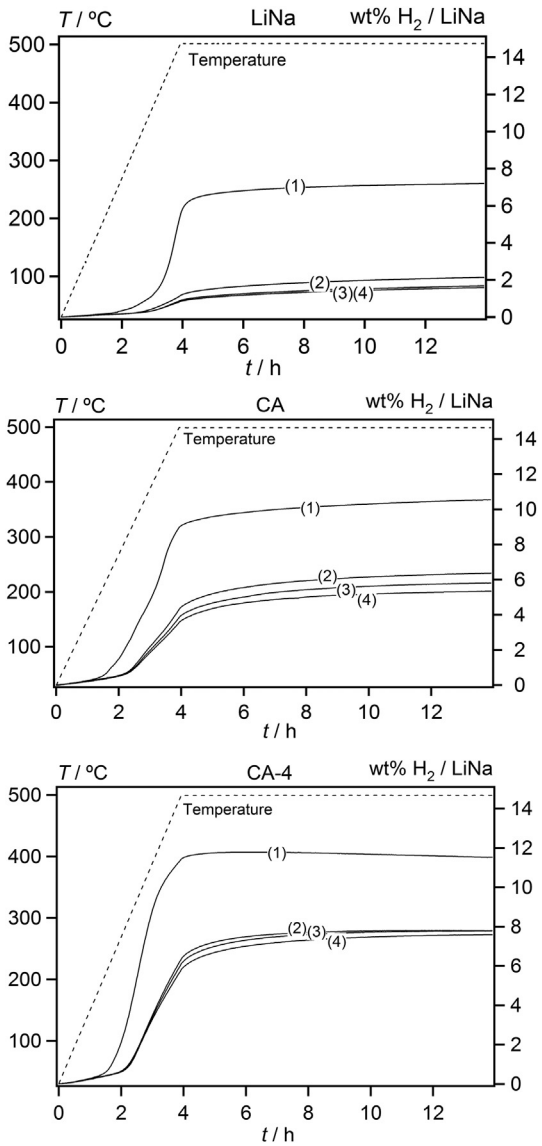

Fig. 4 – Sieverts' measurement showing hydrogen release for cycles 1 to 4 for bulk 0.62$LiBH_4$–0.38$NaBH_4$ (LiNa) (top), LiNa infiltrated into CA (middle) and into CA-4 (bottom). Hydrogen desorption was performed at a fixed temperature of 500 °C ($\triangle T/\triangle t = 2$ °C) for 10 h and at $p(H_2) = 1$ bar. Hydrogen absorption was performed at 400 °C and $p(H_2) = 140$ bar for 10 h.

aerogel CA-4 are further improved compared to sample CA-LiNa, in well agreement with previous studies [13,23,36]. The first desorption releases 11.5 wt.% H_2/LiNa (~94% of the theoretical available hydrogen content), corresponding to 6.4 wt.% H_2/sample. During the second, third and fourth desorption cycles, sample CA-4 releases 7.9, 7.8 and 7.7 wt.% H_2/LiNa *i.e.* ~67% of the initial hydrogen capacity is retained during four cycles.

In general the employment of CA for nanoconfinement of LiNa is associated with 51% retention of hydrogen capacity after four desorption cycles, in contrast to only 22% for bulk LiNa under the selected physical conditions for hydrogen release and uptake. However, further enhancement in cyclic stability is obtained using the high surface area scaffold CA-4 maintaining 67% of the total capacity after four desorption cycles. This is considered a significant enhancement of the hydrogen storage properties of eutectic nanocomposite of $LiBH_4$–$NaBH_4$, which is a rather unexplored system.

The FTIR spectra indicate reversible hydrogen storage of 0.62$LiBH_4$–0.38$NaBH_4$ and formation of metal borohydrides during rehydrogenation. In Fig. 5, bulk $LiBH_4$ and $NaBH_4$ both demonstrates three characteristic B–H stretching modes in the range of 2000–2500 cm^{-1} as well as B–H bending bands at 1093, 1236 and 1298 cm^{-1} in $LiBH_4$ and a single signal at 1095 cm^{-1} for that of $NaBH_4$. The bulk eutectic LiNa mixture evidently exhibits a combination of the previously mentioned B–H bending and stretching bands (red spectrum), however after nanoconfinement, these signals are significantly reduced due to the presence of the carbon scaffold (green spectra). As the nanoconfined sample has been completely dehydrogenated *i.e.* heated to 500 °C for 10 h, the FTIR spectrum (blue) only displays a single B–H stretch at 2345 cm^{-1}. This stretch is at a slightly higher wave number than for the stretch originating from the borohydrides, and therefore could be assigned to another borohydride compound e.g. *closo*-borane, though it is amorphous as demonstrated with PXD in Fig. 6. The FTIR spectra closely resemble that of $Li_2B_{12}H_{12}$ [41]. Furthermore, rehydrogenation of the decomposed sample at 400 °C for 10 h at a hydrogen pressure of 140 bar (orange spectra) results in the observation of low intensity B–H stretching in the wave number range between 2000 and 2500 cm^{-1}. The sharp signals in this range can be clearly assigned to the B–H stretching of $NaBH_4$. From powder diffraction it is confirmed that $NaBH_4$ is formed during rehydrogenation at 400 °C, 140 bar hydrogen after 10 h. Decomposition of nanoconfined LiNa facilitates the formation of the product Li_3BO_3 and the lack of B–H stretching modes for $LiBH_4$

Table 2 – The theoretical hydrogen content, $\rho_m(H_2)$ relative to the amount of hydrogen storage material 0.62$LiBH_4$–0.38$NaBH_4$ (LiNa). The measured hydrogen release during the first desorption calculated relative to the mass of the sample, and in percentage of the relative theoretical content (in brackets). The amount of released hydrogen relative to the amount of added $LiBH_4$–$NaBH_4$ during desorption cycles one to four. The data is extracted from Fig. 4.

Sample	ρ_m (H_2) wt.% H_2/sample	1.des/sample wt.% H_2	1.des/LiNa wt.% H_2	2.des/LiNa wt.% H_2	3.des/LiNa wt.% H_2	4.des/LiNa wt.% H_2
LiNa	12.2	7.2 (59.0)	7.2 (100)	2.1 (29.2)	1.6 (22.2)	1.6 (22.2)
CA	4.0	3.4 (86.0)	10.5 (100)	6.3 (60.0)	5.8 (55.2)	5.4 (51.4)
CA-4	6.8	6.4 (93.8)	11.5 (100)	7.9 (68.7)	7.8 (67.8)	7.7 (66.9)

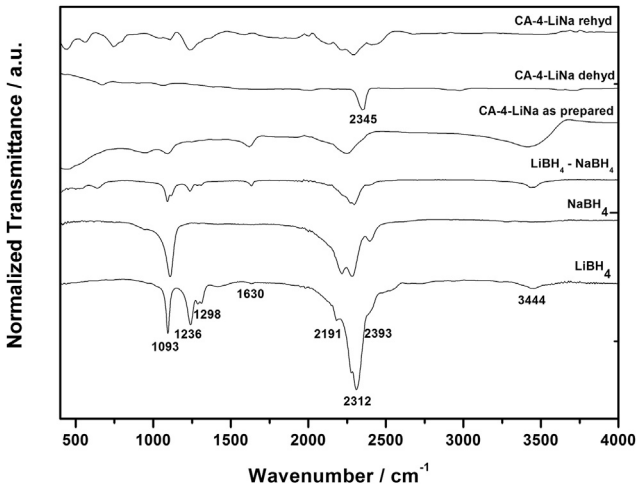

Fig. 5 – FTIR spectra of bulk $LiBH_4$ and $NaBH_4$, ball milled $0.62LiBH_4$–$0.38NaBH_4$, sample CA-4 post melt infiltration of LiNa, CA-4-LiNa after being dehydrogenated at 500 °C for the fourth time and CA-4-LiNa rehydrogenated for 10 h at 400 °C after four desorption cycles. The intensity of the top spectrum has been upscaled corresponding to added amount of LiNa for better comparison.

in the rehydrogenated FTIR spectrum (orange spectrum) may be due to the oxidation of a significant proportion of the initial $LiBH_4$. However, once this reaction has taken place and all of the 'framework oxygen', i.e. functional groups on the carbon aerogel surface and possibly small amounts of adsorbed water, has been converted to stable Li_3BO_3, the remaining nanoconfined $LiBH_4$–$NaBH_4$ is reversible. These results suggest that the reversible source may be an amorphous compound of $LiBH_4$ and $NaBH_4$. Weak LiH diffraction peaks are observed after rehydrogenation of the nanoconfined sample (see Fig. 6). This implies that metallic Li should be formed after decomposition, which is converted to LiH after rehydrogenation under the applied conditions. However, the lack of metallic Li diffraction peaks in the decomposed sample might suggest that Li nanoparticles are present, and combined with the fact that even having the theoretical amount of Li in the carbon aerogel means that it is only a small proportion of the sample.

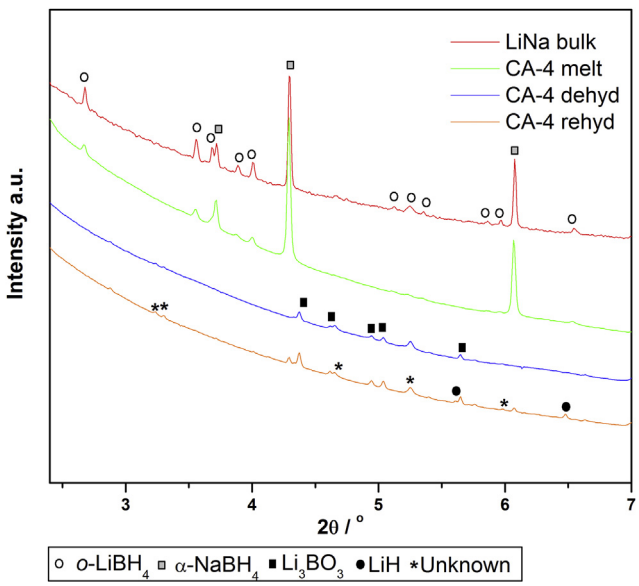

Fig. 6 – *Ex-situ* SR-PXD of bulk $0.62LiBH_4$–$0.38NaBH_4$ (LiNa) (red), nanoconfined into CA-4 (green), CA-4 after being dehydrogenated at 500 °C in 10 h for the fourth time (blue) and CA-4 rehydrogenated at $p(H_2) = 140$ bar and 400 °C in 10 h after being desorbed four times (orange). The unknown compound in the dehydrogenated and rehydrogenated samples could possibly be an oxide ($\lambda = 0.23088$ Å). (For interpretation of the references to colour in this figure legend, the reader is referred to the web version of this article.)

Conclusion

The eutectic melting composite $0.62LiBH_4$–$0.38NaBH_4$ (LiNa) is a physical mixture of the respective borohydrides with a melting point of T_{melt} ~ 225 °C. This composite has been successfully melt infiltrated into a pristine carbon aerogel scaffold (CA) and a CO_2-activated high surface area carbon aerogel scaffold (CA-4). The effect of CO_2-activated carbon aerogel allows infiltration of larger quantities of hydride. Furthermore, the activation procedure appears to make the carbon more inert, thereby reducing the amount of possible formed borates and oxides which could contribute to the improved reversibility. The employment of CA significantly improves the hydrogen desorption kinetics compared to bulk $0.62LiBH_4$–$0.38NaBH_4$ and facilitates a reduction in hydrogen release temperature of ~107 °C. There is no substantial impact on the kinetics between the two types of carbon. This is also illustrated by the apparent activation energies (E_A) of hydrogen desorption of bulk and nanoconfined LiNa, in CA and CA-4 which is estimated to be 139, 116 and 118 kJ mol^{-1}, respectively. However, the reversible hydrogen storage capacity during hydrogen release and uptake is significantly improved by nanoconfinement into the high surface area scaffold CA-4, releasing 6.4 wt% H_2 relative to the sample mass, using only 60 vol% pore filling. In fact considering 100 vol% pore filling of $0.62LiBH_4$–$0.38NaBH_4$ into CA-4, would give rise to an available hydrogen storage capacity of ~11 wt.% H_2 after the first desorption and possibly ~7 wt.% H_2 after four desorption cycles.

Acknowledgements

We acknowledge funding from the European Community's Seventh Framework Programme, The Fuel Cells and Hydrogen Joint Undertaking (FCH JU), project BOR4STORE (303428) and the COST Action MP1103 "Nanostructured materials for solid-state hydrogen storage". Beamline I711, MAX-IV laboratories, Lund, Sweden are thanked for the allocated beam time. This work was supported by The Innovation Fund Denmark via the research project HyFillFast, the Danish National Research Foundation, Center for Materials Crystallography (DNRF93)

and by the Danish Research Council for Nature and Universe (Danscatt). We are grateful to the Carlsberg Foundation.

We acknowledge the 2012 Australian Research Council Linkage Grant (LP120100435).

Appendix A. Supplementary data

Supplementary data related to this article can be found at http://dx.doi.org/10.1016/j.ijhydene.2015.08.075

REFERENCES

[1] Ley MB, Jepsen LH, Lee YS, Cho YW, von Colbe JMS, Dornheim M, et al. Complex hydrides for hydrogen storage – new perspectives. Mater Today 2014;17:122–8.
[2] Schlesinger HI, Brown HC. Metallo borohydrides. III. Lithium borohydride. J Am Chem Soc 1940;62:3429–35.
[3] Orimo SI, Nakamori Y, Eliseo JR, Züttel A, Jensen CM. Complex hydrides for hydrogen storage. Chem Rev 2007;107:4111–32.
[4] Mauron P, Buchter F, Friedrichs O, Remhof A, Bielmann M, Zwicky CN, et al. Stability and reversibility of $LiBH_4$. J Phys Chem B 2008;112:906–10.
[5] Adams RM. Borax to boranes. Advances in chemistry. Washington, DC: American Chemical Society; 1961.
[6] Semenenko KN, Chavgun AP, Surov VN. Interaction of sodium tetrahydroborate with potassium and lithium tetrahydroborates. Russ J Inorg Chem 1971;16:271–3.
[7] Paskevicius M, Ley MB, Sheppard DA, Jensen TR, Buckley CE. Eutectic melting in metal borohydrides. Phys Chem Chem Phys 2013;15:19774–89.
[8] Lee HS, Lee YS, Suh JY, Kim M, Yu JS, Cho YW. Enhanced desorption and absorption properties of eutectic $LiBH_4$-$Ca(BH_4)_2$ infiltrated into mesoporous carbon. J Phys Chem C 2011;115:20027–35.
[9] Lee JY, Ravnsbæk D, Lee YS, Kim Y, Cerenius Y, Shim JH, et al. Decomposition reactions and reversibility of the $LiBH_4$-$Ca(BH_4)_2$ composite. J Phys Chem C 2009;113:15080–6.
[10] Bardaji EG, Zhao-Karger Z, Boucharat N, Nale A, van Setten MJ, Lohstroh W, et al. $LiBH_4$-$Mg(BH_4)_2$: a physical mixture of metal borohydrides as hydrogen storage material. J Phys Chem C 2011;115:6095–101.
[11] Sartori S, Knudsen KD, Hage FS, Heyn RH, Bardaji EG, Zhao-Karger Z, et al. Influence of nanoconfinement on morphology and dehydrogenation of the $Li^{11}BD_4$-$Mg(^{11}BD_4)_2$ system. Nanotechnology 2012;23:25.
[12] Zhao-Karger Z, Witter R, Bardaji EG, Wang D, Cossement D, Fichtner M. Altered reaction pathways of eutectic $LiBH_4$–$Mg(BH_4)_2$ by nanoconfinement. J Mater Chem A 2013;1:3379–86.
[13] Javadian P, Jensen TR. Enhanced hydrogen reversibility of nanoconfined $LiBH_4$-$Mg(BH_4)_2$. Int J Hydrogen Energy 2014;39:9871–6.
[14] de Jongh PE, Adelhelm P. Nanosizing and nanoconfinement: new strategies towards meeting hydrogen storage goals. Chem Sustain Chem 2010;3:1332–48.
[15] Vajo JJ. Influence of nano-confinement on the thermodynamics and dehydrogenation kinetics of metal hydrides. Curr Opin Solid St M 2011;15:52–61.
[16] Nielsen TK, Besenbacher F, Jensen TR. Nanoconfined hydrides for energy storage. Nanoscale 2011;3:2086–98.
[17] Fichtner M. Nanoconfinement effects in energy storage materials. Phys Chem Chem Phys 2011;13:21186–95.
[18] Ward PA, Teprovich JA, Peters B, Wheeler J, Compton RN, Zidan R. Reversible hydrogen storage in a LiBH4-C60 nanocomposite. J Phys Chem C 2013;117:22569–75.
[19] Chumphongphan S, Filsø U, Paskevicius M, Sheppard DA, Jensen TR, Buckley CE. Nanoconfinement degradation in $NaAlH_4$/CMK-1. Int J Hydrogen Energy 2014;39:11103–9.
[20] Gosalawit-Utke R, Milanese C, Javadian P, Girella A, Laipple D, Puszkiel J, et al. $2LiBH_4$–MgH_2–$0.13TiCl_4$ confined in nanoporous structure of carbon aerogel scaffold for reversible hydrogen storage. J Alloy Compd 2014;599:78–86.
[21] Lee HS, Hwang SJ, Kim HK, Lee YS, Park J, Yu JS, et al. In situ NMR study on the interaction between $LiBH_4$–$Ca(BH_4)_2$ and mesoporous scaffolds. J Phys Chem Lett 2012;3:2922–7.
[22] Ampoumogli A, Charalambopoulou G, Javadian P, Richter B, Jensen TR, Steriotis Th. Hydrogen desorption and cycling properties of composites based on mesoporous carbons and a $LiBH_4$–$Ca(BH_4)_2$ eutectic mixture. J Alloy Compd 2015;645:480–4.
[23] Javadian P, Sheppard DA, Buckley CE, Jensen TR. Hydrogen storage properties of nanoconfined $LiBH_4$-$Ca(BH_4)_2$. Nano Energy 2015;11:96–103.
[24] Javadian P, Zlotea C, Ghimbeu CM, Latroche M, Jensen TR. Hydrogen storage properties of nanoconfined $LiBH_4$–Mg_2NiH_4 reactive hydride composites. J Phys Chem C 2015;119:5819–26.
[25] Liu X, Peaslee D, Sheehan TP, Majzoub EH. Decomposition behavior of eutectic $LiBH_4$–$Mg(BH_4)_2$ and its confinement effects in ordered nanoporous carbon. J Phys Chem C 2014;118:27265–71.
[26] Xia G, Meng Q, Guo Z, Gu Q, Liu H, Liu Z, et al. Nanoconfinement significantly improves the thermodynamics and kinetics of co-infiltrated $2LiBH_4$–$LiAlH_4$ composites: stable reversibility of hydrogen absorption/resorption. Acta Mater 2013;61:6882–93.
[27] Thiangviriya S, Plerdsranoy P, Wiset N, Javadian P, Jensen TR, Utke R. Hydrogen sorption and reaction mechanisms of nanoconfined $2LiBH_4$–$NaAlH_4$. J Alloy Compd 2015;633:484–93.
[28] Nielsen TK, Bösenberg U, Gosalawit R, Dornheim M, Cerenius Y, Besenbacher F, et al. A reversible nanoconfined chemical reaction. ACS Nano 2010;4(7):3903–8.
[29] Gosalawit–Utke R, Thiangviriya S, Javadian P, Laipple D, Pistidda C, Bergemann Nils, et al. Effective nanoconfinement of $2LiBH_4$–MgH_2 via simply MgH_2 premilling for reversible hydrogen storages. Int J Hydrogen Energy 2014;39:15614–26.
[30] Gosalawit-Utke R, Milanese C, Javadian P, Jepsen J, Laipple D, Karimi F, et al. Nanoconfined $2LiBH_4$-MgH_2-$TiCl_3$ in carbon aerogel scaffold for reversible hydrogen storage. Int J Hydrogen Energy 2013;38:3275–82.
[31] Gosalawit–Utke R, Milanese C, Nielsen TK, Karimi F, Saldan I, Pranzas K, et al. Nanoconfined $2LiBH_4$–MgH_2 for reversible hydrogen storages: reaction mechanisms, kinetics and thermodynamics. Int J Hydrogen Energy 2013;38:1932–42.
[32] Baumann TF, Worsley MA, Han TYJ, Satcher Jr JH. High surface area carbon aerogel monoliths with hierarchical porosity. J Non-Cryst Solids 2008;354:3513–5.
[33] Al-Muhtaseb SA, Ritter JA. Preparation and properties of resorcinol-formaldehyde organic and carbon gels. Adv Mater 2003;15:101–14.
[34] Lin C, Ritter JA. Carbonization and activation of sol–gel derived carbon xerogels. Carbon 2000;38:849–61.
[35] Nielsen TK, Javadian P, Polanski M, Besenbacher F, Bystrzycki J, Jensen TR. Nanoconfined $NaAlH_4$: determination of distinct prolific effects from pore size, crystallite size, and surface interactions. J Phys Chem C 2012;116:21046–51.

[36] Nielsen TK, Javadian P, Polanski M, Besenbacher F, Bystrzycki J, Skibsted, et al. Nanoconfined $NaAlH_4$: prolific effects from increased surface area and pore volume. Nanoscale 2014;6:599–607.

[37] Hansen BRS, Moller KT, Paskevicius M, Dippel AC, Walter P, Webb CJ, et al. In situ X-ray diffraction environments for high-pressure reactions. J Appl Cryst 2015;48:1234–41.

[38] Barrett EP, Joyner LG. Determination of nitrogen adsorption-desorption isotherms – estimation of total pore volumes of porous solids. Anal Chem 1951;23:791–2.

[39] Brunauer S, Emmett PH, Teller E. Adsorption of gases in multimolecular layers. J Am Chem Soc 1938;60:309–19.

[40] Hansen BRS, Ravnsbæk DB, Skibsted J, Jensen TR. Hydrogen reversibility of $LiBH_4$-MgH_2-Al composites. Phys Chem Chem Phys 2014;16:8970–80.

[41] Pitt MP, Paskevicius M, Brown DH, Sheppard DA, Buckley CE. Thermal stability of $Li_2B_{12}H_{12}$ and its role in the decomposition of $LiBH_4$. J Am Chem Soc 2013;135:6930–41.

3.3. Hydrogen desorption properties of bulk and nanoconfined $LiBH_4$-$NaAlH_4$

$LiBH_4$ is considered a high temperature and $NaAlH_4$ is considered a low temperature, medium capacity complex hydride due to its relatively low decomposition temperature. The combination of these two complex hydrides, $LiBH_4$-$NaAlH_4$, when nanoconfined allows this system to act as a potential HTMH and LTMH.

crystals

MDPI

Article

Hydrogen Desorption Properties of Bulk and Nanoconfined $LiBH_4$-$NaAlH_4$

Payam Javadian [1,2], Drew A. Sheppard [2], Craig E. Buckley [2] and Torben R. Jensen [1,*]

1 Center for Energy Materials, Interdisciplinary Nanoscience Center (iNANO), and Department of Chemistry, Aarhus University, DK-8000 Aarhus, Denmark; payam_javadian@hotmail.com

2 Department of Imaging and Applied Physics, Curtin University, GPO Box U 1987, Perth, WA 6845, Australia; drew.sheppard@gmail.com (D.A.S.); C.Buckley@curtin.edu.au (C.E.B.)

* Corresponding: trj@chem.au.dk; Tel.: +45-87-155939 or +45-22-721486; Fax: +45-87-196199

Academic Editors: Umit B. Demirci, Philippe Miele and Pascal G. Yot
Received: 10 April 2016; Accepted: 9 June 2016; Published: 20 June 2016

Abstract: Nanoconfinement of $2LiBH_4$-$NaAlH_4$ into a mesoporous carbon aerogel scaffold with a pore size, BET surface area and total pore volume of D_{max} = 30 nm, S_{BET} = 689 m^2/g and V_{tot} = 1.21 mL/g, respectively is investigated. Nanoconfinement of $2LiBH_4$-$NaAlH_4$ facilitates a reduction in the temperature of the hydrogen release by 132 °C, compared to that of bulk $2LiBH_4$-$NaAlH_4$ and the onset of hydrogen release is below 100 °C. The reversible hydrogen storage capacity is also significantly improved for the nanoconfined sample, maintaining 83% of the initial hydrogen content after three cycles compared to 47% for that of the bulk sample. During nanoconfinement, $LiBH_4$ and $NaAlH_4$ reacts to form $LiAlH_4$ and $NaBH_4$ and the final dehydrogenation products, obtained at 481 °C are LiH, LiAl, AlB_2 and Al. After rehydrogenation of the nanoconfined sample at T = 400 °C and $p(H_2)$ = 126 bar, amorphous $NaBH_4$ is recovered along with unreacted LiH, AlB_2 and Al and suggests that $NaBH_4$ is the main compound that can reversibly release and uptake hydrogen.

Keywords: nanoconfinement; metal borohydride; sodium alanate

1. Introduction

Solid state hydrogen storage has received significant attention during the past few decades and is associated with a future carrier of renewable energy [1,2]. Initially, metal hydrides and magnesium hydride were the focus for much research and several useful applications have been developed [3–6]. In particular, lithium borohydride, $LiBH_4$, is considered a potential candidate as a hydrogen storage material due to its relatively high gravimetric hydrogen storage capacity of ρ_m = 13.6 wt. % based on decomposition reaction (1) taking place above 375 °C in vacuum.

$$LiBH_4(s) \rightarrow 2LiH(s) + B(s) + 3H_2(g) \quad (1)$$

However, the kinetics for hydrogen release and uptake is very sluggish *i.e.*, hydrogen uptake requires elevated temperatures and pressures, T = 600 °C and $p(H_2)$ > 155 bar [7]. One way to alter kinetic properties for hydrogen release of reactive composites of $LiBH_4$ is by additives using transition metals such as Ti, V, Cr or Sc [8–11]. Other metals like Al and Mg have also shown significant destabilization abilities as a reactive hydride composite (RHC) with $LiBH_4$, by reducing the enthalpy of reversible dehydrogenation and rehydrogenation reactions [12–14]. Al nanoparticles have also been considered as an Al-source but the properties are generally inhibited due to an oxide layer, which limits the reactivity [10]. Another drawback for the $LiBH_4$-Al system is the significant reduction of the hydrogen content, which has pointed attention towards $NaAlH_4$ as the Al source. Furthermore,

$NaAlH_4$ can reversibly store hydrogen at moderate conditions according to the two-step decomposition reaction shown in reactions (2) and (3).

$$3NaAlH_4(s) \rightarrow Na_3AlH_6(s) + 2Al(s) + 3H_2(g) \quad (2)$$

$$Na_3AlH_6(s) \rightarrow Al(s) + 3NaH(s) + 3/2H_2(g) \quad (3)$$

The hydrogen storage capacity associated with the two-step reaction is ρ_m = 5.6 wt. % [15,16]. Mixed hydride systems have previously been studied in various ratios, *i.e.*, $LiBH_4$-$NaAlH_4$, $2LiBH_4$-$NaAlH_4$ and $2LiBH_4$-$3NaAlH_4$ [17], and with selected Ti-based additives [18]. Different reaction pathways may occur, depending on the composition as shown in reactions (4) and (5).

$$LiBH_4(s) + NaAlH_4(s) \rightarrow NaBH_4(s) + LiAlH_4(s) \quad (4)$$

where $LiAlH_4$ also release hydrogen in two steps according to reactions (5) and (6)

$$3LiAlH_4(s) \rightarrow Li_3AlH_6(s) + 2Al(s) + 3H_2(g) \quad (5)$$

Above 100 °C, without doping, Li_3AlH_6 reacts to release hydrogen according to reaction (6)

$$Li_3AlH_6(s) \rightarrow 3LiH(s) + Al(s) + 3/2H_2(g) \quad (6)$$

Furthermore, it is found that with excess $NaAlH_4$ in the $2LiBH_4$-$3NaAlH_4$ system, the decomposition product NaH reacts reversibly forming $LiNa_2AlH_6$ at T = 180 °C and $p(H_2)$ = 80 bar [18] according to reaction (7):

$$LiNa_2AlH_6(s) \leftrightarrow LiH(s) + 2NaH(s) + Al + 3/2H_2(g) \quad (7)$$

In the case of excess $LiBH_4$ ($2LiBH_4$-$NaAlH_4$), mixed phases of $NaBH_4$ and $LiAlH_4$ are formed. However, during dehydrogenation AlB_x, $Al_{1-x}Li_xB_2$ and LiAl were observed at 425 and 450 °C, respectively [17].

Nanoconfinement of metal hydrides may change the reaction mechanism for reactive hydride composites, and may also improve the kinetics for chemical reactions significantly [19–21]. Confinement of $NaAlH_4$ in carbon aerogel, which was also activated or functionalized, has been investigated. The fastest kinetics are observed for $TiCl_3$ functionalized scaffolds, while CO_2 activated scaffolds provide slower kinetics but more efficient infiltration and higher reversible hydrogen storage capacity over several cycles of hydrogen release and uptake [22–24].

This work presents hydrogen release and uptake properties of nanoconfined $2LiBH_4$-$NaAlH_4$ into a nanoporous carbon aerogel scaffold, synthesised via melt infiltration for further improvement of the system, with the purpose of destabilizing the borohydride in the solid state. Various techniques are used to investigate hydrogen storage properties of this system.

2. Experimental Details

2.1. Sample Preparation

The resorcinol formaldehyde carbon aerogel was prepared by mixing 82.87 g resorcinol (Aldrich, 99%), 113.84 mL formaldehyde (37 wt. % stabilized by ~10%–15% methanol, Merck), 113.28 mL deionized water and 0.0674 g Na_2CO_3 (Aldrich, 99.999%) in a beaker with continuous stirring until complete dissolution was obtained. The pH of the final solution was measured to be 5.91. The preparation and characterization of the aerogel was performed according to previously published procedures [22,25,26]. Prior to use, the scaffolds were all degassed at 400 °C in a dynamic vacuum for several hours, in order to remove possible adsorbed air and water confined inside the porous structure.

This carbon aerogel scaffold is denoted CA. All subsequent handling was performed in a glovebox with a purified argon atmosphere.

Commercially available $NaAlH_4$ (Aldrich, 93%) was physically mixed with $LiBH_4$ (Aldrich, ⩾95.0%) in the molar ratio $2LiBH_4$-$NaAlH_4$ which was recently reported to show suitable melt infiltration abilities [27]. This sample is denoted LiNa.

An amount of hydride was selected in order to obtain ~33 vol. % pore filling of the carbon scaffold based on the total pore volume, V_{tot}, of the scaffold and the average bulk densities of the hydrides, ρ(LiNa) = 0.8482 g/mL. Melt infiltration was performed in a custom made rig, by heating to T = 310 °C ($\Delta T/\Delta t$ = 2 °C/min) with the temperature kept fixed at 310 °C for 30 min, at a hydrogen pressure of 110 bar. Afterwards the sample was cooled naturally to room temperature (RT).

2.2. Sample Characterization

Synchrotron radiation powder X-ray diffraction (SR-PXD) data was collected at beamline I711 at MAX-lab, Lund, Sweden. The samples were mounted in a sapphire capillary tube (0.79 mm I.D.), in an airtight sample holder inside an argon filled glovebox [28,29]. The sample holder was removed from the glovebox and attached to a gas control system at the synchrotron diffractometer. The data was collected using a MAR165 CCD detector with a selected wavelength of λ = 0.991779 Å. Heating was applied by a tungsten wire placed under the capillary, whereas the temperature was controlled by an external PID regulator and thermocouple inserted into the powder-bed as previously shown [28].

A Perkin Elmer STA 6000 was utilized to conduct thermogravimetric analysis (TGA) coupled with a Hiden Analytical quadrupole mass spectrometer (MS) for differential scanning calorimetry (DSC). Thus, temperature-programmed desorption mass spectroscopy (TPD-MS) data is provided. Data was collected with a constant flow (64 mL/min) of argon (99.99%). A powdered sample (<5 mg), was placed in an Al_2O_3 crucible with lid and heated in the temperature range of 40 to 550 °C ($\Delta T/\Delta t$ = 10 °C/min). The MS signals at m/e = 2, 18 and 34 were recorded in order to detect H_2, H_2O and B_2H_6.

The reversible hydrogen storage capacity of nanoconfined and bulk $2LiBH_4$-$NaAlH_4$ was studied during multiple hydrogen release and uptake cycles. The samples were sealed in an autoclave under argon and attached to the Sieverts' apparatus (PCTpro 2000). Hydrogen desorption data was collected starting under an initial H_2 pressure of 1 bar and was performed in the temperature range of RT to 500 °C, ($\Delta T/\Delta t$ = 5 °C/min), with the temperature kept constant at 500 °C for 10 h. Hydrogen absorption was performed in the pressure range of $p(H_2)$ = 140 to 150 bar, at a temperature of 400 °C ($\Delta T/\Delta t$ = 5 °C/min) during 10 h, and then the sample was cooled naturally to RT.

The Fourier transform infrared spectrometry (FTIR) analyses were carried out on a NICOLET 380 FT-IR from Thermo-Electronic Corporation with permanently aligned optics and proprietary diamond-turned pinned-in-place mirror optics. A small amount of sample was placed on the baseplate and subsequently the diamond pin was pressed on to the sample, forming a thin film. The samples were examined within the wave number range of 400–4000 cm^{-1}. The samples were briefly exposed to air when mounted in the instrument.

3. Results and Discussion

3.1. In Situ Synchrotron Radiation—Powder X-Ray Diffraction of Bulk and Nanoconfined $2LiBH_4$-$NaAlH_4$

The decomposition of physically mixed bulk $2LiBH_4$-$NaAlH_4$ (LiNa) has been investigated using *in situ* SR-PXD during heating up to 487 °C, see Figure 1. At RT a physical mixture of the low temperature polymorph orthorhombic $LiBH_4$, *o*-$LiBH_4$, and $NaAlH_4$ are present in the sample. The polymorphic transition from *o*-$LiBH_4$ to hexagonal *h*-$LiBH_4$ takes place in the temperature range 98 to 105 °C. A metathesis reaction between $LiBH_4$ and $NaAlH_4$ occurs at 116 °C observed by formation of $NaBH_4$. This may be the metathesis reaction described by reaction (4), however $LiAlH_4$ is not observed. Lithium tetrahydridoaluminate, $LiAlH_4$, may decompose immediately according to reaction (5), which explains observation of Li_3AlH_6 in the temperature range 116 to 227 °C. Since diffraction from

Crystals **2016**, *6*, 70

Na_3AlH_6 and NaH is not observed, $NaAlH_4$ is expected to be fully converted by the metathesis reaction (4) rather than decomposition via reactions (2) and (3). Characteristic strong diffraction at $2\theta = 25^\circ$ and 28° from Al occur at $T = 115$ °C and is assumed mainly to be formed via the decomposition of $LiAlH_4$. Similarly, diffraction from *h*-$LiBH_4$ is not visible in the data possibly due to reaction (4). $NaBH_4$ is observed in the temperature range from 116 to 435 °C. Weak diffraction from LiH, is also observed in the temperature range 116 and 485 °C, partially overlapping with the Al peaks and is expected mainly to be formed by decomposition of Li_3AlH_6. Furthermore, two unknown peaks are observed at $2\theta \sim 20^\circ$ and $2\theta \sim 23^\circ$, forming simultaneous to Li_3AlH_6. A shift of Bragg peaks towards smaller 2θ angles is observed due to thermal expansion and the associated increase in unit cell parameters. During natural cooling of the sample, thermal contraction is observed along with formation of Al, $LiAl_3$, and $NaBH_4$ along with an unknown compound. A difference plot of the *in situ* SR-PXD data is shown in supporting information to accentuate changes in weaker peaks.

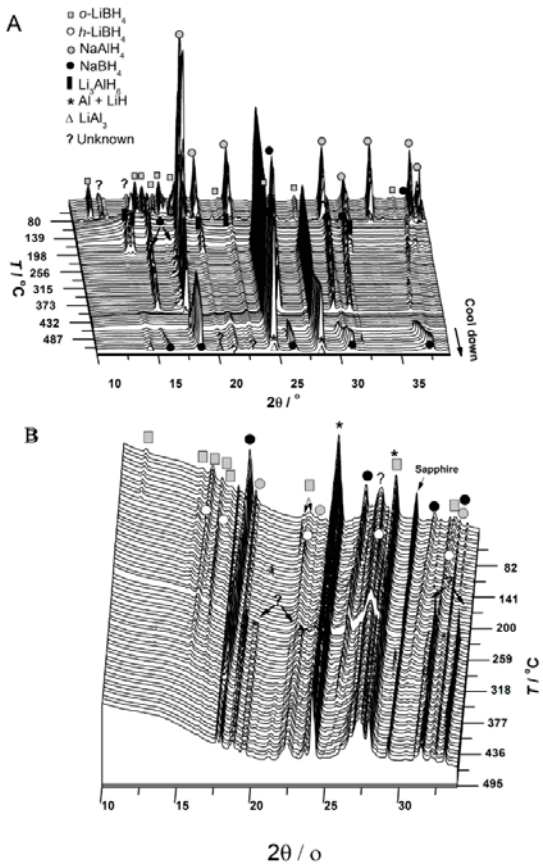

Figure 1. *In situ* SR-PXD during dehydrogenation of (**A**) bulk $2LiBH_4$-$NaAlH_4$ heated from room temperature (RT) to 487 °C, with subsequent natural cooling to RT in $p(H_2) = 1$ bar and (**B**) nanoconfined $2LiBH_4$-$NaAlH_4$ in carbon aerogel (CA) heated from RT to 495 °C ($\Delta T/\Delta t = 5$ °C/min, $\lambda = 0.991779$ Å).

A decrease in the background scattering occurs between 160 and 198 °C which coincides with the maximum rate of Li_3AlH_6 and Al formation. Further work would be required to determine if this relationship is causative or correlative. The Li_3AlH_6 diffraction decreases at $T > 192$ °C and disappears at $T \sim 227$ °C. The decomposition of Li_3AlH_6 is associated with further production of Al and the observation of weak diffraction from LiH. Following decomposition reactions could take place:

$$2LiBH_4 + Al \rightarrow 2LiH + AlB_2 + 3H_2 \quad (8)$$

$$2NaBH_4 + Al \rightarrow 2NaH + AlB_2 + 3H_2 \quad (9)$$

$$NaH \rightarrow Na + 1/2H_2 \quad (10)$$

Diffraction of $NaBH_4$ decreases in intensity at 412 to 435 °C just prior to a slight increase in the background intensity. Weak peaks of an unknown compound at 2θ ~14°, ~21° and ~22° are also observed to form simultaneously. It should be noted that the disappearance of $NaBH_4$ at 435 °C occurs well below both its melting point of 505 °C and the decomposition temperature of T(1 bar) ~515–534 °C [30]. The simultaneous decrease in diffracted intensity of LiH and $NaBH_4$ may suggest eutectic melting supported by the reappearance of $NaBH_4$ and LiH upon cooling at 487 °C. We note that eutectic melting of $NaBH_4$-NaH at T = 395 °C has previously been observed [31].

In situ SR-PXD of nanoconfined $LiBH_4$-$NaAlH_4$ measured during heating to 495 °C is shown in Figure 1. At RT diffraction of $LiBH_4$ and small amounts of $NaAlH_4$ are observed and partial decomposition due to the temperature used for the melt infiltration would explain the presence of diffraction peaks assigned to Al. Furthermore, the presence of $NaBH_4$ at RT also indicates metathesis reaction (4) during melt infiltration. A broad unknown peak at 2θ = 27° is observed throughout the measurement. The *o*-$LiBH_4$ to *h*-$LiBH_4$ polymorphic transition is observed, however only during a short temperature range of 97 to 110 °C. The background intensity decrease in the temperature range T ~ 238 to 250 °C but is most pronounced below 2θ = 15° and is associated with the formation of two peaks from an unknown phase at 2θ ~ 19° and 2θ ~ 23°. These peaks are similar to those formed in the bulk sample. At T = 318 °C, a diffraction peak appears at 2θ ~ 21.3° which coincides with a decrease in diffraction intensity from $NaBH_4$. This peak continues to slowly grow until all of the $NaBH_4$ decomposes at T ~ 406 °C. At ~487 °C, unknown peaks begin to form at 2θ ~ 19°, 22° and 31.4° and these slowly grow until the heating stops. The growth of these peaks is associated with a slight decrease in the intensity of the Al peaks. The unknown peaks may result from a reaction between the hydride(s) and possible oxygen impurities in the aerogel scaffold. However, due to the relatively weak and overlapping Bragg reflections, indexation remain unsuccessful.

3.2. Nanoporous Carbon Aerogel Composite

The synthesized resorcinol formaldehyde carbon aerogel (CA) scaffold has a maximum pore size distribution centred on D_{max} = 30 nm, a specific BET surface area of S_{BET} = 689 m^2/g and a total pore volume of V_{tot} = 1.21 mL/g (see Table 1).

Table 1. Texture parameters of as prepared carbon aerogel scaffold (CA). The gravimetric hydrogen content of the confined sample is also provided.

Scaffold	S_{BET} (m^2/g)	V_{micro} (mL/g)	V_{meso} (mL/g)	V_{tot} (mL/g)	D_{max} (nm)	LiNa * (wt. %)	Theoretical H_2 Content (wt. %)#
CA	689 ± 26	0.21 ± 0.02	1.06 ± 0.10	1.21 ±0.10	30 ± 0.15	-	-
CA-LiNa	257 ± 26	0.06 ± 0.02	0.71 ± 0.10	0.78 ±0.10	21 ± 0.15	25.3	2.6

* Amount of $2LiBH_4$-$NaAlH_4$ used for the infiltration per weight and volume of the scaffold; # Prior to melt infiltration.

The binary hydride composite $2LiBH_4$-$NaAlH_4$ (LiNa) has been successfully melt infiltrated into the mesoporous carbon scaffold via melt infiltration upon elevated hydrogen pressures of $p(H_2)$ = 110 bar, in order to avoid decomposition of the respective hydrides (please see note about this in experimental section). Confinement of the hydride mixture facilitates the formation of nanoparticles of the respective hydrides, in accordance with previous studies [27]. The amount of $2LiBH_4$-$NaAlH_4$ added to CA is 25.3 wt. % corresponding to 33 vol. % pore filling. The theoretical hydrogen content of the binary hydride system is ρ_m(LiNa) = 10.33 wt. % calculated using the bulk densities of the respective hydride according to the molar ratios and reaction (11)

$$2LiBH_4(s) + NaAlH_4(s) \rightarrow 2LiH(s) + Na(s) + AlB_2(s) + 5H_2(g) \quad (11)$$

The available hydrogen capacity of the CA-LiNa confined sample is determined to be 2.6 wt. % H_2. However, considering 100 vol. % pore filling would potentially give a 7.8 wt. % hydrogen capacity.

3.3. Decomposition of Bulk and Nanocomposites of $2LiBH_4$-$NaAlH_4$

The of hydrogen desorption from bulk $2LiBH_4$-$NaAlH_4$ (LiNa), LiNa physically mixed with carbon aerogel scaffold (CA) and LiNa melt infiltrated into CA, was analysed by TG-DSC-MS during heating from 40 to 550 °C with the results shown in Figure 2. The TG-DSC-MS measurements can provide information about the endothermic and exothermic nature of any transitions or chemical reactions that take place during heating. In addition, if the same transitions and chemical reactions occur in different samples, TG-DSC-MS can provide information about the relative kinetic differences between samples. Each data set is normalized to the maximum hydrogen desorption rate to allow for qualitative comparison between data sets. Hydrogen emission from bulk $2LiBH_4$-$NaAlH_4$ is observed as two local maxima at 234 and 496 °C. The first hydrogen release peak in the MS spectrum (T = 200–250 °C) is associated with the decomposition of Li_3AlH_6 in accord with the *in situ* SR-PXD data (see Figure 1). This temperature range is in good agreement with previous reports on decomposition of bulk Li_3AlH_6 (180–230 °C) [32,33]. A mass loss of 3.36 wt. % is observed by TGA in the temperature range 200 to 250 °C. Differential scanning calorimetry data reveal two thermal events at 112 and 120 °C, which may be assigned to the polymorphic *o*- to *h*-$LiBH_4$ transition and the metathesis reaction (reaction 4), respectively. Partial amorphisation or melting of the sample may occur, which may be observed as a significant increase in the background of the diffraction data in the temperature range 70 to 150 °C (see Figure 1). Several thermal events in the temperature range ~200 to 220 °C may be associated with partial melting of the sample and decomposition of Li_3AlH_6 [32]. Eutectic melting of the $LiBH_4$-$NaBH_4$ is reported to occur at ~250 °C without release of hydrogen [30].

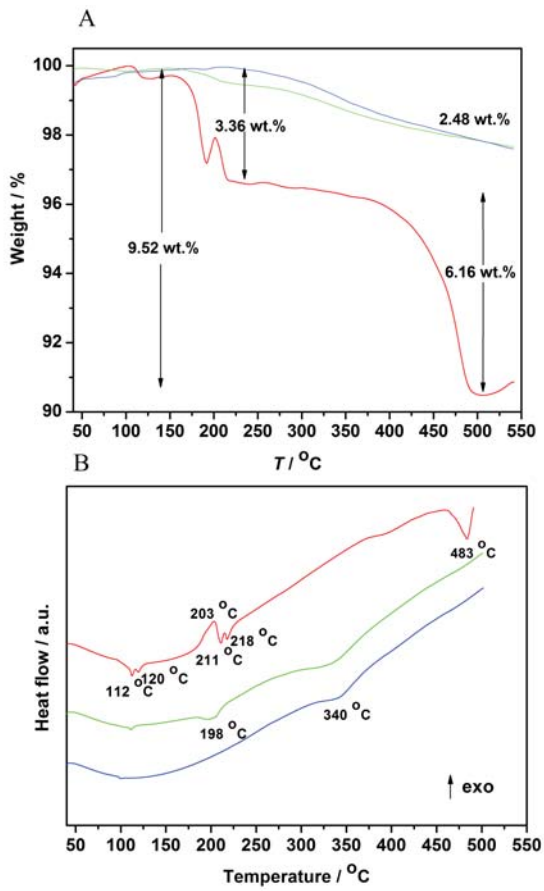

Figure 2. *Cont.*

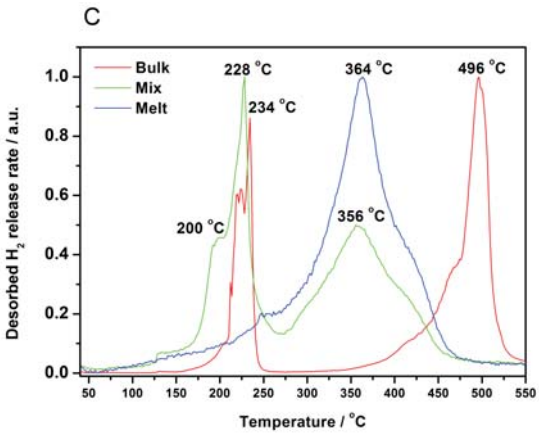

Figure 2. (**A**) Thermal programmed desorption mass spectroscopy (TPD-MS) profiles of the hydrogen release (H_2^+ ions, m/e = 2); (**B**) thermogravimetric analysis (TGA); and (**C**) differential scanning calorimetry (DSC) measurements of bulk $2LiBH_4$-$NaAlH_4$ (LiNa) (red), LiNa mixed with carbon aerogel scaffold (CA) (green) and LiNa melt infiltrated into CA (blue). The data is measured in the temperature range 40 to 550 °C and TPD-MS for each data set is normalized by its maximum hydrogen release rate to allow for qualitative comparison ($\Delta T/\Delta t$ = 10 °C/min).

The second MS hydrogen release event (T = 350–500 °C) of bulk LiNa is assigned to the decomposition of remaining $LiBH_4$ and $NaBH_4$, which corresponds to a weight loss of 6.16 wt. %. The total TGA mass loss in the temperature range 40 to 550 °C is 9.52 wt. %, which corresponds to 92% of the available hydrogen content (ρ_m(LiNa) = 10.33 wt. %).

The carbon containing samples (physically mixed and melt infiltrated) both release 2.48 wt. % H_2 when heated from 40 to 550 °C, which corresponds to 95% of the theoretical hydrogen content in the sample (see Figure 2). However, the physically mixed sample has a hydrogen release profile similar to that of bulk LiNa at T < ~250 °C with a peak value at T = 228 °C shifted 6 °C towards lower temperatures. The nanoconfined sample LiNa-CA does not show the aforementioned desorption peak. The temperature of the maximum hydrogen release rate of the mixed (T = 356 °C) and melt infiltrated samples (T = 364 °C) occur at significantly reduced temperatures (ΔT ~ 130 °C) as compared to that of bulk $LiBH_4$-$NaAlH_4$ (T = 496 °C). This effect has previously been reported for other nanoconfined binary hydride systems that showed a reduction in the temperature of the maximum hydrogen release rate compared to bulk, e.g., $LiBH_4$-$Mg(BH_4)_2$ (ΔT_{max} ~ −60 °C), $LiBH_4$-$Ca(BH_4)_2$ (ΔT_{max} ~ −95 °C) and $LiBH_4$-$NaBH_4$ (ΔT_{max} ~ −107 °C) [33–35].

The improvement of hydrogen release kinetics due to the carbon scaffold, is assigned to the effect induced by nanoconfinement and possible catalytic properties of the carbon surface [36]. In addition, the DSC signal assigned to the major hydrogen desorption at T ~ 340 °C is reduced by ~140 °C as compared to that of bulk LiNa.

According to Figure S2, after decomposition of the nanoconfined sample AlB_2, $LiAl_3$, LiH and some unknown phases are formed. No diffraction Bragg peaks of $NaBH_4$ are displayed suggesting possible formation of amorphous metal borides. This is supported by the FTIR data discussed later.

3.4. Cyclic Stability

The reversible hydrogen storage properties of bulk and nanoconfined $2LiBH_4$-$NaAlH_4$ (LiNa) have been investigated by the Sieverts' method during multiple hydrogen release and uptake cycles and the data is displayed in Figure 3. During heating of bulk LiNa from RT to 500 °C, hydrogen is released in two steps with a plateau of slow hydrogen evolution in the temperature range 160 to 190 °C. The total amount of hydrogen released from the sample during the first desorption in the temperature range RT to 500 °C is 8.37 wt. %, which is 81% of the theoretical available hydrogen content. After subsequent rehydrogenation at $p(H_2)$ = 126 bar, T = 400 °C for 10 h, the second, third and

Crystals **2016**, *6*, 70

fourth desorption cycle release 4.65, 3.94 and 3.38 wt. % H_2, corresponding to 56%, 47% and 40% of the initial hydrogen content, respectively. The slow hydrogen release at 160 to 190 °C is only observed during the first desorption, as clearly demonstrated in Figure 4. Thus, the reversible fraction of the sample may be $LiBH_4$ and/or $NaBH_4$ formed in a possibly amorphous form. Sodium and lithium alanate are not expected to form at the high temperatures used for rehydrogenation. This fact along with the formation of stable decomposition products LiH, $LiAl_3$ and Al, may explain the significant difference between the hydrogen storage capacities observed after the first desorption.

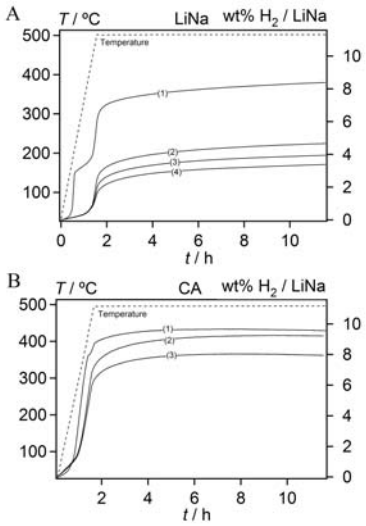

Figure 3. Sieverts' measurement showing four and three hydrogen release cycles for (**A**) bulk $2LiBH_4$-$NaAlH_4$ and (**B**) infiltrated into CA, LiNa-CA. Hydrogen desorption was performed at a fixed temperature of 500 °C ($\Delta T/\Delta t$ = 5 °C) for 10 h under an initial hydrogen pressure of 1 bar. Hydrogen absorption was performed at 400 °C, $p(H_2)$ = 126 bar for 10 h.

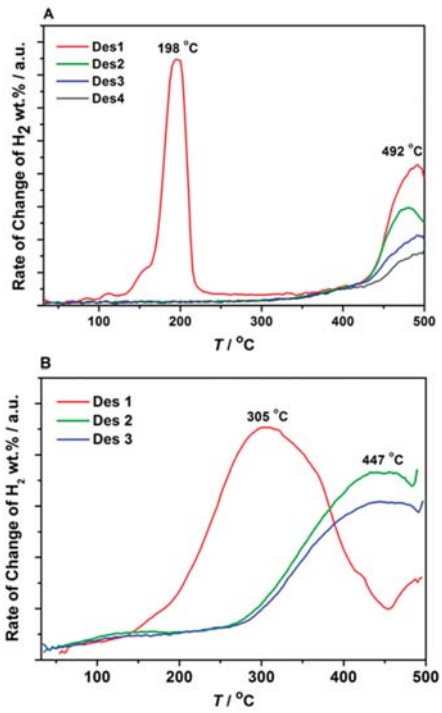

Figure 4. Differentiated Sieverts' data for four and three desorption cycles of (**A**) bulk $2LiBH_4$-$NaAlH_4$ and (**B**) nanoconfined $2LiBH_4$-$NaAlH_4$ in CA.

The nanoconfined sample, LiNa-CA, showed substantially improved cyclic stability and improved hydrogen storage capacity compared to that of bulk LiNa as shown in Figure 3. The hydrogen release of LiNa-CA is shown relative to the amount of $2LiBH_4$-$NaAlH_4$ in the nanoconfined to facilitate comparison with LiNa. The hydrogen release from the nanoconfined system also has a two-step behaviour for the first H_2 desorption profile similar to bulk LiNa but at higher temperatures (~380 °C). The first desorption of LiNa-CA releases 9.6 wt. % H_2 with respect to LiNa and 2.4 wt. % releative to the total mass of the sample. This corresponds to 93% of the theoretical available hydrogen content (ρ_m(LiNa-CA) = 2.6 wt. % H_2). It is worth noting that the nanoconfined sample is fully desorbed after 2 h at 500 °C, whereas bulk $2LiBH_4$-$NaAlH_4$, on the contrary continues to release hydrogen throughout the entire measurement. The second and third desorptions release 9.2 and 7.9 wt. % H_2/LiNa corresponding to 96% and 83% of the initial hydrogen content, and equivalent to 89% and 77% of the available hydrogen content, respectively. These results demonstrate that nanoconfinement has significantly improved hydrogen release kinetics and cyclic stability compared to bulk $2LiBH_4$-$NaAlH_4$.

Differentiated Sieverts' data provides the change in rate of H_2 release during each desorption cycle upon heating from RT to 500 °C (see Figure 4). Selected desorption profiles from Figure 4 resemble the TPD-MS data shown in Figure 2, despite different measurement conditions and heating rates. During the first hydrogen release cycle of bulk LiNa, the maximum H_2 release rate is observed at 198 °C which corresponds to the first plateau observed in Figure 3. A second peak value at 492 °C is in good agreement with TPD-MS measurements in Figure 3. During the second, third and fourth desorption, only one hydrogen release event is observed with onset at T ~ 440 °C, which decreases in intensity with increasing desorption cycles.

The major hydrogen release of the nanoconfined sample (Figure 4B) is exhibited as a broad peak with maxima at 305 °C during the first desorption. However during the second and third desorption an event is observed with a local maxima at 447 °C. The lack of exothermic signal in the DSC measurement suggests that this hydrogen release is not due to a one-time irreversible reaction with oxygen impurities in the carbon framework. Instead it suggests that the hydrogen pressure applied at the temperature used for rehydriding was insufficient to fully reverse all of the hydrogen desorption reactions. *In situ* SR-PXD of the nanoconfined sample suggests that the first hydrogen release event on the first desorption cycle is due to residual unreacted $LiBH_4$ from incomplete metathesis (reaction 4). Once the remaining $LiBH_4$ has decomposed, it is not reformed under the applied hydriding conditions, thus it is not observed during the second desorption. Based on the *in situ* SR-PXD on the bulk sample, the compounds that are not regenerated under the applied temperatures and hydrogen pressures are possibly $LiAlH_4$ and/or Li_3AlH_6 [37].

FT-IR measurements on selected samples are presented in Figure 5. Bulk $2LiBH_4$-$NaAlH_4$ demonstrates multiple peaks in the fingerprint region (500–1500 cm^{-1}). The three signals at 1095, 1241 and 1315 cm^{-1}, corresponds to the characteristic B-H bending bands of $LiBH_4$. The signal at 1626 cm^{-1} is assigned to the $[AlH_4]^-$ stretching band of $NaAlH_4$ and the large broad signal ranging from 2000 to 2500 cm^{-1}, with a maximum at 2307 cm^{-1}, originates from the B-H stretch of $LiBH_4$. Furthermore, the small signal at 3444 cm^{-1}, is assigned to –OH, most likely from exposure to atmospheric moisture moist during measurement. It is worth noting that moisture and air cannot be completely avoided during collection of FT-IR data using the selected apparatus. A completely dehydrogenated sample of melt infiltrated $2LiBH_4$-$NaAlH_4$ in CA, *i.e.*, heated at 500 °C for 10 h shows a distinct signals at 1100 and 2462 cm^{-1}. These positions are close to those reported for $Li_2B_{12}H_{12}$ [38] and are nearly identical to positions reported by Mao *et al.* [39] after the decomposition of $NaBH_4$ which suggests that one of the decomposition products may be $Na_2B_{12}H_{12}$. Rehydrogenation of the decomposed sample after three desorption cycles at 400 °C for 10 h, show B-H stretching signals at 2113 and 2283 cm^{-1} and the respective B-H bending. Furthermore, signals at 1234 and 1080 cm^{-1} are observed in the fingerprint region. These results may suggest that the 1234 and 2283 can be assigned to $NaBH_4$ in combination with another unknown complex boron hydride. It is difficult to make any statement about the possible presence of $NaAlH_4$ signals due to the high amount of carbon and low total quantity of hydrides in

the sample. Based on these results it can be suggested that the partial reversibility of the system is due to the formation and decomposition of $NaBH_4$ inside the scaffold.

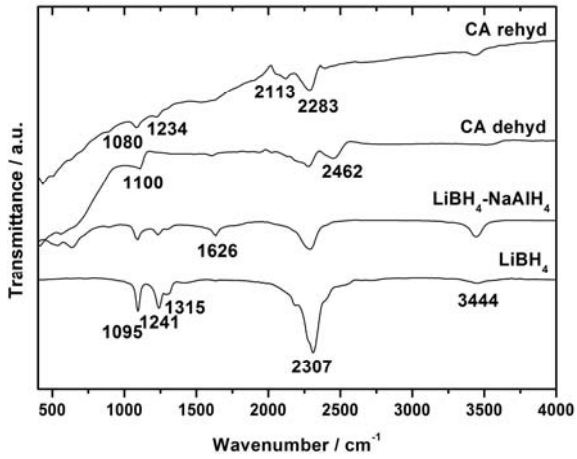

Figure 5. FTIR spectra of bulk $LiBH_4$, $2LiBH_4$-$NaAlH_4$ (LiNa), and nanoconfined $2LiBH_4$-$NaAlH_4$ CA-LiNa after dehydrogenation at 500 °C for the third time and finally CA-LiNa rehydrogenated at $p(H_2)$ = 140 bar, T = 400 °C for 10 h after three desorption cycles. The intensity of the spectra with the carbon containing samples was scaled corresponding to their quantity of LiNa to allow for better comparison.

Fu *et al.* [40] reports elemental analysis of carbon aerogel prepared using alternative reagents but similar pyrolysis conditions. Analysis of carbon and oxygen concentration of the carbon aerogels after pyrolysis reveal C and O are 94.00 wt. % and 5.87 wt. %, respectively (re-calculated by excluding K). Assuming similar oxygen levels in our scaffolds and a 1:1 reaction with LiH would reduce the released amount of hydrogen to 2.066 wt. % H_2 for the nanoconfined sample.

4. Conclusions

Nanoconfinement of $2LiBH_4$-$NaAlH_4$ was obtained via melt infiltration under H_2 pressure and the reversibility and the reaction mechanisms during infiltration and decomposition are investigated. Nanoconfinement of $2LiBH_4$-$NaAlH_4$ into a mesoporous carbon aerogel scaffold significantly enhances the kinetics for hydrogen desorption, the hydrogen storage capacity and reversibility during hydrogen release and uptake cycling of $2LiBH_4$-$NaAlH_4$, compared to that of bulk. The temperature of the maximum hydrogen desorption rate is reduced by 132 °C when employing the carbon scaffold, which is assigned to the effect induced by nanoconfinement and the carbon surface acting as a catalyst for hydrogen release on $2LiBH_4$-$NaAlH_4$. The stability during cycling is significantly enhanced by melt infiltration of the hydride. Bulk $2LiBH_4$-$NaAlH_4$ releases 81% of the available hydrogen content during the first desorption, compared to 96% when nanoconfined. During the third desorption cycle of the bulk sample, only 47% of the initial hydrogen content is retained compared to 83% for that of the nanoconfined sample. These results demonstrate significant stabilization of the cyclic hydrogen storage capacity of metal borohydrides compared to those previously presented.

Acknowledgments: The work was supported by the Innovation Fund Denmark (project HyFill-Fast), and by the Danish Research Council for Nature and Universe (Danscatt), the Danish National Research Foundation, Center for Materials Crystallography (DNRF93). Torben R. Jensen is grateful to the Carlsberg Foundation. Craig E. Buckley, Drew A. Sheppard and Payam Javadian acknowledge the financial support of the Australian Research Council (ARC) for ARC Linkage Grant LP120100435.

Author Contributions: Payam Javadian prepared the samples, obtained the experimental results and conducted the characterization experiments in collaboration with Drew A. Sheppard. All authors contributed to data analysis and to writing of the manuscript.

Conflicts of Interest: The authors declare no conflict of interest.

References

1. Ley, M.B.; Jepsen, L.H.; Lee, Y.S.; Cho, Y.W.; von Colbe, J.M.B.; Dornheim, M.; Rokni, M.; Jensen, J.O.; Sloth, M.; Filinchuk, Y.; *et al.* Complex hydrides for hydrogen storage—New perspectives. *Mater. Today* **2014**, *17*, 122–128. [CrossRef]
2. Callini, E.; Atakli, Z.Ö.K.; Hauback, B.C.; Orimo, S.-I.; Jensen, C.; Dornheim, M.; Grant, D.; Cho, Y.W.; Chen, P.; Hjörvarsson, B.; *et al.* Complex and liquid hydrides for energy storage. *Appl. Phys. A* **2016**, *122*, 1–22. [CrossRef]
3. Crivello, J.C.; Denys, R.V.; Dornheim, M.; Felderhoff, M.; Grant, D.M.; Huot, J.; Jensen, T.R.; de Jongh, P.; Latroche, M.; Walker, G.S.; *et al.* Mg-based compounds for hydrogen and energy storage. *Appl. Phys. A* **2016**, *122*, 1–17. [CrossRef]
4. Crivello, J.C.; Dam, B.; Denys, R.V.; Dornheim, M.; Grant, D.M.; Huot, J.; Jensen, T.R.; de Jongh, P.; Latroche, M.; Milanese, C.; *et al.* Review of magnesium hydride-based materials: Development and optimisation. *Appl. Phys. A* **2016**, *122*, 1–20. [CrossRef]
5. Yartys, V.; Noreus, D.; Latroche, M. Metal hydrides as negative electrode materials for Ni-MH batteries. *Appl. Phys. A* **2016**, *122*, 1–11. [CrossRef]
6. Lototskyy, M.V.; Yartys, V.A.; Pollet, B.G.; Bowman, R.C. Metal hydride hydrogen compressors: A review. *Int. J. Hydrog. Energy* **2014**, *39*, 5818–5851. [CrossRef]
7. Zuttel, A.; Wenger, P.; Rentsch, S.; Sudan, P.; Mauron, P.; Emmenegger, C. $LiBH_4$ a new hydrogen storage material. *J. Power Sour.* **2003**, *118*, 1–7. [CrossRef]
8. Yang, J.; Sudik, A.; Wolverton, C. Destabilizing $LiBH_4$ with a metal (M = Mg, Al, Ti, V, Cr, or Sc) or metal hydride (MH_2, MgH_2, TiH_2, or CaH_2). *J. Phys. Chem. C* **2007**, *111*, 19134–19140. [CrossRef]
9. Yu, X.B.; Grant, D.A.; Walker, G.S. Low-temperature dehydrogenation of $LiBH_4$ through destabilization with TiO_2. *J. Phys. Chem. C* **2008**, *112*, 11059–11062. [CrossRef]
10. Meggouh, M.; Grant, D.M.; Walker, G.S. Optimizing the destabilization of $LiBH_4$ for hydrogen storage and the effect of different Al sources. *J. Phys. Chem. C* **2011**, *115*, 22054–22061. [CrossRef]
11. Purewal, J.; Hwang, S.J.; Bowman, R.C.; Ronnebro, E.; Fultz, B.; Ahn, C. Hydrogen sorption behavior of the ScH_2-$LiBH_4$ system: Experimental assesment of chemical destabilization effects. *J. Phys. Chem. C* **2008**, *112*, 8481–8485. [CrossRef]
12. Ravnsbaek, D.B.; Jensen, T.R. Mechanism for reversible hydrogen storage in $LiBH_4$-Al. *J. Appl. Phys.* **2012**, *111*, 112621. [CrossRef]
13. Kang, X.D.; Wang, P.; Ma, L.P.; Cheng, H.M. Reversible hydrogen storage in $LiBH_4$ destabilized by milling with Al. *Appl. Phys. A* **2007**, *89*, 963–966. [CrossRef]
14. Hansen, B.R.S.; Ravnsbaek, D.B.; Reed, D.; Book, D.; Gundlach, C.; Skibsted, J.; Jensen, T.R. Hydrogen storage capacity loss in a $LiBH_4$-Al composite. *J. Phys. Chem. C* **2013**, *117*, 7423–7432. [CrossRef]
15. Gao, J.; Adelhelm, P.; Verkuijlen, M.H.W.; Rongeat, C.; Herrich, M.; van Bentum, P.J.M.; Gutfleisch, O.; Kentgens, A.P.M.; de Jong, K.P.; de Jongh, P.E. Confinement of $NaAlH_4$ in nanoporous carbon: Impact on H_2 release, reversibility, and thermodynamics. *J. Phys. Chem. C* **2010**, *114*, 4675–4682. [CrossRef]
16. Bogdanovic, B.; Brand, R.A.; Marjanovic, A.; Schwickardi, M.; Tolle, J. Metal-doped sodium aluminium hydrides as potential new hydrogen storage materials. *J. Alloys Compd.* **2000**, *302*, 36–58. [CrossRef]
17. Ravnsbaek, D.B.; Jensen, T.R. Tuning hydrogen storage properties and reactivity: Investigation of the $LiBH_4$-$NaAlH_4$ system. *J. Phys. Chem. Solids* **2010**, *71*, 1144–1149. [CrossRef]
18. Shi, Q.; Yu, X.; Feidenhans'l, R.; Vegge, T. Destabilized $LiBH_4$-$NaAlH_4$ mixtures doped with titanium based catalysts. *J. Phys. Chem. C* **2008**, *112*, 18244–18248. [CrossRef]
19. De Jongh, P.E.; Adelhelm, P. Nanosizing and nanoconfinement: New strategies towards meeting hydrogen storage goals. *ChemSusChem* **2010**, *3*, 1332–1348. [CrossRef] [PubMed]
20. Nielsen, T.K.; Besenbacher, F.; Jensen, T.R. Nanoconfined hydrides for energy storage. *Nanoscale* **2011**, *3*, 2086–2098. [CrossRef] [PubMed]
21. Paskevicius, M.; Sheppard, D.A.; Buckley, C.E. Thermodynamic changes in mechanochemically synthesized magnesium hydride nanoparticles. *J. Am. Chem. Soc.* **2010**, *132*, 5077–5083. [CrossRef] [PubMed]
22. Nielsen, T.K.; Polanski, M.; Zasada, D.; Javadian, P.; Besenbacher, F.; Bystrzycki, J.; Skibsted, J.; Jensen, T.R. Improved hydrogen storage kinetics of nanoconfined $NaAlH_4$ catalyzed with $TiCl_3$ nanoparticles. *ACS Nano* **2011**, *5*, 4056–4064. [CrossRef] [PubMed]

23. Javadian, P.; Nielsen, T.K.; Ravnsbaek, D.B.; Jepsen, L.H.; Polanski, M.; Plocinski, T.; Kunce, I.; Besenbacher, F.; Bystrzycki, J.; Jensen, T.R. Scandium functionalized carbon aerogel: Synthesis of nanoparticles and structure of a new ScOCl and properties of $NaAlH_4$ as a function of pore size. *J. Solid State Chem.* **2015**, *231*, 190–197. [CrossRef]
24. Nielsen, T.K.; Javadian, P.; Polanski, M.; Besenbacher, F.; Bystrzycki, J.; Jensen, T.R. Nanoconfined $NaALH_4$: Determination of distinct prolific effects from pore size, crystallite size, and surface interactions. *J. Phys. Chem. C* **2012**, *116*, 21046–21051. [CrossRef]
25. Nielsen, T.K.; Bösenberg, U.; Gosalawit, R.; Dornheim, M.; Cerenius, Y.; Besenbacher, F.; Jensen, T.R. A reversible nanoconfined chemical reaction. *ACS Nano* **2010**, *4*, 3903–3908. [CrossRef] [PubMed]
26. Al-Muhtaseb, S.A.; Ritter, J.A. Preparation and properties of resorcinol-formaldehyde organic and carbon gels. *Adv. Mater.* **2003**, *15*, 101–114. [CrossRef]
27. Thiangviriya, S.; Plerdsranoy, P.; Wiset, N.; Javadian, P.; Jensen, T.R.; Utke, R. Hydrogen sorption and reaction mechanisms of nanoconfined $2LiBH_4$-$NaAlH_4$. *J Alloys Compd* **2015**, *633*, 484–493. [CrossRef]
28. Jensen, T.R.; Nielsen, T.K.; Filinchuk, Y.; Jorgensen, J.-E.; Cerenius, Y.; Gray, E.M.; Webb, C.J. Versatile *in situ* powder X-ray diffraction cells for solid-gas investigations. *J. Appl. Crystallogr.* **2010**, *43*, 1456–1463. [CrossRef] [PubMed]
29. Hansen, B.R.S.; Moller, K.T.; Paskevicius, M.; Dippel, A.C.; Walter, P.; Webb, C.J.; Pistidda, C.; Bergemann, N.; Dornheim, M.; Klassen, T.; *et al.* *In situ* X-ray diffraction environments for high-pressure reactions. *J. Appl. Crystallogr.* **2015**, *48*, 1234–1241. [CrossRef]
30. Paskevicius, M.; Ley, M.B.; Sheppard, D.A.; Jensen, T.R.; Buckley, C.E. Eutectic melting in metal borohydrides. *Phys. Chem. Chem. Phys.* **2013**, *15*, 19774–19789. [CrossRef] [PubMed]
31. Stasinevich, D.; Egorenko, G.; Gnedina, G. Tiermograficzieskoie Issliedovanie Systiemy Gidridoborat Natrija-Gidrid Natrija. *Dokl. Akad. Nauk SSSR* **1966**, *168*, 610–612.
32. Dilts, J.A.; Ashby, E.C. Study of thermal-decomposition of complex metal hydrides. *Inorg. Chem.* **1972**, *11*, 1230. [CrossRef]
33. Javadian, P.; Jensen, T.R. Enhanced hydrogen reversibility of nanoconfined $LiBH_4$-$Mg(BH_4)_2$. *Int. J. Hydrog. Energy* **2014**, *39*, 9871–9876. [CrossRef]
34. Javadian, P.; Sheppard, D.A.; Buckley, C.E.; Jensen, T.R. Hydrogen storage properties of nanoconfined $LiBH_4$-$Ca(BH_4)_2$. *Nano Energy* **2015**, *11*, 96–103. [CrossRef]
35. Javadian, P.; Sheppard, D.A.; Buckley, C.E.; Jensen, T.R. Hydrogen storage properties of nanoconfined $LiBH_4$-$NaBH_4$. *Int. J. Hydrog. Energy* **2015**, *40*, 14916–14924. [CrossRef]
36. Ward, P.A.; Teprovich, J.A.; Peters, B.; Wheeler, J.; Compton, R.N.; Zidan, R. Reversible hydrogen storage in a $LiBH_4$-C_{60} nanocomposite. *J. Phys. Chem. C* **2013**, *117*, 22569–22575. [CrossRef]
37. Varin, R.A.; Zbroniec, Z. Decomposition behavior of unmilled and ball milled lithium alanate ($LiAlH_4$) including long-term storage and moisture effects. *J. Alloys Compd.* **2010**, *504*, 89–101. [CrossRef]
38. Pitt, M.P.; Paskevicius, M.; Brown, D.H.; Sheppard, D.A.; Buckley, C.E. Thermal stability of $Li_2B_{12}H_{12}$ and its role in the decomposition of $LiBH_4$. *J. Am. Chem. Soc.* **2013**, *135*, 6930–6941. [CrossRef] [PubMed]
39. Mao, J.F.; Guo, Z.P.; Nevirkovets, I.P.; Liu, H.K.; Dou, S.X. Hydrogen de-/absorption improvement of $NaBH_4$ catalyzed by titanium-based additives. *J. Phys. Chem. C* **2012**, *116*, 1596–1604. [CrossRef]
40. Fu, R.; Yoshizawa, N.; Dresselhaus, M.S.; Dresselhaus, G.; Satcher, J.H.; Baumann, T.F. XPS Study of Copper-Doped Carbon Aerogels. *Langmuir* **2002**, *18*, 10100–10104. [CrossRef]

3.4. **Hydrogen storage properties of nanoconfined $LiBH_4$-$Ca(BH_4)_2$**

$LiBH_4$ is considered a high temperature, high capacity borohydride hydride and $Ca(BH_4)_4$ is considered a medium temperature borohydride. However, due to the improved reversibility and kinetics obtain, from the eutectic composite, $LiBH_4$-$Ca(BH_4)_2$ may potentially act as a HTMH (due to $LiBH_4$) and as a LTMH (due to $Ca(BH_4)_2$).

Nano Energy (2015) 11, 96–103

Available online at www.sciencedirect.com

ScienceDirect

journal homepage: www.elsevier.com/locate/nanoenergy

RAPID COMMUNICATION

Hydrogen storage properties of nanoconfined $LiBH_4$-$Ca(BH_4)_2$

Payam Javadian[a,b], Drew A. Sheppard[b], Craig E. Buckley[b], Torben R. Jensen[a,*]

[a]*Center for Materials Crystallography, Interdisciplinary Nanoscience Center (iNANO), and Department of Chemistry, Aarhus University, DK-8000 Aarhus, Denmark*
[b]*Department of Imaging and Applied Physics, Curtin University, GPO Box U 1987, Perth, Western Australia 6845, Australia*

Received 9 July 2014; received in revised form 2 September 2014; accepted 29 September 2014
Available online 28 October 2014

KEYWORDS
Hydrogen storage;
Reversibility;
Nanoconfinement;
Carbon aerogel;
CO_2-activation

Abstract
The hydrogen storage properties of the eutectic melting metal borohydrides, $0.7LiBH_4$-$0.3Ca(BH_4)_2$, nanoconfined in two carbon aerogel scaffolds with different surface areas and pore volumes (pristine and CO_2-activated) are presented and compared to the bulk properties. The temperature of hydrogen release investigated by temperature programmed desorption mass spectroscopy is reduced by 83 °C for nanoconfined $LiBH_4$-$Ca(BH_4)_2$ in the pristine scaffold and by 95 °C in the CO_2-activated scaffold, compared to that of the bulk. This corresponds to apparent activation energies, E_A, of 204, 156 and 130 kJ/mol. Several cycles of reversible, continuous release and uptake of hydrogen is investigated by the Sieverts' method. Nanoconfined $LiBH_4$-$Ca(BH_4)_2$ in the CO_2-activated scaffolds demonstrate high degree of stability, releasing 80% and 73% of the original hydrogen content in the second and third hydrogen release cycle, respectively. However most importantly, this study shows that CO_2-activated carbon aerogel, CA-6, is more stabile against reaction with the metal hydride and a lower amount of borates and oxides are formed during melt infiltration and hydrogen release and uptake cycling. We conclude that the CO_2-activated scaffold is more inert, provides faster kinetics and higher stability over several cycles of hydrogen release and uptake and has the potential to provide useful hydrogen storage densities in the range ~12 wt% H_2.

*Correspondence to: iNANO and Department of Chemistry, Langelandsgade 140, DK-8000 Aarhus C, Aarhus University, Denmark. Tel.: +45 87155939, mobile: +45 2272 1486, fax: +45 8619 6199.
E-mail address: trj@chem.au.dk (T.R. Jensen).

http://dx.doi.org/10.1016/j.nanoen.2014.09.035
2211-2855/

Introduction

In today's society, there are increasing efforts to utilize renewable energy sources as a substitute for fossil fuels. Fossil fuel consumption may give climatic changes and cause health issues due to harmful emissions of particles, smoke and exhaust gasses. Hydrogen is considered a possible future energy carrier due to its high gravimetric energy content; three times higher than that for gasoline [1,2]. Unfortunately, hydrogen is a gas at ambient conditions so the current challenge is to store hydrogen in a safe, cheap and compact way, preferably in a light weight solid state material, *e.g.* MgH_2, $LiBH_4$, $Ca(BH_4)_2$ and $Mg(BH_4)_2$ [2-9]. These materials possess high gravimetric and volumetric hydrogen content, but suffer from slow kinetics and unfavorable thermodynamics that hampers the useable hydrogen storage capacity. One way to improve the hydrogen storage properties of metal hydrides is by confinement in a nanoporous scaffold, such as a carbon aerogel [7,10-12]. Nanoconfinement of metal hydrides allow formation of nanoparticles inside the pores of the scaffold, which are restricted in size and shape by the structural characteristics of the scaffold. Tuning the pore size, surface area and pore volume of the scaffold enables the design and synthesis of metal hydride particles with a desired morphology and properties [13,14]. Furthermore, nanoconfinement prevents particle growth and agglomeration during repeated hydrogen release and uptake cycles [15-17]. Obviously, the addition of the inert carbon scaffold is a weight penalty, which reduces the hydrogen storage capacity. However, post modification of the carbon scaffold *via* CO_2 activation provides increased surface area and pore volume while retaining an almost constant pore size [14,18-20].

Lithium and calcium borohydride, $LiBH_4$ and $Ca(BH_4)_2$, release up to 13.9 and 9.6 wt% H_2, respectively. Unfortunately, this occurs at the relatively high temperatures of 380 and >350 °C, respectively [21,22]. These two complex metal hydrides form a eutectic binary system with a melting point of ~200 °C at a molar composition of $0.7LiBH_4$-$0.3Ca(BH_4)_2$, which has a theoretical hydrogen content of 12.8 wt% H_2 [23-26]. In this study, $LiBH_4$-$Ca(BH_4)_2$ has been nanoconfined into two different carbon aerogel scaffolds with very different surface areas and pore volumes and the hydrogen storage properties are compared to those of the bulk composite.

Experimental details

Sample preparation

The resorcinol formaldehyde carbon aerogel was prepared by mixing 82.87 g resorcinol (Aldrich, 99%), 113.84 mL formaldehyde (37 wt% stabilized by ~10-15% methanol, Merck), 113.28 mL deionized water and 0.0674 g Na_2CO_3 (Aldrich, 99.999%) in a beaker with continuous stirring until complete dissolution was obtained. The pH of the final solution was measured to be 5.91. The preparation and characterization of the aerogel was performed according to previously published procedures [27-29]. Selected fractions of the prepared carbon aerogel (CA) were CO_2-activated in order to increase the surface area and pore volume [18,30]. Monoliths of CA were placed in an Al_2O_3 crucible, transferred to a tube furnace, and heated to 950 °C ($\Delta T/\Delta t$=6.67 °C/min) under continuous CO_2 flow (25 mL/min). The temperature was kept constant for 6 h, and afterwards the CO_2 flow and the furnace was turned off and allowed to cool naturally. Approximately 70% of the sample mass was removed after 6 h of activation and this sample is denoted CA-6 [18,28,30]. Prior to use, the scaffolds were all degassed at 400 °C in dynamic vacuum for several hours, in order to remove possible adsorbed air and water confined inside of the porous structure. All subsequent handling was performed in a glovebox with a purified argon atmosphere.

Calcium borohydride, $Ca(BH_4)_2$, was synthesized according to previously published methods using CaH_2 as starting reactant [31] and mixed with commercially available $LiBH_4$ (Aldrich, ≥95%) in the molar ratio $0.7LiBH_4$-$0.3Ca(BH_4)_2$ which is reported to show eutectic melting [23,24,26]. The borohydride mixture was ball milled using a tungsten carbide bowl (80 mL) and balls (∅: 10 mm), with a planetary Fritsch P4 mill and a powder to ball ratio of 1:24. The milling was performed at 250 rpm for 2 min with interruptions every 2 min to allow cooling of the milling vial. This was repeated 60 times *i.e.* a total milling time of 120 min, and this sample is denoted LiCa.

The amount of hydride was selected in order to obtain a degree of pore filling corresponding to ~60 vol%, calculated based on the total pore volume, V_{tot}, of the scaffold and the average bulk densities ρ(LiCa)=0.855 g/mL. Melt infiltration was performed in a custom made rig, by heating to T=210 °C ($\Delta T/\Delta t$=2 °C/min) with the temperature fixed at 190 °C for 30 min, reaching a hydrogen pressure in the range of 110-130 bar. Afterwards the sample was cooled naturally to RT.

Sample characterization

Synchrotron radiation powder X-ray diffraction (SR-PXD) data were collected at beamline I711 at MAX-lab, Lund, Sweden. The samples were mounted in a sapphire capillary tube (0.79 mm. I.D.), in an airtight sample holder inside an argon filled glovebox [32]. The sample holder was removed from the glovebox and attached to a gas control system at the synchrotron diffractometer. The data was collected using a CCD detector and a selected wavelength of λ=0.9941 Å.

A Perkin Elmer STA 6000 was utilized to conduct thermogravimetric analysis (TGA), differential scanning calorimetry (DSC) coupled with a Hiden Analytical quadrupole mass spectrometer (MS). Thus, temperature-programmed desorption mass spectroscopy (TPD-MS) data is provided. Data was collected with a constant flow (64 mL/min) of argon (99.99%). A powdered sample (<5 mg), was placed in an Al_2O_3 crucible with lid and heated in the temperature range of 30-500 °C ($\Delta T/\Delta t$=2 °C/min). The MS signals at m/e=2, 18 and 34 were recorded in order to detect H_2, H_2O and B_2H_6. Kissinger plots were obtained from the DSC data by heating selected samples at 3, 6 and 9 °C/min from which the temperature for maximum DSC signal of hydrogen desorption is utilized.

The reversible hydrogen storage capacity of nanoconfined and bulk $0.7LiBH_4$-$0.3Ca(BH_4)_2$ was studied during three hydrogen release and uptake cycles. The samples were sealed in an autoclave under argon and attached to the Sieverts' apparatus (PCTpro 2000). Hydrogen desorption data was collected in the temperature range of RT to 500 °C ($\Delta T/$

$\Delta t = 2\ ^\circ C/min$), and with the temperature kept constant at 500 °C for 10 h, at $p(H_2) = 1$ bar. Hydrogen absorption was performed in the pressure range of 140-150 bar, at a temperature of 400 °C ($\Delta T/\Delta t = 5\ ^\circ C/min$) during 10 h, and then the sample was cooled naturally to RT.

The Fourier transform infrared spectrometry (FTIR) analyses were carried out on a NICOLET 380 FT-IR from Thermo-Electronic Corporation with permanently aligned optics and proprietary diamond-turned pinned-in-place mirror optics. A small amount of sample was placed on the baseplate and subsequently the diamond pin was pressed on to the sample, forming a thin film. The samples were examined within the wave number range of 4000-400 cm^{-1}. The samples were shortly exposed to air when they were mounted.

Results and discussion

Characterization of mesoporous carbon aerogel scaffold

Mesoporous carbon aerogel (CA) used in this study has a pore size distribution centered at $D_{max} = 30$ nm, a surface area and pore volume of $S_{BET} = 689\ m^2/g$ and $V_{tot} = 1.21$ mL/g, respectively. CO_2-activation of the CA for six hours (CA-6) significantly increases the surface area and pore volume of 2660 m^2/g and 3.13 mL/g, while still maintaining the nanoscale pore size, see Table 1. Structure alterations obtained by CO_2-activation are assigned to an increased formation of graphite/graphene like carbon material [13,30]. The eutectic composite of $0.7LiBH_4$-$0.3Ca(BH_4)_2$ is infiltrated in CA and CA-6, and the amount of hydride added is 38.4 and 64.9 wt%, respectively corresponding to 60 vol% pore filling.

In situ X-ray diffraction study of nanoconfined $0.7LiBH_4$-$0.3Ca(BH_4)_2$

Melt infiltration of bulk $0.7LiBH_4$-$0.3Ca(BH_4)_2$ in carbon aerogel (CA) has been followed by *in situ* synchrotron radiation powder X-ray diffraction, SR-PXD, in the temperature range of RT to 210 °C at a hydrogen pressure of $p(H_2) = 120$ bar (Figure 1A). At RT the initial Bragg peaks of *o*-$LiBH_4$, α- and γ-$Ca(BH_4)_2$ are present. Upon heating the polymorphic transformation to *h*-$LiBH_4$ is observed at $T = 110$ °C, and at $T = 125$ °C, α-$Ca(BH_4)_2$ and γ-$Ca(BH_4)_2$ transform to β-$Ca(BH_4)_2$ in agreement with previous reports [24]. Direct evidence of eutectic melting of $0.7LiBH_4$-$0.3Ca(BH_4)_2$ is displayed at $T \sim 200$ °C, as diffraction patterns of β-$Ca(BH_4)_2$ and *h*-$LiBH_4$ disappears. Formation of

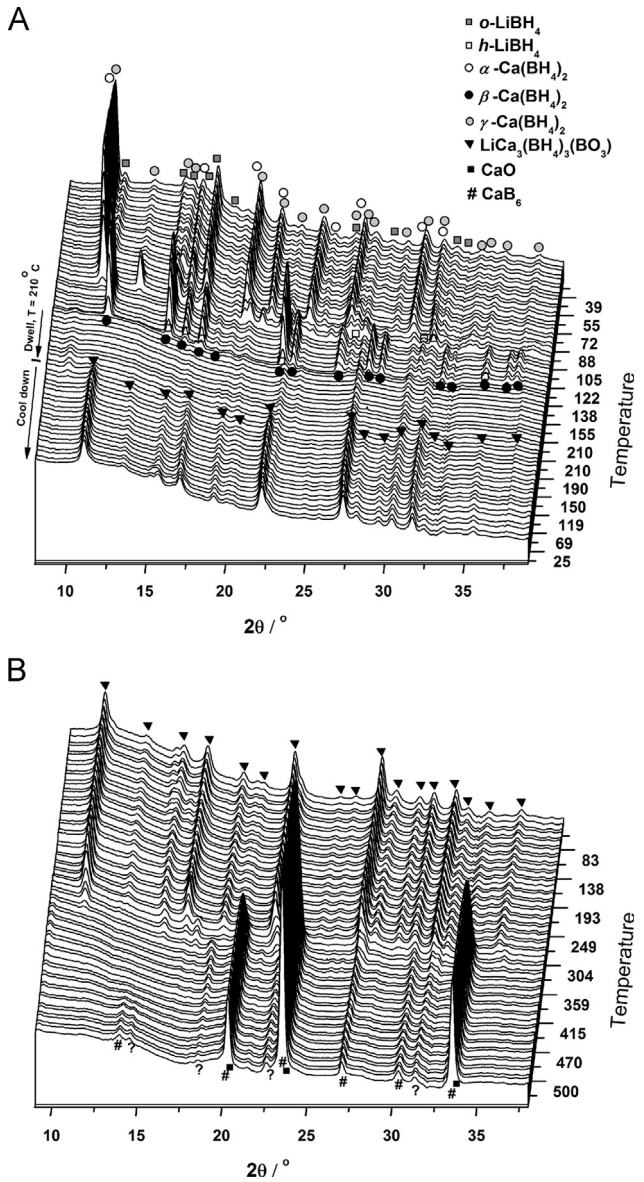

Figure 1 *In situ* synchrotron radiation powder X-ray diffraction (SR-PXD) data of $0.7LiBH_4$-$0.3Ca(BH_4)_2$ mixed with CA. (A) The sample was heated from RT to 210 °C ($\Delta T/\Delta t = 3\ ^\circ C/min$) at $p(H_2) = 120$ bar, with the temperature held constant at 210 °C, for 15 min. (B) In continuation of the experiment in panel A (using the same sample) the dehydrogenation is measured at RT to 500 °C ($\Delta T/\Delta t = 10\ ^\circ C/min$) at $p(H_2) = 5$ bar ($\lambda = 0.99149$ Å, time propagates from top to bottom).

Table 1 Structure parameters; specific surface area (S_{BET}), micro-, meso- and total pore volumes (V_{micro}, V_{meso}, V_{tot}) and the maximum pore size distribution value (D_{max}) of the pristine carbon aerogel scaffold (CA) and CO_2-activated scaffold (CA-6). The volumetric and gravimetric content of $0.7LiBH_4$-$0.3Ca(BH_4)_2$ (LiCa) in the samples are also provided, calculated according to the theoretical hydrogen capacity of the bulk $\rho_m(LiCa) = 12.54$ wt% H_2.

Sample	S_{BET} (m^2/g)	V_{micro} (mL/g)	V_{meso} (mL/g)	V_{tot} (mL/g)	D_{max} (nm)	LiCa (wt%)	LiCa [a](vol%)	ρ_m(LiCa) wt% H_2
CA	689 ± 26	0.21 ± 0.02	1.06 ± 0.10	1.21 ± 0.10	30 ± 1	38.4	60.2	4.8
CA-6	2660 ± 208	0.85 ± 0.04	2.08 ± 0.34	3.13 ± 0.59	30 ± 1	64.9	60.0	8.1

[a]Calculated using V_{tot} and the bulk density of $0.7LiBH_4$-$0.3Ca(BH_4)_2$.

the borate $LiCa_3(BH_4)(BO_3)_2$ [23,33] is observed, starting at $T=210$ °C, possibly due to oxidation of the metal borohydride by oxygen remaining in the carbon aerogel. $LiCa_3(BH_4)(BO_3)_2$ has previously been observed during heating of $LiBH_4$-$Ca(BH_4)_2$-carbon composite [23]. Furthermore, an unidentified intense peak at $2\theta=12°$ and $T\sim110$ °C is observed.

As the sample is cooled to RT, no diffraction peaks from $LiBH_4$ and $Ca(BH_4)_2$ are observed. However, it is assumed that the respective hydrides solidify as X-ray amorphous material inside the scaffolds. There is no size induced peak broadening of $LiCa_3(BH_4)(BO_3)_2$ from 210 °C to resolidification at RT, which indicates that the compound is formed due to the carbon surface and is possibly residing on the outer surface of the scaffold during melt infiltration.

In order to determine any crystalline decomposition product formed, the dehydrogenation of nanoconfined 0.7$LiBH_4$-0.3Ca$(BH_4)_2$ measured at $p(H_2)\sim5$ bar is investigated by *in situ* SR-PXD as shown in Figure 1B. Since $LiBH_4$ and $Ca(BH_4)_2$ are X-ray amorphous after melt infiltration, the *o*- to *h*-$LiBH_4$ and α- and γ- to β-$Ca(BH_4)_2$ polymorphic transitions are not observed during heating. $LiCa_3(BH_4)(BO_3)_2$ forms during melt infiltration, and have diffraction peaks in the temperature range from RT to above ~280 °C where it starts to partially decompose to CaB_6, CaO and an unknown compound, which is possibly attributed to hydrogen release. According to Ref. [24] the decomposition and rehydrogenation reaction of the system is described by

$$4LiBH_4+Ca(BH_4)_2\leftrightarrow4LiH+CaB_6+10H_2$$

which to some extent agrees well with the data shown.

Hydrogen desorption kinetics

Thermogravimetric analysis, TGA, and temperature programmed desorption mass spectroscopy, TPD-MS, data of selected samples are displayed in Figure 2. Bulk 0.7$LiBH_4$-0.3$Ca(BH_4)_2$ (LiCa) has a mass loss of 12.08 wt% in the temperature range of 40-500 °C, which corresponds to 96% of the calculated hydrogen content, ρ_m(LiCa)=12.54 wt% H_2. LiCa infiltrated in CA and CA-6 loses 3.36 and 7.71 wt% in the same temperature range, which corresponds to 70 and 95% of the hydrogen content of the samples, respectively (see Table 1). The high surface area scaffold (CA-6) successfully infiltrates the highest amount of LiCa during melt infiltration, in accordance with previous studies [13]. Noteworthy, the lower mass loss from LiCa infiltrated in CA may be due to partial decomposition during the infiltration process and/or a reaction with the non-activated scaffold. In the TGA data, temperature regime 1 (200-270 °C) and 2 (270-300 °C) are introduced to compare the mass loss of the two different nanoconfined samples. In region 1, sample CA releases 1 wt% H_2 and CA-6 releases >2 wt% H_2 from 200 to 270 °C. During temperature region 2 (from 270 to 331 °C), both samples release 3 times more hydrogen than in region 1 *i.e.* CA releases ~3 wt% H_2, and CA-6 releases 6.8 wt% H_2. The increase in the TGA curves at low temperatures is assigned to an artifact, possibly buoyancy.

TPD-MS data reveals that a minor hydrogen release occurs at 200 °C (onset peak **A**) from LiCa, possibly due to the eutectic melting of $LiBH_4$-$Ca(BH_4)_2$, which is in agreement with previous results [23,24]. The desorption event A is not observed for nanoconfined LiCa or may be associated with

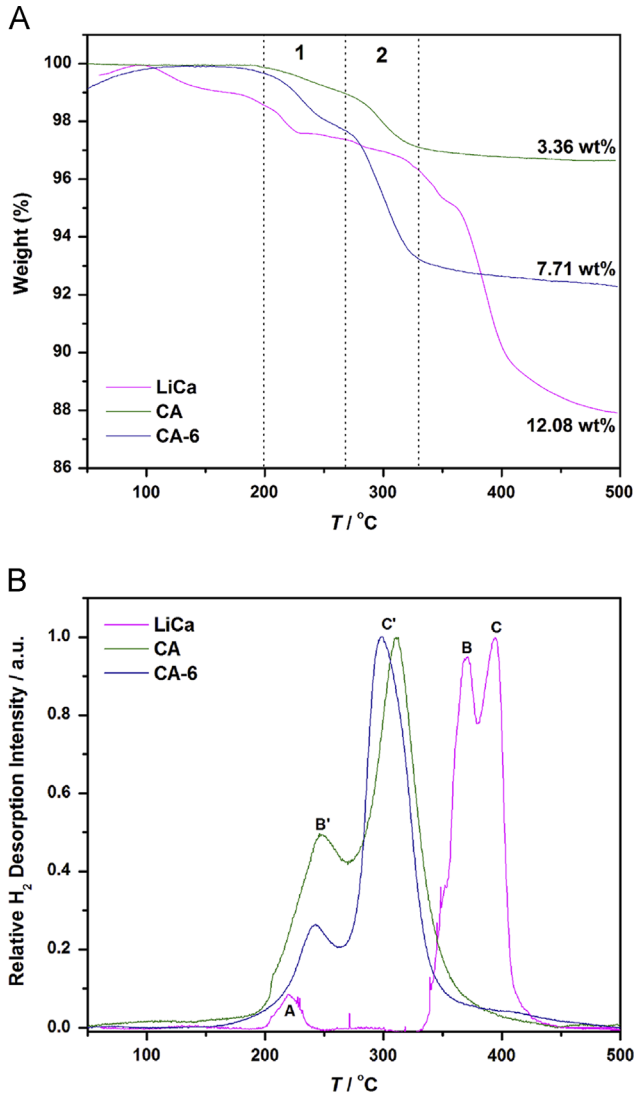

Figure 2 Thermogravimetric analysis (top) and simultaneous normalized temperature programmed desorption mass spectroscopy (bottom) displaying the hydrogen release rate during heating from 50 to 500 °C ($\Delta T/\Delta t=2$ °C/min). Mass spectroscopy detected the H_2^+ ions ($m/e=2$). Bulk 0.7$LiBH_4$-0.3Ca$(BH_4)_2$ (pink) and melt infiltrated LiCa into CA (green), and CA-6 (blue). Non-normalized data is included in Supporting information. (For interpretation of the references to color in this figure legend, the reader is referred to the web version of this article.)

the first heating of the sample only. However, the major hydrogen desorption of bulk LiCa has an onset at 335 °C, and is characterized by two distinct peak temperatures of 370 and 393 °C (denoted **B** and **C**, respectively).

Clearly, melt infiltration of LiCa into CA and CA-6 facilitates hydrogen release at lower temperatures, compared to that of bulk LiCa. The temperature for maximum hydrogen release rate (peak **C'**) is shifted significantly towards lower temperatures due to nanoconfinement, occurring at 310 and 298 °C for CA and CA-6 *i.e.* $\Delta T=-83$ and -95 °C, respectively. A similar decrease in the hydrogen desorption temperature is observed for event **B** at 246 and 243 °C *i.e.*

$\Delta T = -124$ and -127 °C for CA and CA-6, respectively. Thus, there is only a small kinetic improvement of hydrogen release of LiCa infiltrated in the CO_2 activated scaffold, CA-6 as compared to the non-activated scaffold. The TPD peaks **B** and **C** seem to relate to the decomposition of the $LiBH_4$ and $Ca(BH_4)_2$, respectively. However, it is not clear from the data collected which peak corresponds to which borohydride. The temperature difference between **B'** and **C'** compared to **B** and **C** may be due to the difference in the interaction between the carbon scaffold and the respective borohydrides, *i.e.* a possible catalytic effect [36].

The kinetics for hydrogen release was further analyzed by differential scanning calorimetry and the Kissinger approach, see Figure 3. A significant decrease in apparent activation energy, E_A, for hydrogen release of nanoconfined LiCa compared to bulk LiCa is observed. The apparent activation energies (E_A) of hydrogen desorption of bulk and nanoconfined LiCa, in CA and CA-6 and are estimated to be 204, 156 and 130 kJ/mol, respectively (see Figure 3). Thus, CO_2-activation clearly reduces the activation energy further. Nanoconfinement and different carbon materials have previously shown to have a significant improvement of kinetics and a reduction of the apparent activation energy [17,36].

Cyclic stability during hydrogen release and uptake

The cyclic stability during continuous hydrogen release and uptake of the three samples, *i.e.* bulk $0.7LiBH_4$-$0.3Ca(BH_4)_2$ (LiCa) and nanoconfined LiCa in CA and in CA-6, has been studied using Sieverts' measurements. The bulk and nanoconfined samples have been rehydrogenated at $p(H_2) = 140$ bar after each desorption, and the dehydrogenations are conducted against an initial H_2 back pressure of 1 bar, see Figure 4. The amount of released hydrogen is given relative to the amount of added hydride in the sample for better comparison. Bulk LiCa releases 10.92, 8.72 and 7.95 wt% H_2/LiCa during first, second and third desorption, corresponding to 80 and 73% of the initial hydrogen storage capacity during the second and third desorption. It is worth noting that the initial hydrogen desorption only releases 90% of what is released according to the mass loss measured by TGA (12.08 wt% H_2). This may be due to the difference in measurement conditions as under an argon flow, the CA and CA-6 samples are still evolving small amounts of hydrogen at 400 °C. Hence a H_2 back pressure of 1 bar would be sufficient to inhibit the reaction associated with this H_2 release at 400 °C. The decomposition product consists of CaO, CaB_6 and possibly LiH which is assumed to form $LiBH_4$, during rehydrogenation [24].

LiCa melt infiltrated into scaffold CA, releases 6.23 wt% H_2/LiCa (relative to added amount of LiCa) during the first desorption and 3.57 and 3.18 wt% H_2/LiCa during the second and third desorption, which is equivalent to 2.4, 1.4 and 1.2 wt% H_2 relative to the mass of the sample. This corresponds to 57.3 and 51.0% of the initially available hydrogen content being retained during the second and third desorption, respectively.

Melt infiltration of LiCa into the CO_2-activated scaffold CA-6, significantly improves the hydrogen storage capacity,

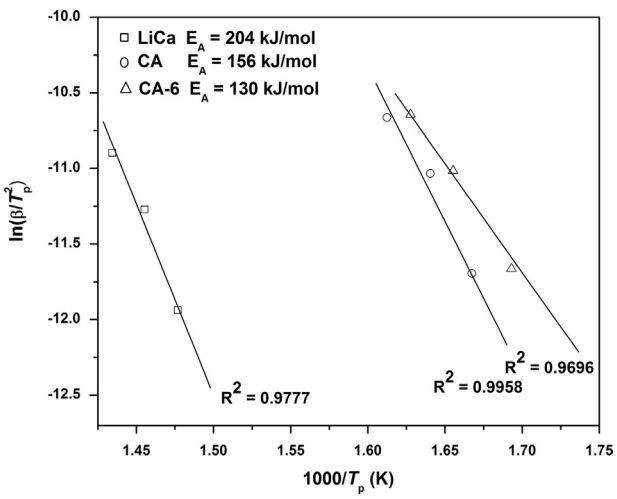

Figure 3 Kissinger plot obtained of DSC data at heating rates of 3, 6 and 9 °C/min for bulk $0.7LiBH_4$-$0.3Ca(BH_4)_2$ (LiCa) and LiCa nanoconfined in CA and CA-6.

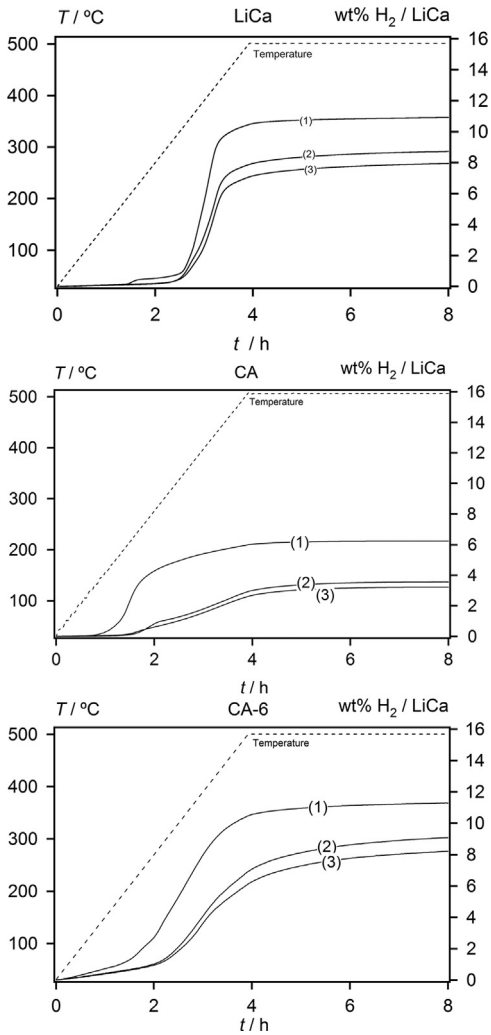

Figure 4 Sieverts' measurement showing hydrogen desorption cycles 1–3 for bulk $0.7LiBH_4$-$0.3Ca(BH_4)_2$ LiCa (top), infiltrated into CA (middle) and CA-6 (bottom). Hydrogen desorption was performed during heating to 500 °C ($\Delta T/\Delta t = 2$ °C) and for 4 h at a fixed temperature of 500 °C. Hydrogen absorption was performed at 400 °C and $p(H_2) = 140$ bar during 10 h.

compared to that obtained using CA. The hydrogen release of CA-6 is 11.3, 9.08 and 8.21 wt% H_2/LiCa during the first, second, and third desorption, corresponding to 7.34, 5.90 and 5.33 wt% H_2/sample, respectively, and a decreases in capacity of 80 and 73% for the second and third cycle. Thus, the decrease in hydrogen storage capacity on cycling for bulk LiCa and CA-6 are identical and significantly smaller than for LiCa infiltrated in CA. In this investigation, only 60% of the available pore volume was filled with hydrogen storage material, LiCa. Assuming 100% filling of the pore volume corresponds to a potential maximum hydrogen storage capacity of 12.0 wt% H_2. Thus, the higher surface area and more inert CO_2 activated scaffolds have the potential for future applications, and may be further optimized by catalytic nanoparticle functionalisation [13].

$LiBH_4$-$Ca(BH_4)_2$ nanoconfined in CA show hydrogen release at lower temperatures as compared to CA-6 during the first cycle, which may be assigned to a reaction with the scaffold. This is in agreement with the PXD investigations, which indicate formation of smaller amounts of the bi-metallic borate $LiCa_3(BH_4)(BO_3)_2$ for the CO_2-activated scaffold. Furthermore, powder X-ray diffraction of the desorbed nanoconfined samples show the formation of CaB_6, CaO and possibly an unknown compound, see Figure 1. This may suggest that the decrease in hydrogen storage capacity can be assigned to irreversible formation of $LiCa_3(BH_4)(BO_3)_2$ during melt infiltration and formation of increasing amounts of CaO during hydrogen release at elevated temperature.

Infrared spectroscopy (FTIR) data of bulk $LiBH_4$ and $Ca(BH_4)_2$ (see Figure 5) both demonstrate three characteristic B-H stretching modes, in the range of 2000-2500 cm^{-1}, as well as B-H bending bands at 1093, 1240 and 1294 cm^{-1} in $LiBH_4$ and two signals at 1130 and 1261 cm^{-1} for that of $Ca(BH_4)_2$, in accord with reference spectra [34,35]. The bulk eutectic $LiBH_4$-$Ca(BH_4)_2$ mixture evidently exhibits a combination of the previously mentioned B-H bending and stretching bands (green spectra), however after nanoconfinement, these signals are significantly reduced due to the presence of the carbon scaffold (blue spectra). Rehydrogenation of the decomposed sample, CA, at 400 °C for 10 h at a hydrogen pressure of 140 bar (pink spectra) has low intensity B-H stretching in the wave number range 2000-2500 cm^{-1} possibly originating from $LiBH_4$-$Ca(BH_4)_2$ B-H stretching. This suggests that the reversible source displayed in Figure 5, could be amorphous $LiBH_4$ and $Ca(BH_4)_2$, which are difficult to distinguish with FTIR. The FTIR spectrum for CA-6 is nearly identical to that of CA and has been included in the Supporting Information for completeness. The FTIR on CA and CA-6 suggests that some borohydride is formed on rehydriding but that strong signals at ~787 cm^{-1} and ~1352 cm^{-1} are associated with an unknown phase. The ex-situ XRD on CA-6 also reveals diffraction peaks associated with an unknown phase upon re-hydriding and it is likely that it is this phase that is responsible for the signals seen in the FTIR data.

Conclusion

The eutectic melting binary borohydride $LiBH_4$-$Ca(BH_4)_2$ (LiCa) is successfully melt infiltrated into a carbon aerogel scaffold (CA) and a CO_2 activated scaffold (CA-6) with different surface areas of 689 and 2660 m^2/g, respectively. Nanoconfinement significantly improves the kinetics for hydrogen release observed as a reduction of the temperature for maximum hydrogen release rate as compared to the bulk. There is also a small kinetic improvement of hydrogen release using the CO_2 activated scaffold, CA-6 as compared to the non-activated scaffold. This is also illustrated by the apparent activation energies (E_A) of hydrogen desorption of bulk and nanoconfined LiCa, in CA and CA-6 estimated to be 204, 156 and 130 kJ/mol, respectively. The CO_2 activated carbon aerogel has a number of advantages over as-synthesized carbon aerogel for borohydride loading: the activation possibly remove oxygen impurities from the carbon aerogel and increases pore volume. This results in decreased borate and oxide formation due to the reaction between the scaffold and borohydrides; higher borohydride loading levels; improved total and reversible H_2 capacity and; improved hydrogen desorption kinetics. This work reveal that high surface area and more inert CO_2 activated scaffolds have the potential for future applications, *e.g.* within hydrogen storage, and may also be functionalized with catalytic nanoparticles.

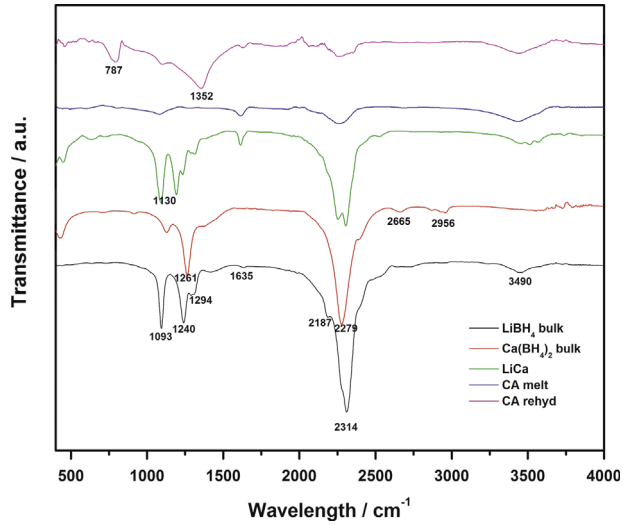

Figure 5 FTIR spectra of $LiBH_4$ (black), $Ca(BH_4)_2$ (red), mixed $LiBH_4$-$Ca(BH_4)_2$ (LiCa: green), LiCa melt infiltrated in CA (blue) and of nanoconfined LiCa rehydrogenated after 3 times (pink). The intensity of the pink curve has been upscaled relative to the amount of active hydride for better comparison. (For interpretation of the references to color in this figure legend, the reader is referred to the web version of this article.)

Acknowledgment

MAXIV laboratories and beamline I711 staff, Lund, Sweden are thanked for the allocated beam time. This work was supported by the Danish Council for Strategic Research via the research project HyFillFast, the Danish National Research Foundation, Center for Materials Crystallography (DNRF93) and by the Danish Research Council for Nature and Universe (Danscatt). We are grateful to the Carlsberg Foundation.

Appendix A. Supporting information

Supplementary data associated with this article can be found in the online version at http://dx.doi.org/10.1016/j.nanoen.2014.09.035.

References

[1] L. Schlapbach, A. Züttel, Nature 414 (2001) 353–358.
[2] M.B. Ley, L.H. Jepsen, Y.S. Lee, Y.W. Cho, J.M.B. von Colbe, M. Dornheim, M. Rokni, J.O. Jensen, M. Sloth, Y. Filinchuk, J.E. Jorgensen, F. Besenbacher, T.R. Jensen, Mater. Today 17 (2014) 122–128.
[3] S.I. Orimo, Y. Nakamori, J.R. Eliseo, A. Züttel, C.M. Jensen, Chem. Rev. 107 (2007) 4111–4132.
[4] R.A. Varin, L. Zbroniec, M. Polanski, J. Bystrzycki, Energies 4 (2011) 1–25.
[5] L.H. Rude, T.K. Nielsen, D.B. Ravnsbaek, U. Bosenberg, M.B. Ley, B. Richter, L.M. Arnbjerg, M. Dornheim, Y. Filinchuk, F. Besenbacher, T.R. Jensen, Phys. Status Solidi A 208 (2011) 1754–1773.
[6] P. Javadian, T.R. Jensen, Int. J. Hydrogen Energy 39 (2014) 9871–9876.
[7] M. Fichtner, Adv. Eng. Mater. 7 (2005) 443–455.
[8] R. Gosalawit-Utke, C. Milanese, P. Javadian, J. Jepsen, D. Laipple, F. Karmi, J. Puszkiel, T.R. Jensen, A. Marini, T. Klassen, M. Dornheim, Int. J. Hydrogen Energy 38 (2013) 3275–3282.
[9] R. Gosalawit-Utke, C. Milanese, P. Javadian, A. Girella, D. Laipple, J. Puszkiel, A.S. Cattaneo, C. Ferrara, J. Wittayakhun, J. Skibsted, T.R. Jensen, A. Marini, T. Klassen, M. Dornheim, J. Alloy. Compd. 599 (2014) 78–86.
[10] T.K. Nielsen, F. Besenbacher, T.R. Jensen, Nanoscale 3 (2011) 2086–2098.
[11] P.E. de Jongh, P. Adelhelm, ChemSusChem 3 (2010) 1332–1348.
[12] J.J. Vajo, Curr. Opin. Solid State Mater. 15 (2011) 52–61.
[13] T.K. Nielsen, P. Javadian, M. Polanski, F. Besenbacher, J. Bystrzycki, J. Skibsted, T.R. Jensen, Nanoscale 6 (2014) 599–607.
[14] T.K. Nielsen, P. Javadian, M. Polanski, F. Besenbacher, J. Bystrzycki, T.R. Jensen, J. Phys. Chem. C 116 (2012) 21046–21051.
[15] R.D. Stephens, A.F. Gross, S.L. Van Atta, J.J. Vajo, F.E. Pinkerton, Nanotechnology 20 (2009) 204018.
[16] M.H.W. Verkuijlen, J. Gao, P. Adelhelm, P.J.M. van Bentum, P.E. de Jongh, A.P.M. Kentgens, J. Phys. Chem. C 114 (2010) 4683–4692.
[17] A.F. Gross, J.J. Vajo, S.L. Van Atta, G.L. Olson, J. Phys. Chem. C 112 (2008) 5651–5657.
[18] C. Lin, J.A. Ritter, Carbon 38 (2000) 849–861.
[19] R.W. Pekala, J.C. Farmer, C.T. Alviso, T.D. Tran, S.T. Mayer, J.M. Miller, B. Dunn, J. Non-Cryst. Solids 225 (1998) 74–80.
[20] B. Fang, Y.Z. Wei, K. Maruyama, M. Kumagai, J. Appl. Electrochem. 35 (2005) 229–233.
[21] J.H. Kim, S.A. Jin, J.H. Shim, Y.W. Cho, J. Alloy. Compd. 461 (2008) L20–L22.
[22] A. Zuttel, P. Wenger, S. Rentsch, P. Sudan, P. Mauron, C. Emmenegger, J. Power Sources 118 (2003) 1–7.
[23] H.S. Lee, Y.S. Lee, J.Y. Suh, M. Kim, J.S. Yu, Y.W. Cho, J. Phys. Chem. C 115 (2011) 20027–20035.
[24] J.Y. Lee, D. Ravnsbaek, Y.S. Lee, Y. Kim, Y. Cerenius, J.H. Shim, T.R. Jensen, N.H. Hur, Y.W. Cho, J. Phys. Chem. C 113 (2009) 15080–15086.
[25] G. Capurso, F. Agresti, L. Crociani, G. Rossetto, B. Schiavo, A. Maddalena, S. Lo Russo, G. Principi, Int. J. Hydrogen Energy 37 (2012) 10768–10773.
[26] M. Paskevicius, M.B. Ley, D.A. Sheppard, T.R. Jensen, Craig E. Buckley, Phys. Chem. Chem. Phys. 15 (2013) 19774–19789.
[27] T.K. Nielsen, K. Manickam, M. Hirscher, F. Besenbacher, T.R. Jensen, ACS Nano 3 (2009) 3521–3528.
[28] S.A. Al-Muhtaseb, J.A. Ritter, Adv. Mater. 15 (2003) 101–114.
[29] T.K. Nielsen, M. Polanski, D. Zasada, P. Javadian, F. Besenbacher, J. Bystrzycki, J. Skibsted, T.R. Jensen, ACS Nano 5 (2011) 4056–4064.
[30] T.F. Baumann, M.A. Worsley, T.Y.J. Han, J.H. Satcher, J. Non-Cryst. Solids 354 (2008) 3513–3515.
[31] M.D. Riktor, M.H. Sorby, K. Chlopek, M. Fichtner, F. Buchter, A. Zuettel, B.C. Hauback, J. Mater. Chem. 17 (2007) 4939–4942.
[32] T.R. Jensen, T.K. Nielsen, Y. Filinchuk, J.E. Jorgensen, Y. Cerenius, E.M. Gray, C.J. Webb, J. Appl. Crystallogr. 43 (2010) 1456–1463.
[33] Y.S. Lee, Y. Filinchuk, H.S. Lee, J.Y. Suh, J.W. Kim, J.S. Yu, Y.W. Cho, J. Phys. Chem. C 115 (2011) 10298–10304.
[34] M. Fichtner, K. Chlopek, M. Longhini, H. Hagemann, J. Phys. Chem. C 112 (2008) 11575–11579.
[35] V. D'Anna, A. Spyratou, M. Sharma, H. Hagemann, Spectrochim. Acta A 128 (2014) 902–906.
[36] P.A. Ward, J.A. Teprovich, B. Peters, J. Wheeler, R.N. Compton, R. Zidan, J. Phys. Chem. C 117 (2013) 22569.

Payam Javadian received his BSc and Cand. Polyt. in Chemical Engineering from Aarhus University, Denmark in 2010 and 2012. He has joined the research group of Prof. Torben R. Jensen for many years, exploring effects of nanoconfinement on complex metal hydrides for hydrogen storage. In 2014, he was awarded a Curtin International Postgraduate Research Scholarship (CIPRS) at Curtin University, and is currently working as a PhD student in the group of Prof. Craig Buckley at Curtin University of Technology in Perth, Australia. His current research program focuses on metal hydrides as energy storage for concentrated solar thermal applications.

Drew A. Sheppard received the Ph.D. degree in 2009. He was a founding member of the Hydrogen Storage Research Group, Curtin University, Bentley, W.A., Australia, and in 2011 was awarded an Australian Post-Doctoral Industry Fellowship (APDI). His main expertise is in the synthesis and thermodynamic characterisation of metal hydrides with his research focus on unconventional hydrogen storage materials that have the potential to translate to practical applications that can reduce society's carbon footprint.

Professor **Craig Buckley** is Dean of Research in The Faculty of Science and Engineering, Professor of Physics, Head of the Hydrogen Storage Research Group and Deputy Director of the Fuels & Energy Technology Institute at Curtin University, Australia. Since being awarded his Ph.D. in 1994 from Griffith University he has held various research positions in the U.K, USA and Australia prior to being awarded tenure at Curtin University. His research is focussed on hydrogen storage materials and the investigation of the structural properties of a wide range of materials. Craig has published over 100 scientific papers in peer reviewed journals.

Torben R. Jensen received his PhD degree from Odense University, SDU, 1999, and became an Associate Professor (2002) at the Interdisciplinary Nanoscience Center (iNANO) and Department of Chemistry, Aarhus University. He was awarded a Steno research stipend (2002), a Carlsberg research stipend (2005) from the Carlsberg Foundation and the Doctor of science degree (dr. scient.) in 2014, by the Faculty of Science and Technology, Aarhus University. His research interests are focused on synthesis, structural, physical and chemical properties of inorganic materials and utilisation of synchrotron X-ray radiation for materials characterization, which is the topic for his 180 scientific publications.

3.5. Reversibility of $LiBH_4$ facilitated by the $LiBH_4$-$Ca(BH_4)_2$ eutectic

The demonstration of full reversibility of $LiBH_4$ opens new intriguing possible utilization of $LiBH_4$ as a high performance H_2 storage material and a heat storage material. The thermodynamics of H_2 release from molten $LiBH_4$ has a unique advantage as a heat storage candidate. i.e. the reaction entropy associated with H_2 release from molten $LiBH_4$ is substantially lower than for H_2 release from solid-state hydrides. The consequence of this is that, for molten $LiBH_4$, the H_2 equilibrium pressure increases more slowly with temperature than for solid-state hydrides.

THE JOURNAL OF PHYSICAL CHEMISTRY C

Article

pubs.acs.org/JPCC

Reversibility of $LiBH_4$ Facilitated by the $LiBH_4$–$Ca(BH_4)_2$ Eutectic

Payam Javadian,[†,‡] SeyedHosein Payandeh GharibDoust,[†] Hai-Wen Li,[†,§] Drew A. Sheppard,[‡] Craig E. Buckley,[‡] and Torben R. Jensen*,[†]

[†]Center for Materials Crystallography, Interdisciplinary Nanoscience Center (iNANO), and Department of Chemistry, Aarhus University, DK-8000 Aarhus, Denmark

[‡]Department of Physics and Astronomy, Curtin University, GPO Box U 1987, Perth, Western Australia 6845, Australia

[§]International Research Center for Hydrogen Energy, and International Institute for Carbon-Neutral Energy Research (WPI-I2CNER), Kyshu University, Fukuoka 819-0395, Japan

Supporting Information

ABSTRACT: The hydrogen storage properties of eutectic melting $0.68LiBH_4$–$0.32Ca(BH_4)_2$ (LiCa) as bulk and nanoconfined into a high surface area, $S_{BET} = 2421 \pm 189$ m^2/g, carbon aerogel scaffold, with an average pore size of 13 nm and pore volume of $V_{tot} = 2.46 \pm 0.46$ mL/g, is investigated. Hydrogen desorption and absorption data were collected in the temperature range of RT to 500 °C ($\Delta T/\Delta t = 5$ °C/min) with the temperature then kept constant at 500 °C for 10 h at hydrogen pressures in the range of 1–8 and 134–144 bar, respectively. The difference in the maximum H_2 release rate temperature, T_{max}, between bulk and nanoconfined LiCa during the second cycle is $\Delta T_{max} \approx 40$ °C, which over five cycles becomes smaller, $\Delta T_{max} \approx 10$ °C. The high temperature, $T_{max} \approx 455$ °C, explains the need for high temperatures for rehydrogenation in order to obtain sufficiently fast reaction kinetics. This work also reveals that nanoconfinement has little effect on the later cycles and that nanoconfinement of pure $LiBH_4$ has a strong effect in only the first cycle of H_2 release. The hydrogen storage capacity is stable for bulk and nanoconfined LiCa in the second to the fifth cycle, which contrasts to nanoconfined $LiBH_4$ where the H_2 storage capacity continuously decreases. Bulk and nanoconfined LiCa have hydrogen storage capacities of 5.4 and 3.7 wt % H_2 in the fifth H_2 release, which compare well with the calculated hydrogen contents of $LiBH_4$ only and in LiCa, which are 5.43 and 3.69 wt % H_2, respectively. Thus, decomposition products of $Ca(BH_4)_2$ appear to facilitate the full reversibility of the $LiBH_4$, and this approach may lead to new hydrogen storage systems with stable energy storage capacity over multiple cycles of hydrogen release and uptake.

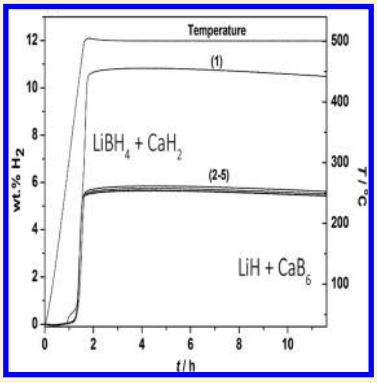

INTRODUCTION

Binary metal borohydride systems, such as $LiBH_4$–$Mg(BH_4)_2$, $LiBH_4$–$Ca(BH_4)_2$, $LiBH_4$–$NaBH_4$, and $LiBH_4$–KBH_4, are considered interesting hydrogen storage materials due to their relatively high gravimetric hydrogen content, sometimes >10 wt %.[1–5] However, due to their thermal stability, the release of hydrogen occurs at temperatures significantly higher than 300 °C, and full hydrogen uptake is not observed, even at temperatures of 500–600 °C. The poor reversibility may be due to unwanted side reactions such as formation of stable *closo*-boranes.[5,6] Lithium borohydride has a tendency to form $Li_2B_{12}H_{12}$ when hydrogen release occurs at low hydrogen pressure (e.g., $p(H_2) < 0.15$ bar and $T \approx 400$ °C), and $Li_2B_{12}H_{12}$ can only react with hydrogen at more aggressive conditions (e.g., $p(H_2) \approx 1000$ bar and $T \approx 500$ °C).[7] These effects often lead to degradation of the hydrogen storage system and loss of storage capacity, which hampers their potential in practical applications. Nanoconfinement of metal borohydrides in an inert nanoporous scaffold, such as activated carbon, carbon aerogel (CA), or porous silica, has been investigated as a technique to improve the hydrogen absorption properties, prevent particle growth and agglomeration during cycling, limit the mobility of the decomposition product, and keep particles in intimate contact.[7,8] There is often a strong surface effect from interaction between the hydrides and the scaffold that gives enhanced kinetics for hydrogen release.[9,10]

Multiple binary metal borohydride systems based on $LiBH_4$ and various other hydrides such as $NaBH_4$,[11] KBH_4,[12] $Mg(BH_4)_2$,[13–16] $Ca(BH_4)_2$,[4,17–21] $LiAlH_4$,[22] and $NaAlH_4$,[23] have been nanoconfined and reported in the literature. The combination of two relatively stable metal borohydrides may facilitate mutual decomposition and eutectic melting properties.[12,24] Most of these nanoconfined metal borohydride systems display improved hydrogen release kinetics and increasing stability of hydrogen storage capacity over several cycles. Eutectic melting bimetallic borohydrides are suitable for melt infiltration into porous scaffolds such as CAs. The stability of the hydrogen storage capacity over multiple cycles of hydrogen release and uptake is a crucial property to assess prior considerations for practical energy storage applications.

Received: June 26, 2017
Revised: July 31, 2017
Published: August 1, 2017

DOI: 10.1021/acs.jpcc.7b06228
J. Phys. Chem. C 2017, 121, 18439–18449

The Journal of Physical Chemistry C Article

Numerous publications describe metal borohydride-based systems, which reveal initial improvements in hydrogen release properties. However, very few papers discuss the storage stability over multiple cycles of hydrogen absorption/desorption.

The $LiBH_4$–MgH_2 system has reversible capacities of ~9.1 wt % after 20 cycles, corresponding to 79% of the available 11.54 wt % theoretical value.[25] This capacity retention is similar to a number of well-studied hydrides with lower capacities such as Mg_2NiH_4 (82.0%), MgH_2–Ni (80.2%), and Mg_2FeH_6 (91.4%).[26] The consequence of destabilization of $LiBH_4$ facilitates change in the H_2 equilibrium pressure, which would be an advantage or drawback depending on the application.

In most published work, on borohydride systems a maximum of three absorption/desorption cycles are reported and usually with decreasing hydrogen storage capacity between cycles. Here we show that the first three hydrogen releases may be different, but the third may be similar to the following cycles. Therefore, investigation of more than three cycles of hydrogen release and uptake may be important in order to evaluate the stability of the hydrogen storage capacity during cycling. Nanoconfined $LiBH_4$ in zeolite-templated carbon retains 54% of the initial capacity during five cycles[27], and nanoconfined $LiBH_4$–$Ca(BH_4)_2$ in CA retains 73% during three cycles.[4] Nanoconfined $LiBH_4$–$NaAlH_4$ displays a high stability of 83% during three desorption cycles.[23]

The molar composition determined from ^{11}B MAS NMR for the sample $LiBH_4$–MgH_2–Al (4:1:1) after three hydrogen release and uptake cycles was $LiBH_4$–$Li_2B_{12}H_{12}$ 19.1:80.9 and 8.7:91.3 applying hydrogen pressures of $p(H_2)$ = 0.15 or 5.0 bar, respectively, during hydrogen release, which reveals that physical conditions are important to tailor the reaction mechanism for hydrogen release and uptake to achieve full reversibility.[28]

An investigation of the decay in the hydrogen storage capacity during 10 cycles of hydrogen release and uptake for the reactive composite $LiBH_4$–Al (2:3) was also conducted with hydrogen desorption at 500 °C, $p(H_2) = 10^{-2}$ bar for 2.5 h and absorption at 400 °C, $p(H_2)$ = 100 bar for 2 h. The composite $LiBH_4$–Al (2:3) reveals a significant loss in the hydrogen storage capacity, and only 45 and 15% of the theoretically available hydrogen content remains after 4 and 10 cycles. This capacity loss is also assigned to the formation of $Li_2B_{12}H_{12}$.[28,29] Thus, all of the above-mentioned systems display a gradual decrease in capacity, and so far, no fully stable complex borohydride system has been reported.

In this work, the cyclic stability of bulk and nanoconfined eutectic melting $0.68LiBH_4$–$0.32Ca(BH_4)_2$ (LiCa) with a total gravimetric hydrogen content of ρ_m(**tot**-LiCa) = 14.34 wt % H_2 is examined. However, the hydrogen capacity of this composite depends on the reaction mechanism for the hydrogen release reactions. A reaction between the two metal borohydrides has previously been suggested; see the reaction scheme (reaction 1).[17] Thus, two scenarios can be considered, (**a**) decomposition via reaction 1 with excess $Ca(BH_4)_2$ decomposing via reaction 3 and (**b**) independent decomposition via reactions 2 and 3. Assuming that reaction 1 dominates (scenario **a**) and the remaining $Ca(BH_4)_2$ decomposes via reaction 3, the calculated gravimetric hydrogen content is ρ_m(**a**-LiCa) = 11.94 wt % H_2. In the scenario that the two metal borohydrides, $LiBH_4$ and $Ca(BH_4)_2$, decompose individually according to reactions 2 and 3 (scenario **b**), the calculated gravimetric hydrogen content is ρ_m(**b**-LiCa) = 11.34 wt % H_2.

$$4LiBH_4 + Ca(BH_4)_2 \leftrightarrow 4LiH + CaB_6 + 10H_2 \qquad 12.85\ \text{wt\%}\ H_2 \tag{1}$$

$$LiBH_4 \leftrightarrow LiH + B + 1.5H_2 \qquad 13.88\ \text{wt\%}\ H_2 \tag{2}$$

$$Ca(BH_4)_2 \rightarrow (1/3)CaB_6 + (2/3)CaH_2 + (10/3)H_2 \qquad 9.63\ \text{wt\%}\ H_2 \tag{3}$$

In this work, we examine the stability of the hydrogen capacity for both the bulk and nanoconfined $0.68LiBH_4$–$0.32Ca(BH_4)_2$ eutectic system over five cycles of hydrogen release and uptake.

■ EXPERIMENTAL DETAILS

Sample Preparation. The preparation of resorcinol formaldehyde CA was done by mixing 82.87 g of resorcinol (Aldrich, 99%), 113.8 mL of formaldehyde (37 wt % stabilized by ~10–15% methanol, Merck), 113.3 mL of deionized water, and 0.0674 g of Na_2CO_3 (Aldrich, 99.999%) in a beaker with continuous stirring until a homogeneous solution was obtained. The pH of the final solution was measured to be 5.91. The aerogels were prepared and characterized according to previously published procedures.[9,30–32] The gels were aged at RT for 24 h in a fume hood and then at 50 °C for 24 h and subsequently at 90 °C for 72 h. Afterward, the monoliths were cut into smaller pieces (ca. 0.4 cm^3) and carbonized in a tube furnace under a nitrogen flow by heating at a constant temperature of 800 °C (heating rate = 2.6 °C/min) for 6 h. The furnace was then turned off, and the samples were left to cool naturally to RT. The gels were further treated at 400 °C in vacuum for several hours in order to remove moisture and gases from the porous structure. Selected fractions of the CA were CO_2-activated at 950 °C ($\Delta T/\Delta t$ = 6.67 °C/min) under continuous CO_2 flow (25 mL/min) for 6 h in order to increase the surface area and pore volume. Afterward, the CO_2 flow and the furnace were turned off and allowed to cool naturally. Approximately 70% of the sample mass was removed after 6 h of activation, and this sample is denoted CA.[31,32] Prior to use, the scaffold was degassed at 400 °C in a dynamic vacuum for several hours in order to remove possible air and water adsorbed within the porous structure. All subsequent handling was performed in a glovebox with a purified argon atmosphere.

The eutectic binary borohydride composite mixture was prepared by mixing calcium borohydride, $Ca(BH_4)_2$ (synthesized via CaH_2 (Aldrich, 99.99%) as starting reactant[33]) with commercially available $LiBH_4$ (Aldrich, ≥ 95%) in the molar ratio $0.68LiBH_4$-$0.32Ca(BH_4)_2$ based on the reported eutectic melting composition.[17,18,24] The borohydride mixture was ball milled with a planetary Fritsch P4 mill using a tungsten carbide bowl (80 mL) and balls (o.d. 10 mm) and a powder to ball ratio of 1:24. Milling was carried out at 250 rpm for 2 min, with interruptions every 2 min to allow cooling of the milling vial. This was repeated 60 times for a total milling time of 120 min. This sample is denoted LiCa.

The quantity of $0.68LiBH_4$–$0.32Ca(BH_4)_2$ added to CA corresponds to a pore filling of ~94 vol %, which was calculated based on the total pore volume, V_{tot}, of the scaffold and the density of bulk LiCa, ρ(LiCa) = 0.864 g/mL. The eutectic melting temperature of $0.68LiBH_4$–$0.32Ca(BH_4)_2$ is reported to be ~200 °C; therefore, melt infiltration was performed in a custom-made steel autoclave by heating to T = 210 °C ($\Delta T/\Delta t$ = 2 °C/min) and keeping the temperature at there for 30 min, reaching a hydrogen pressure in the range of 110–130 bar.

DOI: 10.1021/acs.jpcc.7b06228
J. Phys. Chem. C 2017, 121, 18439–18449

The Journal of Physical Chemistry C Article

Afterward, the sample was cooled naturally to RT and denoted CA-LiCa.

A sample of nanoconfined lithium borohydride, $LiBH_4$, was prepared as a reference by mixing CA with $LiBH_4$ and placed in a stainless steel autoclave. The sample was heated to 300 °C ($\Delta T/\Delta t$ = 2 °C/min) under an initial H_2 pressure of 120 bar, with the temperature kept constant for 30 min at 300 °C, reaching a final pressure of 140 bar. Afterward, the sample was naturally cooled to RT under H_2 pressure. The added amount of $LiBH_4$ relative to CA corresponds to a pore filling of ~100 vol % (~63 wt % $LiBH_4$), calculated based on the total pore volume, V_{tot}, of the scaffold and the density of bulk $LiBH_4$, $\rho(LiBH_4)$ = 0. 67 g/mL.

Sample Characterization. The mesoporous CA scaffold was characterized by N_2 adsorption and desorption measurements using a Nova 2200e surface area and pore size analyzer from Quantachrome. Prior to the measurements, the aerogels were degassed under vacuum for several hours at 300 °C. A full adsorption and desorption isotherm was measured in the pressure range of 0−1p/p_0 at liquid N_2 temperatures. Data was analyzed using the *t*-plot method,[34] the Brunauer−Emmet−Teller (BET) method,[35] and the Barrett−Joyner−Halenda (BJH), and the total pore volume was calculated from a single point at $p/p_0 \approx 1$.[36]

Powder X-ray Diffraction (PXD) data was collected at RT on a Rigaku SMARTLAB diffractometer, equipped with a rotating Cu anode (Cu Kα radiation, 2 kW, λ = 1.54053 Å). The samples were packed in 0.5 mm o.d. capillary tubes in the glovebox, sealed with glue, and transferred to the instrument without air exposure.

The cyclic stability of nanoconfined and bulk $0.68LiBH_4$−$0.32Ca(BH_4)_2$ was studied during five hydrogen release and uptake cycles. The samples were sealed in a stainless steel autoclave inside of the glovebox and attached to a custom-made Sievert's type apparatus. Desorption measurements were collected at 500 °C ($\Delta T/\Delta t$ = 5 °C/min) and kept at 500 °C for 10 h. The initial pressure of hydrogen was 1 bar and reached final pressures of 5 and 8 bar for the bulk and nanoconfined samples, respectively. Hydrogen absorption was performed by applying a hydrogen pressure of between 134 and 144 bar at RT, at a constant temperature of 500 °C ($\Delta T/\Delta t$ = 5 °C/min) kept for 10 h. At the end of the heat treatment, the sample was cooled naturally to RT. Hydrogen release and uptake conditions for nanoconfined lithium borohydride were exactly as described for the nanoconfined and bulk $0.68LiBH_4$−$0.32Ca(BH_4)_2$.

Selected samples were characterized by Fourier transform infrared spectroscopy (FT-IR) analysis on a NICOLET 380 FT-IR from Thermo-Electronic Corporation with permanently aligned optics and proprietary diamond-turned pinned-in-place mirror optics. The samples were placed on the baseplate, and subsequently, the diamond pin was pressed onto the sample, forming a thin film. The FTIR spectra were collected within a wavenumber range of 400−4000 cm^{-1}. The samples were shortly exposed to air when mounted.

RESULTS AND DISCUSSION

Sample Preparation and Initial Characterization. The bulk sample of $0.68LiBH_4$−$0.32Ca(BH_4)_2$, denoted LiCa, obtained by ball milling the two hydrides, consist of a physical mixture of $LiBH_4$ and $Ca(BH_4)_2$ as Bragg peaks of $LiBH_4$ and $Ca(BH_4)_2$ are observed in the PXD pattern in Figure 1. In order to further improve the hydrogen absorption and desorption kinetics and preserve the storage capacity, a mesoporous CA has been employed as an inert scaffold for infiltration of LiCa. The CA has a pore size distribution centered around D_{max} = 13 nm and a specific BET surface area and total pore volume of S_{BET} = 2421 m^2/g and V_{tot} = 2.46 mL/g, respectively (see Table 1). Details on N_2 adsorption analysis used to conduct the structure parameters are displayed in Figure S1 in the Supporting Information. The amount of LiCa added to the scaffold corresponds to 94 vol % pore filling in order to establish the full potential hydrogen storage capacity of the system.

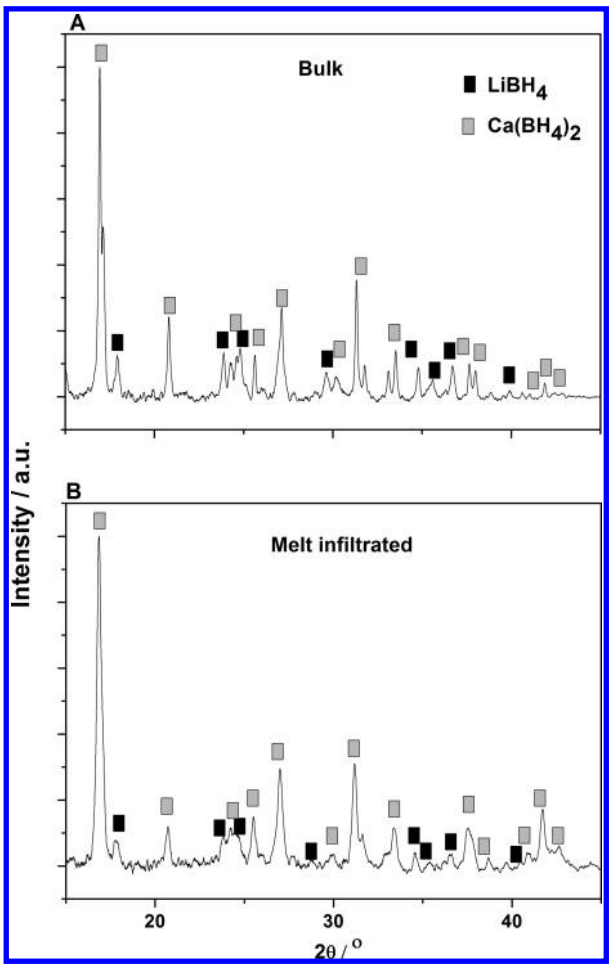

Figure 1. PXD of (A) bulk $0.68LiBH_4$−$0.32Ca(BH_4)_2$ (LiCa) and (B) after melt infiltration of $0.68LiBH_4$−$0.32Ca(BH_4)_2$ (LiCa-CA) (λ = 1.54053 Å).

PXD of melt infiltrated LiCa in the activated CA scaffold shows no significant changes in the PXD data compared to that of bulk. However, the metal borohydride Bragg peaks show increased full width at half-maximum (fwhm), for example, fwhm($LiBH_4$) increases from 0.26 to 0.42° (peak at 2θ = 17.94°) and fwhm($Ca(BH_4)_2$) increases from 0.17 to 0.31° (peak at 2θ = 20.83°) for the bulk and nanoconfined samples, respectively. The Scherrer formula provides an estimate of particle sizes of $LiBH_4$, 35 and 20 nm, and $Ca(BH_4)_2$, 67 and 28 nm, for bulk and nanoconfined samples, respectively.

Evolution of the Hydrogen Storage Capacity during Cycling. Bulk $0.68LiBH_4$−$0.32Ca(BH_4)_2$ (LiCa) has been cycled five times, and the hydrogen desorption profiles are displayed in Figure 2A as a function of time and temperature. The first hydrogen desorption releases 10.5 wt % H_2, which

DOI: 10.1021/acs.jpcc.7b06228
J. Phys. Chem. C 2017, 121, 18439−18449

The Journal of Physical Chemistry C Article

Table 1. Structural Parameters, BET Surface Area (S_{BET}), Micro, Meso, and Total Pore Volume, (V_{micro}, V_{meso}, V_{tot}), and Pore Size (D_{max}) of the CA Scaffold[a]

scaffold	S_{BET} (m^2/g)	V_{micro} (mL/g)	V_{meso} (mL/g)	V_{tot} (mL/g)	D_{max} (nm)	LiCa[b] wt %	LiCa[b] vol %	ρ_m(tot-CA-LiCa)[c] wt % H_2/sample
CA	2421 ± 189	0.72 ± 0.04	1.59 ± 0.26	2.46 ± 0.46	12.9 ± 1	66.7	94	9.56

[a]The added amount of $0.68LiBH_4$–$0.32Ca(BH_4)_2$ in the samples is also provided gravimetrically and volumetrically. [b]The amount of $0.68LiBH_4$–$0.32Ca(BH_4)_2$ (LiCa) relative to weight and volume of the CA scaffold for the nanoconfined sample (CA-LiCa). [c]Calculation is based on the total hydrogen content of the bulk $0.68LiBH_4$–$0.32Ca(BH_4)_2$ composite (ρ_m(tot-LiCa) = 14.34 wt % H_2).

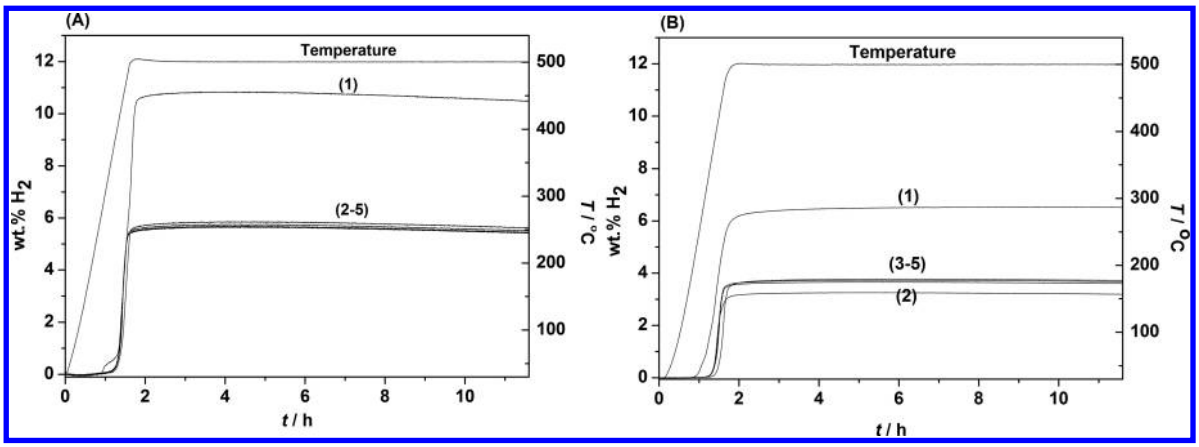

Figure 2. Sievert's data displaying five hydrogen release profiles for (A) bulk $0.68LiBH_4$–$0.32Ca(BH_4)_2$ (LiCa) and (B) nanoconfined $0.68LiBH_4$–$0.32Ca(BH_4)_2$ in CA (CA-LiCa). Samples were heated from RT to 500 °C ($\Delta T/\Delta t$ = 5 °C/min) with the temperature held constant at 500 °C for 10 h and a pressure of $p(H_2)$ = 1–8 bar.

Table 2. Calculated Gravimetric Hydrogen Content Relative to Scenario a, ρ_m(a), for the Bulk $0.68LiBH_4$–$0.32Ca(BH_4)_2$ (LiCa) and Nanoconfined Sample (CA-LiCa) Compared to the Measured Hydrogen Release Relative to the Mass of the Sample[a]

sample	ρ_m(a) wt % H_2 / sample	1.des wt % H_2	2.des wt % H_2	3.des wt % H_2	4.des wt % H_2	5.des wt % H_2
LiCa	11.94	10.5 (100)	5.6 (53)	5.5 (52)	5.4 (51)	5.4 (51)
$p_{max}(H_2)$		1.0–5.3	1.0–3.4	1.0–3.4	1.0–3.3	1.0–3.3
CA-LiCa	7.97	6.5 (100)	3.2 (49)	3.7 (57)	3.7 (57)	3.7 (57)
$p_{max}(H_2)$		1.0–8.5	1.0–4.7	1.0–5.4	1.0–5.4	1.0–5.4
CA-$LiBH_4$	8.70	6.0 (100)	2.0 (33)	1.6 (27)	1.3 (22)	1.1 (18)
$p_{max}(H_2)$		1.0–5.9	1.0–2.2	1.0–2.1	1.0–1.9	1.0–1.8

[a]The hydrogen release of cycles 2–5 is compared to the release of the first cycle (in %, in brackets). The partial pressure of hydrogen varied in the range of 1 < $p(H_2)$ < p_{max} during hydrogen release reactions. The data is extracted from Figure 2.

corresponds to 88% of the hydrogen capacity ρ_m(**a**-LiCa) = 11.94 wt % H_2. Scenarios **a** and **b** cannot be distinguished based on the amount of released hydrogen and previously published powder diffraction data.[4,18]

The majority of the hydrogen is released during heating at T < 500 °C. The capacity of LiCa decreases significantly (47%) with a release of 5.6 wt % H_2 during the second desorption. However, the following desorption cycles (3–5) shows significant stability, releasing 5.5, 5.4, and 5.4 wt % H_2 during the third, fourth, and fifth desorptions, respectively, that is, 96% of the hydrogen storage capacity between the second and fifth desorptions is maintained; see Table 2. The released amount of hydrogen compares well to the calculated release of hydrogen from $LiBH_4$ only, which is 5.43 wt % H_2.

The nanoconfined composite $0.68LiBH_4$–$0.32Ca(BH_4)_2$ (CA-LiCa) has a total gravimetric hydrogen content of ρ_m(**tot**-CA-LiCa) = 9.56 wt % H_2, which is reduced to ρ_m(**a**-CA-LiCa) = 7.97 wt % H_2 and ρ_m(**b**-CA-LiCa) = 7.55 wt % H_2 for the two scenarios (**a**) and (**b**) because the added amount of LiCa to CA is 66.7 wt %. Figure 2B displays the cyclic stability of CA-LiCa. The first desorption releases 6.5 wt % H_2, which corresponds to 82% of the calculated available hydrogen content. The second desorption releases 3.2 wt % H_2, equivalent to 49% of the initial hydrogen release followed by a release of 3.7, 3.7, and 3.7 wt % H_2 during the third, fourth, and fifth desorptions, respectively. The released amount of hydrogen for CA-LiCa compares well to the calculated release of hydrogen from $LiBH_4$ only, which is 3.69 wt % H_2. Thus, a slightly higher fraction of the original release of hydrogen is preserved during five continuous cycles of hydrogen release and uptake for the nanoconfined sample, CA-LiCa, 57% as compared to bulk LiCa, 51%; see Table 2. The normalized hydrogen storage capacity during each desorption cycle for the bulk and nanoconfined samples is also displayed in Figure 3.

Kinetics of Hydrogen Release. The hydrogen release rate as a function of temperature for the two samples during heating is obtained by taking the derivative of the Sievert's hydrogen desorption data (Figure 2) from RT to 500 °C. Figure 4 displays the hydrogen emission rate as a function of the hydrogen desorption cycle number for bulk and nanoconfined LiCa. Bulk LiCa exhibits the characteristic desorption peak from eutectic melting of LiCa during the first desorption, as

DOI: 10.1021/acs.jpcc.7b06228
J. Phys. Chem. C 2017, 121, 18439−18449

The Journal of Physical Chemistry C Article

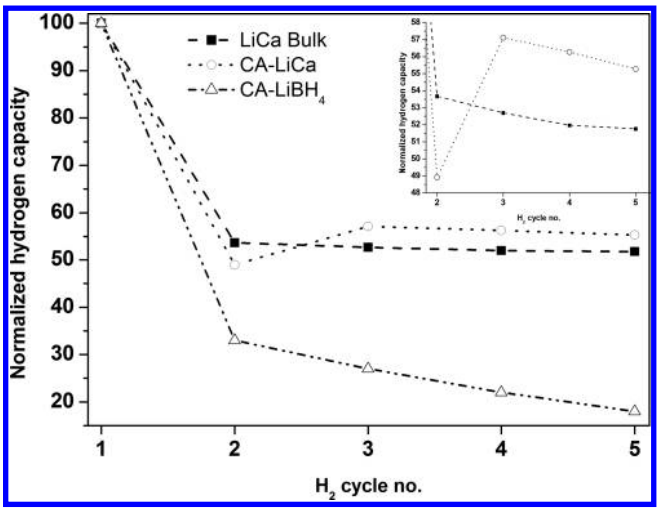

Figure 3. Normalized hydrogen storage capacities for bulk (LiCa, squares, dashed line) and nanoconfined (CA-LiCa, circles, dotted line) $0.68LiBH_4-0.32Ca(BH_4)_2$ and nanoconfined $LiBH_4$ (CA-$LiBH_4$, triangles, dot−dash line). The inset is an enlargement of a selected section of the data.

previously reported,[4,18] which takes place in the temperature range of 250−280 °C with local maxima at 266 °C. The major H_2 desorption takes place in the temperature range of 350−500 °C with three distinctive peaks at 405, 440, and the maxima at 483 °C. The three peaks are assigned to the major desorption peaks of $LiBH_4$ and $Ca(BH_4)_2$.[18]

The desorption profiles for the second, third, fourth, and fifth cycles of bulk LiCa are similar to each other but different from the first. The onset temperature for H_2 release for the second to fifth cycles is at 360 °C, however with the exception of the relatively low desorption intensity and slightly higher maximum temperature exhibited for the second desorption. The desorption profiles for the third to fifth cycles are almost identical with temperatures for a maximum hydrogen release rate ranging between 452 and 455 °C, though with a consistent increase in intensity with increasing cycle number.

The first hydrogen release profile of the nanoconfined sample CA-LiCa has a total of five hydrogen release maxima, which are significantly broader as compared to those of the bulk LiCa. The peak associated with the melting of LiCa, at $T \approx 264$ °C, is only observed for the first hydrogen release profile and is suppressed during melt infiltration (due to the elevated hydrogen pressures and slightly lower temperatures, $T = 210$ °C). A H_2 release maximum observed at 337 °C, observed only for the first profile of CA-LiCa, may be assigned to a reaction between hydrides and the oxide impurities of the carbon scaffold. The following two events, at 397 and 483 °C, resemble those of bulk LiCa. The following desorption cycles progressively resemble that of the bulk LiCa, exhibiting a single maximum desorption temperature at ∼446 °C, although a minor shoulder peak is observed in the temperature range of 400−430 °C.

Overall, nanoconfinement provides kinetic improvement of the hydrogen release reactions for cycles three to five, which is observed by a reduction of T_{max} from ∼455 to ∼446 °C and also the onset of hydrogen release from ∼350 to ∼310 °C for the bulk and nanoconfined samples, respectively. This is illustrated by the inset in Figure 4B, which compares the fifth hydrogen release (Des5) of the bulk and nanoconfined sample.

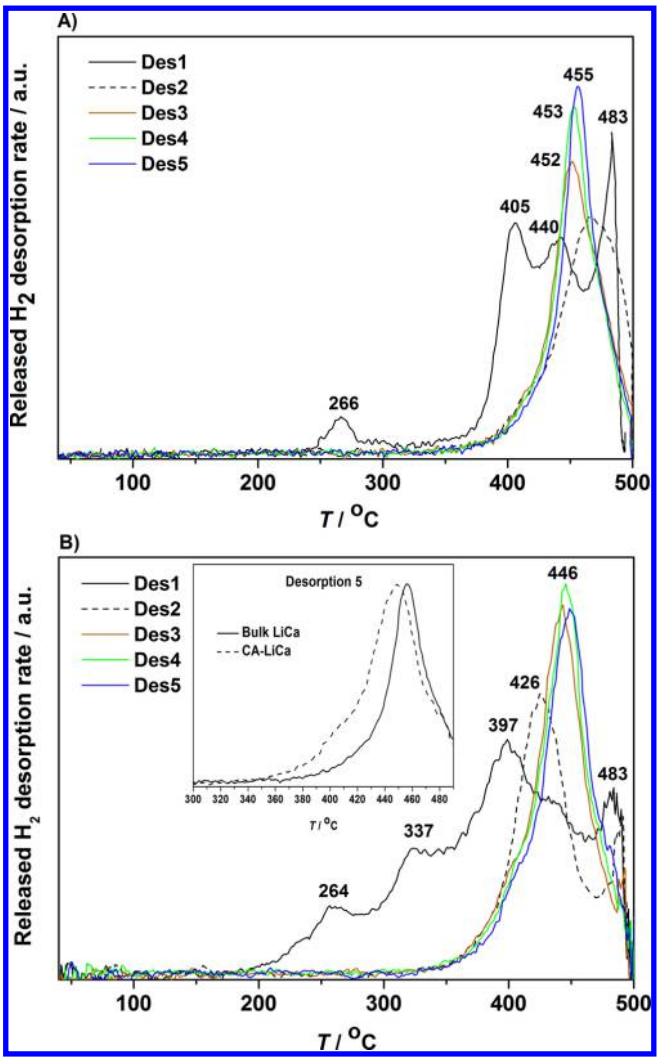

Figure 4. Hydrogen release rate as a function of temperature of (A) bulk LiCa and (B) nanoconfined $0.68LiBH_4-0.32Ca(BH_4)_2$ (CA-LiCa) obtained as the derivative of the Sievert's hydrogen desorption data (Figure 2) of the first to fifth cycle during heating from RT to 500 °C. The inset compares the fifth desorption of both bulk and nanoconfined LiCa.

Spectroscopic Investigation. The FT-IR spectra of bulk $LiBH_4$ and $Ca(BH_4)_2$ (Figure 5a,b) displays the characteristic borohydride B−H stretch in the range of 2000−2500 cm^{-1} with a maximum transmittance signal at ∼2300 cm^{-1} in addition to the B−H bending bands ranging between 1090 and 1300 cm^{-1}, in accord with published data.[37] The bulk LiCa (Figure 5c) merely shows combined signals of $LiBH_4$ and $Ca(BH_4)_2$.

The nanoconfined sample, CA-LiCa (Figure 5d), displays the expected B−H bending and stretching modes as described for the bulk metal borohydrides. However, an unassigned signal is observed at ∼1619 cm^{-1}, which is also observed for bulk $LiBH_4$ and LiCa (Figure 5a,c). The signals in the nanoconfined sample are weaker due to the reduced gravimetric hydride content and absorption from the black carbon scaffold. All samples also exhibit a weak characteristic O−H stretching band from adsorbed H_2O, which is present due to short air exposure prior to the FT-IR measurements. CAs synthesized at the same conditions as those used here have no significant IR absorption at >3000 cm^{-1}, but elemental analysis of C and O suggests that

DOI: 10.1021/acs.jpcc.7b06228
J. Phys. Chem. C 2017, 121, 18439−18449

The Journal of Physical Chemistry C Article

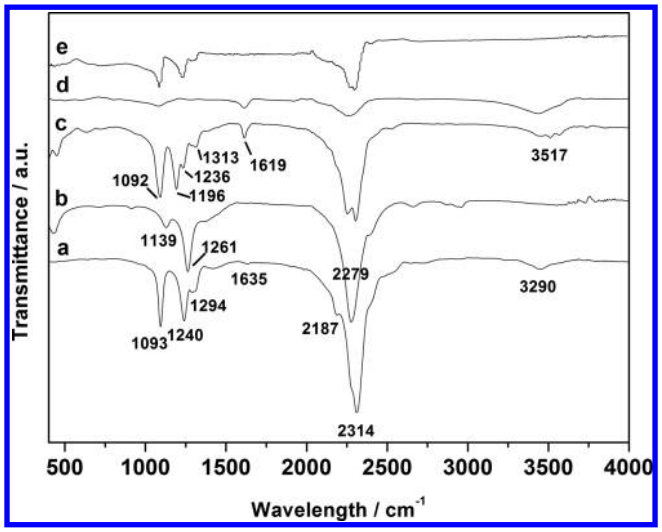

Figure 5. FT-IR spectra of (a) bulk $LiBH_4$, (b) as-prepared bulk $Ca(BH_4)_2$, (c) bulk $0.68LiBH_4-0.32Ca(BH_4)_2$ (LiCa), (d) nanoconfined $0.68LiBH_4-0.32Ca(BH_4)_2$ (CA-LiCa), and (e) nanoconfined $LiBH_4-Ca(BH_4)_2$ after the fifth rehydrogenation.

oxygen mainly exists as ether groups (C−O−C) in the scaffold.[38,39]

FT-IR data of the sample CA-LiCa after the fifth rehydrogenation (Figure 5e) clearly exhibits a B−H stretching mode centered at ~2300 cm^{-1} along with the characteristic B−H bend signals at 1100−1300 cm^{-1}. The relative intensity of the two B−H stretching modes observed at 1090 and 1240 cm^{-1} in the rehydrogenated nanoconfined sample is more characteristic of B−H stretching modes in $LiBH_4$, which suggests that the sample is relatively deficient in $Ca(BH_4)_2$. Calcium hydride, CaH_2, is reported to show weak Ca−H bending modes only around 1000−1300 cm^{-1}.[38] Therefore, the FT-IR signals in Figure 5e are assigned mainly to $LiBH_4$. The bulk sample after the fifth rehydrogenation also clearly shows B−H bending and stretching bands originating from $LiBH_4$ (see Figure S3 in the Supporting Information).

Mechanism for Hydrogen Release. PXD data of bulk (A) and nanoconfined (B) $0.68LiBH_4-0.32Ca(BH_4)_2$ measured after the fifth rehydrogenation is shown in Figure 6. Both samples contain crystalline $LiBH_4$ and decomposition products of $Ca(BH_4)_2$, that is, CaH_2, CaB_6 and CaO after the fifth hydrogenation. No diffraction of $Ca(BH_4)_2$ is observed due lack of $Ca(BH_4)_2$ formation during rehydrogenation.[39] Rietveld refinement of the PXD data measured for nanoconfined CA-LiCa is provided in the Supporting Information Figure S2 and reveals the composition $LiBH_4$ (70.8 mol %), CaH_2 (7.6 mol %), CaB_6 (7.5 mol %), and CaO (14.1 mol %). $LiBH_4-Ca(BH_4)_2$ in CA (CMK-3) has previously been reported to form $LiCa_3(BH_4)(BO_3)_2$ during decomposition in the temperature range of 300−400 °C due to oxides in the metal borohydride reactants, the carbon framework, or adsorbed water.[40] This compound is reported to decompose to CaO and other reaction products in the temperature range of 400−500 °C.[4,17,40] The compound, $LiCa_3(BH_4)(BO_3)_2$, was assumed to be outside of the scaffold in a previous study and decompose to inert CaO and unidentified products.[4]

In this work, a significant amount of lithium borohydride $LiBH_4$ is observed as the main component responsible for the reversible hydrogen storage properties of the composite $0.68LiBH_4-0.32Ca(BH_4)_2$. Assuming that only $LiBH_4$ contributes to the reversible hydrogen storage, the calculated capacities are 5.54 and 3.69 wt % H_2 for LiCa and CA-LiCa, respectively, which is in excellent agreement with the measured hydrogen capacities of 5.4 and 3.7 wt % H_2 (Table 2) in the fifth cycle of hydrogen release. The Bragg peak width of bulk and nanoconfined $LiBH_4$ is similar (see Figure 6) and suggests similar crystallite size and that a major fraction of $LiBH_4$ may be outside of the scaffold of sample CA-LiCa. Thus, this work suggests that full reversibility may be achieved for $LiBH_4$.

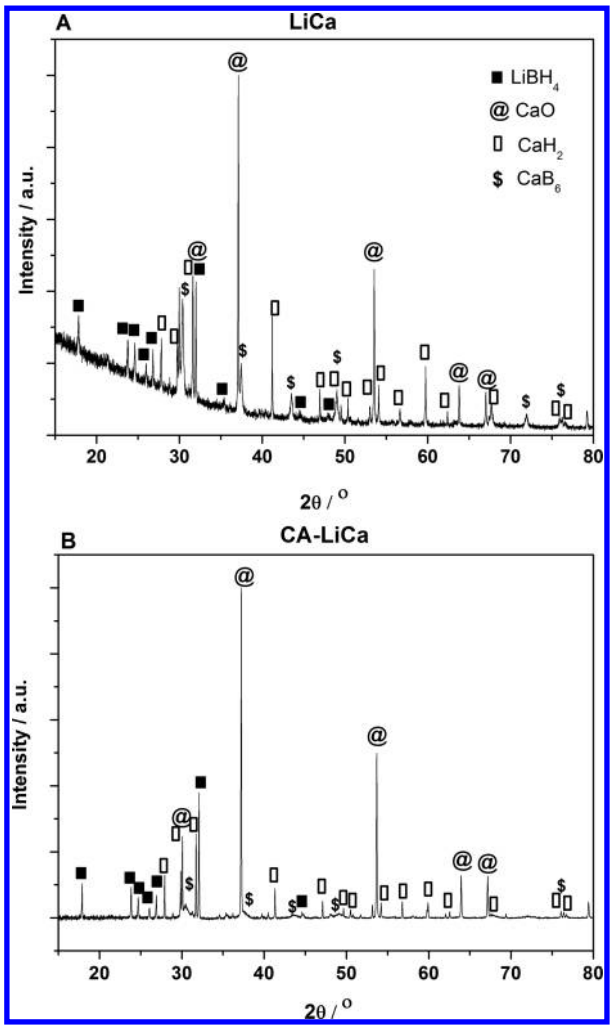

Figure 6. PXD data of bulk (A) and nanoconfined (B) $0.68LiBH_4-0.32Ca(BH_4)_2$ measured after the fifth rehydrogenation (λ = 1.54053 Å).

This work reveals that the mechanisms for hydrogen release and uptake reactions may not be identical. Two scenarios for decomposition were proposed in the Introduction: (**a**) decomposition via reaction 1 and remaining $Ca(BH_4)_2$ via reaction 3 and (**b**) independent decomposition via reactions 2 and 3. However, (**a**) and (**b**) provide similar amounts of released hydrogen and are challenging to distinguish. To which extent reactions 1−3 are coupled via scenarios (**a**) and (**b**) may depend on physical conditions such as heating rate, maximum temperature, pressure, and gas composition. Diffraction and spectroscopy reveal that $Ca(BH_4)_2$ is mainly present prior to the first decomposition reaction,; thereafter, $LiBH_4$ is mainly responsible for hydrogen reversible capacity of the sample. Thus, scenario (**a**) and/or (**b**) may be the mechanism for

DOI: 10.1021/acs.jpcc.7b06228
J. Phys. Chem. C 2017, 121, 18439−18449

The Journal of Physical Chemistry C Article

hydrogen release during the first cycles, whereas reaction 2 becomes dominating during later cycles.

Other reactions, for example, those involving decomposition products of $Ca(BH_4)_2$, such as CaH_2 and CaB_6, may also be involved, which may explain the minor shoulder peak observed in the temperature range of 400−430 °C (see Figure 4B). Such a possible reaction includes that between lithium borohydride and calcium hydride according to reaction 4. This reaction has a calculated hydrogen capacity of 11.67 wt % H_2 that translates to a hydrogen capacity of 12.05 wt % H_2 if it occurs as part of the decomposition of the $LiBH_4$−$Ca(BH_4)_2$ eutectic.[41]

$$6LiBH_4 + CaH_2 \leftrightarrow 6LiH + CaB_6 + 10H_2 \quad (4)$$

The hydrogen uptake reaction may also change during cycling and may be different from the hydrogen release reactions discussed above. Decomposition products from $Ca(BH_4)_2$ may facilitate the hydrogen uptake and formation of $LiBH_4$ either directly, as suggested by reaction 4, or indirectly by preventing foaming and sample segregation.

This work reveals that the detailed mechanism for hydrogen release and uptake may change during cycling, in particular, during the first three cycles. This highlights the importance of investigating hydrogen release and uptake during multiple cycles. The hydrogen release rate, Figure 4, reveals that three cycles are needed before the temperature of desorption for the nanoconfined sample stabilizes. This seems to be a general trend for nanoconfined hydrides, and was also observed for the $LiBH_4$−$NaBH_4$ and $LiBH_4$−$Mg(BH_4)_2$ composites.[11,15]

Nanoconfined complex metal hydrides show significant loss of hydrogen storage capacity during hydrogen release and uptake cycling due to irreversible reactions, possibly with oxygen in the scaffold.[42] In the present investigation, full reversibility of the nanoconfined $LiBH_4$ appears to be achieved due to preferential oxidation of calcium, that is, calcium acts an oxygen scavenger by formation of a stable oxide, CaO.

Reversible Hydrogen Storage Properties. The temperature of rehydrogenation acts as a driving force to obtain full reversibility of metal borohydrides. In this investigation, the maximum for hydrogen release rate is observed at ∼455 °C after three cycles and assumed to be hydrogen release from $LiBH_4$. This implies that fast rehydrogenation kinetics will be obtained only at $T > 450$ °C in the case that the mechanisms for hydrogen release and uptake are identical.

Previous work presented rehydrogenation at 400 °C,[4] that is, $T < 450$ °C; thus, full reversibility was not achieved. However, because rehydrogenation in the current work is conducted at 500 °C, that is, $T > 450$ °C, full reversibility is achieved. Under these applied rehydrogenation conditions ($T = 500$ °C, $p(H_2) = 144$ bar for 10 h), the decomposition product of $Ca(BH_4)_2$ does not reform $Ca(BH_4)_2$. Previous attempts have been made to reform $Ca(BH_4)_2$ after decomposition. Kim et al. reports rehydrogenation of $Ca(BH_4)_2$ at 330 °C and $p(H_2) = 90$ bar for 24 h; however, only 50% reversibility is obtained, whereas Li et al. report 90% of $Ca(BH_4)_2$ is formed during hydrogenation at 400 °C and $p(H_2) = 400$ bar.[39,43] Minella et al. succeeded to reform $Ca(BH_4)_2$ with additives at 350 °C at $p(H_2) = 145$ bar for 24 h;[44] however, shorter time (a few hours) was less successful.[45] Reversibility of $Ca(BH_4)_2$ during rehydrogenation is not occurring because the duration time used at 500 °C is insufficient.[43,45]

Additional effects may also account for the reversibility observed in this work. Metal borohydrides may undergo foaming and volume expansion, and hydrogen release may occur from a molten state. Lithium borohydride is known to significantly change viscosity in the molten state and climb reaction vessel walls and block filters during decomposition.[24] These effects may be suppressed by the use of additives or by the decomposition products from other components within the system.

However, weak foaming may occur from the bulk $LiBH_4$−$Ca(BH_4)_2$ eutectic composite during decomposition but is significantly less than that for bulk $LiBH_4$, and the composite's viscosity does not provide experimental challenges such as material "climbing vessel walls" and blocking filters.

The cyclic stability during hydrogen release and uptake of nanoconfined $LiBH_4$ is shown in Figure 7. This data clearly

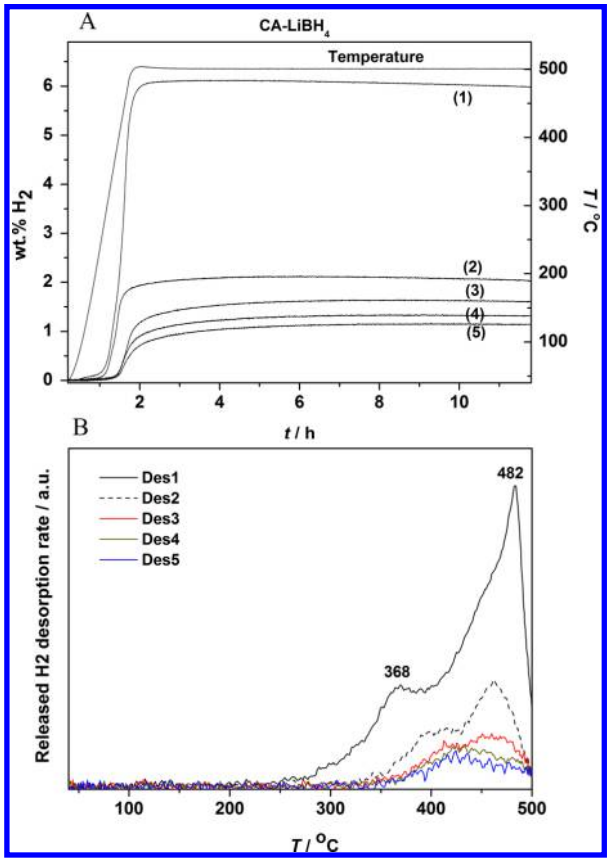

Figure 7. (A) Sievert's data displaying five hydrogen release profiles for nanoconfined $LiBH_4$ in CA (CA-$LiBH_4$). The sample was heated from RT to 500 °C ($\Delta T/\Delta t = 5$ °C/min) with the temperature held constant at 500 °C for 10 h and a pressure of $p(H_2) = 1$−6 bar. Hydrogen absorption was performed by heating the sample from RT to 500 °C ($\Delta T/\Delta t = 5$ °C/min) and holding the sample at this temperature for 10 h at $p(H_2) = 134$−144 bar. (B) Derivative of the Sievert's hydrogen desorption data from "A" of the first to fifth cycle during heating from RT to 500 °C.

illustrates that $LiBH_4$ does not single handedly exhibit a similar reversibility as compared to the LiCa sample. This emphasizes the importance of the $Ca(BH_4)_2$ decomposition product to promote full hydrogen absorption and desorption of $LiBH_4$. The full reversibility of $LiBH_4$ in the bulk and nanoconfined state has not been reported so far in the literature.[27,46−62] Other attempts to rehydrogenate $LiBH_4$ at temperatures of 500 °C and higher have been made but with no success in obtaining full reversibility.[63]

DOI: 10.1021/acs.jpcc.7b06228
J. Phys. Chem. C 2017, 121, 18439−18449

The cyclic stability of bulk $LiBH_4$−CaH_2 has also been reported by Li.[64] Bulk $LiBH_4$−CaH_2 decreases in capacity by 66% during 10 desorption cycles with rehydrogenation conditions of 450 °C under 8 MPa for 16 h and with dehydrogenation performed at 450 °C under 0.1 MPa H_2 pressure. In comparison to our results, 450 °C is insufficient to obtain stable reversibility of $LiBH_4$. Li's results suggest that the driving force for obtaining stable $LiBH_4$ is temperature, rather than the quantity of CaH_2. It could be suggested that rehydrogenation at 500 °C possibly would induce enhanced stability and would be in direct comparison to our results.

Potential Applications. The demonstration here of full reversibility of $LiBH_4$ opens new intriguing possible utilization of $LiBH_4$ as a high-performance H_2 storage material, for example, for use in conjunction with high-temperature molten carbonate or solid oxide fuel cells operating at T > 600 °C,[65] but also as a possible heat storage material for concentrating solar power (CSP) plants.[66−72] Molten $LiBH_4$ at 627 °C (900 K) has a theoretical heat storage capacity of 3915 kJ/kg[73] at 627 °C (900 K), and if operated above the melting point of LiH (689 ± 5 °C[74]), a capacity of 4936 kJ/kg is theoretically possible at 727 °C (1000 K).

The reversible thermochemical heat storage capacity of pure $LiBH_4$ is one of the highest known and is only exceeded by two oxidation reactions of methane[75] and three reversible metal hydride systems, $NaBH_4$, CaH_2, and LiH.[69] The methane oxidation reactions have the disadvantages of requiring high temperatures (950 °C) for the heat charging reactions and a large temperature decrease (>400 °C) for the heat release reactions.[75] For the metal hydrides with higher theoretical heat storage capacity than $LiBH_4$, LiH and CaH_2 also require impractical operating temperatures of (∼950 °C), while $NaBH_4$ suffers from limited reversibility. Despite the weight penalty associated with the $LiBH_4$−$Ca(BH_4)_2$ eutectic composition investigated here, the heat storage capacity is still 2351 and 2964 kJ/kg at 627 and 727 °C, respectively. Further research to determine the minimum amount of $Ca(BH_4)_2$ required to still allow $LiBH_4$ reversibility would only increase these values.

One obvious problem associated with the large-scale use of $LiBH_4$ for either H_2 or heat storage is the high cost of lithium that would limit its use to high-performance and niche applications. However, the thermodynamics of H_2 release from molten $LiBH_4$ means that it has a unique advantage over other metal hydrides that have been extensively studied as heat storage candidates, such as MgH_2 and Mg_2FeH_6.[17,26,76,77] The reaction entropy associated with H_2 release from molten $LiBH_4$, ∼ 78 J/mol·H_2·K is substantially lower than that for H_2 release from typical solid-state hydrides ∼ 130 J/mol·H_2·K. The consequence of this is that for molten $LiBH_4$ the H_2 equilibrium pressure increases more slowly with temperature than that for solid-state hydrides. For example, temperatures of ∼460, ∼282, and ∼304 °C are required to produce a H_2 equilibrium pressure of $p(H_2)$ = 1 bar for $LiBH_4$, MgH_2, and Mg_2FeH_6, respectively. At 727 °C (1000 K, i.e., 267 °C above the $T(p(H_2) = 1\ \text{bar})$ of $LiBH_4$), the H_2 equilibrium pressure for molten $LiBH_4$ is increased to ∼13 bar,[73] whereas that of MgH_2 and Mg_2FeH_6 is as high as ∼183 and ∼165 bar at 549 °C and 571 °C, respectively. This allows molten $LiBH_4$ to be used as heat storage for CSP at higher temperatures and lower operating pressures that lead to a reduction in the cost of a real system due to higher power efficiency generation and a reduction in engineering cost associated with the hydride containment vessel.[67,78]

CONCLUSIONS

The eutectic melting metal borohydride system 0.68$LiBH_4$−0.32$Ca(BH_4)_2$ has been nanoconfined into a high surface area (2421 m^2/g) CA scaffold by melt infiltration. Hydrogen release (at T = 500 °C, $p(H_2)$ = 1−8 bar for 10 h) and uptake (at T = 500 °C, $p(H_2)$ = 134−144 bar for 10 h) were repeated 5 times. After three cycles, nanoconfinement had little effect on the kinetics of hydrogen release. The hydrogen release rate was maximal at ∼455 °C, which suggests that fast rehydrogenation kinetics is only achieved at T > 455 °C. After five cycles of hydrogen release and uptake of bulk and nanoconfined 0.68$LiBH_4$−0.32$Ca(BH_4)_2$, a stable hydrogen capacity of 5.4 and 3.7 wt % H_2 remained in the sample, which corresponds to full reversibility of $LiBH_4$ with a calculated capacity of 5.43 and 3.69 wt % H_2, respectively. Lithium borohydride $LiBH_4$ was observed as the main component responsible for the reversible hydrogen storage properties. This suggests that other reactions may be involved in forming a reactive hydride composite, for example, involving CaH_2 and CaB_6. Stable hydrogen storage capacity is only observed for a few metal borohydride-based systems; therefore, these new observations are relevant and call for further investigations. There is a new intriguing possible utilization of $LiBH_4$ or other metal borohydrides as a high-performance H_2 storage material, for example, in conjunction with high-temperature fuel cells or as a possible heat storage material for CSP plants.

ASSOCIATED CONTENT

Supporting Information

The Supporting Information is available free of charge on the ACS Publications website at DOI: 10.1021/acs.jpcc.7b06228.

> N_2 sorption isotherm at −196 °C of the pristine carbon aerogel scaffold; Rietveld refinement analysis of the nanoconfined sample after rehydrogenation; FTIR spectrum of bulk $LiBH_4$−$Ca(BH_4)_2$ after rehydrogenation; and up to date review table of all nanoconfined systems and their cycling conditions (PDF)

AUTHOR INFORMATION

Corresponding Author

*E-mail: trj@chem.au.dk.

ORCID

Torben R. Jensen: 0000-0002-4278-3221

Notes

The authors declare no competing financial interest.

ACKNOWLEDGMENTS

The work was supported by the Aarhus University Research Foundations (AUFF), the Innovation Fund Denmark (project HyFill-Fast), the Danish Research Council for Nature and Universe (Danscatt), Danish council for independent research (HyNanoBorN, DFF-4181-00462), the Danish National Research Foundation, Center for Materials Crystallography (DNRF93), and the European Union's Seventh Framework Program FP7/2007-2013/under REA Grant Agreement No. 607040 (Marie Curie ITN ECOSTORE). We are grateful to the Carlsberg Foundation. H.-W.L. acknowledges financial support from JSPS KAKENHI Grant Number 25709067. C.E.B., D.A.S., and P.J. acknowledge financial support from the Australian Research Council (ARC) for ARC Linkage Grant LP120100435.

REFERENCES

(1) Paskevicius, M.; Jepsen, L. H.; Schouwink, P.; Ravnsbæk, D. B.; Filinchuk, Y.; Dornheim, M.; Ĉerný, R.; Besenbacher, F.; Jensen, T. R. Metal Borohydrides and Derivatives − Synthesis, Structure and Properties. *Chem. Soc. Rev.* **2017**, *46*, 1565−1634.

(2) Callini, E.; Atakli, Z. Ö. K.; Hauback, B. C.; Orimo, S.-I.; Jensen, C.; Dornheim, M.; Grant, D.; Cho, Y. W.; Chen, P.; Hjörvarsson, B.; et al. Complex and Liquid Hydrides for Energy Storage. *Appl. Phys. A: Mater. Sci. Process.* **2016**, *122*, 1−22.

(3) Ley, M. B.; Jepsen, L. H.; Lee, Y. S.; Cho, Y. W.; Bellosta von Colbe, J. M.; Dornheim, M.; Rokni, M.; Jensen, J. O.; Sloth, M.; Filinchuk, Y.; et al. Complex Hydrides for Hydrogen Storage − New Perspectives. *Mater. Today* **2014**, *17*, 122−128.

(4) Javadian, P.; Sheppard, D. A.; Buckley, C. E.; Jensen, T. R. Hydrogen Storage Properties of Nanoconfined $LiBH_4$-$Ca(BH_4)_2$. *Nano Energy* **2015**, *11*, 96−103.

(5) Callini, E.; Aguey-Zinsou, K. F.; Ahuja, R.; Ares, J. R.; Bals, S.; Biliškov, N.; Chakraborty, S.; Charalambopoulou, G.; Chaudhary, A.-L.; Cuevas, F.; et al. Nanostructured Materials for Solid-State Hydrogen Storage: A Review of the Achievement of COST Action MP1103. *Int. J. Hydrogen Energy* **2016**, *41*, 14404−14428.

(6) Hansen, B. R.; Paskevicius, M.; Li, H.-W.; Akiba, E.; Jensen, T. R. Metal Boranes: Progress and Applications. *Coord. Chem. Rev.* **2016**, *323*, 60−70.

(7) White, J. L.; Newhouse, R. J.; Zhang, J. Z.; Udovic, T. J.; Stavila, V. Understanding and Mitigating the Effects of Stable Dodecahydrocloso-Dodecaborate Intermediates on Hydrogen-Storage Reactions. *J. Phys. Chem. C* **2016**, *120*, 25725−25731.

(8) Nielsen, T. K.; Besenbacher, F.; Jensen, T. R. Nanoconfined Hydrides for Energy Storage. *Nanoscale* **2011**, *3*, 2086−2098.

(9) de Jongh, P. E.; Adelhelm, P. Nanosizing and Nanoconfinement: New Strategies Towards Meeting Hydrogen Storage Goals. *ChemSusChem* **2010**, *3*, 1332−1348.

(10) Nielsen, T. K.; Javadian, P.; Polanski, M.; Besenbacher, F.; Bystrzycki, J.; Jensen, T. R. Nanoconfined $NaAlH_4$: Determination of Distinct Prolific Effects from Pore Size, Crystallite Size, and Surface Interactions. *J. Phys. Chem. C* **2012**, *116*, 21046−21051.

(11) Nielsen, T. K.; Javadian, P.; Polanski, M.; Besenbacher, F.; Bystrzycki, J.; Skibsted, J.; Jensen, T. R. Nanoconfined $NaAlH_4$: Prolific Effects from Increased Surface Area and Pore Volume. *Nanoscale* **2014**, *6*, 599−607.

(12) Javadian, P.; Sheppard, D. A.; Buckley, C. E.; Jensen, T. R. Hydrogen Storage Properties of Nanoconfined $LiBH_4$−$NaBH_4$. *Int. J. Hydrogen Energy* **2015**, *40*, 14916−14924.

(13) Roedern, E.; Hansen, B. R.; Ley, M. B.; Jensen, T. R. Effect of Eutectic Melting, Reactive Hydride Composites, and Nanoconfinement on Decomposition and Reversibility of $LiBH_4$−KBH_4. *J. Phys. Chem. C* **2015**, *119*, 25818−25825.

(14) Sartori, S.; Knudsen, K. D.; Hage, F. S.; Heyn, R. H.; Bardaji, E. G.; Zhao-Karger, Z.; Fichtner, M.; Hauback, B. C. Influence of Nanoconfinement on Morphology and Dehydrogenation of the $Li^{11}BD_4$−$Mg(^{11}BD_4)_2$ system. *Nanotechnology* **2012**, *23*, 255704.

(15) Zhao-Karger, Z.; Witter, R.; Bardají, E. G.; Wang, D.; Cossement, D.; Fichtner, M. Altered Reaction Pathways of Eutectic $LiBH_4$−$Mg(BH_4)_2$ by Nanoconfinement. *J. Mater. Chem. A* **2013**, *1*, 3379−3386.

(16) Javadian, P.; Jensen, T. R. Enhanced Hydrogen Reversibility of Nanoconfined $LiBH_4$−$Mg(BH_4)_2$. *Int. J. Hydrogen Energy* **2014**, *39*, 9871−9876.

(17) Liu, X.; Peaslee, D.; Sheehan, T. P.; Majzoub, E. H. Decomposition Behavior of Eutectic $LiBH_4$−$Mg(BH_4)_2$ and Its Confinement Effects in Ordered Nanoporous Carbon. *J. Phys. Chem. C* **2014**, *118*, 27265−27271.

(18) Lee, H.-S.; Lee, Y.-S.; Suh, J.-Y.; Kim, M.; Yu, J.-S.; Cho, Y. W. Enhanced Desorption and Absorption Properties of Eutectic $LiBH_4$−$Ca(BH_4)_2$ Infiltrated into Mesoporous Carbon. *J. Phys. Chem. C* **2011**, *115*, 20027−20035.

(19) Lee, J. Y.; Ravnsbæk, D.; Lee, Y.-S.; Kim, Y.; Cerenius, Y.; Shim, J.-H.; Jensen, T. R.; Hur, N. H.; Cho, Y. W. Decomposition Reactions and Reversibility of the $LiBH_4$−$Ca(BH_4)_2$ Composite. *J. Phys. Chem. C* **2009**, *113*, 15080−15086.

(20) Lee, H.-S.; Hwang, S.-J.; Kim, H. K.; Lee, Y.-S.; Park, J.; Yu, J.-S.; Cho, Y. W. In Situ NMR Study on the Interaction Between $LiBH_4$−$Ca(BH_4)_2$ and Mesoporous Scaffolds. *J. Phys. Chem. Lett.* **2012**, *3*, 2922−2927.

(21) Ampoumogli, A.; Charalambopoulou, G.; Javadian, P.; Richter, B.; Jensen, T. R.; Steriotis, T. Hydrogen Desorption and Cycling Properties of Composites Based on Mesoporous Carbons and a $LiBH_4$−$Ca(BH_4)_2$ Eutectic Mixture. *J. Alloys Compd.* **2015**, *645*, S480−S484.

(22) Lee, H. S.; Hwang, S. J.; To, M.; Lee, Y. S.; Cho, Y. W. Discovery of Fluidic $LiBH_4$ on Scaffold Surfaces and Its Application for Fast Co-confinement of $LiBH_4$-$Ca(BH_4)_2$ into Mesopores. *J. Phys. Chem. C* **2015**, *119*, 9025−9035.

(23) Xia, G.; Meng, Q.; Guo, Z.; Gu, Q.; Liu, H.; Liu, Z.; Yu, X. Nanoconfinement Significantly Improves the Thermodynamics and Kinetics of Co-infiltrated $2LiBH_4$−$LiAlH_4$ Composites: Stable Reversibility of Hydrogen Absorption/Resorption. *Acta Mater.* **2013**, *61*, 6882−6893.

(24) Javadian, P.; Sheppard, D. A.; Buckley, C. E.; Jensen, T. R. Hydrogen Desorption Properties of Bulk and Nanoconfined $LiBH_4$-$NaAlH_4$. *Crystals* **2016**, *6*, 70.

(25) Paskevicius, M.; Ley, M. B.; Sheppard, D. A.; Jensen, T. R.; Buckley, C. E. Eutectic Melting in Metal Borohydrides. *Phys. Chem. Chem. Phys.* **2013**, *15*, 19774−19789.

(26) Jepsen, J.; Milanese, C.; Girella, A.; Lozano, G. A.; Pistidda, C.; Bellosta von Colbe, J. M.; Marini, A.; Klassen, T.; Dornheim, M. Compaction Pressure Influence on Material Properties and Sorption Behaviour of $LiBH_4$−MgH_2 Composite. *Int. J. Hydrogen Energy* **2013**, *38*, 8357−8366.

(27) Reiser, A.; Bogdanović, B.; Schlichte, K. The Application of Mg-based Metal-Hydrides as Heat Energy Storage Systems. *Int. J. Hydrogen Energy* **2000**, *25*, 425−430.

(28) Shao, J.; Xiao, X. Z.; Fan, X. L.; Huang, X.; Zhai, B.; Li, S. Q.; Ge, H. W.; Wang, Q. D.; Chen, L. X. Enhanced Hydrogen Storage Capacity and Reversibility of $LiBH_4$ Nanoconfined in the Densified Zeolite-Templated Carbon with High Mechanical Stability. *Nano Energy* **2015**, *15*, 244−255.

(29) Hansen, B. R.; Ravnsbæk, D. B.; Skibsted, J.; Jensen, T. R. Hydrogen Reversibility of $LiBH_4$−MgH_2−Al Composites. *Phys. Chem. Chem. Phys.* **2014**, *16*, 8970−8980.

(30) Hansen, B. R.; Ravnsbæk, D. B.; Reed, D.; Book, D.; Gundlach, C.; Skibsted, J.; Jensen, T. R. Hydrogen Storage Capacity Loss in a $LiBH_4$−Al Composite. *J. Phys. Chem. C* **2013**, *117*, 7423−7432.

(31) Baumann, T. F.; Worsley, M. A.; Han, T. Y. J.; Satcher, J. H. High Surface Area Carbon Aerogel Monoliths with Hierarchical Porosity. *J. Non-Cryst. Solids* **2008**, *354*, 3513−3515.

(32) Al-Muhtaseb, S. A.; Ritter, J. A. Preparation and Properties of Resorcinol-Formaldehyde Organic and Carbon Gels. *Adv. Mater.* **2003**, *15*, 101−114.

(33) Lin, C.; Ritter, J. A. Carbonization and Activation of Sol-Gel Derived Carbon Xerogels. *Carbon* **2000**, *38*, 849−861.

(34) Riktor, M.; Sørby, M.; Chłopek, K.; Fichtner, M.; Buchter, F.; Züttel, A.; Hauback, B. In Situ Synchrotron Diffraction Studies of Phase Transitions and Thermal Decomposition of $Mg(BH_4)_2$ and $Ca(BH_4)_2$. *J. Mater. Chem.* **2007**, *17*, 4939−4942.

(35) De Boer, J.; Linsen, B.; Van der Plas, T.; Zondervan, G. Studies on Pore Systems in Catalysts: VII. Description of the Pore Dimensions of Carbon Blacks by the T Method. *J. Catal.* **1965**, *4*, 649−653.

(36) Brunauer, S.; Emmett, P. H.; Teller, E. Adsorption of Gases in Multimolecular Layers. *J. Am. Chem. Soc.* **1938**, *60*, 309−319.

(37) Barrett, E.; Joyner, L. Determination of Nitrogen Adsorption-Desorption Isotherms. *Anal. Chem.* **1951**, *23*, 791−792.

(38) Tian, H. Y.; Buckley, C. E.; Mule, S.; Paskevicius, M.; Dhal, B. B. Preparation, Microstructure and Hydrogen Sorption Properties of Nanoporous Carbon Aerogels under Ambient Drying. *Nanotechnology* **2008**, *19*, 475605.

DOI: 10.1021/acs.jpcc.7b06228
J. Phys. Chem. C 2017, 121, 18439−18449

(39) Nielsen, T. K.; Polanski, M.; Zasada, D.; Javadian, P.; Besenbacher, F.; Bystrzycki, J.; Skibsted, J.; Jensen, T. R. Improved Hydrogen Storage Kinetics of Nanoconfined NaAlH4 Catalyzed with $TiCl_3$ Nanoparticles. *ACS Nano* **2011**, *5*, 4056−4064.

(40) D'Anna, V.; Spyratou, A.; Sharma, M.; Hagemann, H. FT-IR Spectra of Inorganic Borohydrides. *Spectrochim. Acta, Part A* **2014**, *128*, 902−906.

(41) Rongeat, C.; D'Anna, V.; Hagemann, H.; Borgschulte, A.; Züttel, A.; Schultz, L.; Gutfleisch, O. Effect of Additives on the Synthesis and Reversibility of $Ca(BH_4)_2$. *J. Alloys Compd.* **2010**, *493*, 281−287.

(42) Li, H.-W.; Akiba, E.; Orimo, S.-I. Comparative Study on the Reversibility of Pure Metal Borohydrides. *J. Alloys Compd.* **2013**, *580*, S292−S295.

(43) Lee, Y.-S.; Filinchuk, Y.; Lee, H.-S.; Suh, J.-Y.; Kim, J. W.; Yu, J.-S.; Cho, Y. W. On the Formation and the Structure of the First Bimetallic Borohydride Borate, $LiCa_3(BH_4)(BO_3)_2$. *J. Phys. Chem. C* **2011**, *115*, 10298−10304.

(44) Pinkerton, F. E.; Meyer, M. S. Reversible Hydrogen Storage in the Lithium Borohydride—Calcium Hydride Coupled system. *J. Alloys Compd.* **2008**, *464*, L1−L4.

(45) Ngene, P.; van den Berg, R.; Verkuijlen, M. H. W.; de Jong, K. P.; de Jongh, P. E. Reversibility of the Hydrogen Desorption from $NaBH_4$ by Confinement in Nanoporous Carbon. *Energy Environ. Sci.* **2011**, *4*, 4108−4115.

(46) Kim, Y.; Hwang, S. J.; Shim, J. H.; Lee, Y. S.; Han, H. N.; Cho, Y. W. Investigation of the Dehydrogenation Reaction Pathway of $Ca(BH_4)_2$ and Reversibility of Intermediate Phases. *J. Phys. Chem. C* **2012**, *116*, 4330−4334.

(47) Bonatto Minella, C.; Pellicer, E.; Rossinyol, E.; Karimi, F.; Pistidda, C.; Garroni, S.; Milanese, C.; Nolis, P.; Baro, M. D.; Gutfleisch, O.; et al. Chemical State, Distribution, and Role of Ti- and Nb-Based Additives on the $Ca(BH_4)_2$ System. *J. Phys. Chem. C* **2013**, *117*, 4394−4403.

(48) Bonatto Minella, C.; Garroni, S.; Pistidda, C.; Gosalawit-Utke, R.; Barkhordarian, G.; Rongeat, C.; Lindemann, I.; Gutfleisch, O.; Jensen, T. R.; Cerenius, Y.; et al. Effect of Transition Metal Fluorides on the Sorption Properties and Reversible Formation of $Ca(BH_4)_2$. *J. Phys. Chem. C* **2011**, *115*, 2497−2504.

(49) Brun, N.; Janot, R.; Sanchez, C.; Deleuze, H.; Gervais, C.; Morcrette, M.; Backov, R. Preparation of $LiBH_4$@Carbon Micro-Macrocellular Foams: Tuning Hydrogen Release Through Varying Microporosity. *Energy Environ. Sci.* **2010**, *3*, 824−830.

(50) Cahen, S.; Eymery, J. B.; Janot, R.; Tarascon, J. M. Improvement of the $LiBH_4$ Hydrogen Desorption by Inclusion into Mesoporous Carbons. *J. Power Sources* **2009**, *189*, 902−908.

(51) Fang, Z. Z.; Wang, P.; Rufford, T. E.; Kang, X. D.; Lu, G. Q.; Cheng, H. M. Kinetic- and Thermodynamic-Based Improvements of Lithium Borohydride Incorporated into Activated Carbon. *Acta Mater.* **2008**, *56*, 6257−6263.

(52) Fang, Z. Z.; Kang, X. D.; Yang, Z. X.; Walker, G. S.; Wang, P. Combined Effects of Functional Cation and Anion on the Reversible Dehydrogenation of $LiBH_4$. *J. Phys. Chem. C* **2011**, *115*, 11839−11845.

(53) Guo, L. J.; Jiao, L. F.; Li, L.; Wang, Q. H.; Liu, G.; Du, H. Y.; Wu, Q.; Du, J.; Yang, J. Q.; Yan, C.; et al. Enhanced Desorption Properties of $LiBH_4$ Incorporated into Mesoporous TiO_2. *Int. J. Hydrogen Energy* **2013**, *38*, 162−168.

(54) Liu, X. F.; Peaslee, D.; Jost, C. Z.; Baumann, T. F.; Majzoub, E. H. Systematic Pore-Size Effects of Nanoconfinement of $LiBH_4$: Elimination of Diborane Release and Tunable Behavior for Hydrogen Storage Applications. *Chem. Mater.* **2011**, *23*, 1331−1336.

(55) Ngene, P.; Adelhelm, P.; Beale, A. M.; de Jong, K. P.; de Jongh, P. E. $LiBH_4$/SBA-15 Nanocomposites Prepared by Melt Infiltration under Hydrogen Pressure: Synthesis and Hydrogen Sorption Properties. *J. Phys. Chem. C* **2010**, *114*, 6163−6168.

(56) Wan, X. F.; Shaw, L. L. Novel Dehydrogenation Properties Derived from Nanoscale $LiBH_4$. *Acta Mater.* **2011**, *59*, 4606−4615.

(57) Ward, P. A.; Teprovich, J. A.; Peters, B.; Wheeler, J.; Compton, R. N.; Zidan, R. Reversible Hydrogen Storage in a $LiBH_4$-C_{60} Nanocomposite. *J. Phys. Chem. C* **2013**, *117*, 22569−22575.

(58) Wellons, M. S.; Berseth, P. A.; Zidan, R. Novel Catalytic Effects of Fullerene for $LiBH_4$ Hydrogen Uptake and Release. *Nanotechnology* **2009**, *20*, 204022.

(59) Xu, J.; Cao, J. Y.; Yu, X. B.; Zou, Z. Q.; Akins, D. L.; Yang, H. Enhanced Catalytic Hydrogen Release of $LiBH_4$ by Carbon-Supported Pt Nanoparticles. *J. Alloys Compd.* **2010**, *490*, 88−92.

(60) Xu, J.; Meng, R. R.; Cao, J. Y.; Gu, X. F.; Qi, Z. Q.; Wang, W. C.; Chen, Z. D. Enhanced Dehydrogenation and Rehydrogenation Properties of $LiBH_4$ Catalyzed by Graphene. *Int. J. Hydrogen Energy* **2013**, *38*, 2796−2803.

(61) Xu, J.; Yu, X. B.; Ni, J.; Zou, Z. Q.; Li, Z. L.; Yang, H. Enhanced Catalytic Dehydrogenation of $LiBH_4$ by Carbon-Supported Pd Nanoparticles. *Dalton Trans.* **2009**, 8386−8391.

(62) Yuan, P. P.; Liu, B. H.; Li, Z. P. A Comparative Study of $LiBH_4$-Based Composites with Metal Hydrides and Fluorides for Hydrogen Storage. *Int. J. Hydrogen Energy* **2011**, *36*, 15266−15272.

(63) Yuan, P. P.; Liu, B. H.; Zhang, B. J.; Li, Z. P. Reversible Hydrogen Storage Composite Based on $6LiBH_4 + CaF_2$. *J. Phys. Chem. C* **2011**, *115*, 7067−7075.

(64) Zhang, H.; Cao, Z.; Sun, L. X.; Sun, Y. J.; Xu, F.; Liu, H.; Zhang, J.; Huang, Z. Q.; Jiang, X.; Li, Z. B.; et al. Improved Dehydrogenation/Rehydrogenation Performance of $LiBH_4$ by Doping Mesoporous Fe_2O_3 or/and TiF_3. *J. Therm. Anal. Calorim.* **2013**, *112*, 1407−1414.

(65) Zhu, Y. Y.; Zou, J. X.; Zeng, X. Q. Study on Reversible Hydrogen Sorption Behaviors of $3LiBH_4$/Graphene and $3LiBH_4$/Graphene-10 wt% CeF_3 Composites. *RSC Adv.* **2015**, *5*, 82916−82923.

(66) Mauron, P.; Buchter, F.; Friedrichs, O.; Remhof, A.; Bielmann, M.; Zwicky, C. N.; Züttel, A. Stability and Reversibility of $LiBH_4$. *J. Phys. Chem. B* **2008**, *112*, 906−910.

(67) Li, Y.; Li, P.; Qu, X. Investigation on $LiBH_4$−CaH_2 Composite and Its Potential for Thermal Energy Storage. *Sci. Rep.* **2017**, *7*, 41754.

(68) Dicks, A. L. Molten Carbonate Fuel Cells. *Curr. Opin. Solid State Mater. Sci.* **2004**, *8*, 379−383.

(69) Harries, D. N.; Paskevicius, M.; Sheppard, D. A.; Price, T.; Buckley, C. E. Concentrating Solar Thermal Heat Storage Using Metal Hydrides. *Proc. IEEE* **2012**, *100*, 539−549.

(70) Sheppard, D. A.; Corgnale, C.; Hardy, B.; Motyka, T.; Zidan, R.; Paskevicius, M.; Buckley, C. E. Hydriding Characteristics of $NaMgH_2F$ with Preliminary Technical and Cost Evaluation of Magnesium-Based Metal Hydride Materials for Concentrating Solar Power Thermal Storage. *RSC Adv.* **2014**, *4*, 26552−26562.

(71) Fellet, M.; Buckley, C. E.; Sheppard, D. A.; Paskevicius, M. Research on Metal Hydrides Revived for Next-Generation Solutions to Renewable Energy Storage. *MRS Bull.* **2013**, *38*, 1012−1013.

(72) Sheppard, D. A.; Humphries, T. D.; Buckley, C. E. Sodium-based hydrides for thermal energy applications. *Appl. Phys. A: Mater. Sci. Process.* **2016**, *122*, 406.

(73) Ward, P. A.; Corgnale, C.; Teprovich, J. A.; Motyka, T.; Hardy, B.; Sheppard, D. A.; Buckley, C. E.; Zidan, R. Technical challenges and future direction for high-efficiency metal hydride thermal energy storage systems. *Appl. Phys. A: Mater. Sci. Process.* **2016**, *122*, 462.

(74) Humphries, T. D.; Sheppard, D. A.; Rowles, M. R.; Sofianos, M. V.; Buckley, C. E. Flouride Substitution in Sodium Hydride for Thermal Energy Storage Applications. *J. Mater. Chem. A* **2016**, *4*, 12170−12178.

(75) Javadian, P.; Sheppard, D. A.; Jensen, T. R.; Buckley, C. E. Destabilization of Lithium Hydride and the Thermodynamic Assessment of the Li-Al-H System for Solar Thermal Energy Storage. *RSC Adv.* **2016**, *6*, 94927−94933.

(76) El Kharbachi, A.; Pinatel, E.; Nuta, I.; Baricco, M. A Thermodynamic Assessment of $LiBH_4$. *CALPHAD: Comput. Coupling Phase Diagrams Thermochem.* **2012**, *39*, 80−90.

(77) Sangster, J.; Pelton, A. D. *H−Li (Hydrogen−Lithium) in Phase Diagram of Binary Hydrogen Alloys*; Manchester, F. D., Ed.; ASM International: Materials Park, OH, 2000; pp 74−81.

(78) Pardo, P.; Deydier, A.; Anxionnaz-Minvielle, Z.; Rouge, S.; Cabassud, M.; Cognet, P. A Review on High Temperature

The Journal of Physical Chemistry C Article

Thermochemical Heat Energy Storage. *Renewable Sustainable Energy Rev.* **2014**, *32*, 591−610.

DOI: 10.1021/acs.jpcc.7b06228
J. Phys. Chem. C 2017, 121, 18439−18449

Chapter 4: CONCLUSION

The presented work in this thesis examined potential HTMH and LTMH systems as thermal heat storage for implementation in Concentrated Solar Power systems. The aim was achieved by investigating destabilisation and the hydrogen absorption and desorption, kinetics and thermodynamics properties of the three complex metal hydride systems $LiBH_4$-$Ca(BH_4)_2$, $LiBH_4$-$NaBH_4$, and $LiBH_4$-$NaAlH_4$ and the simple metal hydride system LiH-Al.

4.1. **Li-Al-H**

High temperature metal hydrides have recently been considered as thermochemical heat storage media that can operate with the next generation of Concentrating Solar Thermal power (CST) plants operating at between 600 ºC and 800 ºC. Lithium hydride shows promise for thermal heat storage applications due to its high theoretical capacity (8397 kJ/kg) but its cost and operating temperature (> 950 ºC) are prohibitively high. In this work the properties and cost of lithium hydride destabilised by the addition of aluminium (1:1 mole ratio) were systematically studied and its suitability as a thermal energy storage system in Concentrating Solar Thermal power (CST) applications was assessed. Pressure composition temperature (PCT) isotherms at selected temperatures ranging between 506 ˚C and 652 ˚C were conducted to investigate the thermodynamics of H_2 release.

Below 596 ˚C, the hydrogen desorption enthalpy and entropy were measured as ΔH_{des} = 96.8 kJ/mol.H_2 and ΔS_{des} = 114.3 J/K·mol.H_2, respectively. Compared to pure LiH, the Li-Al-H system has a reduced operating temperature (1 bar H_2 pressure ~574 ˚C) that, combined with favourable attributes such as high reversibility, good kinetics and negligible hysteresis, makes the Li-Al-H system a potential candidate for solar thermal energy storage applications. Our analysis shows that, compared to pure LiH, the addition of Al can reduce the cost of the raw materials by up to 44 % for equivalent thermal storage capacities. While this cost reduction still falls short of the targets for thermal storage materials in next generation CST, it highlights the potential to improve the properties and cost of high temperature hydrides via destabilisation.

This work is of high novelty since it is the first thermodynamic investigation of the Li-Al-H system using pressure-composition-temperature (PCT) measurements over the full composition range spanning from LiAl to LiH + Al. The novelty of this experimental work is extended by exploring the Li-Al-H system as a thermal storage material for Concentrating Solar-Thermal power (CST) systems and the cost savings available compared to the pure Li-H system.

From a fundamental perspective, it provides experimental thermodynamic data that can contribute to the assessment of the Li-Al binary phase diagram. It also explores properties of the Li-Al-H system relevant to engineering applications such as the shape of the absorption/desorption plateau, hysteresis between hydrogen absorption and desorption as well the kinetics of hydrogen absorption/desorption.

In particular, it demonstrates a generalised means to alter the properties and, most importantly, the cost of high temperature hydrides to bring them one step closer to practical application. It presents the experimental thermodynamic assessment of the Li-Al-H system and uses these results as a basis for its economic assessment as a thermochemical heat storage material for CST systems. As such, this work bridges the gap between research, development and implementation.

4.2. **$LiBH_4$-$NaBH_4$**

The hydrogen storage properties of the eutectic melting metal borohydrides, $0.62LiBH_4$-$0.38NaBH_4$, nanoconfined in two carbon aerogel scaffolds with different surface area and pore volumes (pristine and CO_2-activated) are presented and compared to the bulk properties. This study shows that CO_2-activated carbon aerogel stabilizes the metal hydride and a lower amount of borates and oxides are formed during melt infiltration and cycling hydrogen release and uptake. We conclude, that the CO_2-activated scaffold is more inert, provides faster kinetics and higher stability over several cycles of hydrogen release and uptake and has the potential to provide useful hydrogen storage densities in the range ~11 wt% H_2.

The eutectic composite $LiBH_4$-$NaBH_4$ melts from ~200 °C, and the majority of the H_2 desorption (7.56 wt.% H_2) occurs in the temperature range between 350 – 500 °C, when measured in argon flow ($\Delta T/\Delta t$ = 2 °C /min).

4.3. **$LiBH_4$-$NaAlH_4$**

Nanoconfinement of $2LiBH_4$–$NaAlH_4$ into a mesoporous carbon aerogel scaffold with an average pore size of D_{max} = 30 nm and surface area S_{BET} = 689 m^2/g is investigated. Nanoconfinement of $2LiBH_4$–$NaAlH_4$ facilitates a reduction in the temperature of the hydrogen release by 132 °C, compared to that of bulk $2LiBH_4$–$NaAlH_4$ and the onset of hydrogen release is below 100 °C. The reversible hydrogen storage capacity is also significantly improved for the nanoconfined sample, maintaining 83 % of the initial hydrogen content after three cycles compared to 47 % for that of the bulk sample. During nanoconfinement, $LiBH_4$ and $NaAlH_4$ reacts to form $LiAlH_4$ and $NaBH_4$ and the final dehydrogenation products, obtained at 481 °C are LiH, LiAl, AlB_2 and Al. After rehydrogenation of the nanoconfined sample at T = 400 °C and $p(H_2)$ = 126 bar, amorphous $NaBH_4$ is recovered along with unreacted LiH, AlB_2 and Al, which suggests that $NaBH_4$ is the main compound that can reversibly release and uptake hydrogen.

4.4. **$LiBH_4$-$Ca(BH_4)_2$**

The eutectic binary complex borohydride composite $LiBH_4$-$Ca(BH_4)_2$ melts at ~200 °C with a minor quantity of decomposition when heated in argon flow. The decomposition may be suppressed by melting under H_2 pressure, as was done during melt infiltration into a nanoporous carbon scaffold.

The major initial release of H_2 occurs in the temperature range between 340 – 450 °C under argon flow (heating rate: $\Delta T/\Delta t$ = 2 °C /min), corresponding to 12 wt% (96 % of the available H_2 content). The activation energy, E_{act}, for the majority of the H_2 was found to be E_{act} = 204 kJ/mol, which was estimates from DSC data. However, the presence of carbon, lowered the activation energy down to E_{act} = 130 kJ/mol due to destabilization effects of the carbon. It was found that $LiBH_4$-$Ca(BH_4)_2$ is a reversible system. The cyclic stability during H_2 release and uptake cycling retained 8 wt.% H_2/sample during the third desorption cycle, corresponding to 73 % of the initial hydrogen storage capacity (11 wt% H_2), when heated to 500 °C. The effect of employing the nanoporous carbon scaffold was minimal in term of improved stability, as the desorption profiles during cycling looked similar to the bulk system. Therefore, no justification for employing the carbon scaffold can be made in this system. The large decrease after first desorption, was due to stable impurity formation such as CaB_6 and CaO, which were not reforming $Ca(BH_4)$ under the applied rehydrogenation conditions (T = 400 °C and $p(H_2)$ = 140 for 10 h). The second part of the investigation on the $LiBH_4$-$Ca(BH_4)_2$ was aimed to optimize the system by improving the reversibility and conduct more than 3 cycles to determine if full reversibility could be obtained by changing the rehydrogenation conditions (T = 500 °C, $p(H_2)$ = 134 for 10 h). By increasing the temperature of rehydrogenation to 500 °C significantly improved the reversibility compared to rehydrogenation at 400 °C.

The full reversibility of $LiBH_4$ combined with its low mass means that it may have an application as a high performance heat storage material. At 727 °C, pure $LiBH_4$ has one of the highest known heat storage capacities, 4936 kJ/kg, with a mild hydrogen equilibrium press of 13.2 bar. Even taking into account the additional mass starting from $Ca(BH_4)_2$, the practical heat storage capacity is 2964 kJ/kg.

Hydrogen release (at T = 500 °C, $p(H_2)$ = 1 - 8 bar for 10 hours) and uptake (at T = 500 °C, $p(H_2)$ = 134 - 144 bar for 10 hours) was repeated 5 times. After five cycles of hydrogen release and uptake of bulk and nanoconfined $0.68LiBH_4$−$0.32Ca(BH_4)_2$ a cyclic stability of 5.4 and 3.7 wt.% H_2 remain in the sample, which corresponds to 51 and 57 % of the initial hydrogen storage capacity. Our study shows an improved stability of the reversible hydrogen storage capacity for the metal borohydride composite compared to that previously reported (Javadian, Sheppard, et al. 2015a). This stability originates from the reversibility of $LiBH_4$ formation during each cycle. An irreversible capacity loss is formed after the first H_2 desorption, followed by a stable reversible H_2 capacity. Our analysis suggests that the stable H_2 capacity is entirely due to full reversibility of the $LiBH_4$ in the sample. This $LiBH_4$ reversibility occurs at significantly lower temperature and pressure conditions than previously reported (Orimo et al. 2005). A portion of $Ca(BH_4)_2$ is preferentially oxidised and the reversibility of $LiBH_4$ requires the decomposition products of $Ca(BH_4)_2$ without directly taking part in the reaction. The decomposition products may act to disperse $LiBH_4$ and prevent agglomeration and aggregation of $LiBH_4$ decomposition products.

Chapter 5: FUTURE WORK

5.1. **LiH-Al**

The discrepancies of the result from measurements above 600 °C needs to be understood, as these result seem to have a random outcome. Sometimes a full PCT is obtained while other times the plateau is short. This may be due to segregation, as above ~595 °C part of the system may be liquid depending on composition. A possible reason for why this is occurring on a random basis, could be due to a temperature gradient from the external heat source, which doesn't allow homogenous heat distribution into the sample. The phase segregation also forms an inhomogeneous sample composite, which generates uneven hydrogen diffusion throughout the sample.

5.2. **$LiBH_4$-$NaAlH_4$ / $LiBH_4$-$NaBH_4$**

The effect of carbon improves the cyclic stability of the $LiBH_4$-$NaAlH_4$ system. Unfortunately, only 3 desorption cycles were done and no clear stability was shown from only three desorption cycles. Therefore, more cycles are required to determine when full stability can be obtained. The added amount of $LiBH_4$-$NaAlH_4$ confined inside the scaffold, corresponds to 33 vol.%, which gave rise to 2 wt% H_2 from the sample (7.9 wt% / LiNa) after the third desorption. By considering a 100 vol.% pore filling of the same scaffold could potentially release 6 wt.% from the sample during the third desorption.

Similarly, in the $LiBH_4$-$NaBH_4$, the added amount of $LiBH_4$-$NaBH_4$ confined inside the scaffold, corresponds to 60 vol.%, which gave rise to 4.3 wt% H_2 from the sample (7.7 wt% / LiNa) after the fourth desorption. By considering a 100 vol.% pore filling of the same scaffold could potentially release > 7 wt% from the sample during the fourth desorption. However, the difference between $LiBH_4$-$NaAlH_4$ and the $LiBH_4$-$NaBH_4$, is that $LiBH_4$-$NaBH_4$, is already stable after the first desorption.

5.3. **$LiBH_4$-$Ca(BH_4)_2$**

The interesting results obtained from this leave room for optimization of the different systems. For instance the future work of the $LiBH_4$-$Ca(BH_4)_2$ would entail the investigation of the minimum amount of $Ca(BH_4)_2$ needed to make $LiBH_4$ fully reversible. This may be done by adjusting the $LiBH_4$-$Ca(BH_4)_2$ composition. Furthermore, to investigate if the formation of the eutectic is a requirement to make the decomposition products intimately mixed, which then allows reversibility.

Another important consideration is to determine if rehydrogenation of $LiBH_4$ can be obtained at temperatures above 500 °C using lower H_2 pressure than the ~130 - 140 bar used at 500 °C. For example, the theoretical H_2 equilibrium pressure at 727 °C is only about 13 bar, so ideally lower pressures should be possible.

APPENDIX I: Supplementary Information of all publications

Supplementary Information of "Destabilization of lithium hydride and the thermodynamic assessment of the Li-Al-H system for solar thermal energy storage"

Destabilization of lithium hydride and the thermodynamic assessment of the Li-Al-H system for solar thermal energy storage

Payam Javadian,[1] Drew A. Sheppard,[1]* Torben R. Jensen,[2] Craig E. Buckley,[1]

[1] Department of Physics and Astronomy, Curtin University of Technology, GPO Box U 1987, Perth, Western Australia 6845, Australia

[2] Center for Energy Materials, Interdisciplinary Nanoscience Center (iNANO), and Department of Chemistry, Aarhus University, DK-8000 Aarhus, Denmark

* Corresponding author: drew.sheppard@gmail.com

Drew A. Sheppard, Ph.D.,
Post Doctoral Research Fellow | Fuels and Energy Technology Institute
Department of Physics and Astronomy

Curtin University
Tel | +61 8 9266 1381
Fax | +61 8 9266 2377
Mobile | 0406 966 146

Email | drew.sheppard@gmail.com

Table S1. Possible reactions taking place at the various temperatures and the respective H_2 capacities. These reactions are determined according to the Li-Al phase diagram.

Temperature	Reaction	wt.% H_2
506	$2\ LiH + 3.23Li_{0.126}Al_{0.874} \rightarrow 5.23Li_{0.46}Al_{0.54} + H_2$	2.12
540	$2\ LiH + 3.28Li_{0.131}Al_{0.869} \rightarrow 5.28Li_{0.46}Al_{0.54} + H_2$	2.10
560	$2\ LiH + 3.40Li_{0.142}Al_{0.858} \rightarrow 5.40Li_{0.46}Al_{0.54} + H_2$	2.06
573	$2\ LiH + 3.42Li_{0.144}Al_{0.856} \rightarrow 5.42Li_{0.46}Al_{0.54} + H_2$	2.05
585	$2\ LiH + 3.48Li_{0.150}Al_{0.850} \rightarrow 5.48Li_{0.46}Al_{0.54} + H_2$	2.03

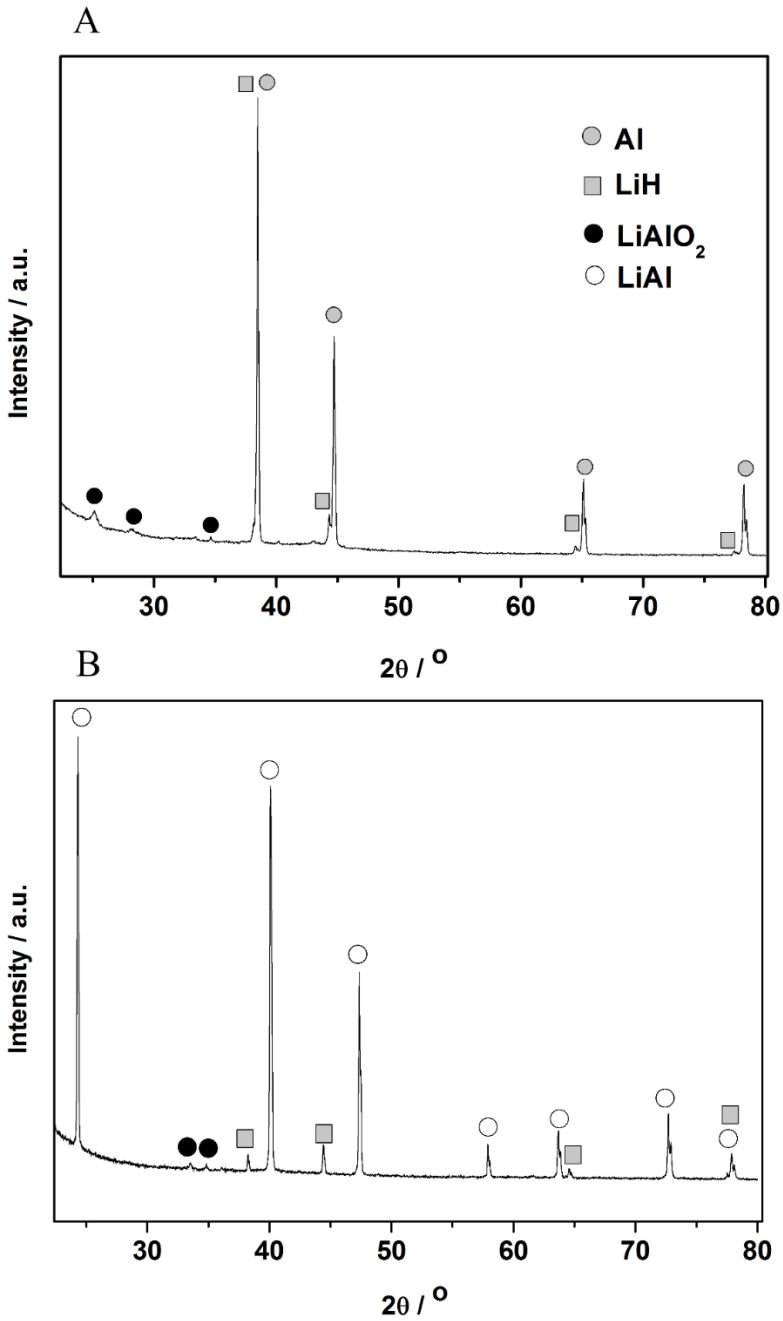

Figure S1 Powder X-ray diffraction pattern of the Li-Al-H sample after rehydrogenation at 618 ˚C (A) and after desorption (B).

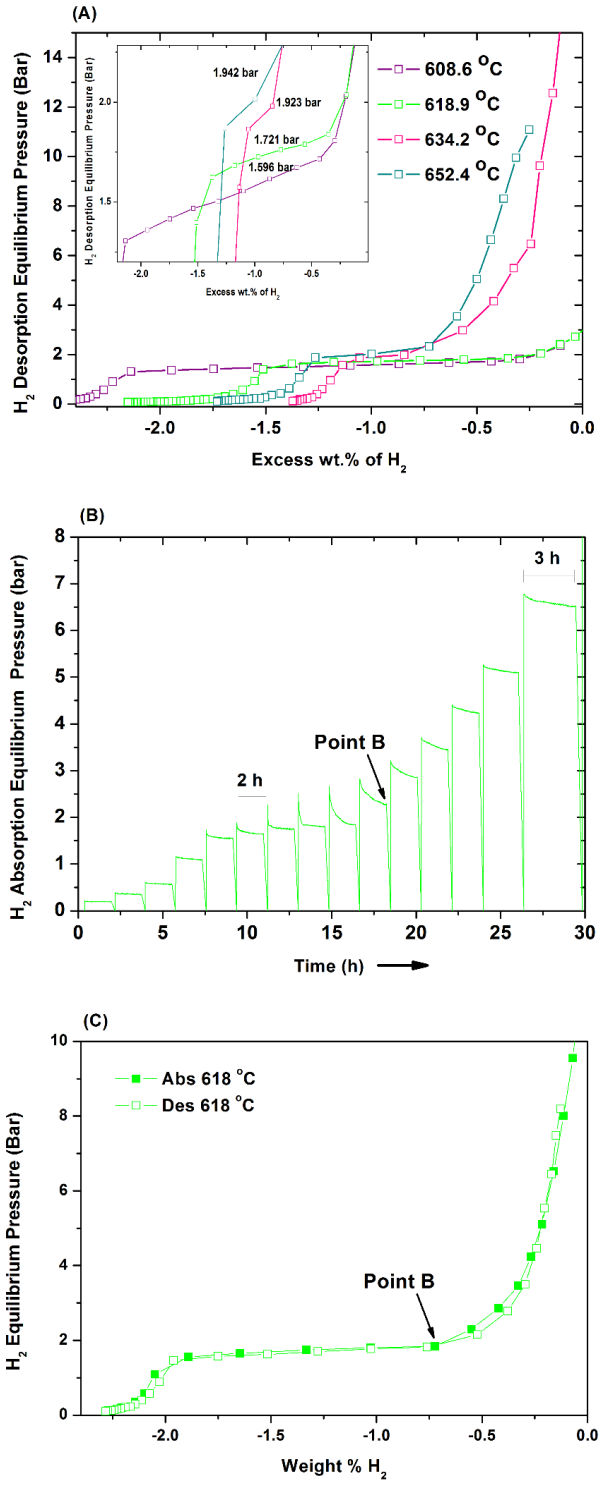

Figure S2. (a) Hydrogen desorption pressure – composition isotherms for reaction (2) performed at various temperatures above 600 ˚C. Hydrogen desorption equilibrium data below ~2.5 wt.% desorption has been displayed, and the inset of the figure provides the apparent equilibrium pressures. (b) Kinetic H_2 absorption data performed at 617.8 ˚C. (c) Desorption PCT followed by an absorption PCT performed at 617.8 ˚C. The slight hysteresis between the two curves either side of the plateau is the result of slow kinetics.

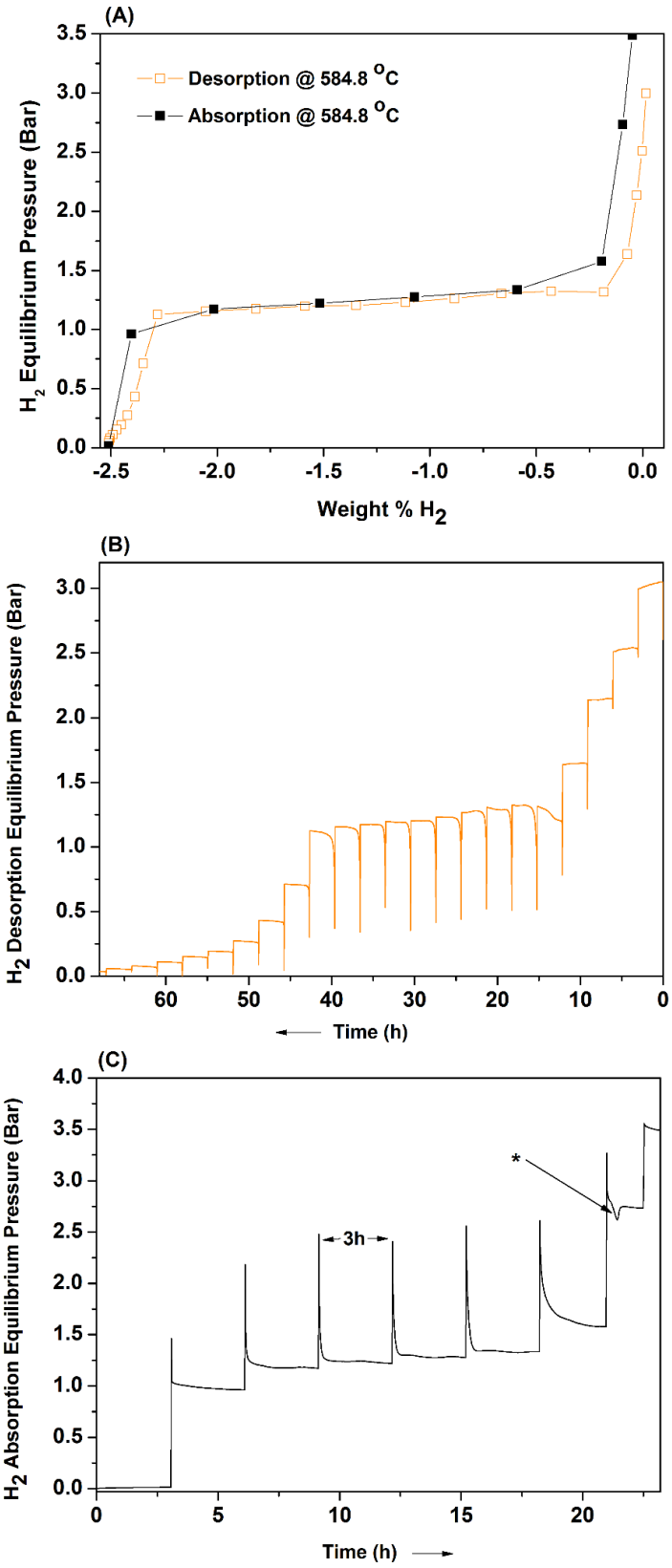

Figure S3 (A) Desorption-Absorption PCT at 585 ˚C. The respective desorption kinetics (B) and absorption kinetics (C) are also displayed. * is due to a sudden temperature fluctuation which caused and artict in the last step.

Supplementary Information of "Hydrogen storage properties nanoconfined $LiBH_4$-$NaBH_4$"

Hydrogen storage properties of nanoconfined $LiBH_4$-$NaBH_4$

Payam Javadian,[1,2] Drew A. Sheppard,[2] Craig E. Buckley,[2] Torben R. Jensen[1*]

[1] Center for Energy Materials, Interdisciplinary Nanoscience Center (iNANO), and Department of Chemistry, Aarhus University, DK-8000 Aarhus, Denmark

[2] Department of Imaging and Applied Physics, Curtin University, GPO Box U 1987, Perth, Western Australia 6845, Australia

* Corresponding author: trj@chem.au.dk (T. R. Jensen)

Torben R. Jensen, Dr. Scient., Associate Professor
iNANO and Department of Chemistry
Langelandsgade 140
DK-8000 Aarhus C
Aarhus University
Denmark
Phone: +45 87155939
mobile: +45 2272 1486
Fax: +45 8619 6199
E-mail: trj@chem.au.dk

Nitrogen sorption analysis

Table S1 Structure parameters of 0.62LiBH4-0.38NaBH4 (LiNa) post melt infiltrated into CA.

Scaffold	S_{BET} (m^2/g)	V_{micro} (mL/g)	V_{meso} (mL/g)	V_{tot} (mL/g)	D_{max} (nm)
CA-4-LiNa	101 ± 12	0.01 ± 0.02	0.57 ± 0.09	0.58 ± 0.14	19 ± 0.4

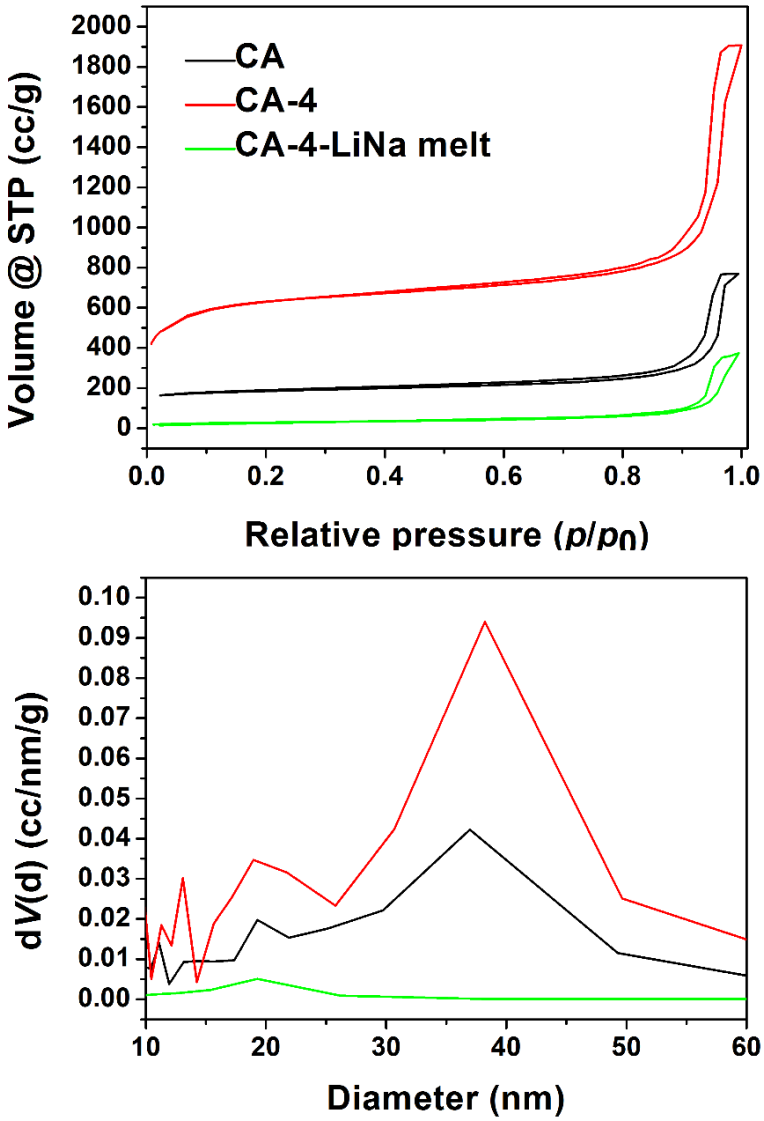

Figure S1. (Top) Nitrogen sorption isotherms and (bottom) BJH desorption profiles of pristine CA (black), pristine CA-4 (red) and LiBH4-NaBH4 nanoconfined into CA-4 (green).

Activation Energy Determination

The Kissinger plots presented in the manuscript are based on DSC data. The calculated activation energies, E_A, are found from the hydrogen desorption profile at which the major desorption event is exhibited. The bulk and nanoconfined samples have been heated from RT to 500 °C at heating rates of β = 2, 5, 10, 15 °C/min, and from the DSC curves the temperature of the endothermic event assigned to the major hydrogen desorption (peak "**d**′" from figure 2 in the article), T_p, is used for the Kissinger plots. Figure S1 illustrates how E_A is found for sample CA. T_p is taking place at 316, 349, 361 and 372 °C, at 2, 5, 10, 15 °C/min, respectively and is plotted as shown in the figure (note T_p is in K). The activation energy, E_A, is related to the slope of the Kissinger plot and the ideal gas constant (R) in J/mol·K. In this example E_A = 116 kJ/mol.

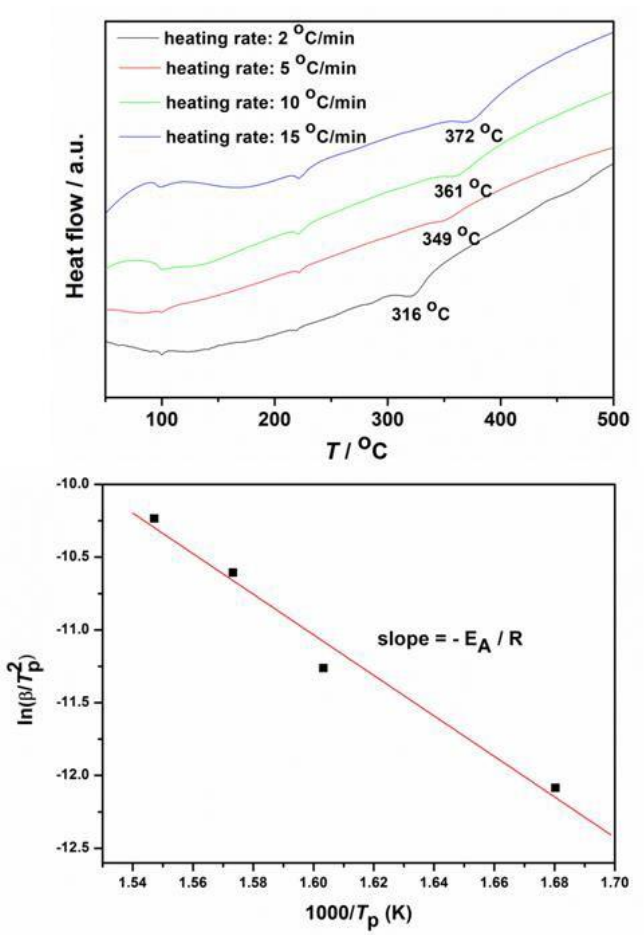

Figure S2 (Top) DSC profile of sample nanoconfined LiNa in CA that is heated at 50 to 500 °C, at heating rates of β = 2, 5, 10, 15 °C/min, respectively. (Bottom) Kissinger plot based on the four temperatures from the top figure at which the maximum hydrogen desorption is taking place (316, 349, 361 and 372 °C).

Temperature programmed desorption mass spectroscopy (TPD-MS)

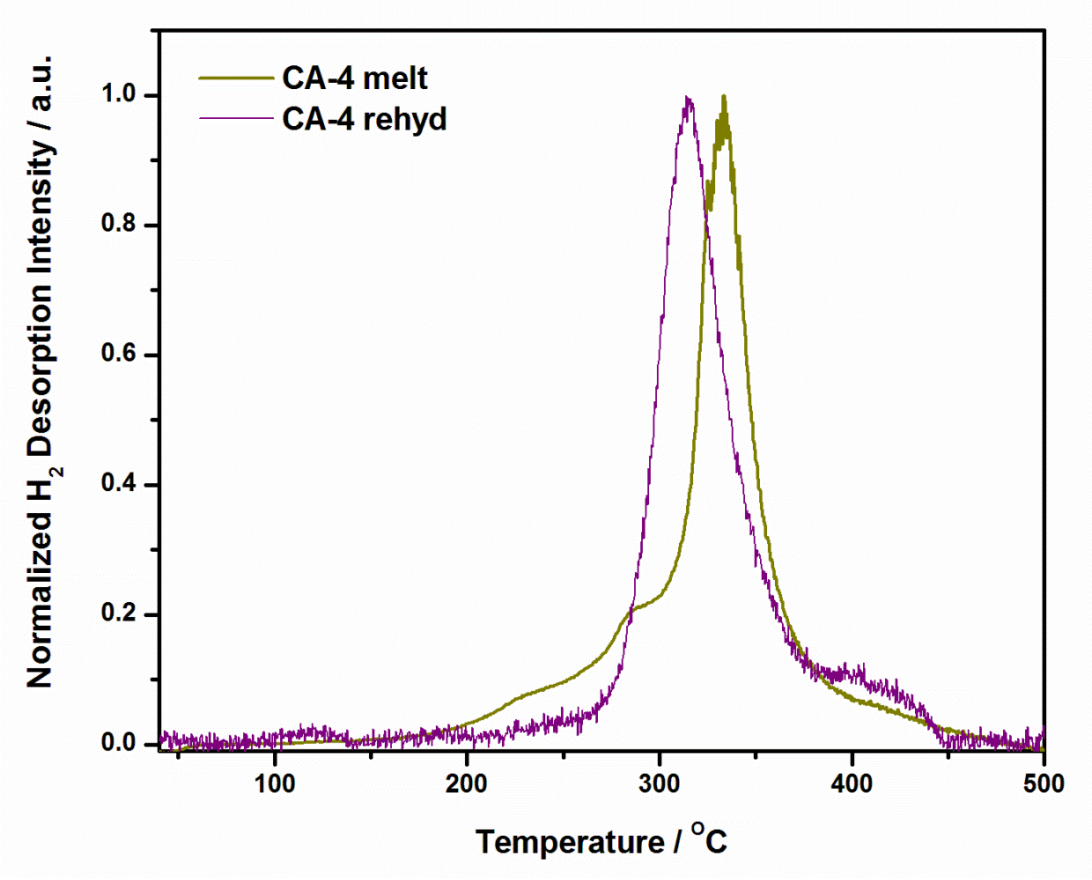

Figure S3 TPD-MS data profiles of 0.62LiBH4-0.38NaBH4 (LiNa) melt infiltrated into CA-4 (green) and the same sample rehydrogenated for 10 h at 400 °C after four desorption cycles (violet). Samples are heated from 40 to 500 °C ($\Delta T/\Delta t$ = 2 °C/min). The mass spectroscopy detected the H2 signals (m/e = 2).

Supplementary Information of "Hydrogen desorption properties of $LiBH_4$-$NaAlH_4$: Bulk vs Nanoconfined"

Hydrogen desorption properties of $LiBH_4$-$NaAlH_4$: Bulk vs. Nanoconfined

Payam Javadian,[1,2] Drew A. Sheppard,[2] Craig E. Buckley,[2] Torben R. Jensen[1]*

[1] Center for Energy Materials, Interdisciplinary Nanoscience Center (iNANO), and Department of Chemistry, Aarhus University, DK-8000 Aarhus, Denmark

[2] Department of Imaging and Applied Physics, Curtin University, GPO Box U 1987, Perth, Western Australia 6845, Australia

* Corresponding author: trj@chem.au.dk (T. R. Jensen)

Torben R. Jensen, Dr. Scient., Associate Professor
iNANO and Department of Chemistry
Langelandsgade 140
DK-8000 Aarhus C
Aarhus University
Denmark
Phone: +45 87155939
mobile: +45 2272 1486
Fax: +45 8619 6199
E-mail: trj@chem.au.dk

Nitrogen sorption analysis

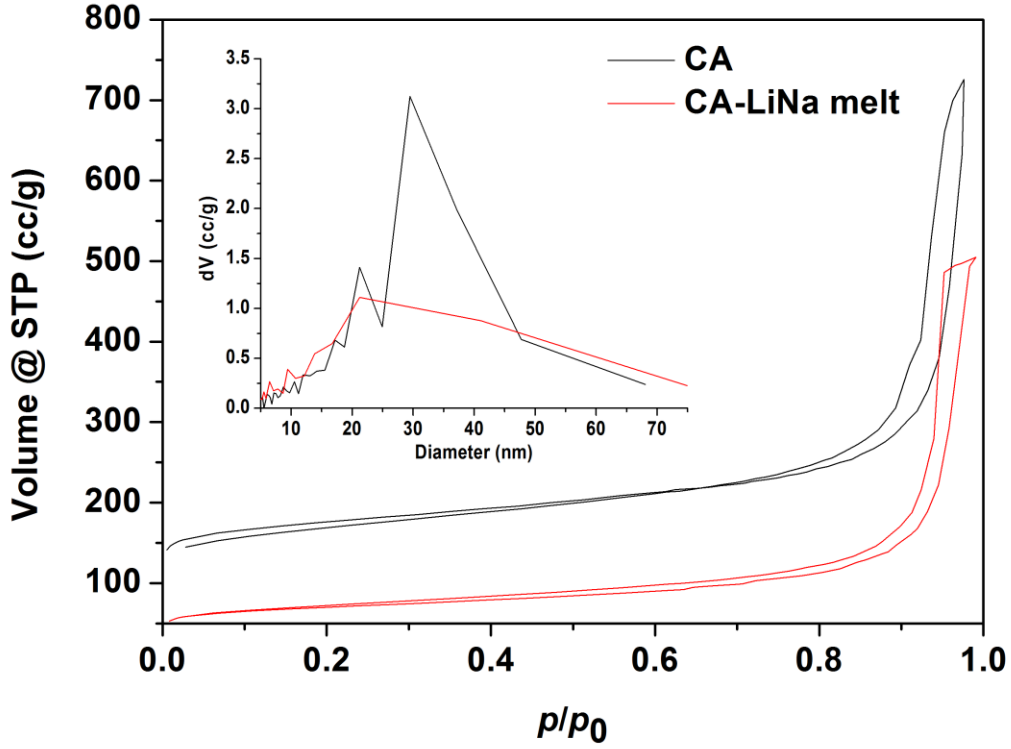

Figure S1. Nitrogen ad- and desorption measurements of the pristine aerogel scaffold (black) and $LiBH_4$-$NaAlH_4$ melt infiltrated into CA (red). The accumulated volume of N_2 versus the pore size destribution is also displayed.

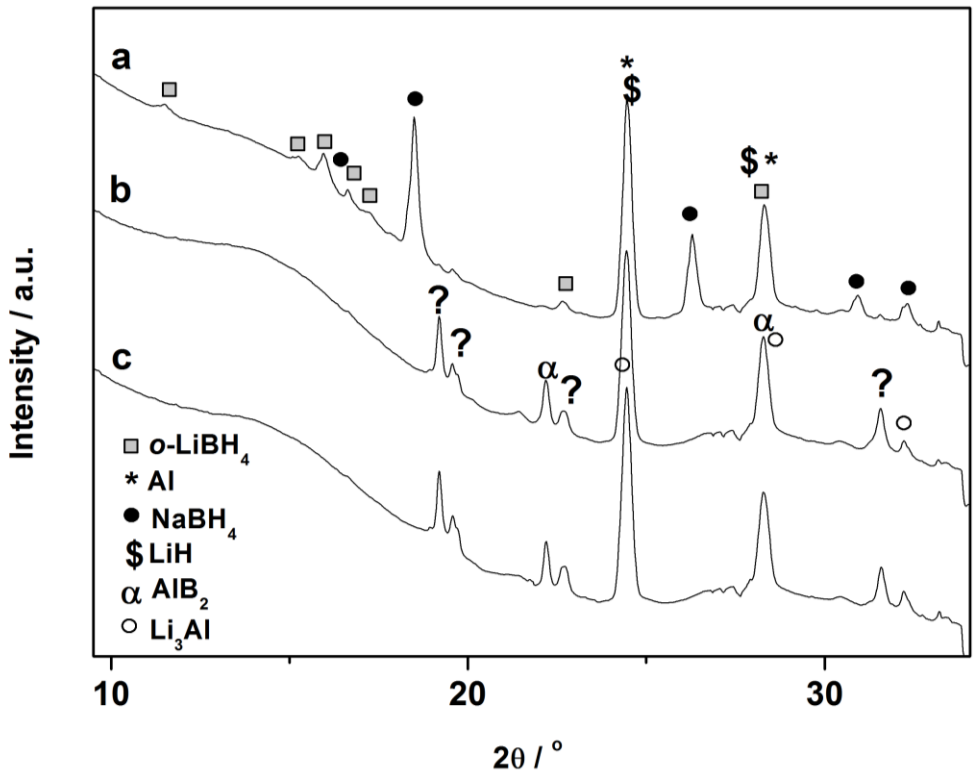

Figure S2 Ex-situ SR-PXD of CA + $2LiBH_4$-$NaAlH_4$ a) after melt infiltration, b) after dehydrogenation at temperatures reaching 400 ˚C under $p(H_2)$ = 1 bar and c) after absorption at temperatures reaching 343 ˚C under $p(H_2)$ = 130 bar. ($\Delta T/\Delta t$ = 5 ˚C/min λ = 0.991779 Å).

***In situ* SR-PXD Difference plots**

In the systems studied a large number of phases often simultaneously formed and decomposed. Many of the phase transitions involved relatively weak peak intensities in patterns dominated by peaks from one or two very intense phases. This made identification of the weak phases difficult and so derivative technique was applied to identify when weakly scattering phases form and decompose. This was achieved by importing the intensities of X-ray patterns at each temperature into the software Igor Pro [1] and constructing a two dimensional matrix of intensities. A 5 x 5 Gaussian smoothing algorithm was first applied to the matrix to help reduce noise in the background and then the derivative along the temperature direction was taken at each 2θ value. The resulting two dimensional surfaces contain positive peaks that correspond to phase formation and negative peaks that correspond to phase decomposition. In order to aid in visualisation, plots contain both the derivative and the negative of the derivative. The resulting data (Fig S3 and S4) are displayed so that only the positive intensity peaks are visible which are then colour coded to differentiate between peaks that correspond to phase formation (blue coloured peaks) and decomposition (red coloured peaks), respectively. Where there is no change between sequential patterns, the difference plot intensity is usually zero (white coloured) but parallel blue and red lines can also occur that are indicative of the thermal expansion of a phase. Henceforth these plots shall be referred to generically as difference plots.

[1] Igor Pro v 6.3.6.4, Copyright 1988 - 2014, WaveMetrics, Inc, Oregon, USA, www.wavemetrics.com

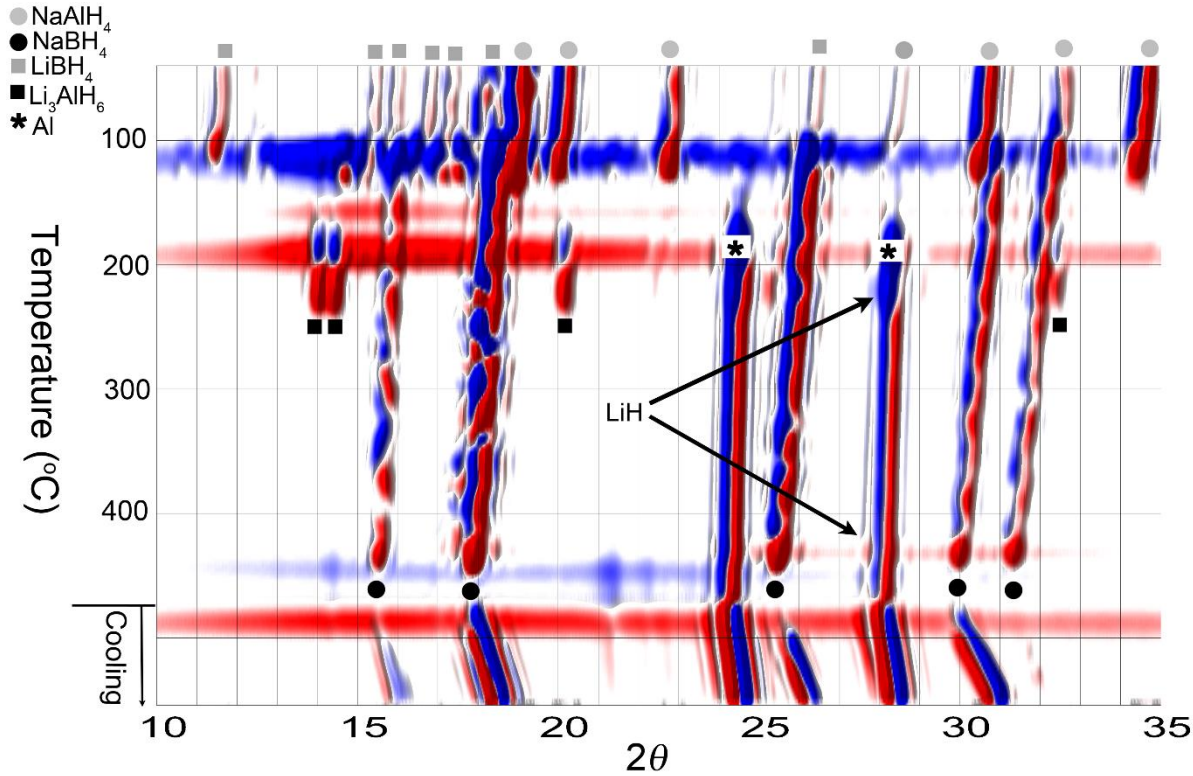

Figure S3 *In situ* SR-PXD difference plot of bulk $2LiBH_4$-$NaAlH_4$ during dehydrogenation from RT to 487 °C, with subsequent natural cooling to RT in $p(H_2)$ = 1 bar. ($\Delta T/\Delta t$ = 5 °C /min, λ = 0.991779 Å)

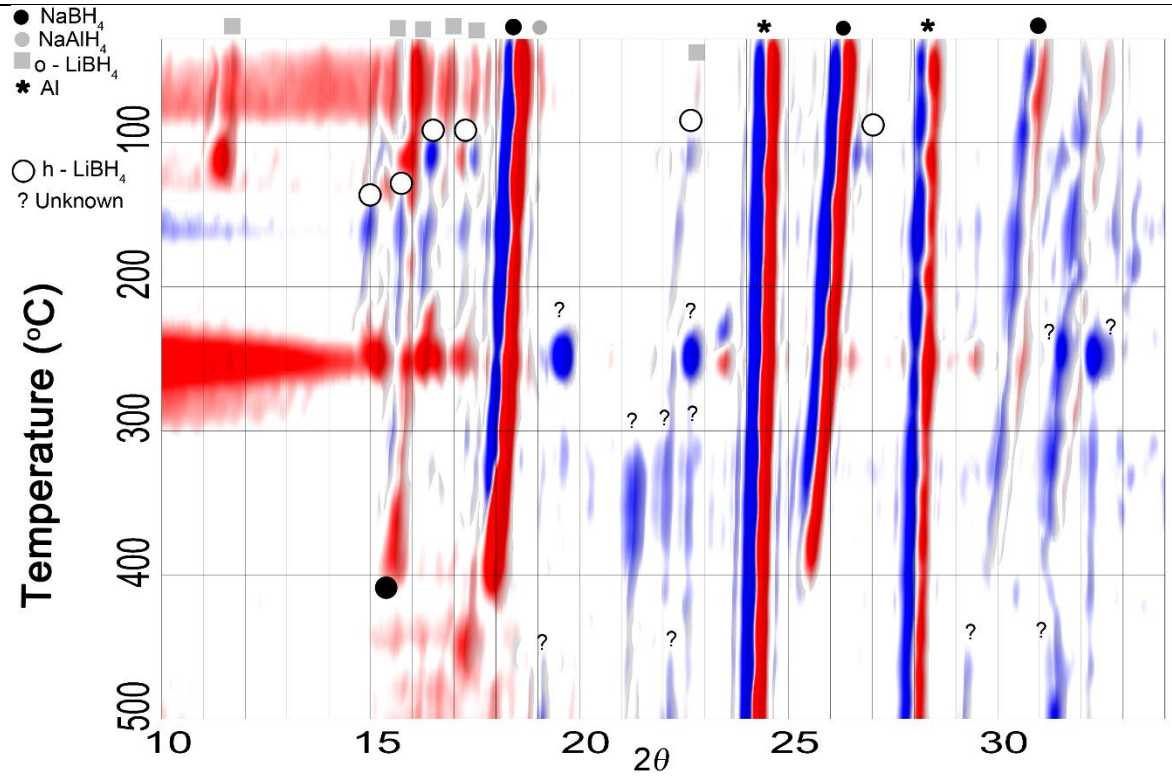

Figure S4 *In situ* SR-PXD difference plot of nanoconfined $2LiBH_4$-$NaAlH_4$ in CA heated from RT to 500 °C,. ($\Delta T/\Delta t$ = 5 °C /min, λ = 0.991779 Å)

Table S1. Data obtained from the Sieverts' measurements for the bulk (LiNa) and nanoconfined (CA-LiNa) sample displaying the release of hydrogen relative to the amount of hydride in the sample and relative to the mass of sample (in brackets), i.e. including the mass of inert carbon aerogel, during each desorption cycle. The data is shown in Figure 3.

Sample	1.des/LiNa wt.% H_2 (1.des/sample wt.% H_2)	2.des/LiNa wt.% H_2 (2.des/sample wt.% H_2)	3.des/LiNa wt.% H_2 (3.des/sample wt.% H_2)	4.des/LiNa wt.% H_2 (4.des/sample wt.% H_2)
LiNa	8.4 (-)	4.7(-)	3.9 (-)	3.4 (-)
CA-LiNa	9.6 (2.4)	9.2 (2.3)	7.8 (2.0)	-

Supplementary Information of "Hydrogen storage properties of nanoconfined $LiBH_4$-$Ca(BH_4)_2$"

Hydrogen storage properties of nanoconfined $LiBH_4$-$Ca(BH_4)_2$

Payam Javadian,[1,2] Drew A. Sheppard,[2] Craig E. Buckley,[2] Torben R. Jensen[1]*

[1] Center for Energy Materials, Interdisciplinary Nanoscience Center (iNANO), and Department of Chemistry, Aarhus University, DK-8000 Aarhus, Denmark

[2] Department of Imaging and Applied Physics, Curtin University of Technology, GPO Box U 1987, Perth, Western Australia 6845, Australia

* Corresponding author: trj@chem.au.dk (T. R. Jensen)

Torben R. Jensen, Dr. Scient., Associate Professor
iNANO and Department of Chemistry
Langelandsgade 140
DK-8000 Aarhus C
Aarhus University
Denmark
Phone: +45 87155939
mobile: +45 2272 1486
Fax: +45 8619 6199
E-mail: trj@chem.au.dk

Activation Energy Determination

The Kissinger plots presented in the manuscript are based on DSC data. The calculated activation energies, E_A, are found from the hydrogen desorption profile at which the major desorption event is exhibited. The bulk and nanoconfined samples have been heated from RT to 500 °C at heating rates of β = 3, 6 and 9 °C, and from the DSC curves the temperature of the exothermic event assigned to the major hydrogen desorption (peak **C´** from figure 2 in the article), T_p, is used for the Kissinger plots. Figure S1 illustrates how E_A is found for sample CA-6. T_p is taking place at 316, 330 and 340 °C, at 3, 6 and 9 °C/min, respectively and is plotted as shown in the figure (note T_p is in °K). The activation energy, E_A, is related to the slope of the Kissinger plot and the ideal gas constant (R) in J/mol·K. In this example E_A = 130 KJ/mol.

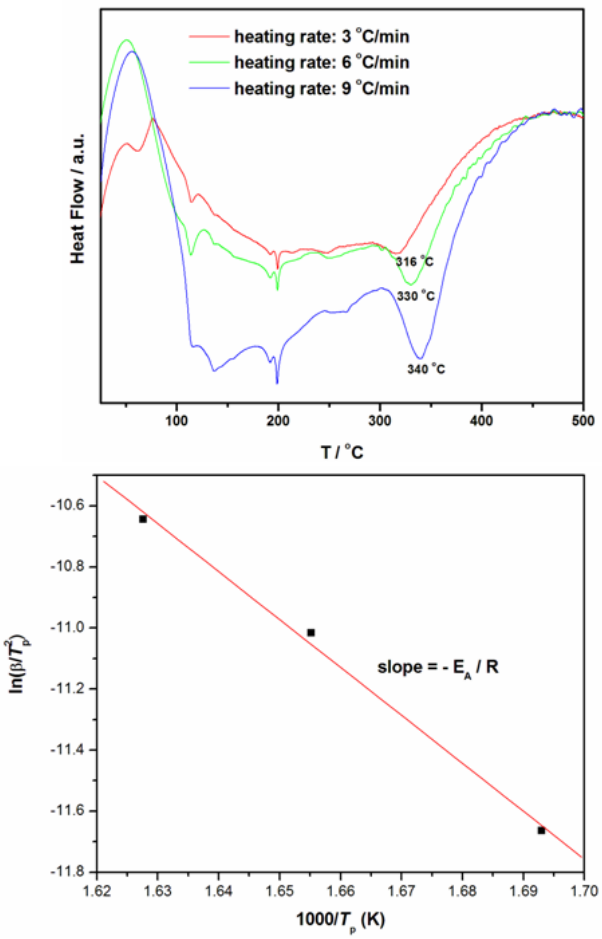

Figure S 1 (Top) DSC profile of sample nanoconfined LiCa in CA-6 that is heated at RT to 500 °C, at heating rates of β = 3, 6, 9 °C/min, respectively. (Bottom) Kissinger plot based on the three temperatures from the top figure at which the maximum hydrogen desorption is taking place (316, 330 and 340 °C).

Powder X-ray diffraction

The peaks that belongs to the unknown compound **1** has been indexed, and we find that it has a cubic crystal structure.

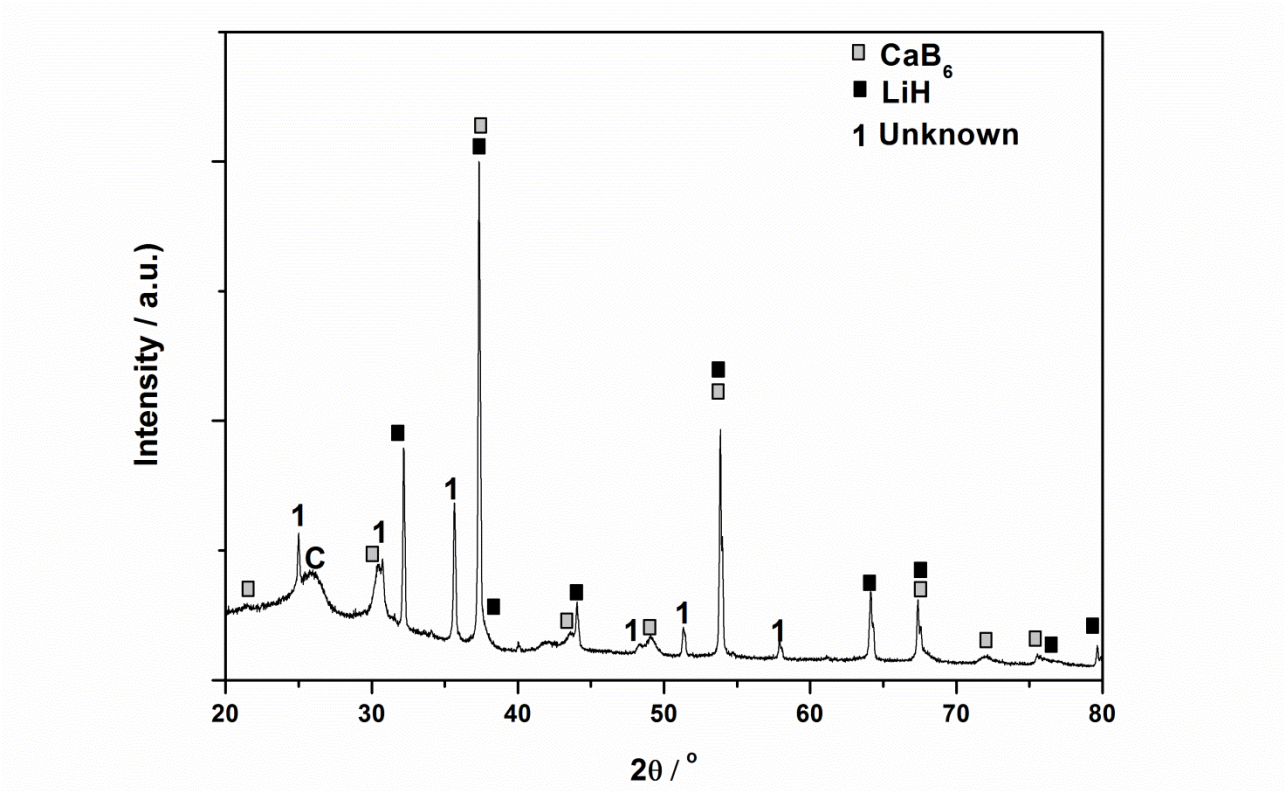

Figure S2 Powder X-ray diffraction of sample CA-6 after rehydrided at 400 ^{O}C and $p(H_2)$ = 140 bar during 10 hours

Non-normalized TPD-MS

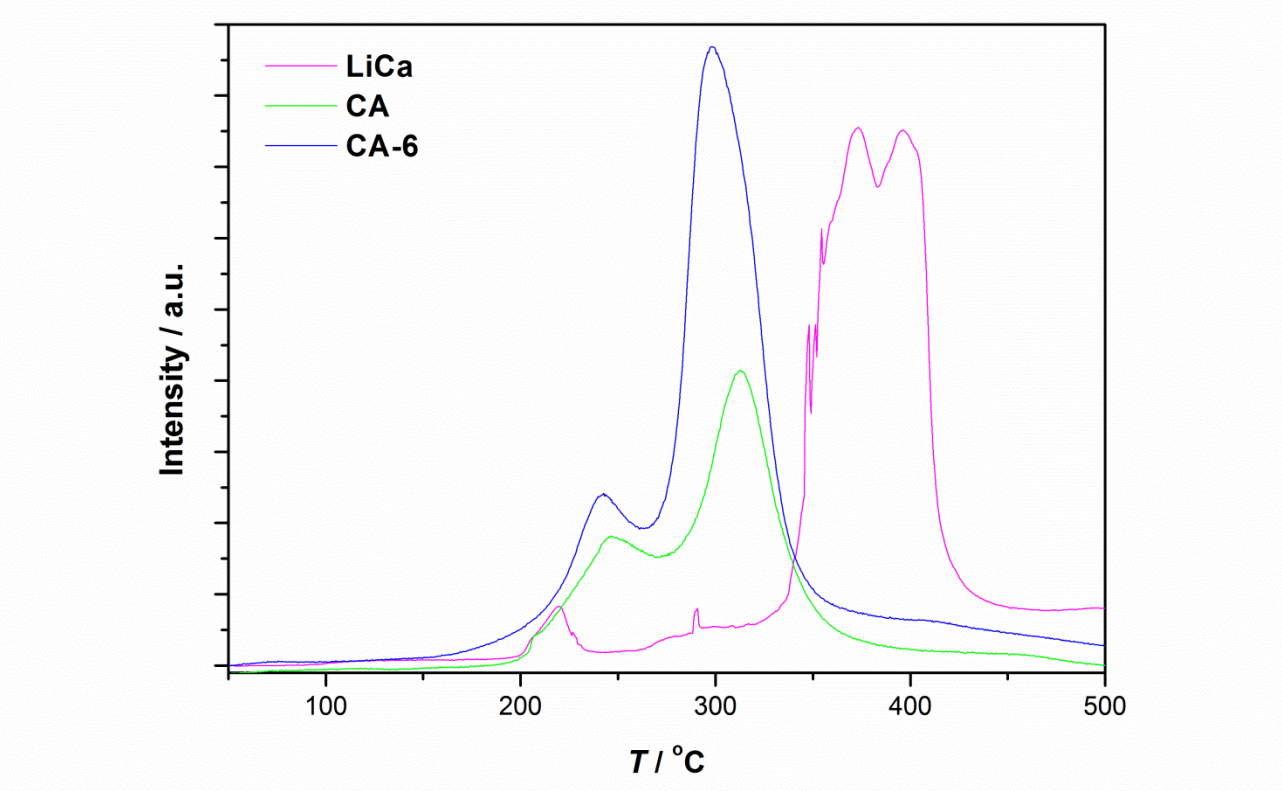

Figure S3 Temperature programmed desorption mass spectroscopy displaying the hydrogen release rate during heating from 50 to 500 °C ($\triangle T/\triangle t$ = 2 °C/min). Mass spectroscopy detected the H_2^+ ions (*m/e* = 2). Bulk $0.7LiBH_4$-$0.3Ca(BH_4)_2$ (pink) and melt infiltrated LiCa into CA (green), and CA-6 (Blue).

FT-IR

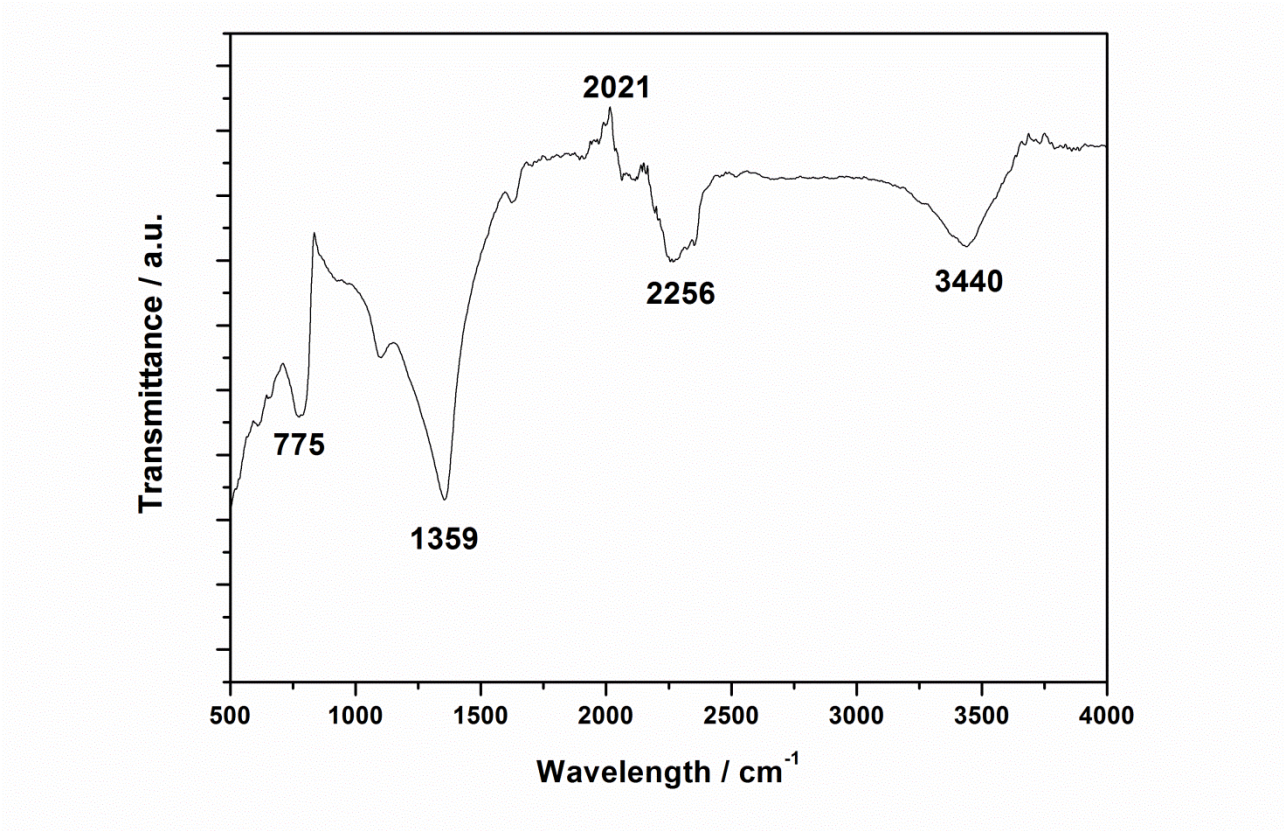

Figure S4 FT-IR of sample CA-6 rehydrided at 400 ^{O}C and $p(H_2)$ = 140 bar during 10 hours after three desorption

Supplementary Information of "Reversibility of $LiBH_4$ facilitated by the $LiBH_4$-$Ca(BH_4)_2$ eutectic"

Supporting Information

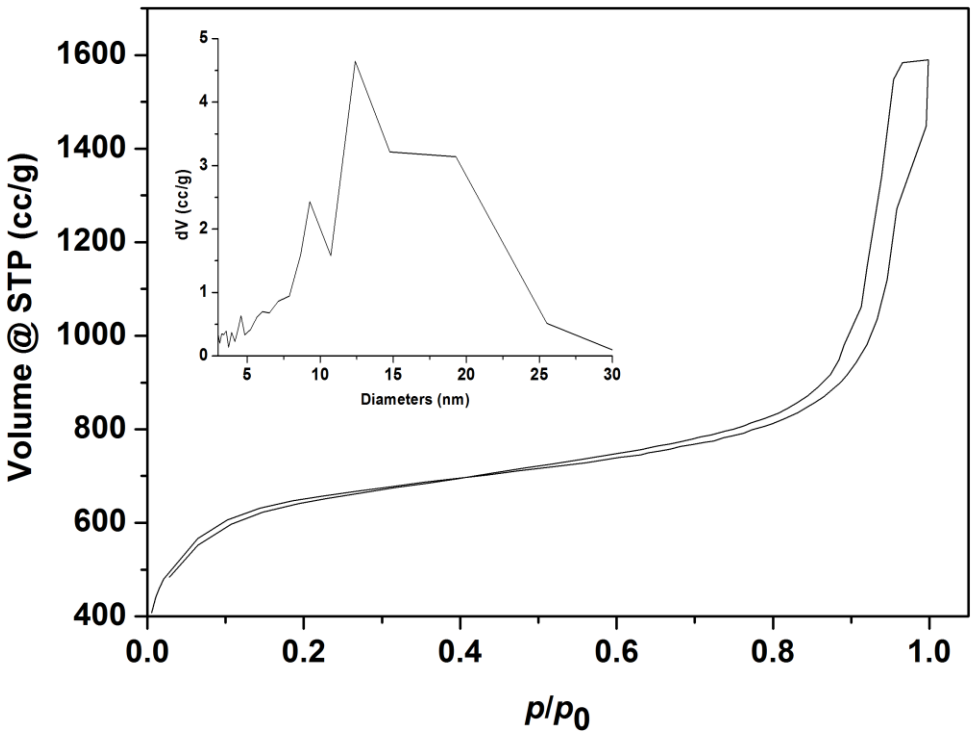

Figure S1 Nitrogen absorption-desorption isotherm of the carbon aerogel scaffold. The inset displays the pore size distribution of the scaffold D_{max} centred at 12.9 nm.

Rietveld Refinement

The quantity of the respective component present in the rehydrogenated sample is determined by Rietveld refinement of the PXD spectra using TOPAS. The background was described by a linear interpolation between selected points, Thompson-Cow-Hasting pseudo-Voigt Axial divergence asymmetry profile functions were used to fit the diffraction peaks. In the refinement, cell parameters, scale factors, profile parameters (V, W, Y), zero point and the background was refined. Possible stress and strain was neglected in the refinement.

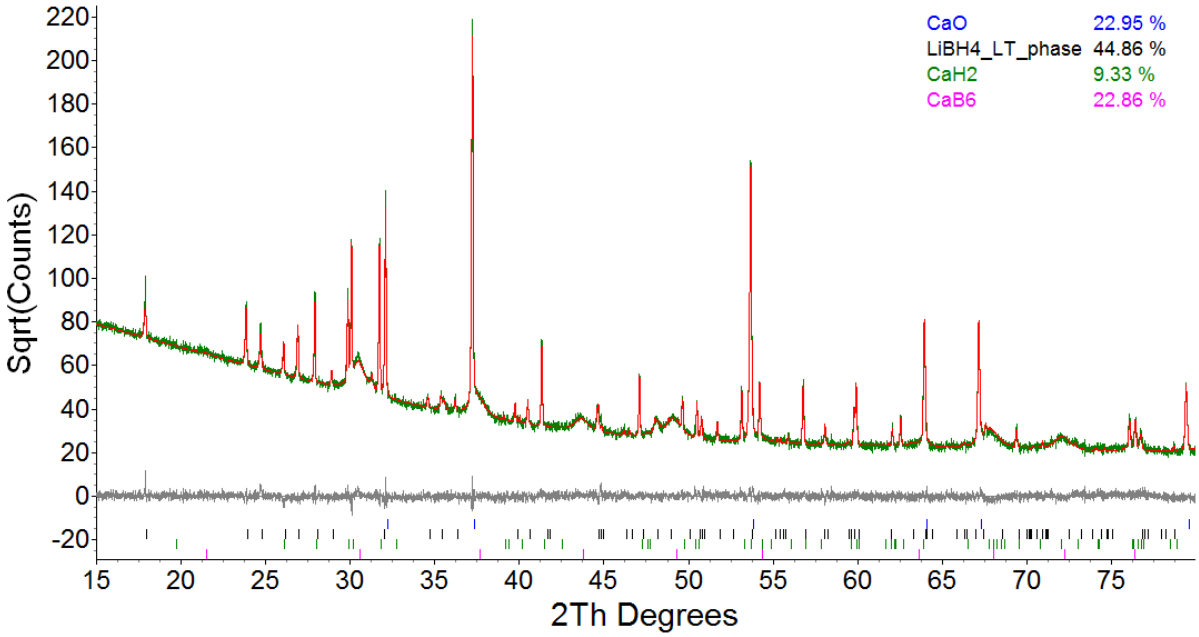

Figure S2 Rietveld refinement of the nanoconfined sample after the fifth rehydrogenation at 500 ˚C for 10 h at $p(H_2)$ = 134-144 bar. The fitted R_w value is 5.37 with a goodness of fit (GOF) of 2.59. Colour coded tic marks represents the respective compounds: CaO (blue), $LiBH_4$ (black), CaH_2 (green) and CaB_6 (pink).

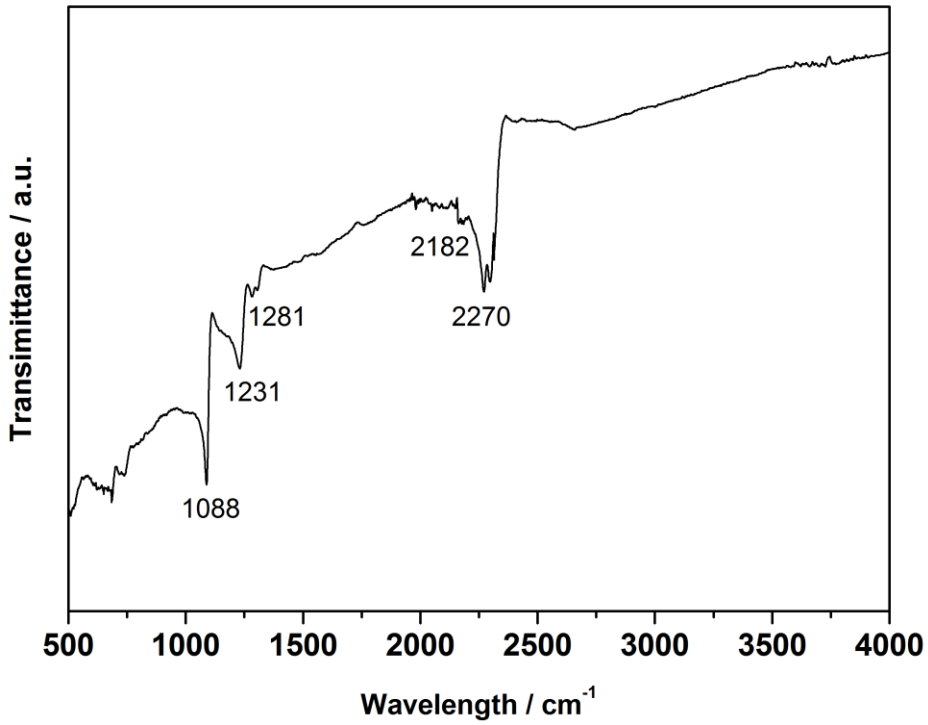

Figure S3 FT-IR spectrum of bulk $LiBH_4$-$Ca(BH_4)_2$ after the fifth rehydrogenation at 500 ˚C, p(H_2) = 134-144 bar.

Table S1 Cycling properties reported of selected bulk complex borohydrides and reactive hydride composite (RHC). The rehydrogenation conditions and notes on reversibility are displayed.

Compound	Rehydrogenation Conditions (*T/p/t*)	Cycling Stability	Reference
Pure Borohydride Systems			
$LiBH_4$@ZTC-750	260/120/12	54 % after 5 cycles	1
$LiBH_4$	265/90/5	D1: 3.5 wt.%, D2: 1.85 wt.%	2
$LiBH_4$-C_{60}	330/100/5	9 cycles. D1: 13.2 wt.%, D9: 3 wt.%	3
10wt.% Pt/C - $LiBH_4$	600/30/24	30 cycles 6.1 wt.% stable	4
10wt.% Pt/C - $LiBH_4$	600/30/24	D1: 9.3 wt.%, 4.3 wt% stable, 30 cycles	5
CA-$LiBH_4$	400/100/2	70 % retained after 3 desorption	6
Bulk $LiBH_4$	600/155/3.5	D1 to 600 °C = 10.9 wt.% H_2. D2 to 600 °C = 8.3 wt.%.	7

US patent - bulk $LiBH_4$	650/150/48	4 cycles. 77 % reversible after 4 cycles	8
$Ca(BH_4)_2$	350/90/24	1 rehyd. 50 % rehydrogenation. 3.8 wt.%	9
$Mg(BH_4)_2$	400/960/108	11.4 wt.% rehydrided	10
Borohydrides in RHC Systems			
$2LiBH_4$-MgF_2	450/100/24	3 cycles. 6.2 wt.% stable	11
$6LiBH_4$-CaF_2	450/92/-	3cycles D1: 9.3 wt.% D3:8 wt.%	12
CA-$2LiBH_4$-MgH_2	425/145/12	4 cycles stable 3.5 wt%	13
$LiBH_4$-$NaAlH_4$	400/140/10	4 desorptions, not stable, 3.38 wt.% after 4th desorption	14
CA-$LiBH_4$-$NaAlH_4$	400/140/10	4 desorptions, not stable, 3.4 wt.% after 4th desorption	14
$LiBH_4$-MgH_2	350/50/-	20 cycles. 9.2 wt.% H_2 after 20 desorption. Slowly decreasing pr. cycle	15
$LiBH_4$ – Al	400/100/2	10 cycles. Not stable. 1.8 wt% H_2 after 10th cycle	16
$LiBH_4$ - MgH_2 - Al	400/100/2.5	3 cycles. Not stable, 6.2 wt.% H_2	17
CA-$LiBH_4$-Mg_2NiH_4	450/176/10	5 cycles. Not Stable. 1.7 wt.% after 5th cycle	18
$4LiBH_4$ + YH_3	350/90/-	1 rehyd. 5.2 wt.% H_2	19
$LiBH_4$-CaH_2 - $TiCl_3$	450/80/16	10 cycles not fully stable. 7.1 wt.% after 10 desorption	20
$LiBH_4$-$NaBH_4$	400/140/10	4 cycles. Not Stable after 4 cycle. 1.6 wt.% H_2 stable	21
CA-$LiBH_4$-$NaBH_4$	400/140/10	4 cycles. Stable after 1 cycle. 6.4 wt% stable	21
$LiBH_4$-$Mg(BH_4)_2$	400/140/10	4 cycles. Stable after 3 cycle. 3.1 wt% stable	22
CA-$LiBH_4$-$Mg(BH_4)_2$	400/140/10	4 cycles. Stable after 2 cycle. 4.4 wt% stable	22
$LiBH_4$-$0.2MgCl_2$-$0.1TiCl_3$	600/70/-	D1:4.9 wt.%, D2:4.9 wt.%, D3: 4.24 wt.%	23
$LiBH_4$-$Ca(BH_4)_2$	330/40/-	1 Cycle 7 wt.%	24
$LiBH_4$-$Ca(BH_4)_2$	400/140/10	3 cycles, 73 % after 3rd desorption	25

References

1. J. Shao, X. Z. Xiao, X. L. Fan, X. Huang, B. Zhai, S. Q. Li, H. W. Ge, Q. D. Wang and L. X. Chen, *Nano Energy*, 2015, **15**, 244-255.
2. X. F. Wan and L. L. Shaw, *Acta Mater.*, 2011, **59**, 4606-4615.
3. P. A. Ward, J. A. Teprovich, B. Peters, J. Wheeler, R. N. Compton and R. Zidan, *J. Phys. Chem. C*, 2013, **117**, 22569-22575.
4. J. Xu, X. Yu, Z. Zou, Z. Li, Z. Wu, D. L. Akins and H. Yang, *Chem. Comm.*, 2008, 5740-5742.
5. J. Xu, X. B. Yu, J. Ni, Z. Q. Zou, Z. L. Li and H. Yang, *Dalton Trans.*, 2009, 8386-8391.
6. A. F. Gross, J. J. Vajo, S. L. Van Atta and G. L. Olson, *J. Phys. Chem. C*, 2008, **112**, 5651-5657.
7. P. Mauron, F. Buchter, O. Friedrichs, A. Remhof, M. Bielmann, C. N. Zwicky and A. Züttel, *J. Phys. Chem. B*, 2008, **112**, 906-910.
8. A. Muller, L. Havre, F. Mathey, V. Petit and J. Bensoam, *US Patent 4,193,978*, 1980.
9. J.-H. Kim, S.-A. Jin, J.-H. Shim and Y. W. Cho, *Scripta Mater.*, 2008, **58**, 481-483.
10. G. Severa, E. Rönnebro and C. M. Jensen, *Chem. Comm.*, 2010, **46**, 421-423.
11. P. P. Yuan, B. H. Liu and Z. P. Li, *Int. J. Hydrogen Energy*, 2011, **36**, 15266-15272.
12. P. P. Yuan, B. H. Liu, B. J. Zhang and Z. P. Li, *J. Phys. Chem. C*, 2011, **115**, 7067-7075.
13. R. Gosalawit-Utke, T. K. Nielsen, I. Saldan, D. Laipple, Y. Cerenius, T. R. Jensen, T. Klassen and M. Dornheim, *J. Phys. Chem. C*, 2011, **115**, 10903-10910.
14. P. Javadian, D. A. Sheppard, C. E. Buckley and T. R. Jensen, *Crystals*, 2016, **6**.
15. J. Jepsen, C. Milanese, A. Girella, G. A. Lozano, C. Pistidda, J. M. B. von Colbe, A. Marini, T. Klassen and M. Dornheim, *Int. J. Hydrogen Energy*, 2013, **38**, 8357-8366.
16. B. R. Hansen, D. B. Ravnsbæk, D. Reed, D. Book, C. Gundlach, J. Skibsted and T. R. Jensen, *J. Phys. Chem. C*, 2013, **117**, 7423-7432.
17. B. R. Hansen, D. B. Ravnsbæk, J. Skibsted and T. R. Jensen, *Phys. Chem. Chem. Phys.*, 2014, **16**, 8970-8980.
18. P. Javadian, C. Zlotea, C. M. Ghimbeu, M. Latroche and T. R. Jensen, *J. Phys. Chem. C*, 2015, **119**, 5819-5826.
19. J.-H. Shim, J.-H. Lim, S.-u. Rather, Y.-S. Lee, D. Reed, Y. Kim, D. Book and Y. W. Cho, *J. Phys. Chem. Lett.*, 2009, **1**, 59-63.
20. Y. Li, P. Li and X. Qu, *Sci. Rep.*, 2017, **7**.
21. P. Javadian, D. A. Sheppard, C. E. Buckley and T. R. Jensen, *Int. J. Hydrogen Energy*, 2015, **40**, 14916-14924.
22. P. Javadian and T. R. Jensen, *Int. J. Hydrogen Energy*, 2014, **39**, 9871-9876.
23. M. Au and A. Jurgensen, *J. Phys. Chem. B*, 2006, **110**, 7062-7067.
24. Y. Yan, A. Remhof, P. Mauron, D. Rentsch, Z. Łodziana, Y.-S. Lee, H.-S. Lee, Y. W. Cho and A. Züttel, *J. Phys. Chem. C*, 2013, **117**, 8878-8886.
25. P. Javadian, D. A. Sheppard, C. E. Buckley and T. R. Jensen, *Nano Energy*, 2015, **11**, 96-103.

APPENDIX II: Statement of Contribution of Others

Statement of Contribution of Others for "Destabilization of lithium hydride and the thermodynamic assessment of the Li-Al-H system for solar thermal energy storage".

1st June 2017

To Whom It May Concern

I, Prof. C.E. Buckley, contributed by project supervision and manuscript editing of the paper/publication entitled

Javadian, P.; Sheppard, D. A.; Jensen, T. R.; Buckley, C. E., *RSC Adv*, **2016**, 6, 94927.

Undertaken with Payam Javadian

(Signature of Co-Author)

C. E. Buckley

(Signature of First Author) Payam Javadian

Statement of Contribution of Others for "Destabilization of lithium hydride and the thermodynamic assessment of the Li-Al-H system for solar thermal energy storage".

1st June 2017

To Whom It May Concern

I, Prof. T.R. Jensen, contributed by project supervision and manuscript editing of the paper/publication entitled

Javadian, P.; Sheppard, D. A.; Jensen, T. R.; Buckley, C. E., *RSC Adv*, **2016**, 6, 94927.

Undertaken with Payam Javadian

(Signature of Co-Author)

T. R. Jensen

(Signature of First Author) Payam Javadian

Statement of Contribution of Others for "Destabilization of lithium hydride and the thermodynamic assessment of the Li-Al-H system for solar thermal energy storage".

1st June 2017

To Whom It May Concern

I, Dr. D.A. Sheppard, contributed by project supervision and manuscript editing of the paper/publication entitled

Javadian, P.; Sheppard, D. A.; Jensen, T. R.; Buckley, C. E., *RSC Adv*, **2016**, 6, 94927.

Undertaken with Payam Javadian

(Signature of Co-Author)

D. A. Sheppard

(Signature of First Author) Payam

Javadian

Statement of Contribution of Others for "Hydrogen Desorption Properties of Bulk and Nanoconfined $LiBH_4$-$NaAlH_4$".

1st June 2017

To Whom It May Concern

I, Prof. C.E. Buckley, contributed by project supervision and manuscript editing of the paper/publication entitled

Javadian, P.; Sheppard, D. A.; Buckley, C. E.; Jensen, T. R., *Crystals*, **2016**, *6*, 70.

Undertaken with Payam Javadian

(Signature of Co-Author)

C. E. Buckley

(Signature of First Author) Payam Javadian

Statement of Contribution of Others for "Hydrogen Desorption Properties of Bulk and Nanoconfined $LiBH_4$-$NaAlH_4$".

1st June 2017

To Whom It May Concern

I, Prof. T.R. Jensen, contributed by project supervision and manuscript editing of the paper/publication entitled

Javadian, P.; Sheppard, D. A.; Buckley, C. E.; Jensen, T. R., *Crystals*, **2016**, *6*, 70.

Undertaken with Payam Javadian

(Signature of Co-Author)

T. R. Jensen

(Signature of First Author) Payam Javadian

Statement of Contribution of Others for "Hydrogen Desorption Properties of Bulk and Nanoconfined $LiBH_4$-$NaAlH_4$".

1st June 2017

To Whom It May Concern

I, Dr. D.A. Sheppard, contributed by project supervision and manuscript editing of the paper/publication entitled

Javadian, P.; Sheppard, D. A.; Buckley, C. E.; Jensen, T. R., *Crystals*, **2016**, *6*, 70.

Undertaken with Payam Javadian

(Signature of Co-Author)

D. A. Sheppard

(Signature of First Author) Payam Javadian

Statement of Contribution of Others for "Hydrogen storage properties of nanoconfined $LiBH_4$-$Ca(BH_4)_2$".

1st June 2017

To Whom It May Concern

I, Prof. C.E. Buckley, contributed by project supervision and manuscript editing of the paper/publication entitled

Javadian, P.; Sheppard, D. A.; Buckley, C. E.; Jensen, T. R., *Nano Energy*, **2015**, *11*, 96-103.

Undertaken with Payam Javadian

(Signature of Co-Author)

C. E. Buckley

(Signature of First Author) Payam

Javadian

Statement of Contribution of Others for "Hydrogen storage properties of nanoconfined $LiBH_4$-$Ca(BH_4)_2$".

1st June 2017

To Whom It May Concern

I, Prof. T.R. Jensen, contributed by project supervision and manuscript editing of the paper/publication entitled

Javadian, P.; Sheppard, D. A.; Buckley, C. E.; Jensen, T. R., *Nano Energy*, **2015**, *11*, 96-103.

Undertaken with Payam Javadian

(Signature of Co-Author)

T. R. Jensen

(Signature of First Author) Payam

Javadian

Statement of Contribution of Others for "Hydrogen storage properties of nanoconfined $LiBH_4$-$Ca(BH_4)_2$".

1st June 2017

To Whom It May Concern

I, Dr. D.A. Sheppard, contributed by project supervision and manuscript editing of the paper/publication entitled

Javadian, P.; Sheppard, D. A.; Buckley, C. E.; Jensen, T. R., *Nano Energy*, **2015**, *11*, 96-103.

Undertaken with Payam Javadian

(Signature of Co-Author)

D. A. Sheppard

(Signature of First Author) Payam Javadian

Statement of Contribution of Others for "Hydrogen storage properties of nanoconfined $LiBH_4$-$NaBH_4$".

1st June 2017

To Whom It May Concern

I, Prof. C.E. Buckley, contributed by project supervision and manuscript editing of the paper/publication entitled

Javadian, P.; Sheppard, D. A.; Buckley, C. E.; Jensen, T. R., *Int. J. Hydrogen Energy*, **2015**, *40*, 14916-14924.

Undertaken with Payam Javadian

(Signature of Co-Author)

C. E. Buckley

(Signature of First Author) Payam

Javadian

Statement of Contribution of Others for "Hydrogen storage properties of nanoconfined $LiBH_4$-$NaBH_4$".

1st June 2017

To Whom It May Concern

I, Prof. T.R. Jensen, contributed by project supervision and manuscript editing of the paper/publication entitled

Javadian, P.; Sheppard, D. A.; Buckley, C. E.; Jensen, T. R., *Int. J. Hydrogen Energy*, **2015**, *40*, 14916-14924.

Undertaken with Payam Javadian

(Signature of Co-Author)

T. R. Jensen

(Signature of First Author) Payam

Javadian

Statement of Contribution of Others for "Hydrogen storage properties of nanoconfined $LiBH_4$-$NaBH_4$".

1st June 2017

To Whom It May Concern

I, Dr. D.A. Sheppard, contributed by project supervision and manuscript editing of the paper/publication entitled

Javadian, P.; Sheppard, D. A.; Buckley, C. E.; Jensen, T. R., *Int. J. Hydrogen Energy*, **2015**, *40*, 14916-14924.

Undertaken with Payam Javadian

(Signature of Co-Author)

D. A. Sheppard

(Signature of First Author)

Payam Javadian

APPENDIX III: Copyright Forms

Copyright information related to; Javadian, P.; Sheppard, D. A.; Jensen, T. R.; Buckley, C. E., *RSC Adv*, 2016, 6, 94927.

Reproduced by permission of The Royal Society of Chemistry

Link to the article:
http://pubs.rsc.org/en/content/articlelanding/2016/ra/c6ra16983j#!divAbstract

Dear Pavam

The Royal Society of Chemistry (RSC) hereby grants permission for the use of your paper(s) specified below in the printed and microfilm version of your thesis. You may also make available the PDF version of your paper(s) that the RSC sent to the corresponding author(s) of your paper(s) upon publication of the paper(s) in the following ways: in your thesis via any website that your university may have for the deposition of theses, via your university's Intranet or via your own personal website. We are however unable to grant you permission to include the PDF version of the paper(s) on its own in your institutional repository. The Royal Society of Chemistry is a signatory to the STM Guidelines on Permissions (available on request).

Please note that if the material specified below or any part of it appears with credit or acknowledgement to a third party then you must also secure permission from that third party before reproducing that material.

Please ensure that the thesis states the following:

Reproduced by permission of The Royal Society of Chemistry

and include a link to the paper on the Royal Society of Chemistry's website.

Please ensure that your co-authors are aware that you are including the paper in your thesis.

Regards

Gill Cockhead
Publishing Contracts & Copyright Executive

Gill Cockhead
Publishing Contracts & Copyright Executive
Royal Society of Chemistry,
Thomas Graham House,
Science Park, Milton Road,
Cambridge, CB4 0WF, UK
Tel +44 (0) 1223 432134

Copyright information related to; Javadian, P.; Sheppard, D. A.; Buckley, C. E.; Jensen, T. R., *Int. J. Hydrogen Energy*, 2015, *40*, 14916-14924.

ELSEVIER LICENSE
TERMS AND CONDITIONS

Mar 27, 2017

This Agreement between Payam Javadian ("You") and Elsevier ("Elsevier") consists of your license details and the terms and conditions provided by Elsevier and Copyright Clearance Center.

License Number	4062970976154
License date	Mar 06, 2017
Licensed Content Publisher	Elsevier
Licensed Content Publication	International Journal of Hydrogen Energy
Licensed Content Title	Hydrogen storage properties of nanoconfined LiBH4–NaBH4
Licensed Content Author	Payam Javadian,Drew A. Sheppard,Craig E. Buckley,Torben R. Jensen
Licensed Content Date	16 November 2015
Licensed Content Volume	40
Licensed Content Issue	43
Licensed Content Pages	9
Start Page	14916
End Page	14924
Type of Use	reuse in a thesis/dissertation
Portion	full article
Format	electronic
Are you the author of this Elsevier article?	Yes
Will you be translating?	No
Order reference number	
Title of your thesis/dissertation	Metal Hydrides as Energy Storage for Concentrated Solar Thermal Applications
Expected completion date	Apr 2017
Estimated size (number of pages)	150
Elsevier VAT number	GB 494 6272 12
Requestor Location	Payam Javadian Department of Imaging & Applied Physics Perth, GPO Box 1987 Perth, WA 1987 Australia Attn: Payam Javadian
Billing Type	Invoice
Billing Address	Payam Javadian Department of Imaging & Applied Physics Perth, GPO Box 1987

Copyright information related to; Javadian, P.; Sheppard, D. A.; Buckley, C. E.; Jensen, T. R., *Nano Energy*, 2015, *11*, 96-103.

ELSEVIER LICENSE
TERMS AND CONDITIONS

Mar 22, 2017

This Agreement between Payam Javadian ("You") and Elsevier ("Elsevier") consists of your license details and the terms and conditions provided by Elsevier and Copyright Clearance Center.

License Number	4056910319931
License date	Feb 27, 2017
Licensed Content Publisher	Elsevier
Licensed Content Publication	Nano Energy
Licensed Content Title	Hydrogen storage properties of nanoconfined LiBH4–Ca(BH4)2
Licensed Content Author	Payam Javadian,Drew A. Sheppard,Craig E. Buckley,Torben R. Jensen
Licensed Content Date	January 2015
Licensed Content Volume	11
Licensed Content Issue	n/a
Licensed Content Pages	8
Start Page	96
End Page	103
Type of Use	reuse in a thesis/dissertation
Intended publisher of new work	other
Portion	full article
Format	electronic
Are you the author of this Elsevier article?	Yes
Will you be translating?	No
Order reference number	
Title of your thesis/dissertation	Metal Hydrides as Energy Storage for Concentrated Solar Thermal Applications
Expected completion date	Apr 2017
Estimated size (number of pages)	150
Elsevier VAT number	GB 494 6272 12
Requestor Location	Payam Javadian Department of Imaging & Applied Physics Perth, GPO Box 1987 Perth, WA 1987 Australia Attn: Payam Javadian
Total	0.00 AUD
Terms and Conditions	

INTRODUCTION

Copyright information related to; Javadian, P.; Gharibdoust S. H., Li, H-W.; Sheppard, D. A.; Buckley, C. E.; Jensen, T. R., *J. Phys. Chem. C*, 2017, *121*, 18439-18449.

Copyright Clearance Center RightsLink®

Home | Account Info | Help

ACS Publications
Most Trusted. Most Cited. Most Read.

Title: Reversibility of LiBH4 Facilitated by the LiBH4–Ca(BH4)2 Eutectic

Author: Payam Javadian, SeyedHosein Payandeh GharibDoust, Hai-Wen Li, et al

Publication: The Journal of Physical Chemistry C

Publisher: American Chemical Society

Date: Aug 1, 2017

Logged in as:
Payam Javadian
Account #:
3001118027
LOGOUT

PERMISSION/LICENSE IS GRANTED FOR YOUR ORDER AT NO CHARGE

This type of permission/license, instead of the standard Terms & Conditions, is sent to you because no fee is being charged for your order. Please note the following:

- Permission is granted for your request in both print and electronic formats, and translations.
- If figures and/or tables were requested, they may be adapted or used in part.
- Please print this page for your records and send a copy of it to your publisher/graduate school.
- Appropriate credit for the requested material should be given as follows: "Reprinted (adapted) with permission from (COMPLETE REFERENCE CITATION). Copyright (YEAR) American Chemical Society." Insert appropriate information in place of the capitalized words.
- One-time permission is granted only for the use specified in your request. No additional uses are granted (such as derivative works or other editions). For any other uses, please submit a new request.

References

Adelhelm, P., and P. E. De Jongh. 2011. "The impact of carbon materials on the hydrogen storage properties of light metal hydrides." *Journal of Materials Chemistry* 21, 2417-2427.

Adelhelm, P., J. Gao, M. H. Verkuijlen, C. Rongeat, M. Herrich, P. J. M. van Bentum, O. Gutfleisch, A. P. Kentgens, K. P. de Jong, and P. E. de Jongh. 2010. "Comprehensive study of melt infiltration for the synthesis of $NaAlH_4$/C nanocomposites." *Chemistry of Materials* 22, 2233-2238.

Aizawa, T., T. Kuji, and H. Nakano. 1999. "Synthesis of Mg_2Ni alloy by bulk mechanical alloying." *Journal of alloys and compounds* 291, 248-253.

Al-Muhtaseb, S. A., and J. A. Ritter. 2003. "Preparation and properties of resorcinol-formaldehyde organic and carbon gels." *Advanced Materials* 15, 101-114.

Ampoumogli, A., G. Charalambopoulou, P. Javadian, B. Richter, T. R. Jensen, and T. Steriotis. "Hydrogen desorption and cycling properties of composites based on mesoporous carbons and a LiBH4–Ca(BH4)2 eutectic mixture." *Journal of Alloys and Compounds*.

Ampoumogli, A., T. Steriotis, P. Trikalitis, E. G. Bardaji, M. Fichtner, A. Stubos, and G. Charalambopoulou. 2012. "Synthesis and characterisation of a mesoporous carbon/calcium borohydride nanocomposite for hydrogen storage." *International Journal of Hydrogen Energy* 37, 16631-16635.

Au, M., and A. Jurgensen. 2006. "Modified lithium borohydrides for reversible hydrogen storage." *The Journal of Physical Chemistry B* 110, 7062-7067.

Au, Y. S., Y. Yan, K. P. de Jong, A. Remhof, and P. E. de Jongh. 2014. "Pore Confined Synthesis of Magnesium Boron Hydride Nanoparticles." *The Journal of Physical Chemistry C* 118, 20832-20839.

Baumann, T. F., M. A. Worsley, T. Y.-J. Han, and J. H. Satcher. 2008. "High surface area carbon aerogel monoliths with hierarchical porosity." *Journal of Non-Crystalline Solids* 354, 3513-3515.

Beeri, O., D. Cohen, Z. Gavra, and M. Mintz. 2003. "Sites occupation and thermodynamic properties of the $TiCr_{2-x}$-Mn_x–H_2 ($0 \leq x \leq 1$) system: statistical thermodynamics analysis." *Journal of alloys and compounds* 352, 111-122.

Berube, V., G. Chen, and M. Dresselhaus. 2008. "Impact of nanostructuring on the enthalpy of formation of metal hydrides." *international journal of hydrogen energy* 33, 4122-4131.

Bérubé, V., M. S. Dresselhaus, and G. Chen. 2009. "Nanostructuring Impact on the Enthalpy of Formation of Metal Hydrides." *Materials Issues in a Hydrogen Economy*, 92-101

364.

Bérubé, V., G. Radtke, M. Dresselhaus, and G. Chen. 2007. "Size effects on the hydrogen storage properties of nanostructured metal hydrides: a review." *International Journal of Energy Research* 31, 637-663.

Blach, T. P., and E. M. Gray. 2007. "Sieverts apparatus and methodology for accurate determination of hydrogen uptake by light-atom hosts." *Journal of Alloys and Compounds* 446, 692-697.

Blackman, J. M., J. W. Patrick, and C. E. Snape. 2006. "An accurate volumetric differential pressure method for the determination of hydrogen storage capacity at high pressures in carbon materials." *Carbon* 44, 918-927.

Bliznakov, S., N. Drenchev, B. Drenchev, P. Delchev, P. Solsona, and T. Spassov. 2005. "Electrochemical properties of nanocrystalline Mg_2Ni-type alloys prepared by mechanical alloying." *Journal of alloys and compounds* 404, 682-686.

Bogdanović, B., A. Reiser, K. Schlichte, B. Spliethoff, and B. Tesche. 2002. "Thermodynamics and dynamics of the Mg–Fe–H system and its potential for thermochemical thermal energy storage." *Journal of Alloys and Compounds* 345, 77-89.

Bogdanović, B., and M. Schwickardi. 2001. "Ti-doped $NaAlH_4$ as a hydrogen-storage material–preparation by Ti-catalyzed hydrogenation of aluminum powder in conjunction with sodium hydride." *Applied Physics A: Materials Science & Processing* 72, 221-223.

Bonnetot, B., G. Chahine, P. Claudy, M. Diot, and J. M. Letoffe. 1980. "Sodium tetrahydridoaluminate $NaAlH_4$ and hexahydridoaluminate Na_3AlH_6 molar heat capacity and thermodynamic properties from 10 to 300 K." *The Journal of Chemical Thermodynamics* 12, 249-254.

Brunauer, S., P. H. Emmett, and E. Teller. 1938. "Adsorption of gases in multimolecular layers." *Journal of the American chemical society* 60, 309-319.

Chaise, A., P. de Rango, P. Marty, and D. Fruchart. 2010. "Experimental and numerical study of a magnesium hydride tank." *International Journal of Hydrogen Energy* 35, 6311-6322.

Chemistry, H. 2007. "Outotech Research Oy."

Collins, D. J., and H.-C. Zhou. 2007. "Hydrogen storage in metal–organic frameworks." *Journal of materials chemistry* 17, 3154-3160.

Comanescu, C., G. Capurso, and A. Maddalena. 2012. "Nanoconfinement in activated mesoporous carbon of calcium borohydride for improved reversible hydrogen storage." *Nanotechnology* 23.

Conte, M., P. Prosini, and S. Passerini. 2004. "Overview of energy/hydrogen storage: state-of-the-art of the technologies and prospects for nanomaterials." *Materials Science and Engineering: B* 108, 2-8.

Corgnale, C., B. Hardy, T. Motyka, R. Zidan, J. Teprovich, and B. Peters. 2014. "Screening analysis of metal hydride based thermal energy storage systems for concentrating solar power plants." *Renewable and Sustainable Energy Reviews* 38, 821-833.

Corgnale, C., B. J. Hardy, D. A. Tamburello, S. L. Garrison, and D. L. Anton. 2012. "Acceptability envelope for metal hydride-based hydrogen storage systems." *International Journal of Hydrogen Energy* 37, 2812-2824.

David, E. 2005. "An overview of advanced materials for hydrogen storage." *Journal of materials processing technology* 162, 169-177.

de Jongh, P. E., R. W. Wagemans, T. M. Eggenhuisen, B. S. Dauvillier, P. B. Radstake, J. D. Meeldijk, J. W. Geus, and K. P. de Jong. 2007. "The preparation of carbon-supported magnesium nanoparticles using melt infiltration." *Chemistry of materials* 19, 6052-6057.

Dorian, J. P., H. T. Franssen, and D. R. Simbeck. 2006. "Global challenges in energy." *Energy Policy* 34, 1984-1991.

Dornheim, M., S. Doppiu, G. Barkhordarian, U. Boesenberg, T. Klassen, O. Gutfleisch, and R. Bormann. 2007. "Hydrogen storage in magnesium-based hydrides and hydride composites." *Scripta Materialia* 56, 841-846.

Dos Santos, D., M. Bououdina, and D. Fruchart. 2002. "Structural and thermodynamic properties of the pseudo-binary $TiCr_{2-x}V_x$ compounds with $0.0 \leq x \leq 1.2$." *Journal of alloys and compounds* 340, 101-107.

Eberle, U., G. Arnold, and R. Von Helmolt. 2006. "Hydrogen storage in metal–hydrogen systems and their derivatives." *Journal of Power Sources* 154, 456-460.

Eberle, U., M. Felderhoff, and F. Schueth. 2009. "Chemical and physical solutions for hydrogen storage." *Angewandte Chemie International Edition* 48, 6608-6630.

El Kharbachi, A., E. Pinatel, I. Nuta, and M. Baricco. 2012. "A thermodynamic assessment of $LiBH_4$." *Calphad* 39, 80-90.

Fang, Z. Z., P. Wang, T. E. Rufford, X. D. Kang, G. Q. Lu, and H. M. Cheng. 2008. "Kinetic- and thermodynamic-based improvements of lithium borohydride incorporated into activated carbon." *Acta Materialia* 56, 6257-6263.

Felderhoff, M., C. Weidenthaler, R. von Helmolt, and U. Eberle. 2007. "Hydrogen storage: the remaining scientific and technological challenges." *Physical Chemistry Chemical Physics* 9, 2643-2653.

Fellet, M., C. E. Buckley, M. Paskevicius, and D. A. Sheppard. 2013. "Research on metal hydrides revived for next-generation solutions to renewable energy storage." *MRS Bulletin* 38, 1012-1013.

Fichtner, M., Z. Zhao-Karger, J. Hu, A. Roth, and P. Weidler. 2009. "The kinetic properties of $Mg(BH_4)_2$ infiltrated in activated carbon." *Nanotechnology* 20, 204029.

Freeman, E. S. 1956. "The kinetics of the thermal decomposition of sodium nitrate and of the reaction between sodium nitrite and oxygen." *The Journal of Physical Chemistry* 60, 1487-1493.

Furukawa, H., M. A. Miller, and O. M. Yaghi. 2007. "Independent verification of the saturation hydrogen uptake in MOF-177 and establishment of a benchmark for hydrogen adsorption in metal–organic frameworks." *Journal of Materials Chemistry* 17, 3197-3204.

Gao, J., P. Adelhelm, M. H. Verkuijlen, C. Rongeat, M. Herrich, P. J. M. van Bentum, O. Gutfleisch, A. P. Kentgens, K. P. de Jong, and P. E. de Jongh. 2010. "Confinement of $NaAlH_4$ in nanoporous carbon: impact on H_2 release, reversibility, and thermodynamics." *The Journal of Physical Chemistry C* 114, 4675-4682.

Geoscience Australia. 2013. Geoscience Australia. www.geoscience.gov.au.

Gertsman, V. Y., and R. Birringer. 1994. "On the room-temperature grain growth in nanocrystalline copper." *Scripta metallurgica et materialia* 30, 577-581.

Gosalawit-Utke, R., S. Meethom, C. Pistidda, C. Milanese, D. Laipple, T. Saisopa, A. Marini, T. Klassen, and M. Dornheim. 2014. "Destabilization of LiBH4 by nanoconfinement in PMMA–co–BM polymer matrix for reversible hydrogen storage." *International Journal of Hydrogen Energy* 39, 5019-5029.

Gosalawit-Utke, R., C. Milanese, P. Javadian, A. Girella, D. Laipple, J. Puszkiel, A. S. Cattaneo et al. 2014. "2LiBH4–MgH2–0.13TiCl4 confined in nanoporous structure of carbon aerogel scaffold for reversible hydrogen storage." *Journal of Alloys and Compounds* 599, 78-86.

Gosalawit-Utke, R., C. Milanese, P. Javadian, J. Jepsen, D. Laipple, F. Karmi, J. Puszkiel et al. 2013. "Nanoconfined $2LiBH_4$-MgH_2-$TiCl_3$ in carbon aerogel scaffold for reversible hydrogen storage." *International Journal of Hydrogen Energy* 38, 3275-3282.

Gosalawit-Utke, R., C. Milanese, T. K. Nielsen, F. Karimi, I. Saldan, K. Pranzas, T. R. Jensen, A. Marini, T. Klassen, and M. Dornheim. 2013. "Nanoconfined 2LiBH4–MgH2 for reversible hydrogen storages: Reaction mechanisms, kinetics and thermodynamics." *International Journal of Hydrogen Energy* 38, 1932-1942.

Gosalawit-Utke, R., T. K. Nielsen, I. Saldan, D. Laipple, Y. Cerenius, T. R. Jensen, T. Klassen, and M. Dornheim. 2011. "Nanoconfined 2LiBH4–MgH2 Prepared by Direct Melt Infiltration into Nanoporous Materials." *The Journal of Physical Chemistry C* 115, 10903-10910.

Gosalawit−Utke, R., T. K. Nielsen, K. Pranzas, I. Saldan, C. Pistidda, F. Karimi, D. Laipple et al. 2012. "2LiBH4–MgH2 in a Resorcinol–Furfural Carbon Aerogel Scaffold for Reversible Hydrogen Storage." *The Journal of Physical Chemistry C* 116, 1526-1534.

Gosalawit–Utke, R., S. Thiangviriya, P. Javadian, D. Laipple, C. Pistidda, N. Bergemann, C. Horstmann, T. R. Jensen, T. Klassen, and M. Dornheim. 2014. "Effective nanoconfinement of 2LiBH4–MgH2 via simply MgH2 premilling for reversible hydrogen storages." *International Journal of Hydrogen Energy* 39, 15614-15626.

Gross, A. F., J. J. Vajo, S. L. Van Atta, and G. L. Olson. 2008. "Enhanced hydrogen storage kinetics of $LiBH_4$ in nanoporous carbon scaffolds." *The Journal of Physical Chemistry C* 112, 5651-5657.

Gross, K., G. Thomas, and C. Jensen. 2002. "Catalyzed alanates for hydrogen storage." *Journal of Alloys and Compounds* 330, 683-690.

Hansen, B. R., D. B. Ravnsbæk, D. Reed, D. Book, C. Gundlach, J. Skibsted, and T. R. Jensen. 2013. "Hydrogen storage capacity loss in a $LiBH_4$–Al composite." *The Journal of Physical Chemistry C* 117, 7423-7432.

Hansen, B. R., D. B. Ravnsbæk, J. Skibsted, and T. R. Jensen. 2014. "Hydrogen reversibility of $LiBH_4$–MgH_2–Al composites." *Physical Chemistry Chemical Physics* 16, 8970-8980.

Hanzawa, Y., K. Kaneko, R. Pekala, and M. Dresselhaus. 1996. "Activated carbon aerogels." *Langmuir* 12, 6167-6169.

Hardy, B. J., and D. L. Anton. 2009. "Hierarchical methodology for modeling hydrogen storage systems. Part II: Detailed models." *International Journal of Hydrogen Energy* 34, 2992-3004.

Harries, D. N., M. Paskevicius, D. A. Sheppard, T. E. C. Price, and C. E. Buckley. 2012. "Concentrating solar thermal heat storage using metal hydrides." *Proceedings of the IEEE* 100, 539-549.

House, S. D., X. Liu, A. A. Rockett, E. H. Majzoub, and I. M. Robertson. 2014. "Characterization of the Dehydrogenation Process of LiBH4 Confined in Nanoporous Carbon." *The Journal of Physical Chemistry C* 118, 8843-8851.

IEA. 2016. "U.S. Energy Intermation Administration - International Energy Outlook ".

International Energy Agency. 2016. "International Energy Agency. Key World Energy Statistics ".

J. Sangster, P., A. D. 2000. "“H - Li (Hydrogen - Lithium)” in Phase Diagrams of Binary Hydrogen Alloys, ed. Manchester, F. D., ASM International, Materials Park, OH, USA." 74 - 81.

Javadian, P., and T. R. Jensen. 2014. "Enhanced hydrogen reversibility of nanoconfined $LiBH_4$-$Mg(BH_4)_2$." *International Journal of Hydrogen Energy* 39, 9871-9876.

Javadian, P., D. A. Sheppard, C. E. Buckley, and T. R. Jensen. 2015a. "Hydrogen storage properties of nanoconfined $LiBH_4$-$Ca(BH_4)_2$." *Nano Energy* 11, 96-103.

Javadian, P., D. A. Sheppard, C. E. Buckley, and T. R. Jensen. 2015b. "Hydrogen storage properties of nanoconfined $LiBH_4$-$NaBH_4$." *International Journal of Hydrogen Energy* 40, 14916-14924.

Javadian, P., D. A. Sheppard, C. E. Buckley, and T. R. Jensen. 2016. "Hydrogen Desorption Properties of Bulk and Nanoconfined $LiBH_4$-$NaAlH_4$." *Crystals* 6.

Javadian, P., C. Zlotea, C. M. Ghimbeu, M. Latroche, and T. R. Jensen. 2015. "Hydrogen Storage Properties of Nanoconfined LiBH4–Mg2NiH4 Reactive Hydride Composites." *The Journal of Physical Chemistry C* 119, 5819-5826.

Jepsen, J., C. Milanese, A. Girella, G. A. Lozano, C. Pistidda, J. M. B. von Colbe, A. Marini, T. Klassen, and M. Dornheim. 2013. "Compaction pressure influence on material properties and sorption behaviour of $LiBH_4$–MgH_2 composite." *International Journal of Hydrogen Energy* 38, 8357-8366.

Job, N., R. Pirard, J. Marien, and J.-P. Pirard. 2004. "Porous carbon xerogels with texture tailored by pH control during sol–gel process." *Carbon* 42, 619-628.

Khudhair, A. M., and M. M. Farid. 2004. "A review on energy conservation in building applications with thermal storage by latent heat using phase change materials." *Energy conversion and management* 45, 263-275.

Kim, J.-H., S.-A. Jin, J.-H. Shim, and Y. W. Cho. 2008. "Reversible hydrogen storage in calcium borohydride $Ca(BH_4)_2$." *Scripta Materialia* 58, 481-483.

Klose, W., and V. Stuke. 1995. "Investigation of the thermodynamic equilibrium in the hydrogen-magnesium-magnesium hydride system." *International journal of hydrogen energy* 20, 309-316.

Lai, Q., M. Christian, and K.-F. Aguey-Zinsou. 2014. "Nanoconfinement of borohydrides in CuS hollow nanospheres: A new strategy compared to carbon nanotubes." *International Journal of Hydrogen Energy* 39, 9339-9349.

Langford, J. I., and D. Louer. 1996. "Powder diffraction." *Reports on Progress in Physics* 59, 131.

Lee, H.-S., S.-J. Hwang, H. K. Kim, Y.-S. Lee, J. Park, J.-S. Yu, and Y. W. Cho. 2012. "In Situ NMR Study on the Interaction between LiBH4–Ca(BH4)2 and Mesoporous Scaffolds." *The Journal of Physical Chemistry Letters* 3, 2922-2927.

Lee, H. S., Y. S. Lee, J. Y. Suh, M. Kim, J. S. Yu, and Y. W. Cho. 2011. "Enhanced Desorption and Absorption Properties of Eutectic LiBH4-Ca(BH4)(2) Infiltrated into Mesoporous Carbon." *Journal of Physical Chemistry C* 115, 20027-20035.

Lee, S.-M., and T.-P. Perng. 1999. "Correlation of substitutional solid solution with hydrogenation properties of $TiFe_{1-x}M_x$ (M= Ni, Co, Al) alloys." *Journal of alloys and compounds* 291, 254-261.

Lee, S.-M., and T.-P. Perng. 2000. "Effects of boron and carbon on the hydrogenation properties of TiFe and $Ti_{1.1}Fe$." *International journal of hydrogen energy* 25, 831-836.

Leisure, R., K. Foster, J. Hightower, and D. Agosta. 2003. "Elastic properties of intermetallic AB_2 and AB_5 hydrogen-absorbing compounds." *Journal of alloys and compounds* 356, 283-289.

Li, Y., P. Li, and X. Qu. 2017. "Investigation on $LiBH_4$-CaH_2 composite and its potential for thermal energy storage." *Scientific Reports* 7.

Li, Y., G. Zhou, F. Fang, X. Yu, Q. Zhang, L. Ouyang, M. Zhu, and D. Sun. 2011. "De-/re-hydrogenation features of $NaAlH_4$ confined exclusively in nanopores." *Acta materialia* 59, 1829-1838.

Lin, C., and J. Ritter. 1997. "Effect of synthesis pH on the structure of carbon xerogels." *Carbon* 35, 1271-1278.

Lin, C., and J. A. Ritter. 2000. "Carbonization and activation of sol–gel derived carbon xerogels." *Carbon* 38, 849-861.

Liu, M., N. S. Tay, S. Bell, M. Belusko, R. Jacob, G. Will, W. Saman, and F. Bruno. 2016. "Review on concentrating solar power plants and new developments in high temperature thermal energy storage technologies." *Renewable and Sustainable Energy Reviews* 53, 1411-1432.

Liu, X., D. Peaslee, C. Z. Jost, T. F. Baumann, and E. H. Majzoub. 2011. "Systematic Pore-Size Effects of Nanoconfinement of LiBH4: Elimination of Diborane Release and Tunable Behavior for Hydrogen Storage Applications." *Chemistry of Materials* 23, 1331-1336.

Liu, X., D. Peaslee, T. P. Sheehan, and E. H. Majzoub. 2014. "Decomposition Behavior of Eutectic LiBH4–Mg(BH4)2 and Its Confinement Effects in Ordered Nanoporous Carbon." *The Journal of Physical Chemistry C* 118, 27265-27271.

Liu, X. F., D. Peaslee, C. Z. Jost, and E. H. Majzoub. 2010. "Controlling the Decomposition Pathway of LiBH4 via Confinement in Highly Ordered Nanoporous Carbon." *Journal of Physical Chemistry C* 114, 14036-14041.

Løvvik, O. M., and S. M. Opalka. 2005. "Density functional calculations of Ti-enhanced $NaAlH_4$." *Physical Review B* 71, 054103.

Løvvik, O. M., O. Swang, and S. M. Opalka. 2005. "Modeling alkali alanates for hydrogen storage by density-functional band-structure calculations." *Journal of materials research* 20, 3199-3213.

Mark Paskevicius, L. J., Pascal Schouwink, Dorthe B. Ravnsbæk, Morten B. Ley, Yaroslav Filinchuk, Radovan Ĉerný, Flemming Besenbacher, Torben R. Jensen. 2017. "Metal Borohydrides and derivatives - synthesis, structure and properties." *Chem. Soc. Rev.*

Martelli, P., R. Caputo, A. Remhof, P. Mauron, A. Borgschulte, and A. Züttel. 2010. "Stability and decomposition of $NaBH_4$." *The Journal of Physical Chemistry C* 114, 7173-7177.

Mauron, P., F. Buchter, O. Friedrichs, A. Remhof, M. Bielmann, C. N. Zwicky, and A. Züttel. 2008. "Stability and reversibility of $LiBH_4$." *The Journal of Physical Chemistry B* 112, 906-910.

MAXLAB. 2016. "https://www.maxiv.lu.se/."

Miyamura, H., M. Takada, K. Hirose, and S. Kikuchi. 2003. "Metal hydride electrodes using titanium–iron-based alloys." *Journal of alloys and compounds* 356, 755-758.

Møller, K. T., A. S. Fogh, M. Paskevicius, J. Skibsted, and T. R. Jensen. 2016. "Metal borohydride formation from aluminium boride and metal hydrides." *Physical Chemistry Chemical Physics* 18, 27545-27553.

Mueller, T., and G. Ceder. 2010. "Effect of particle size on hydrogen release from sodium alanate nanoparticles." *ACS nano* 4, 5647-5656.

Mulas, G., R. Campesi, S. Garroni, E. Napolitano, C. Milanese, F. Dolci, E. Pellicer, M. D. Baró, and A. Marini. 2012. "Hydrogen storage in 2NaBH4 + MgH2 mixtures: Destabilization by additives and nanoconfinement." *Journal of Alloys and Compounds* 536, Supplement 1, S236-S240.

Muller, A., L. Havre, F. Mathey, V. Petit, and J. Bensoam. "US Patent 4,193,978, 1980."

Nambu, T., H. Ezaki, H. Yukawa, and M. Morinaga. 1999. "Electronic structure and hydriding property of titanium compounds with CsCl-type structure." *Journal of alloys and compounds* 293, 213-216.

Ngene, P., P. Adelhelm, A. M. Beale, K. P. de Jong, and P. E. de Jongh. 2010. "$LiBH_4$/SBA-15 Nanocomposites Prepared by Melt Infiltration under Hydrogen Pressure: Synthesis and Hydrogen Sorption Properties." *Journal of Physical Chemistry C* 114, 6163-6168.

Ngene, P., R. van den Berg, M. H. W. Verkuijlen, K. P. de Jong, and P. E. de Jongh. 2011. "Reversibility of the hydrogen desorption from $NaBH_4$ by confinement in nanoporous carbon." *Energy & Environmental Science* 4, 4108-4115.

Ngene, P., M. van Zwienen, and P. E. de Jongh. 2010. "Reversibility of the hydrogen desorption from LiBH4: a synergetic effect of nanoconfinement and Ni addition." *Chemical Communications* 46, 8201-8203.

Ngene, P., M. H. W. Verkuijlen, Q. Zheng, J. Kragten, P. J. M. van Bentum, J. H. Bitter, and P. E. de Jongh. 2011. "The role of Ni in increasing the reversibility of the hydrogen release from nanoconfined LiBH4." *Faraday Discussions* 151, 47-58.

Nielsen, T. K., U. Bösenberg, R. Gosalawit, M. Dornheim, Y. Cerenius, F. Besenbacher, and T. R. Jensen. 2010. "A Reversible Nanoconfined Chemical Reaction." *ACS Nano* 4, 3903-3908.

Orimo, S., Y. Nakamori, G. Kitahara, K. Miwa, N. Ohba, S. Towata, and A. Züttel. 2005. "Dehydriding and rehydriding reactions of." *Journal of Alloys and Compounds* 404–406, 427-430.

Panella, B., and M. Hirscher. 2005. "Hydrogen physisorption in metal–organic porous crystals." *Advanced Materials* 17, 538-541.

Pardo, P., A. Deydier, Z. Anxionnaz-Minvielle, S. Rougé, M. Cabassud, and P. Cognet. 2014. "A review on high temperature thermochemical heat energy storage." *Renewable and Sustainable Energy Reviews* 32, 591-610.

Paskevicius, M., D. A. Sheppard, and C. E. Buckley. 2010. "Thermodynamic changes in mechanochemically synthesized magnesium hydride nanoparticles." *Journal of the American chemical Society* 132, 5077-5083.

Pekala, R. 1989. "Organic aerogels from the polycondensation of resorcinol with formaldehyde." *Journal of Materials Science* 24, 3221-3227.

Pekala, R., and D. Schaefer. 1993. "Structure of organic aerogels. 1. Morphology and scaling." *Macromolecules* 26, 5487-5493.

Peru, F., S. Garroni, R. Campesi, C. Milanese, A. Marini, E. Pellicer, M. D. Baró, and G. Mulas. 2013. "Ammonia-free infiltration of NaBH4 into highly-ordered mesoporous silica and carbon matrices for hydrogen storage." *Journal of Alloys and Compounds* 580, Supplement 1, S309-S312.

Plerdsranoy, P., N. Wiset, C. Milanese, D. Laipple, A. Marini, T. Klassen, M. Dornheim, and R. Gosalawit–Utke. 2015. "Improvement of thermal stability and reduction of LiBH4/polymer host interaction of nanoconfined LiBH4 for reversible hydrogen storage." *International Journal of Hydrogen Energy* 40, 392-402.

Principi, G., F. Agresti, A. Maddalena, and S. L. Russo. 2009. "The problem of solid state hydrogen storage." *Energy* 34, 2087-2091.

Ravnsbæk, D. B., and T. R. Jensen. 2012. "Mechanism for reversible hydrogen storage in $LiBH_4$–Al." *Journal of Applied Physics* 111, 112621.

Reilly, J., and R. Wiswall Jr. 1974. "Formation and properties of iron titanium hydride." *Inorganic Chemistry* 13, 218-222.

Remhof, A., P. Mauron, A. Züttel, J. P. Embs, Z. Łodziana, A. J. Ramirez-Cuesta, P. Ngene, and P. de Jongh. 2013. "Hydrogen Dynamics in Nanoconfined Lithiumborohydride." *The Journal of Physical Chemistry C* 117, 3789-3798.

Ritter, J. A., A. D. Ebner, J. Wang, and R. Zidan. 2003. "Implementing a hydrogen economy." *Materials Today* 6, 18-23.

Rongeat, C., I. L. Jansa, S. Oswald, L. Schultz, and O. Gutfleisch. 2009. "Mechanochemical synthesis and XPS analysis of sodium alanate with different additives." *Acta Materialia* 57, 5563-5570.

Rönnebro, E., G. Whyatt, M. Powell, M. Westman, F. Zheng, and Z. Fang. 2015. "Metal Hydrides for High-Temperature Power Generation." *Energies* 8, 8406.

Roque-Malherbe, R. M. 2007. *Adsorption and diffusion in nanoporous materials*: CRC press.

Sabrina, S., D. K. Kenneth, H. Fredrik Sydow, H. H. Richard, B. Elisa Gil, Z.-K. Zhirong, F. Maximilian, and C. H. Bjørn. 2012. "Influence of nanoconfinement on morphology and dehydrogenation of the Li 11 BD 4 –Mg(11 BD 4) 2 system." *Nanotechnology* 23, 255704.

Sakintuna, B., F. Lamari-Darkrim, and M. Hirscher. 2007. "Metal hydride materials for solid hydrogen storage: a review." *International Journal of Hydrogen Energy* 32, 1121-1140.

Saliger, R., V. Bock, R. Petricevic, T. Tillotson, S. Geis, and J. Fricke. 1997. "Carbon aerogels from dilute catalysis of resorcinol with formaldehyde." *Journal of Non-Crystalline Solids* 221, 144-150.

Sarkar, A., and R. Banerjee. 2005. "Net energy analysis of hydrogen storage options." *International Journal of Hydrogen Energy* 30, 867-877.

Sartori, S., K. D. Knudsen, Z. Zhao-Karger, E. G. Bardaij, M. Fichtner, and B. C. Hauback. 2009. "Small-angle scattering investigations of Mg-borohydride infiltrated in activated carbon." *Nanotechnology* 20.

Sartori, S., K. D. Knudsen, Z. Zhao-Karger, E. G. Bardaji, J. Muller, M. Fichtner, and B. C. Hauback. 2010. "Nanoconfined Magnesium Borohydride for Hydrogen Storage Applications Investigated by SANS and SAXS." *The Journal of Physical Chemistry C* 114, 18785-18789.

Satyapal, S., J. Petrovic, C. Read, G. Thomas, and G. Ordaz. 2007. "The US Department of Energy's National Hydrogen Storage Project: Progress towards meeting hydrogen-powered vehicle requirements." *Catalysis today* 120, 246-256.

Schlapbach, L., and A. Züttel. 2001. "Hydrogen-storage materials for mobile applications." *Nature* 414, 353-358.

Seta, S., and H. Uchida. 1995. "Hydrogen solubility in $LaNi_5$." *Journal of alloys and compounds* 231, 448-453.

Severa, G., E. Rönnebro, and C. M. Jensen. 2010. "Direct hydrogenation of magnesium boride to magnesium borohydride: demonstration of >11 weight percent reversible hydrogen storage." *Chemical Communications* 46, 421-423.

Shafiee, S., and E. Topal. 2009. "When will fossil fuel reserves be diminished?" *Energy policy* 37, 181-189.

Shang, C., M. Bououdina, Y. Song, and Z. Guo. 2004. "Mechanical alloying and electronic simulations of (MgH_2+M) systems (M=Al, Ti, Fe, Ni, Cu and Nb) for hydrogen storage." *International Journal of Hydrogen Energy* 29, 73-80.

Shao, J., X. Xiao, X. Fan, L. Zhang, S. Li, H. Ge, Q. Wang, and L. Chen. 2014. "Low-Temperature Reversible Hydrogen Storage Properties of LiBH4: A Synergetic Effect of Nanoconfinement and Nanocatalysis." *The Journal of Physical Chemistry C* 118, 11252-11260.

Shao, J., X. Z. Xiao, X. L. Fan, X. Huang, B. Zhai, S. Q. Li, H. W. Ge, Q. D. Wang, and L. X. Chen. 2015. "Enhanced hydrogen storage capacity and reversibility of $LiBH_4$ nanoconfined in the densified zeolite-templated carbon with high mechanical stability." *Nano Energy* 15, 244-255.

Shaver, G. R., W. D. Billings, F. S. Chapin, A. E. Giblin, K. J. Nadelhoffer, W. C. Oechel, and E. Rastetter. 1992. "Global change and the carbon balance of arctic ecosystems." *BioScience* 42, 433-441.

Sheppard, D., C. Corgnale, B. Hardy, T. Motyka, R. Zidan, M. Paskevicius, and C. Buckley. 2014. "Hydriding characteristics of $NaMgH_2F$ with preliminary technical and cost evaluation of magnesium-based metal hydride materials for concentrating solar power thermal storage." *RSC Advances* 4, 26552-26562.

Sheppard, D., M. Paskevicius, T. Humphries, M. Felderhoff, G. Capurso, J. B. von Colbe, M. Dornheim, T. Klassen, P. Ward, and J. Teprovich Jr. 2016. "Metal hydrides for concentrating solar thermal power energy storage." *Applied Physics A* 122, 1-15.

Shim, J.-H., J.-H. Lim, S.-u. Rather, Y.-S. Lee, D. Reed, Y. Kim, D. Book, and Y. W. Cho. 2009. "Effect of hydrogen back pressure on dehydrogenation behavior of $LiBH_4$-based reactive hydride composites." *The Journal of Physical Chemistry Letters* 1, 59-63.

Solomon, S., G.-K. Plattner, R. Knutti, and P. Friedlingstein. 2009. "Irreversible climate change due to carbon dioxide emissions." *Proceedings of the national academy of sciences*, pnas. 0812721106.

Stephens, R. D., A. F. Gross, S. L. Van Atta, J. J. Vajo, and F. E. Pinkerton. 2009. "The kinetic enhancement of hydrogen cycling in $NaAlH_4$ by melt infusion into nanoporous carbon aerogel." *Nanotechnology* 20, 204018.

Sun, D., H. Enoki, F. Gingl, and E. Akiba. 1999. "New approach for synthesizing Mg-based alloys." *Journal of alloys and compounds* 285, 279-283.

Sunshot. 2012. "Sunshot Vision Study- U.S Department of Energy,."

Tanaka, S., J. Clewley, and T. B. Flanagan. 1977. "Kinetics of hydrogen absorption by lanthanum-nickel ($LaNi_5$)." *The Journal of Physical Chemistry* 81, 1684-1688.

The Guardian. 2003. "Bill McGuire "Will Global warming trigger a new ice age?" The Guadian Thursday 13 November 2003."

Thiangviriya, S., P. Plerdsranoy, N. Wiset, P. Javadian, T. R. Jensen, and R. Utke. 2015. "Hydrogen sorption and reaction mechanisms of nanoconfined 2LiBH4–NaAlH4." *Journal of Alloys and Compounds* 633, 484-493.

Thiangviriya, S., and R. Utke. 2015. "LiBH4 nanoconfined in activated carbon nanofiber for reversible hydrogen storage." *International Journal of Hydrogen Energy* 40, 4167-4174.

Tian, H.-Y., C. Buckley, S. Mule, M. Paskevicius, and B. Dhal. 2008. "Preparation, microstructure and hydrogen sorption properties of nanoporous carbon aerogels under ambient drying." *Nanotechnology* 19, 475605.

Verkuijlen, M. H. W., P. Ngene, D. W. de Kort, C. Barre, A. Nale, E. R. H. van Eck, P. J. M. van Bentum, P. E. de Jongh, and A. P. M. Kentgens. 2012. "Nanoconfined LiBH4 and Enhanced Mobility of Li+ and BH4- Studied by Solid-State NMR." *Journal of Physical Chemistry C* 116, 22169-22178.

Vitousek, P. M. 1994. "Beyond Global Warming: Ecology and Global Change." *Ecology* 75, 1861-1876.

Von Zeppelin, F., M. Haluška, and M. Hirscher. 2003. "Thermal desorption spectroscopy as a quantitative tool to determine the hydrogen content in solids." *Thermochimica acta* 404, 251-258.

Wahab, M. A., Y. Jia, D. J. Yang, H. J. Zhao, and X. D. Yao. 2013. "Enhanced hydrogen desorption from Mg(BH4)(2) by combining nanoconfinement and a Ni catalyst." *Journal of Materials Chemistry A* 1, 3471-3478.

Wahab, M. A., H. Zhao, and X. D. Yao. 2012. "Nano-confined ammonia borane for chemical hydrogen storage." *Frontiers of Chemical Science and Engineering* 6, 27-33.

Wallner, T., H. Lohse-Busch, S. Gurski, M. Duoba, W. Thiel, D. Martin, and T. Korn. 2008. "Fuel economy and emissions evaluation of BMW Hydrogen 7 Mono-Fuel demonstration vehicles." *International Journal of Hydrogen Energy* 33, 7607-7618.

Wan, X. F., and L. L. Shaw. 2011. "Novel dehydrogenation properties derived from nanoscale $LiBH_4$." *Acta Materialia* 59, 4606-4615.

Wang, J., A. D. Ebner, T. Prozorov, R. Zidan, and J. A. Ritter. 2005. "Effect of graphite as a co-dopant on the dehydrogenation and hydrogenation kinetics of Ti-doped sodium aluminum hydride." *Journal of alloys and compounds* 395, 252-262.

Wang, K. K., X. D. Kang, Y. J. Zhong, C. H. Hu, J. W. Ren, and P. Wang. 2014. "Unexpected Dehydrogenation Behaviors of the 2LiBH(4)-MgH2 Composite Confined in a Mesoporous Carbon Scaffold." *Journal of Physical Chemistry C* 118, 26447-26453.

Wang, Y. T., C. B. Wan, X. H. Meng, and X. Ju. "Improvement of the LiBH4 hydrogen desorption by confinement in modified carbon nanotubes." *Journal of Alloys and Compounds*.

Ward, P. A., J. A. Teprovich, B. Peters, J. Wheeler, R. N. Compton, and R. Zidan. 2013. "Reversible Hydrogen Storage in a $LiBH_4$-C_{60} Nanocomposite." *Journal of Physical Chemistry C* 117, 22569-22575.

World Energy Outlook. 2008. "World Energy Outlook 2008, International energy agency, ."

Xia, G., Q. Meng, Z. Guo, Q. Gu, H. Liu, Z. Liu, and X. Yu. 2013. "Nanoconfinement significantly improves the thermodynamics and kinetics of co-infiltrated 2LiBH4–LiAlH4 composites: Stable reversibility of hydrogen absorption/resorption." *Acta Materialia* 61, 6882-6893.

Xia, G. L., L. Li, Z. P. Guo, Q. F. Gu, Y. H. Guo, X. B. Yu, H. K. Liu, and Z. W. Liu. 2013. "Stabilization of NaZn(BH4)(3) via nanoconfinement in SBA-15 towards enhanced hydrogen release." *Journal of Materials Chemistry A* 1, 250-257.

Xu, J., X. Yu, Z. Zou, Z. Li, Z. Wu, D. L. Akins, and H. Yang. 2008. "Enhanced dehydrogenation of $LiBH_4$ catalyzed by carbon-supported Pt nanoparticles." *Chemical Communications*, 5740-5742.

Xu, J., X. B. Yu, J. Ni, Z. Q. Zou, Z. L. Li, and H. Yang. 2009. "Enhanced catalytic dehydrogenation of $LiBH_4$ by carbon-supported Pd nanoparticles." *Dalton Transactions*, 8386-8391.

Yan, Y., Y. S. Au, D. Rentsch, A. Remhof, P. E. de Jongh, and A. Zuttel. 2013. "Reversible hydrogen storage in Mg(BH4)2/carbon nanocomposites." *Journal of Materials Chemistry A* 1, 11177-11183.

Yan, Y., A. Remhof, P. Mauron, D. Rentsch, Z. Łodziana, Y.-S. Lee, H.-S. Lee, Y. W. Cho, and A. Züttel. 2013. "Controlling the dehydrogenation reaction toward reversibility of the $LiBH_4$–$Ca(BH_4)_2$ eutectic system." *The Journal of Physical Chemistry C* 117, 8878-8886.

Yao, X., Z. Zhu, H. Cheng, and G. Lu. 2008. "Hydrogen diffusion and effect of grain size on hydrogenation kinetics in magnesium hydrides."

Yuan, P. P., B. H. Liu, and Z. P. Li. 2011. "A comparative study of $LiBH_4$-based composites with metal hydrides and fluorides for hydrogen storage." *International Journal of Hydrogen Energy* 36, 15266-15272.

Yuan, P. P., B. H. Liu, B. J. Zhang, and Z. P. Li. 2011. "Reversible Hydrogen Storage Composite Based on $6LiBH_4 + CaF_2$." *Journal of Physical Chemistry C* 115, 7067-7075.

Zaluska, A., L. Zaluski, and J. Ström–Olsen. 1999. "Nanocrystalline magnesium for hydrogen storage." *Journal of Alloys and Compounds* 288, 217-225.

Zanto, E. J., S. A. Al-Muhtaseb, and J. A. Ritter. 2002. "Sol− Gel-Derived Carbon Aerogels and Xerogels: Design of Experiments Approach to Materials Synthesis." *Industrial & engineering chemistry research* 41, 3151-3162.

Zhao-Karger, Z., J. Hu, A. Roth, D. Wang, C. Kubel, W. Lohstroh, and M. Fichtner. 2010. "Altered thermodynamic and kinetic properties of MgH2 infiltrated in microporous scaffold." *Chemical Communications* 46, 8353-8355.

Zhao-Karger, Z., R. Witter, E. G. Bardaji, D. Wang, D. Cossement, and M. Fichtner. 2013. "Altered reaction pathways of eutectic LiBH4-Mg(BH4)(2) by nanoconfinement." *Journal of Materials Chemistry A* 1, 3379-3386.

Zheng, S., F. Fang, G. Zhou, G. Chen, L. Ouyang, M. Zhu, and D. Sun. 2008. "Hydrogen storage properties of space-confined $NaAlH_4$ nanoparticles in ordered mesoporous silica." *Chemistry of Materials* 20, 3954-3958.

Züttel, A. 2003. "Materials for hydrogen storage." *Materials today* 6, 24-33.

Züttel, A. 2004. "Hydrogen storage methods." *Naturwissenschaften* 91, 157-172.

Züttel, A., A. Borgschulte, and L. Schlapbach. 2008. "Hydrogen as a Future Energy Carrier." *Wiley-VHC Meinheim Germany*.

Züttel, A., P. Wenger, S. Rentsch, P. Sudan, P. Mauron, and C. Emmenegger. 2003. "LiBH4 a new hydrogen storage material." *Journal of Power Sources* 118, 1-7.

Copyright Declaration

“Every reasonable effort has been made to acknowledge the owners of copyright material. I would be pleased to hear from any copyright owner who has been omitted or incorrectly acknowledged”

Payam Javadian

Signature: Payam Javadian

Date: 30 June 2017